



Ollscoil Chathair  
Bhaile Átha Cliath  
Dublin City University

# **Platforms for the development of Electrochemiluminescent Biosensors**

**Author**

**Miren Ruiz de Eguilaz (MSc)**

A thesis submitted at Dublin City University for the degree of  
Doctor of Philosophy

School of Chemical Sciences

Supervisors:


Prof. Robert J. Forster

Prof. Mary Pryce

September 2023

## DECLARATION

I hereby certify that this material, which I now submit for assessment on the programme of study leading to the award of doctor of philosophy is entirely my own work, that I have exercised reasonable care to ensure that the work is original, and does not to the best of my knowledge breach any law of copyright, and has not been taken from the work of others save and to the extent that such work has been cited and acknowledged within the text of my work.

Signed:.....

ID no.: 20211840....

Date:...08/09/2023...

## **DEDICATION**

Dedicated to my amazing parents.

*“Nothing in life is to be feared, it is only to be understood. Now is the time to understand more, so that we may fear less”.*

**Maria Salomea Skłodowska-Curie**

## ACKNOWLEDGEMENTS

I would like to take this opportunity to thank all the people that since I first started this journey, have helped me professionally and personally to get through it. From the beginning to the end of the completion of this PhD thesis, I encountered with many challenges and obstacles that were not expected, and being surrounded by supportive and wonderful people made possible that today I feel the strength and the confidence necessary to face which is the last step of this process, and for that I'm grateful.

First, I would like to thank my supervisor Prof. Robert Forster for all the guidance, advice and support provided since I joined the group. I will always appreciate the opportunity that he gave me and for trusting that a biologist could also take the challenge of learning electrochemistry and even writing a full thesis about it. I would also like to extend my gratitude to now Associate Prof. Loanda Cumba for introducing me to the group and helping me throughout these years. My sincere thanks to the School of Chemistry, NCSR and NRF and all the staff who made outstanding efforts to make sure the system kept going for all the PhD students, especially during the COVID-19 pandemic.

To my group members and now friends, Ellie, Angelo, and Amanda that shared laughs, tears and the funniest stories that made this experience unique. I will always remember our "distant" morning coffees and how helpful they were during the difficult and isolating times of the COVID-19 pandemic. I feel honoured and lucky that I got to meet and share space with the most intelligent but also good-hearted people on campus. Special thanks to Estefania, who I had the chance to travel with to many places apart from working together. We lived the most unfortunate but also interesting situations during these trips. From colleagues to friends, te quiero amiga!

However, everyone knows who my favourite in this group is, Dr. Fionn O Maolmhuaidh (only a few months ahead of me). The first Irish man that I met who charmed me out and convinced me to date him. I have no words to describe the impact that you had in my life and how much your love, kindness, sarcasm, wittiness and "no pasa nadaa" helped me to get here. Hope we can keep achieving goals together for years, I love you to bits.

My last sentences of gratitude are going to be dedicated to my family. My mam (amatxito), the most resilient and kind person that ever lived in this world. You always encouraged me to follow this path and strongly believed in me, thank you. My twin sister,

who had no doubts that despite the difficult times we went through as a family, I would be able to complete this journey. And finally, my dad (aitatxo), who fought fiercely against cancer the last year and never gave up. You left us one month ago but all your love, teachings and joy for life stayed with us. He is the main reason why I got to the finish line. Dad, we made it together!

# CONTENTS

## Chapter 1

1. INTRODUCTION.....	26
2. CLASSIFICATION OF ELECTROCHEMICAL BIOSENSORS .....	29
2.1. Label based electrochemical biosensors.....	32
2.1.1. Enzyme based labels .....	33
2.1.2. Nanomaterial-based labels .....	36
2.1.3. Electrochemiluminescent labels .....	42
2.2. Label-free electrochemical biosensors.....	49
2.2.1. Electrochemical impedance spectroscopy (EIS).....	49
2.2.2. Detection of enzymes and metabolites released by pathogens.....	51
3. CONCLUSIONS AND FUTURE PERSPECTIVES .....	52

## Chapter 2

1. INTRODUCTION.....	56
2. MATERIALS AND METHODOLOGY.....	59
2.1. Manufacture of 3D printed Ti arrays and workflow .....	59
2.2. Characterization of 3D printed Ti electrodes .....	60
2.3. Surface treatment and gold electrodeposition .....	61
3. RESULTS AND DISCUSSION.....	62
3.1. Bare 3D-printed Ti electrodes.....	62
3.1.1. Surface characterization.....	62
3.1.2. Electrochemical characterization of 3D-printed Ti electrodes .....	64
3.1.3. ECL characterization of 3D printed Ti electrodes in co-reactant system....	66
3.2. Gold coated Ti electrodes .....	68
3.2.1. Gold electrodeposition .....	68
3.2.2. Surface characterization.....	71
3.2.3. Electrochemical characterization of gold coated electrodes.....	73
3.2.4. ECL characterization in co-reactant system .....	79
4. CONCLUSION.....	83

## Chapter 3

1. INTRODUCTION.....	86
----------------------	----

2. MATERIALS AND METHODOLOGY.....	90
2.1. Chemicals.....	90
2.2. DNA-dye conjugation and purification protocol.....	91
2.3. Spectroscopic characterization.....	91
2.4. Electrochemiluminescence characterization.....	92
3. RESULTS AND DISCUSSION.....	92
3.1. Dyes and AuNPs.....	92
3.1.1. UV-Vis, Zeta-potential and DLS.....	92
3.1.2. Fluorescence: steady state and time-resolved spectroscopy.....	96
3.1.3. ECL characterization.....	106
3.2. DNA probe conjugation: [Ru(bpy) <sub>3</sub> -NH <sub>2</sub> ] <sup>2+</sup> and [Ru(bpy) <sub>2</sub> (phen)-NH <sub>2</sub> ] <sup>2+</sup> .....	111
3.2.1. UV-Vis and fluorescence characterization.....	111
4. CONCLUSIONS.....	114

## Chapter 4

1. INTRODUCTION.....	117
2. MATERIALS AND METHODOLOGY.....	120
2.1. Chemical reagents.....	120
2.2. Electrochemical and electrochemiluminescent (ECL) experiments.....	121
2.3. Sequence selection.....	121
2.4. Electrode preparation and modification steps.....	121
3. RESULTS AND DISCUSSION.....	123
3.1. Electrodeposition of AuNPs and electrochemical characterization.....	123
3.2. ECL characterization and co-reactant study.....	128
3.3. Assay development.....	131
3.3.1. Surface modification and characterization.....	131
3.3.2. ECL detection of gene <i>fimH</i> from UTI causing <i>E.coli</i> .....	134
4. CONCLUSIONS.....	137

## Chapter 5

1. INTRODUCTION.....	139
2. MATERIALS AND METHODOLOGY.....	142
2.1. Chemical reagents.....	142
2.2. Synthesis of Fe <sub>3</sub> O <sub>4</sub> core/Au shell particles.....	142
2.2.1. Synthesis Fe <sub>3</sub> O <sub>4</sub> core via the thermal decomposition method.....	142
2.2.2. Washing of synthesized Fe <sub>3</sub> O <sub>4</sub> particles.....	143

2.2.3.	Au coating of Fe <sub>3</sub> O <sub>4</sub> particles .....	144
2.2.4.	Washing step and phase transfer .....	144
2.3.	Characterization of Fe <sub>3</sub> O <sub>4</sub> core/Au shell particles.....	145
3.	RESULTS AND DISCUSSION .....	146
3.1.	Fe <sub>3</sub> O <sub>4</sub> core/Au shell particles characterization .....	146
3.1.1.	SEM and TEM images .....	146
3.1.2.	UV-Vis measurements .....	147
3.2.	Citrate capped Fe <sub>3</sub> O <sub>4</sub> core/Au shell particles characterization: FT-IR and UV-Vis	150
3.3.	Theoretical DNA loading on Fe <sub>3</sub> O <sub>4</sub> /Au shell particles .....	152
4.	CONCLUSIONS .....	155

## Chapter 6

1.	FINAL REMARKS .....	158
2.	FUTURE RESEARCH WORK .....	160
3.	APPLICATIONS OUTSIDE SENSORS .....	162
	BIBLIOGRAPHY .....	164



## LIST OF ABBREVIATIONS

<u>Acronyms</u>	<u>Explanation</u>
2D	Two-dimensional
3D	Three-dimensional
Ab2	Secondary antibody
AFM	Atomic Force Microscopy
AgNPs	Silver nanoparticles
ALP	Alkaline phosphatase
ATR	Attenuated Total Reflectance
AuNPs	Gold nanoparticles
CFU	Colony forming units
CV	Cyclic Voltammetry
DLS	Dynamic Light Scattering
DMF	N,N-Dimethylformamide
DNA	Deoxyribonucleic acid
DPV	Double Pulse Voltammetry
dsDNA	Double stranded deoxyribonucleic acid
DTSP	Dithiobis(succinimidyl/propionate)
ECL	Electrochemiluminescence
EDX	Energy Disperse X-Ray
EIS	Electrochemical Impedance Spectroscopy
ERT	Energy Resonance Transfer
FcnMeOH	Ferrocene methanol
FITC	Fluorescein isothiocyanate
FTIR	Fourier-Transform Infrared Spectroscopy
GCE	Glassy-carbon electrode
GO	Graphene Oxide
HAU	Hemagglutination units

HBAg	Hepatitis B antigen
HCV	Hepatitis C Virus
HER	Hydrogen evolution reaction
HHQ	4-hydroxyquinoline
HOMO	Highest Occupied Molecular Orbital
HPLC	High-performance liquid chromatography
HRI	High Refractive Index
HRP	Horseradish peroxidase
IDE	Interdigitated electrode
IEP	Isoelectric point
IP	3-Indoxylphosphate
ITO	Indium-tin-oxide
LOD	Limit of detection
LSPR	Localize Surface Plasmon Resonance
LUMO	Lower Unoccupied Molecular Orbital
MCH	6-mercapto-1-hexanol
MNPs	Magnetic nanoparticles
MWCNTs	Multiwall carbon nanotubes
NBEA	N-butyl-diethanolamine
NHS	N-Hydroxysuccinimide
NMP	N-Methyl-2-pyrrolidone
NRs	Nanorods
OER	Oxygen evolution reaction
OHP	Outer Helmholtz Plane
PANI	Polyaniline
PB	Prussian Blue
PBS	Phosphate-buffered saline
PCR	Polymerase Chain Reaction
PDMS	Poly(dimethylsiloxane)
PMT	Photon multiplier

PNA	Peptide Nucleic Acid
POC	Point-of-care
PQS	Pseudomonas quinolone
PW	Prussian White
PYO	Pyocyanin
QDs	Quantum Dots
QS	Quorum Sensing
RNA	Ribonucleic acid
rRNA	Ribosomal ribonucleic acid
RSD	Relative Standard Deviation
SEM	Scanning Electron Microscopy
SHE	Standard hydrogen electrode
SLE	Saturated calomel electrode
SLM	Selective Laser Melting
SNP	Single Nucleotide Polymorphism
SPE	Screen-printed electrode
SPR	Surface Plasmon Resonance
ssDNA	Single stranded deoxyribonucleic acid
TCEP	Tris(2-carboxyethyl)phosphine
TE buffer buffer	Tris and Ethylenediaminetetraacetic acid
TEM	Transmission Electron Microscopy
TMAOH	Tetramethylammonium hydroxide
TMB	3,3',5,5'-tetramethyl benzidine
TMPD diamine	N,N,N',N'-tetramethyl-para-phenylene-
TrPA	Tri-n-propylamine
UTIs	Urinary tract infections
UV-Vis	Ultraviolet Visible
ZIKV	Zika Virus

## LIST OF SYMBOLS

<u>Symbols</u>	<u>Explanation</u>	<u>Units</u>
$A_{exp}$	Experimental area	$cm^2$
$A_{geo}$	Geometrical area	$cm^2$
CPE	Constant Phase Element	$F\Omega^{-1} cm^{-2} s^n$
d	Diameter	cm
D	Diffusion coefficient	$cm^2 s^{-1}$
$E^0$	Redox potential	V
$E_p$	Peak potential	V
$E_{pa}$	Anodic peak potential	V
$E_{pc}$	Cathodic peak potential	V
$\epsilon$	Extinction coefficient	$mol\ cm^{-1}$
I	Fluorescence intensity	a.u.
$I_{pa}$	Anodic current	A
$I_{pc}$	Cathodic current	A
$k^0$	Heterogenous electron transfer rate constant	$cm\ s^{-1}$
$K_q$	Quenching rate constant	$L\ mol^{-1}\ s^{-1}$
$K_{SV}$	Stern-Volmer constant	$L\ mol^{-1}$
M	Atomic weight	$g\ mol^{-1}$
n	Number of electrons	(-)
N	Number of gold atoms	(-)
$N_A$	Avogadro's number	(-)
$N_{seed}$	Number of particles per mL	particle $mL^{-1}$
$Q_{exp}$	Experimental charge	C
$Q_{theo}$	Theoretical charge	C
R	Gas constant	$J\ mol^{-1}\ K^{-1}$
$R_{ct}$	Charge transfer resistance	$\Omega$

$R_s$	Solution resistance	$\Omega$
$t$	Time	s
$V$	Volume	L
$A$	Charge transfer coefficient	(-)
$\delta$	Diffusion layer thickness	cm
$\Delta E_p$	Peak-to-peak separation	V
$v$	Scan rate	$V s^{-1}$
$\rho$	Density	$g cm^{-3}$
$\tau$	Excited state lifetime	ns

## LIST OF FIGURES

### Chapter 1:

<b>Figure 1.</b> Overview of the thesis with main issues and challenges studied in every chapter. ....	29
<b>Figure 2.</b> Schematic representation of biosensor elements and label-free and labelled biosensors.....	32
<b>Figure 3.</b> Representation of the PDMS substrate and ZnO nanorods functionalised with the primary capture antibody. The secondary antibody is labelled with horseradish peroxidase, HRP, which oxidises, TMB, generating a current related the viral load in the sample. ....	35
<b>Figure 4.</b> Schematic illustration of the components of the sandwich type immunosensor and the measurement by amperometric i-t curve in H <sub>2</sub> O <sub>2</sub> (applying -0.6V). ....	39
<b>Figure 5.</b> Schematic illustration of the immunosensor using Fe <sub>3</sub> O <sub>4</sub> MNPs as self-sacrificial label. A) Electrochemical conversion of Fe <sub>3</sub> O <sub>4</sub> MNPs in two-potentiostatic steps (first potential applied, +1.6 V, followed by 0V) for PB analogue production (PW), in a solution containing 0.4 mM K <sub>4</sub> Fe(CN) <sub>6</sub> and 0.1M K <sub>2</sub> SO <sub>4</sub> . ....	42
<b>Figure 6.</b> Schematic illustration of ECL annihilation and co-reactant pathways <sup>109</sup> .....	44
<b>Figure 7.</b> Diagram of the Faraday-cage like ECL immunosensor for detection of <i>Vibrio vulnificus</i> . ....	46
<b>Figure 8.</b> Schematic representation of HCV-based sensor and distance-dependent plasmon-enhanced ECL mediated by non-metallic plasmonic MoS <sub>2</sub> nanosheets and QDs. ....	49
<b>Figure 9.</b> Illustration of fabricated EIS immunosensor via immobilization of ZIKV-envelop protein antibody (Zev-Abs) onto self-assembled monolayer (SAM) of dithiobis(succinimidyl propionate) (DTSP) deposited on interdigitated micro-electrode of gold (IDE-Au) array of 10µm <sup>146</sup> . ....	51

### Chapter 2:

<b>Figure 1.</b> Architecture and wiring of electrodes. A) 3D printed Ti electrode. B) Wired 3D printed Ti electrode. C) Mechanically polished 3D printed Ti electrode.....	60
<b>Figure 2.</b> Scheme of Chapter 2 workflow. ....	60
<b>Figure 3.</b> ECL signal recording equipment. A) ECL set up: (1) Potentiostat, (2) power-supply, (3) amplifier/recorder, (4) PC desktop for data visualization and (5) dark box. B)	

Set-up inside dark box: photomultiplier (PMT), secondary amplifier, connectors, and fibre optic for light collection. The circle indicates where the three-electrodes electrochemical cell is placed to record the signal. .... 61

**Figure 4.** SEM images of 3D-printed Ti electrodes using an accelerating voltage that ranges from 1 kV to 2 kV. A) 3D-printed Ti arrays (with cylinders, no etched). Edge, tip of cylinder and base of electrode (from left to right). Scale bars (left to right): 300  $\mu\text{m}$  B) Base of mechanically polished 3D-printed Ti arrays with sandpaper (no cylinders). Scale bars (left to right): 400  $\mu\text{m}$ , 50  $\mu\text{m}$  and 400  $\mu\text{m}$ . .... 63

**Figure 5.** Voltammogram of bare 3D printed Ti electrode in 0.1M LiClO<sub>4</sub> solution as supporting electrolyte. Scan rate at 0.1 V s<sup>-1</sup>. .... 65

**Figure 6.** Voltammograms in 1 mM FcnMeOH as redox probe and 0.1M LiClO<sub>4</sub> as supporting electrolyte (degassed). A) Bare Ti array. Scan rates: 0.05 V s<sup>-1</sup>, 0.1 V s<sup>-1</sup>, 0.15 V s<sup>-1</sup>, 0.2 V s<sup>-1</sup>, 0.25 V s<sup>-1</sup>, 0.5 V s<sup>-1</sup>, 0.7 V s<sup>-1</sup> and 1 V s<sup>-1</sup>. B) Overlay of bare Ti array and bare polished Ti electrode. Scan rate: 0.1 V s<sup>-1</sup>. Electrodes stored in air. .... 66

**Figure 7.** ECL response of Ti electrodes using 0.1mM Ru[bpy]<sub>2</sub><sup>+3</sup> redox probe, 0.1M TrPA as co-reactant and 0.1M LiClO<sub>4</sub> as supporting electrolyte. ECL profiles A) Bare Ti array and B) Bare mechanically polished electrode. Voltammograms C) Bare Ti array and D) Bare mechanically polished electrode. Scan rates: 0.05 V s<sup>-1</sup> (black), 0.1 V s<sup>-1</sup> (red), 0.15 V s<sup>-1</sup> (blue), 0.2 V s<sup>-1</sup> (green). .... 68

**Figure 8.** Electrodeposition of gold on 3D printed Ti electrode. A) Chronoamperometric i-t curve, potential applied -0.9 V for 700 s. B) Voltammogram, scanned from -0.5V to -2.0 V at 0.1 V s<sup>-1</sup>, first cycle. Inset: voltammogram, 28 cycles. .... 71

**Figure 9.** SEM images of gold functionalized 3D-printed Ti electrodes, using 2 kV as accelerating voltage. A) Gold functionalized 3D-printed Ti gold arrays (with cylinders, chemically treated). Cylinder, tip of cylinder and edge of cylinder (from left to right). Scale bars (left to right): 200  $\mu\text{m}$ , 50  $\mu\text{m}$  and 50  $\mu\text{m}$ . B) Mechanically polished gold functionalized 3D-printed Ti arrays with sandpaper (no cylinders, chemically treated). Base of electrode. Scale bars (left to right): 500  $\mu\text{m}$ , 100  $\mu\text{m}$  and 10  $\mu\text{m}$ . .... 72

**Figure 10.** Voltammograms of gold coated 3D-printed Ti electrodes in 0.1M H<sub>2</sub>SO<sub>4</sub> as supporting electrolyte. Scan rate: 0.2 V s<sup>-1</sup>. .... 73

**Figure 11.** Voltammograms in 1 mM FcnMeOH as redox probe and 0.1M LiClO<sub>4</sub> as supporting electrolyte (deaerated). A) Gold coated Ti array. Scan rates: 0.05 V s<sup>-1</sup>, 0.1 V s<sup>-1</sup>, 0.15 V s<sup>-1</sup>, 0.2 V s<sup>-1</sup>, 0.25 V s<sup>-1</sup>, 0.5 V s<sup>-1</sup>, 0.7 V s<sup>-1</sup> and 1 V s<sup>-1</sup>. B) Overlay of gold coated Ti array and gold coated polished Ti electrode. Scan rate 0.1 V s<sup>-1</sup>. .... 75

**Figure 12.** Randles-Sevcik plots using 1mM FcnMeOH as redox probe and 0.1M LiClO<sub>4</sub> as supporting electrolyte. Anodic peak current (ip<sub>a</sub>) and cathodic peak current (ip<sub>c</sub>). A) Gold coated array and B) gold coated polished electrode. The error bar represents the standard deviation from three independent measurements (same electrode, three independent measurements of same electrode after surface cleaning treatment). ..... 75

**Figure 13.** Plots of anodic peak potential and cathodic peak potential vs. the logarithm of scan rate. A) Gold coated Ti array. B) Gold coated polished Ti electrode. .... 76

**Figure 14.** Schematic representation of diffusion model of 3D-Printed Ti electrodes. A) Radial diffusion at the tip of cylinders (blue arrows) and linear diffusion (black arrows) at the wall of the cylinders. B) Structural representation of a section of the electrode., d (distance between cylinders), L (cylinder length) and r (cylinder radius). ..... 79

**Figure 15.** Time dependence of the thickness of the diffusion layer (δ) in dimensional variables for diffusion coefficient (D= 7.0 x 10<sup>-6</sup> cm<sup>2</sup> s<sup>-1</sup>). ..... 79

**Figure 16.** ECL response of gold coated Ti electrodes using 0.1mM Ru[bpy]<sub>2</sub><sup>+3</sup> redox probe, 0.1M TrPA as co-reactant and 0.1M LiClO<sub>4</sub> as supporting electrolyte. ECL profiles A) Gold coated Ti array. Inset: ECL response at 0.1 V s<sup>-1</sup> over 3 cycles. B) mechanically polished and gold coated electrode. Inset: ECL response at 0.1 V s<sup>-1</sup> in 3 cycles. Voltammograms C) Gold coated Ti array and E) Gold coated and mechanically polished electrode. Scan rates: 0.05 V s<sup>-1</sup> (black), 0.1 V s<sup>-1</sup> (red), 0.15 mV s<sup>-1</sup> (blue), 0.2 mV s<sup>-1</sup> (green). ..... 81

**Figure 17.** Plot of ECL intensity over the scan rate. A) Gold modified Ti array. B) Gold modified and polished Ti electrode. The error bar represents the standard deviation from three independent measurements of one array (n=3). ..... 82

### **Chapter 3:**

**Figure 1.** Schematic representation of luminescent processes. A) Photoluminescence<sup>7</sup>. B) Electrochemiluminescence generation through oxidative-reductive co-reactant pathway with [Ru(bpy)<sub>3</sub>]<sup>2+</sup> as luminophore<sup>8</sup>. ..... 87

**Figure 2.** Schematic representation of oscillation of collective plasmons (electron cloud) due to applied electric field (incident light)<sup>18</sup>. ..... 88

**Figure 3.** Molecular structure of ruthenium complexes studied. A) Ru(bpy)<sub>3</sub> (2Cl<sup>-</sup>) 6H<sub>2</sub>O, B) Ru(bpy)<sub>2</sub>(phen-5-NH<sub>2</sub>)(PF<sub>6</sub>)<sub>2</sub> and C) Ru(bpy)<sub>3</sub>-NH<sub>2</sub>. ..... 90



**Figure 4.** Absorption spectra of luminophores (20  $\mu\text{M}$ ) in water. A)  $[\text{Ru}(\text{bpy})_3]^{2+}$  (black) and  $[\text{Ru}(\text{bpy})_3\text{-NH}_2]^{2+}$  (red). B)  $[\text{Ru}(\text{bpy})_2(\text{phen})\text{-NH}_2]^{2+}$  ..... 93

**Figure 5.** Absorption spectrum of 10nm size commercial AuNPs capped with citrate. 94

**Figure 6.** Absorption spectra of Ru dyes (20  $\mu\text{M}$ ) mixed with AuNPs (25.4  $\mu\text{M}$ ). A)  $[\text{Ru}(\text{bpy})_3]^{2+}$  and AuNPs, B)  $[\text{Ru}(\text{bpy})_3\text{-NH}_2]^{2+}$  and AuNPs, C)  $[\text{Ru}(\text{bpy})_2(\text{phen})\text{-NH}_2]^{2+}$  and AuNPs. .... 95

**Figure 7.** Fluorescence spectra (excitation and emission) of luminophores without AuNPs. A)  $[\text{Ru}(\text{bpy})_3]^{2+}$ , B)  $[\text{Ru}(\text{bpy})_3\text{-NH}_2]^{2+}$  and C)  $[\text{Ru}(\text{bpy})_2(\text{phen})\text{-NH}_2]^{2+}$  ..... 97

**Figure 8.** Fluorescence life- time decay curves of luminophores (orange) and with AuNPs (blue). A and B)  $[\text{Ru}(\text{bpy})_3]^{2+}$ , C and D)  $[\text{Ru}(\text{bpy})_3\text{-NH}_2]^{2+}$  and E and F)  $[\text{Ru}(\text{bpy})_2(\text{phen})\text{-NH}_2]^{2+}$ . Logarithmic Y-axis vs. time linear. Each decay was normalised to the maximum number of photons obtained for that recording. Inset: Normalised decay experimental curves (green) and fitted curve (black), linear Y-axis vs. time linear. Solvent: dH<sub>2</sub>O.... 100

**Figure 9.** Fluorescence emission spectra and corresponding Stern-Volmer plots of luminophores (20 $\mu\text{M}$ ) with different concentrations of AuNPs. A to B)  $[\text{Ru}(\text{bpy})_3]^{2+}$ , C to D)  $[\text{Ru}(\text{bpy})_3\text{-NH}_2]^{2+}$  and E to F)  $[\text{Ru}(\text{bpy})_2(\text{phen})\text{-NH}_2]^{2+}$ . (The standard deviations are similar to, or smaller than, the size of the symbols). Solvent: dH<sub>2</sub>O..... 102

**Figure 10.** Quenching percentage of luminophores according to different concentrations of AuNPs (76.2  $\mu\text{M}$ , 127  $\mu\text{M}$  and 178  $\mu\text{M}$ ). ..... 105

**Figure 11.** Illustration of differences of static and dynamic/collisional quenching by A) steady-state, B) time-resolved fluorescence spectroscopy. C) Stern-Volmer plot for static quenching. D) Stern-Volmer plot for dynamic quenching<sup>52</sup>. ..... 105

**Figure 12.** ECL characterization of 0.1mM luminophores without (black) and with 0.0254mM AuNPs (red) and 50mM of TrPA in 0.1M LiClO<sub>4</sub> as supporting electrolyte. A to B)  $[\text{Ru}(\text{bpy})_3]^{2+}$ , C to D)  $[\text{Ru}(\text{bpy})_3\text{-NH}_2]^{2+}$  and E to F)  $[\text{Ru}(\text{bpy})_3(\text{phen})\text{-NH}_2]^{2+}$  .... 108

**Figure 13.** Absorbance spectra of Ru luminophores conjugated to DNA (purified samples). A)  $[\text{Ru}(\text{bpy})_3\text{-NH}_2]^{2+}$  and B)  $[\text{Ru}(\text{bpy})_3(\text{phen})\text{-NH}_2]^{2+}$ . Insets represents a close-up from 300 nm to 600 nm. .... 112

**Figure 14.** Emission spectra of purified and no purified Ru-DNA conjugated probes. A) No purified sample and B) purified sample. .... 114

**Figure 15.** Semi-log plots vs. time of the fluorescence life- time of DNA conjugated to  $[\text{Ru}(\text{bpy})_3\text{-NH}_2]^{2+}$  not purified (A) and DNA conjugated to  $[\text{Ru}(\text{bpy})_3(\text{phen})\text{-NH}_2]^{2+}$  (B). Logarithmic Y-axis vs. time linear. Each decay was normalised to the maximum number

of photons obtained for that recording. Inset: Normalised decay experimental curves (green) and fitted curve (black), linear Y-axis vs. time linear.Solvent: dH<sub>2</sub>O ..... 114

## **Chapter 4:**

- Figure 1.** Overview of UPEC infection in the urinary tract system. Modified from Lo et al<sup>14</sup> ..... 118
- Figure 2.** Schematic and simplified illustration of the SPR-ECL based biosensor developed for the detection of fimH gene of ureopathogenic E.coli. .... 120
- Figure 3.** Voltammograms of AuNPs electrodeposition using 3 mM HAuCl<sub>4</sub> and 0.1 M NaNO<sub>3</sub> as supporting electrolyte (pH solution ~ 3) using GCE area 0.071 cm<sup>2</sup>. A) Scanning from 0 V to +0.9 V for 6 cycles, scan rate 0.05 V s<sup>-1</sup>. B) First cycle of the electrodeposition process (forward and backward scan). .... 124
- Figure 4.** Electrochemical characterization. A) Voltammogram of electrodes in 0.1M H<sub>2</sub>SO<sub>4</sub> scanning from 0 V to +1.6V at 0.1 V s<sup>-1</sup>: AuNPs modified GCE (red), conventional Au disk electrode (black). B) Voltammogram of AuNPs modified GCE and bare GCE (blue) in 1mM FcnMeOH and 0.1M LiClO<sub>4</sub> as supporting electrolyte at 0.1 M. .... 126
- Figure 5.** Scan rate study of AuNPs modified GCE with 1 mM FcnMeOH in 0.1 M LiClO<sub>4</sub>. A) Voltammogram from 0.01 to 1 V s<sup>-1</sup>. B) Randles-Sevcik plot (the standard deviations are similar to, or smaller than, the size of the symbols). .... 127
- Figure 6.** Illustration of convergent diffusion resulting in semi-infinite linear diffusion, when the nanostructure size and interspacing are much smaller than the root mean square of the diffusion length<sup>43</sup>. .... 128
- Figure 7.** Chemical structure of co-reactants tested in this study. A) Tri-n-propylamine (TrPA) and B) N-butyldiethanolamine (NBEA). .... 128
- Figure 8.** Scan rate studies of co-reactants with 0.1mM [Ru(bpy)<sub>3</sub>-NH<sub>2</sub>]<sup>2+</sup> in 0.1M LiClO<sub>4</sub>. A) Voltammogram of 50 mM TrPA and B) ECL characterization of 50mM of TrPA. C) Voltammogram of 10 mM NBEA and D) ECL characterization of 10mM NBEA. Scan rates: 0.01 V s<sup>-1</sup> (black), 0.025 V s<sup>-1</sup> (red), 0.05 V s<sup>-1</sup> (blue), 0.1 V s<sup>-1</sup> (green), 0.15 V s<sup>-1</sup> (purple) and 0.20 V s<sup>-1</sup> (golden). ECL intensity of NBEA was multiplied by a factor of 10 since the gain was changed from 10<sup>9</sup> to 10<sup>8</sup>. .... 130
- Figure 9.** Plot of ECL intensity over the scan rate. A) TrPA as co-reactant. B) NBEA as co-reactant. The error bar represents the standard deviation (n=3). .... 131

**Figure 10.** The voltammogram at  $0.1 \text{ V s}^{-1}$  (A) and EIS curves (B) of GCE-Au bare (black), modified GCE-Au with capture DNA/MCH (blue) and modified GCE-Au with capture DNA/MCH hybridized with  $25 \mu\text{M}$  of DNA target after incubation. Work solution: Work solution:  $0.01 \text{ M}$  phosphate buffer (pH 7.4) containing  $5 \text{ mM}$   $\text{Fe}(\text{CN})_6^{4-/3-}$ . Inset: simplified Randles equivalent circuit. .... 134

**Figure 11.** ECL characterization of the assay at every step of modification. A) Plot of ECL characterization at  $0.01 \text{ V s}^{-1}$  and  $0.1 \text{ M}$  of NBEA in  $0.1 \text{ M}$  of  $\text{LiClO}_4$  as supporting electrolyte. B) Quantification of ECL emission intensity for independent measurements. Standard deviation is represented as error bars. .... 136

## **Chapter 5:**

**Figure 1.** Chemical structure of (A) oleic acid and (B) oleyl amine..... 141

**Figure 2.** Schematic representation of set-up for synthesis of magnetic particles by thermal decomposition method<sup>22</sup>. .... 143

**Figure 3.** Synthesized  $\text{Fe}_3\text{O}_4$  core/Au shell particles. A) Particles in anhydrous toluene, collected using a magnet. B) Isolated particles (without solvent). .... 145

**Figure 4.** SEM images of  $\text{Fe}_3\text{O}_4$  core/Au shell synthesised particles. A) Image taken using an acceleration voltage of  $20.0 \text{ kV}$ . Scale bar  $10 \mu\text{m}$ . b) Image taken using an acceleration voltage of  $1.0 \text{ kV}$ . Scale bar  $5 \mu\text{m}$ . .... 146

**Figure 5.** TEM image of a single  $\text{Fe}_3\text{O}_4$  core/Au shell particle using  $20 \text{ kV}$  acceleration voltage. Scale bar  $200 \text{ nm}$ . .... 147

**Figure 6.** UV-Vis spectroscopy results. A) Absorbance spectra of serial dilutions of  $\text{Fe}_3\text{O}_4$  core/Au shell particles, using toluene as solvent. B) Beer's law calibration curve. .... 148

**Figure 7.** FT-IR spectra of citrate capped  $\text{Fe}_3\text{O}_4$ /Au shell aggregates in water..... 151

**Figure 8.** Absorbance spectra of citrate capped  $\text{Fe}_3\text{O}_4$  core/Au shell aggregates (in water) and  $\text{Fe}_3\text{O}_4$  core/Au shell particles (in toluene). .... 152

**Figure 9.** Schematic representation of the application of  $\text{Fe}_3\text{O}_4$  core/Au shell particles on a ECL platform for nucleic acids detection. Created in BioRender.com. .... 153

**Figure 10.** Model of dsDNA loading as a function of nanoparticle (from  $1 \text{ nm}$  to  $100 \text{ nm}$  diameter). .... 155

## **Chapter 6:**

**Figure 1.** A) Schematic illustration of SPCE containing gold spheres. B) Voltammogram of SPCE containing gold spheres in 0.1M H<sub>2</sub>SO<sub>6</sub> (6 cycles). C) ECL intensities achieved with the electrodes in 0.1 mM [Ru(bpy)<sub>3</sub>]<sup>2+</sup> and 0.1 M TrPA using PBS as supporting electrolyte (scan rate study). ..... 161

## LIST OF TABLES

### Chapter 2:

<b>Table 1.</b> Relative standard deviation (RSD) of 3 consecutive cycles (ECL intensity). Gold coated Ti arrays and gold and polished Ti electrodes. ....	82
--	----

### Chapter 3:

<b>Table 1.</b> Absorption and extinction coefficient values extracted from concentration curves from MLCT of dyes and SPR bands of AuNPs.....	95
<b>Table 2.</b> Zeta potential and DLS values of AuNPs in water and mixed with dyes.....	95
<b>Table 3.</b> Fluorescence data of free ruthenium, life-time values with and without AuNPs and quenching constant ( $K_q$ ) extracted from Stern-Volmer plots. The luminescent lifetimes were fitted with a $\chi^2$ between 1.0 and 1.6. ....	98
<b>Table 4.</b> ECL data of luminophores, relative ECL efficiency and calculated quenching percentage of AuNPs. ....	108
<b>Table 5.</b> Fluorescence data (steady-state and time-resolved spectroscopy) of DNA conjugated luminophores. The luminescent lifetimes were fitted with a $\chi^2$ between 1.0 and 1.6.....	114

### Chapter 4:

<b>Table 1.</b> Sequences of single-stranded DNA used in the bioassay for detection of gene fimH. ....	123
<b>Table 2.</b> Relative standard deviation (RSD) of 3 consecutive ECL cycles using TrPA and NBEA as co-reactants. ....	131
<b>Table 3.</b> The values from the redox probe oxidation ( $E_{pa}$ ) and reduction ( $E_{pc}$ ), separation peak ( $\Delta E_p$ ), constant phase element (CPE) and charge transfer resistance ( $R_{ct}$ ). ....	134

## RESEARCH OUTPUTS

### Publications

1. De Eguilaz MR, Cumba LR, Forster RJ. Electrochemical detection of viruses and antibodies: A mini review. *Electrochem commun.* 2020;116:106762. doi:10.1016/J.ELECOM.2020.106762.
2. Douman SF, De Eguilaz MR, Cumba LR, et al. Electrochemiluminescence at 3D Printed Titanium Electrodes. *Front Chem.* 2021;0:279. doi:10.3389/FCHEM.2021.662810.
3. Forster RJ, De Eguilaz MR, Barhoum A, Cumba LR. Electrochemical (Bio)Sensors for Bacteria and Biofilms. *Ref Modul Biomed Sci.* Published online January 1, 2022. doi:10.1016/B978-0-12-822548-6.00117-5

### Conferences

1. Thesis in 3<sup>rd</sup>. 72nd Irish Chemistry Research Colloquium / University of Limerick. Title: “Photonics and Electrochemistry of 3D Printed Ti Electrodes”. (Speaker).
2. 1<sup>st</sup> symposium on Molecular Biosensing: From Theory to Practice. Talk: “DNA-nanoantenna ECL assay development for bacteria detection”. (Speaker).
3. 7th International Conference on Bio-Sensing Technology/ Sitges (Spain). Poster presentation: “Gold functionalization of 3D printed Ti electrodes for electrochemiluminescence enhancement”. Samantha F. Douman, Miren Ruiz De Eguilaz, Loanda R. Cumba, Stephen Beirne, Gordon G. Wallace, Zhilian Yue, Emmanuel I. Iwuoha and Robert J. Forster.

## ABSTRACT

### “Platforms for the development of Electrochemiluminescent Biosensors”

*Miren Ruiz de Eguilaz*

Electrochemiluminescence (ECL) based biosensors has attracted much attention since they provide high selectivity, controllability, and sensitivity. Therefore, the goal of this work was to study novel gold-based materials for the development ECL platforms using ruthenium based luminophores for future application in bacteria detection. Firstly, 3D Ti electrodes, printed using Ti alloy (Ti-6Al-4V) powder were studied and functionalized with a thin layer of gold and ECL generation was investigated with  $[\text{Ru}(\text{bpy})_3]^{2+}$  and the co-reactant tri-propyl amine. Results demonstrated that the presence of gold improved the diffusion on the electrode surface as well as ECL intensity, suggesting it can provide a unique and optimizable platform for their potential application for biosensors. Gold has very interesting electrochemical applications, but it also presents optical properties that can be exploited for sensing purpose, such as ECL signal amplification through optically driven plasmon excitation. With this purpose, 10 nm gold nanoparticles (AuNPs) were investigated in solution with different luminophores of  $[\text{Ru}(\text{bpy})_3]^{2+}$ ,  $[\text{Ru}(\text{bpy})_3\text{-NH}_2]^{2+}$  and  $[\text{Ru}(\text{bpy})_2(\text{phen})\text{-NH}_2]^{2+}$  (separately), for the development of a SPR-ECL system. According to the fluorescence emission results,  $[\text{Ru}(\text{bpy})_3\text{-NH}_2]^{2+}$  was chosen as the most suitable dye to develop an ECL biosensor for the DNA detection UTI causing *Escherichia coli*. For this, gold nanoparticles coated glassy carbon electrodes were analysed using impedance and cyclic voltammetry technique in order to investigate the suitability of the system for DNA bacterial detection. Finally, Ferromagnetic-Core/Gold-Shell NPs synthesized by thermal decomposition method were also characterised. Results confirmed that the particles were successfully synthesized and covered with gold, however, SEM images shown an aggregate size  $>200\text{nm}$  and a heterogeneous shape, indicating that the synthesis protocol should be further optimized to achieve better particle properties for a magnetic ECL based biosensor. In conclusion, this thesis demonstrated how novel platforms and luminophores could be used in conjunction with gold to develop ECL sensing systems. SPR of AuNPs coupled ECL of luminophores can be exploited to amplify the ECL signal, and overall, the analytical performance of the

sensing platforms and undoubtedly, the development of highly selective and sensitive biosensors for correct detection and diagnosis of diseases such as bacterial infections.



**Chapter 1: Literature review.**  
**Electrochemical biosensors for**  
**pathogen detection**

## 1. INTRODUCTION

The fast emergence of new pathogens, such as COVID-19 and new antibiotic resistant bacteria, has highlighted the need for more sensitive, specific, rapid, and low-cost biosensors as a measure to improve disease detection<sup>1-4</sup>. Besides medical and point of care applications, biosensors are playing increasing roles in the protection of public health (e.g., food and water quality control, environment protection), pharmaceutical research and forensics<sup>5</sup>. Traditional, predominantly in-lab, detection methods include cell culture techniques, polymerase chain reaction (PCR) for either DNA or RNA detection and immunological techniques such as ELISA assay<sup>6</sup>. While these methods are very reliable and selective, they are also time-consuming, expensive and require complicated multi-step sample preparation among other disadvantages. Therefore, biosensors are an important technology to enable portable, cost-effective, and easy operable alternative to laboratory based techniques<sup>7</sup>.

Electrochemical biosensors have attracted much attention recently since they combine the sensitivity of electroanalytical methods with the intrinsic bio selectivity of the biological component<sup>8-11</sup>. Binding of the target can either generate a “label-free” response (e.g., a change in the electrochemical impedance), or involve a redox or electrochemiluminescent (ECL) response that generates a quantifiable signal<sup>12,13</sup>. To date, electrochemical biosensors have provided an optimizable and cheap platform that can enable rapid and *in situ* detection on surfaces, multiplex detection as well as wireless detection of pathogens<sup>11</sup>. However, despite many breakthroughs, these sensors are not easy to commercialize since their long-term stability, specificity and scalability are still a challenge<sup>7</sup>. Moreover, many of the devices developed have a low technology readiness level and require a multidisciplinary approach, including collaborations with industry, if they are to be commercialised<sup>9</sup>. A key emerging development is three-dimensional (3D) electrodes enabled by new manufacturing techniques, e.g., selective laser melting, that work with a wide range of materials and allow very complex geometries and shapes to be produced that can control transport and other properties<sup>14,15</sup>. Many electrochemical biosensors are manufactured manually, which inevitably leads to reproducibility issues, however, 3D printing technologies allow to overcome this limitation and improve properties such as conductivity and analytical performance of the system for a high-throughput detection of analytes<sup>16</sup>. 3D printed electrodes are designed as an alternative

to conventional manufactured electrodes (e.g., glassy-carbon, gold or screen-printed electrodes) and offer multiple advantages such as stability, simple controllability over the entire fabrication process and mass production<sup>15</sup>. Furthermore, 3D printed electrodes show significant improvements in assay performance since different architectures can be designed to achieve a larger surface area, increasing the bio-recognition element coverage on the electrode surface which leads to increase the sensitivity of the sensor<sup>17</sup>. 3D printing offers a solution for the current problem with fabrication of electrodes with different geometries and conductive materials<sup>18</sup>, therefore one of the objectives of this thesis is to address this issue by showing how 3D printed electrodes with a unique architecture, can be further optimized with conductive materials such as gold in order to be used as an electrochemical and/or ECL biosensing platform.

Electrochemical biosensing can provide high sensitivity for detection of small concentrations of targets, however, they are often very vulnerable to external interference, such as an excess of target, which can directly negatively impact on the signal output and processing<sup>19</sup>. Furthermore, very small concentrations of the target does not produce a measurable signal and so signal amplification technology, e.g., through the use of advanced electrochemical or optical labels, has become a very popular research topic<sup>19–21</sup>. Different labels, such as ruthenium metal complexes, have been used to amplify the analyte binding signal in SPR-ECL systems by coupling them with plasmonic materials (e.g., AuNPs, QDs and etc)<sup>22</sup>. Surface plasmon resonance occurs when the electrons at the surface of a plasmonic material are excited by incident light, provoking a collective oscillation of the electrons, which propagates along the surface of the material<sup>23</sup>. This effect has been further exploited in ECL biosensors, since the light produced through ECL reaction can activate the SPR of plasmonic materials and also increase the ECL intensity by achieving higher sensitivity<sup>24</sup>. However more details of these interaction can be found further in this review. Therefore, a second objective of this thesis is to investigate and understand the interaction between different ruthenium dyes and AuNPs using spectroscopic and electrochemical techniques in order to inform the development of a SPR-ECL platform for DNA detection (**Figure 1**).

Nanomaterials, such as AuNPs can improve the performance of biosensing platforms. In this thesis, AuNPs are used to increase the surface area of glassy carbon electrodes as well as exploiting their plasmonic properties to create an ECL sensor for the detection of bacterial DNA. The strategy is to use the AuNPs to increase the surface area and

effectively improve the capacity for biomolecular receptors, as well as enhancing the mass transport of the target to the surface (radial diffusion) to shorten the response time<sup>8</sup>. Another objective is to improve the separation and pre-concentration of the target from complex samples in order to improve the detection limit. This objective is important since increasing the background signal, or decreasing the target signal, leads to a poor sensitivity of the assay<sup>25</sup>. Magnetic beads/particles provide a great approach since they can be further modified to conjugate biomolecules such as antibodies, proteins or nucleic acid for pathogens detection<sup>26</sup>. Therefore, in this thesis a novel synthesis of magnetic particles is reported for their subsequent functionalization with Au, which could then be functionalised with antibodies or DNA for the development of a biosensor for bacteria detection. The different approaches and strategies are presented in **Figure 1**.

Finally, this Chapter's objective is to review and explore the state of the art of electrochemical biosensors (labelled and label-free) for pathogen detection emphasizing the advantages of combining different materials such as luminophores, 3D surfaces, and plasmonic materials to enhance the signal and the analytical performance of ECL detection systems. Furthermore, other parameters such as biosensor design and applicability are critically reviewed for future POC pathogen detection and compared with traditional detection techniques.

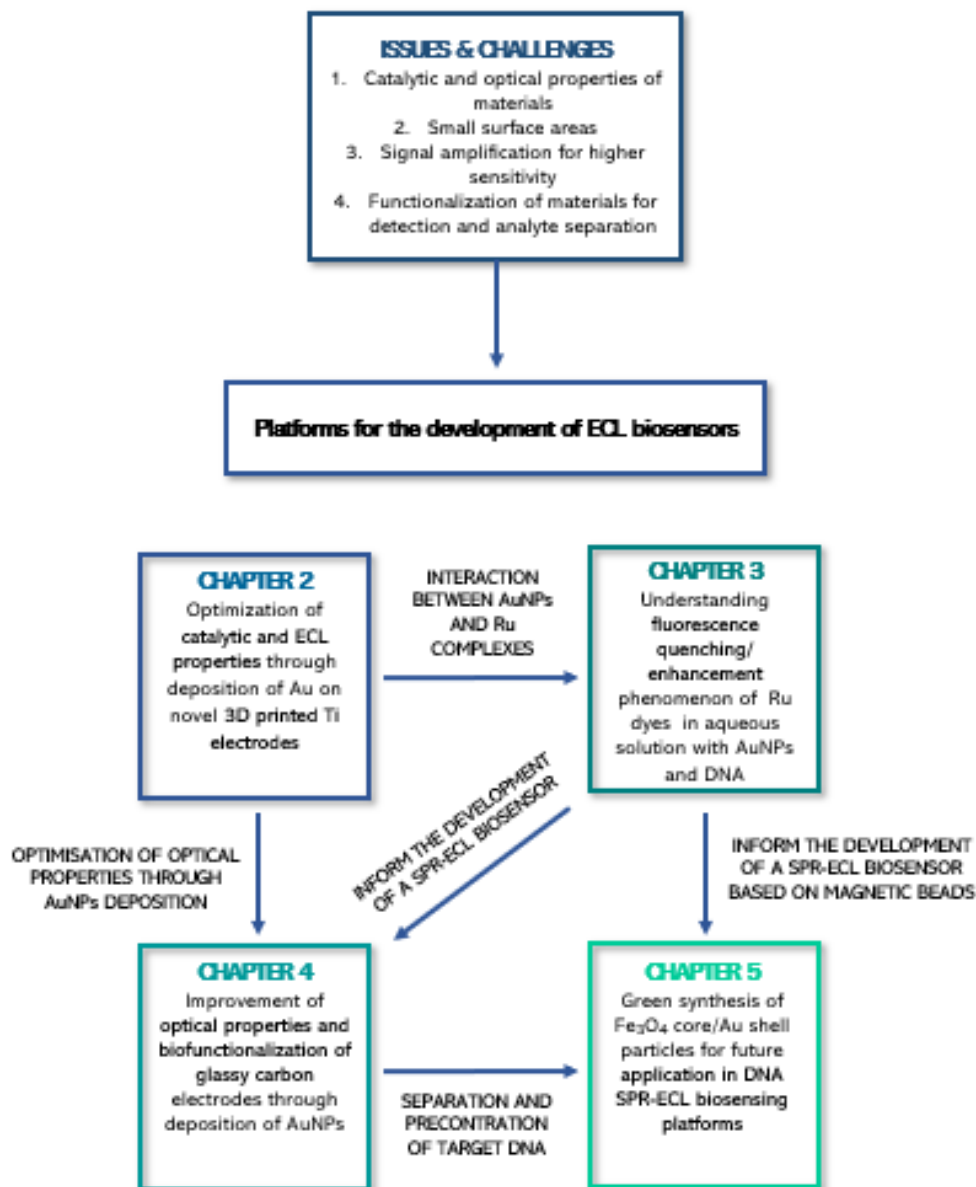


**Figure 1.** Overview of the thesis with main issues and challenges studied in every chapter.

## 2. CLASSIFICATION OF ELECTROCHEMICAL BIOSENSORS

Electrochemical biosensors can be classified according to the signal generation method, i.e., labelled or label-free detection, bio recognition element (e.g., DNA, antibodies, proteins, cells enzymes etc.) or type of transducing technique, such as amperometry, voltammetry, impedance spectroscopy, conductometry, etc. To build a biosensor, numerous factors such as type of target/analyte, experimental set-ups and electrode material, including size and shape are important since it can influence many aspects of

the performance of the sensor<sup>27,28</sup>. For example, label free biosensors have been investigated and reported as very promising type of electrochemical biosensors for POC applications (**Figure 2**)<sup>29</sup>. However, different approaches such as utilisation of labels (e.g., enzymes, luminophores, nanomaterials and etc.) can effectively enhance the electrochemical response associated with binding of target analyte through the label properties<sup>11,30,31</sup>. Combining electrochemistry with optical detection in electrochemiluminescence (ECL), i.e., where light is electrogenerated, represents a powerful approach and offers performance advantages over fluorescence or chemiluminescence since it combines sensitivity and very low interferences with high reliability<sup>32,33</sup>. ECL-based biosensors are very attractive since they do not require any light source, which decreases the background noise from scattered excitation light and unwanted luminescence. Also, the time and the position at which light is generated can be precisely controlled since the light emission is regulated by the application of a specific potential, giving highly sensitive and reproducible results<sup>34</sup>. Furthermore, using advanced luminophores, e.g., transition metal complexes and/or quantum dots, often with surface modifications and incorporation of nanomaterials, have played a significant role in the development of ECL based biosensors<sup>35</sup>. In fact, as reviewed in Yoo et al.<sup>36</sup>, several ECL based kits have been commercialised by companies such as Radiometer, Roche Diagnostics, Meso Scale Diagnostics, and Biometro consisting of either on automated analyser or well plate kits detecting a wide range of biomarkers for detection of diseases ranging from sepsis, myocardial infection, Alzheimer's disease, cancer and kidney, liver and/or bone disorders.

Moreover, where the aim is to increase the sensitivity of biosensors, ECL has been coupled to other techniques such as surface plasmon resonance (SPR) taking advantage of the optical properties of materials such as gold to plasmonically enhance the ECL signal<sup>22</sup>. As explained above, SPR consists of the oscillation of free electrons (plasma) at materials interfaces provoked by incident light, which could perhaps come from ECL<sup>37</sup>. Plasmonic materials can be in the form of nanoparticles, nanowires, nanopore arrays and other micro-nano structures to enhance the sensitivity of ECL sensors by increasing the local electric field strength<sup>37,38</sup>. Moreover, ECL signal can be improved by tuning the proximity of luminophores to the plasmonic substrate, to maximise the electric field interaction and obtain the greatest enhancement<sup>38</sup>. The mechanism of local surface plasmon resonance (LSPR) of plasmonic particles such as AuNPs for ECL enhancement

is similar to the one understood for metal-enhanced fluorescence, where the local electromagnetic field of the particles is activated and enhanced by the light emitted by the luminophore<sup>39</sup>. This enhances the excitation rate of the luminophore since it leads to a higher population of electrons in excited state which provokes an increase of the radiative and non-radiative decays<sup>40</sup>. This enhancement only can occur when the luminophore and the NPs are placed at an appropriate distance since the enhanced magnetic field decreases exponentially to the far distances<sup>40</sup>.

However, for the development of a high sensitive, fast, accurate and specific biosensing platform, the type of target and their properties should be considered for an optimal design and avoid non-specific interactions to obtain a distinguishable signal<sup>41,42</sup>. In fact, of challenges to face in the development of a bioassay regarding the target, which is to improve the robustness of the assay to adapt it for applications *in situ* and/or complex biological samples<sup>43</sup>. In case of pathogens such as bacteria, immunoglobulins (Ig) generated after an infection, antigens such as proteins and/or toxins, and DNA from the bacterial cells are the most common targets, which also help to differentiate between other microorganisms<sup>10</sup>. Whole-cell bacteria in biological samples can be also detected, without the need of extra reagents and processing steps as it is needed for DNA detection, however, detection of DNA enables the design of very specific captures for a successful and complete hybridization with the target achieving high sensitivity and accuracy while preventing non-specific interactions<sup>44,45</sup>.

In this literature review, labelled and label-free electrochemical biosensors are discussed in terms of their advantages and disadvantages, within the context of the challenges and issues mentioned in previous section.

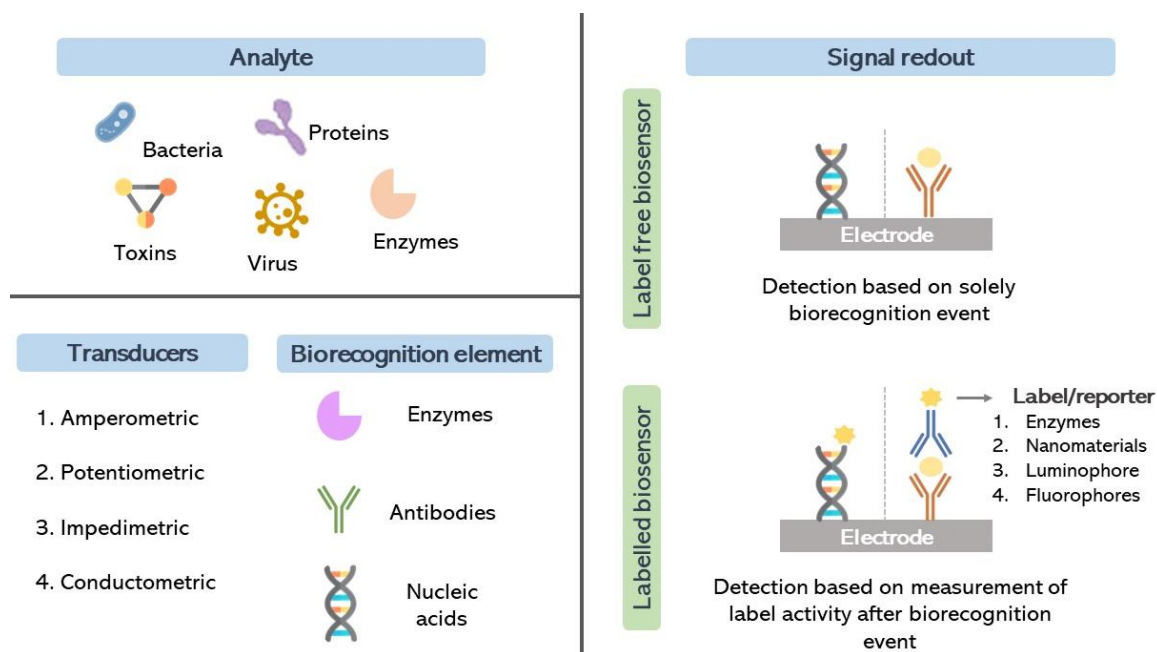


**Figure 2.** Schematic representation of biosensor elements and label-free and labelled biosensors.

## 2.1. Label based electrochemical biosensors

In the recent years, labels have been combined with electrochemical techniques (e.g., voltammetry, amperometry or potentiometry) to create advanced biosensors<sup>11,43,46,47</sup>. A label consists of a tag or “barcode” (e.g. enzymes, luminophores or nanoparticles) that can be conjugated to the recognition element such as proteins, nucleic acids, or antibodies to detect presence of the target<sup>48</sup>. In clinical diagnostics, the food industry and water treatment multiple components need to be analysed within a single sample which can make achieving the required selectivity and sensitivity of the sensor challenging. Using discrete labels for each target can help to overcome these difficulties<sup>49,50</sup>. Signal amplification strategies, often involves design of novel labels that generate enhanced currents with higher signal-to noise ratios and a boarder target detection by avoiding cross-reactions. These attributes can lead to improved sensitivity<sup>48-51</sup>. For example, utilisation of enzymes, nanoparticles, quantum dots (QDs) or luminophores as labels can effectively improve the biosensing response since they increase the magnitude of the current generated<sup>47,49</sup>. While there are many label-free biosensors with simple workflows, the utilisation of the appropriate label can also ensure high performance of the assay with better sensitivity and selectivity<sup>52</sup>.



### 2.1.1. Enzyme based labels

Enzyme based labels are known for their excellent catalytic properties, requiring extremely small quantities of reactants to carry out the assay making them very efficient labels<sup>50,53</sup>. Furthermore, there are a wide variety of enzymatic labels (e.g. horseradish peroxidase, glucose oxidase, alkaline phosphatase,  $\beta$ -galactosidase and etc.), enabling multiplexed detection on the same platform by using different enzymes each of reacts with different target<sup>50,54</sup>. However, the main drawback of using enzymatic labels is the loss of the activity, e.g., when stored, which can compromise the lifetime of the biosensor either in use or in storage<sup>55</sup>. The most efficient enzymes and thus, the most used ones as labels, are horseradish peroxidase (HRP) and alkaline phosphatase (ALP), since they react with the substrate at a sufficiently high reaction rate and exhibit long-term stability<sup>50,53</sup>. A common application of enzymes are the sandwich type immunosensors<sup>56</sup>, such as the one developed for detection of virulence factor p60 secreted by *Listeria monocytogenes* and associated with the bacteria pathogenicity<sup>57</sup>. This assay uses a carbon screen-printed electrode (SPE) modified with monoclonal antibodies that captures p60 and subsequently, a detection antibody labelled with ALP enzyme is introduced that binds to the target. As last step, a mixture of 3-indoxyl phosphate disodium salt and silver nitrate, (3-IP/Ag<sup>+</sup>), is added and, ALP, hydrolyses 3-IP into an unstable indoxyl intermediate, that is oxidized by the silver ions, generating an indigo blue colour in this process. Subsequently, co-deposited silver particles with indigo blue are re-oxidized, generating a stripping peak signal around + 0.2V with cyclic voltammetry. Thus, the amount of Ag<sup>0</sup> formed at the SPE surface at the end of enzymatic reaction is proportional to the concentration of target present in the sample. Similar system using ALP and silver has been reported already<sup>58,59</sup> as well as the use of 3-IP<sup>60</sup> with biosensing purposes. The whole assay is performed in less than 3 hours and under optimal conditions, the immunosensor showed a limit of detection (LOD) of 1.5 ng mL<sup>-1</sup> and a linear range from 5 and 150 ng mL<sup>-1</sup>. When the sensor was tested with spiked milk samples, an average of recovery rate of 98% of p60 (0, 25, 50 and 100 ng mL<sup>-1</sup>) was obtained, proving the suitability of the sensor for *L. monocytogenes* detection in food industry. However, after 15 days of storage (2-8°C), the stability of the sensor is compromised since a 72% decrease in the response was observed, possibly reducing affinity of the antibodies for the protein. Furthermore, even if the assay is carried out in less time than conventional

ELISA test (>3h), other affinity based biosensors can achieve a detection in less than 2 hours<sup>61,62</sup>, suggesting that improvements in the detection time are needed.

Another example of an immunosensor, but using HRP as a label, is the biosensor for multiplex detection of influenza H1N1, H5N1, and H7N9 viruses<sup>63</sup>. As it is shown in **Figure 3**, zinc oxide (ZnO) nanorods were grown on a Poly(dimethylsiloxane) (PDMS) sensor to achieve a higher coverage of immobilised primary antibodies on the surface, to increase the sensitivity of the platform. When secondary antibodies labelled with HRP are introduced, the oxidation of 3,3',5,5'-tetramethylbenzidine (TMB) generates a current that is proportional to the viral load. In addition, an optical colour change of the TMB containing solution occurs as a result of the reaction<sup>63</sup>. Measurements are performed in TMB buffer solution using amperometry as electrochemical technique, applying a voltage of + 0.4 V for 80 s. The presence of ZnO nanorods increases the surface area so a higher coverage of antibodies is achieved. This was confirmed by coating ZnO nanorods with FITC-labelled antibodies and it was observed that the fluorescence intensity of the PDMS with ZnO NRs was approximately 6 times higher than that of the PDMS without ZnO NRs. The nanostructured ZnO nanorods grown on the upper inner surface of the PDMS sensor region provides a relatively stable physiological-like- condition for the biomolecules since they show a high isoelectric point (IEP~9.5) that tends to interact electrostatically with molecules with lower IEP such as antibodies, thus they are very favourable material for biomolecules immobilization<sup>63-65</sup>. Furthermore, the PDMS microfluidic chamber that contains three film gold electrodes, achieves a very small volume of sample (nanolitres). On the other hand, the HRP enzyme acts as an electron carrier when TMB oxidation is induced by applying an electrical potential. With this system, an LOD of 1 pg mL<sup>-1</sup> was achieved as well as a good ability to discriminate between the individual on a mixture of three different types of antigens (H1N1, H5N1 and H7N9). However, further testing with real samples is needed to show the potential applicability in real world<sup>27</sup>, since other biosensing platforms are able to detect presence of influenza particles in chicken<sup>66,67</sup> and human serum<sup>68</sup>, where no enzymatic labels are used.

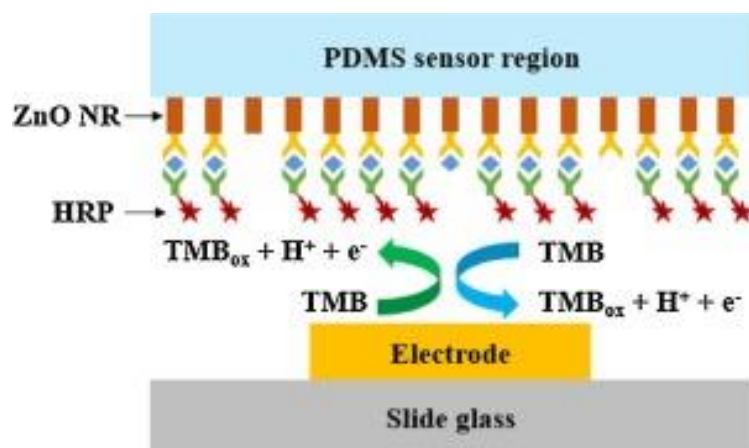


**Figure 3.** Representation of the PDMS substrate and ZnO nanorods functionalised with the primary capture antibody. The secondary antibody is labelled with horseradish peroxidase, HRP, which oxidises, TMB, generating a current related the viral load in the sample.

Quantification of genetic material has been also explored since it is a powerful tool for the identification of pathogens<sup>69</sup>. For instance, a screen-printed electrode (SPE) modified with polyaniline (PANI), along with a HRP labelled antibody to amplify the signal was used to detect a specific region gene of *Escherichia coli* DNA coding for 16S rRNA<sup>70</sup>. The authors describe a system where biotinylated DNA capture probe is immobilized onto the PANI/AuNP/avidin-modified SPE and a digoxigenin label DNA is used as a probe. Next, HRP labelled anti-digoxigenin antibody is introduced to recognize the capture-target-probe complex and produce a signal when TMB/ H<sub>2</sub>O<sub>2</sub> are injected into the solution. The HRP enzyme can electrochemically convert an inactive substrate to an electroactive product that can produce an electrochemical signal<sup>54,71</sup>. Therefore, after the addition of TMB/H<sub>2</sub>O<sub>2</sub>, HRP oxidises TMB using H<sub>2</sub>O<sub>2</sub> forming TMB<sup>2+</sup> which is reduced afterwards on the electrode surface generating a current signal. The whole assay only takes 70 mins and with this strategy, the authors were able to achieve a very low LOD of 4 CFU, and a linear range from 4 x 10<sup>6</sup> to 4 CFU in clean urine samples spiked with different number of bacterial cells (from 10<sup>8</sup> to 10<sup>2</sup> cells of *E. coli*). Further experiments were performed with real samples from 30 patients with urine tract infections (UTIs), where 10<sup>5</sup> CFU of *E. coli* were detected, which was in accordance with previous studies. This means that the biosensor is effective to detect the presence of *E. coli* causing UTI in ongoing infections. The results obtained in this work show the potential of using the

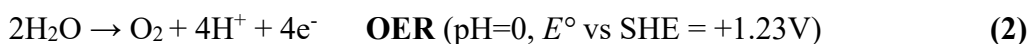
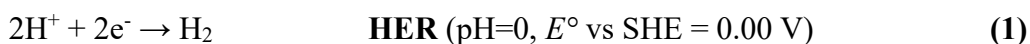
sensor in real world since it also showed a good stability over a 10-week period, however, small currents were detected in the presence of *Staphylococcus haemolytic* and *Serratia marcescens* both known for causing UTIs. Despite the small cross-reactivity with other bacteria's genetic material, this biosensor is a very good candidate for rapid and accurate detection of *E. coli* in patients with UTI that even if they are faster, the achieved LODs are bigger and therefore, less sensitive<sup>72,73</sup>.

### 2.1.2. Nanomaterial-based labels

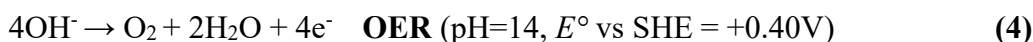
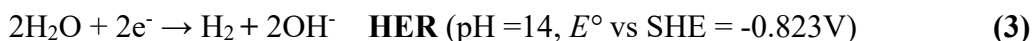
In the recent years, significant progress has been achieved in the development of nanomaterials with tailored characteristics such as size, shape, or surface charge, for their application in electrochemical biosensors<sup>74</sup>. Nanomaterials present several advantages over traditional enzymes e.g., higher stability, signal amplification capacity and sensitive electrochemical response that leads to build more cost-effective biosensors<sup>50,74,75</sup>. A wide range of nanomaterials have been typically used as labels, ranging from gold, silver copper and silicon-based nanoparticles<sup>76–78</sup> to carbon-based materials such as carbon nanotubes or graphene<sup>79,80</sup>. Among the metallic nanoparticles, gold nanoparticles (AuNPs), are very attractive since they show stability against oxidation, a large surface-to-volume ratio, and good electrocatalytic properties<sup>75,81</sup>. Carbon-based nanomaterials, also show many useful properties such as large surface area, biocompatibility, favourable conductivity, ease of manipulation and they can be functionalized with other signal tags for signal amplification<sup>75</sup>. For instance, the immunoassay developed for hepatitis B antigen (HBAg) detection, uses multiwall carbon nanotubes (MWCNTs) functionalized with molybdenum disulphide (MoS<sub>2</sub>) crystals and gold-palladium (Au@Pd) NPs, that together act as a label of the secondary antibody<sup>82</sup> (**Figure 4**). MWCNTs comprise concentric tubes of rolled-up graphene, separated by  $\approx 0.35$  nm, and they have gained a lot of attention due to their advantageous characteristics for biosensing applications such as high yield after synthesis and low production cost per unit, thermochemical stability, and ability to maintain or improve electrical properties even after different functionalization processes<sup>83</sup>. Furthermore, nanoparticle functionalization of MWCNTs can improve the analytical performance of the biosensor<sup>84</sup>. Incorporation of bimetallic nanoparticles such as dendritic Au@Pd, can bring benefits compared to their monometallic counterparts, since they enhance superior catalytic activity and tolerability

to oxygen due to the synergistic effect of the two metals<sup>82,85</sup>. It has been suggested that Au@Pd NPs accelerate the electron transfer since they present a larger surface area over their monometallic counterparts<sup>86</sup>. Therefore, AuNPs can be exploited in many ways to improve their electrochemical properties. These dendritic Au@Pd nanoparticles consists on discrete anisotropic Pd nanostructures densely packed on and around the surface of Au sphere nanoparticles that acts as core, providing active surface area for electrocatalytic activities and/or binding sites<sup>87</sup>. Therefore, the dendritic shape of Au@Pd nanoparticles increases the number of antibodies that can be conjugated through the affinity interaction between Pd and amine group of antibodies<sup>82</sup>. Additionally, incorporation of metallic complexes such as MoS<sub>2</sub> to carbon-based materials and noble metallic materials (e.g., Au, Pt or Pd) have been reported to increase the surface area and produce catalysts with excellent conductivity making them very suitable as analytical probes<sup>88,89</sup>. As shown in **Figure 4**, when the target (HBAg) is captured by the primary antibody immobilized on graphene oxide and Au NPs nanocomposite (on the glassy carbon electrode surface), the secondary antibody labelled with Au@Pd/MoS<sub>2</sub>@MWCNTs is added, resulting in a typical sandwich like immunoassay. The dendrite shape with numerous catalytic sites of Au@Pd NPs and the presence of unsaturated sulphur atoms in MoS<sub>2</sub> creates a synergistic effect, enhancing the catalysis of H<sub>2</sub>O<sub>2</sub> and achieving higher current drop This was demonstrated after investigating the currents produces by the bioconjugates of the secondary antibody (Ab2) with MWCNTs-Ab2, MoS<sub>2</sub>@MWCNTs-Ab2, Au@Pd/MoS<sub>2</sub>@MWCNTs-Ab2, showing the last one generates the largest currents under the same conditions. Measurements were performed with amperometric i-t curve, applying a potential of - 0.6V, towards electrocatalytic reduction of H<sub>2</sub>O<sub>2</sub> on PBS at pH 7.38, which was reported to be the optimal conditions. However, the authors do not discuss the impact of water splitting under such conditions. The redox potential at which water splitting or electrolysis happens is highly influenced by solution pH, electrode potential, temperature, and pressure<sup>90</sup>. The water splitting can be considered in terms of its two half reactions: i) the hydrogen evolution reaction (HER) and, ii) the oxygen evolution reaction (OER) and these reactions differ somewhat depending on the pH at which the water splitting is carried out (see **Equations 1-4** below)<sup>91</sup>:

### Acid conditions



### Alkaline conditions



Although the redox potentials ( $E^\circ$ ) displayed above were originally obtained with SHE as reference electrode, other reference electrodes such as SCE and Ag/AgCl also vary the reaction potential with the solution pH<sup>92</sup>. Therefore, the negative potential (-0.6 V) applied by the authors at such neutral pH for the amperometric measurements should be further investigated, for example by using cyclic voltammetry, to find out if water electrolysis is contributing to the signal. Nevertheless, the results reported showed that the biosensor has a very narrow linear dynamic range from 0.1 pg mL<sup>-1</sup> to 500 pg mL<sup>-1</sup>, LOD of approximately 26 fg mL<sup>-1</sup> and good stability after 15 days of storage at 4°C (current response maintains to 90.4% of the initial value). However, the platform was only tested at antigen concentrations < 500 pg mL<sup>-1</sup>, therefore, higher concentrations should be tested since the larger the dynamic range is, the easier it is to discern the true signal from the noise<sup>93</sup> and it also could improve the ability to monitor the viral load<sup>94</sup>. Furthermore, no information is provided about the time it takes to run the assay, which is a very important feature in biosensors. On the other hand, one of the main disadvantages of using carbon-based nanomaterials such as MWCNTs, is the difficulty of controlling the manufacturing process, since there is a tendency to form aggregates leading to low uniformity of response between individual MWCNTs<sup>84</sup>. Besides, synthesis of the label comprises many steps that are time consuming and very difficult to scale-up for commercial purposes.

Another example of combining AuNPs with other nanomaterials is the immunosensor that utilizes a nanostructure of AuNP doped in a polyaniline (PANI) matrix as an electrochemical label for single-cell immunodetection of *Escherichia coli* O157:H7 in buffer<sup>95</sup>. As it has been mentioned above, AuNPs are good candidates for labelling since

they show many properties that can be exploited, such as high conductivity, biocompatibility, easy functionalization, simple synthesis, and useful optical properties<sup>96,97</sup>. Other nanomaterials such as PANI also show excellent chemical and electrical characteristics (e.g., high conductivity, redox reversibility, long-term environmental stability, high solution process ability), being the first conductive polymer that has been commercialized<sup>98</sup>. However, it loses its conductivity above pH 4, therefore, in order to address this issue, PANI is usually combined with other conductive materials such as polymers, nanoparticles, or carbon nanomaterials which conductivity is conserved at low pH levels<sup>99</sup>. Forming nanostructures with conductive polymers as PANI is an excellent strategy for biosensing, since it combines unique properties of polymers with the ones provided by nanomaterials (e.g., large surface area, flexibility for biomolecules immobilization and quantum effect) improving the analytical sensitivity<sup>100,101</sup>. In fact, PANI nanostructures show higher sensitivity as well as faster time response than its conventional bulk counterpart since it provides a larger active surface area (enhanced signal) and shorter penetration depth for molecules (shorter sample-to-answer time)<sup>100</sup>.

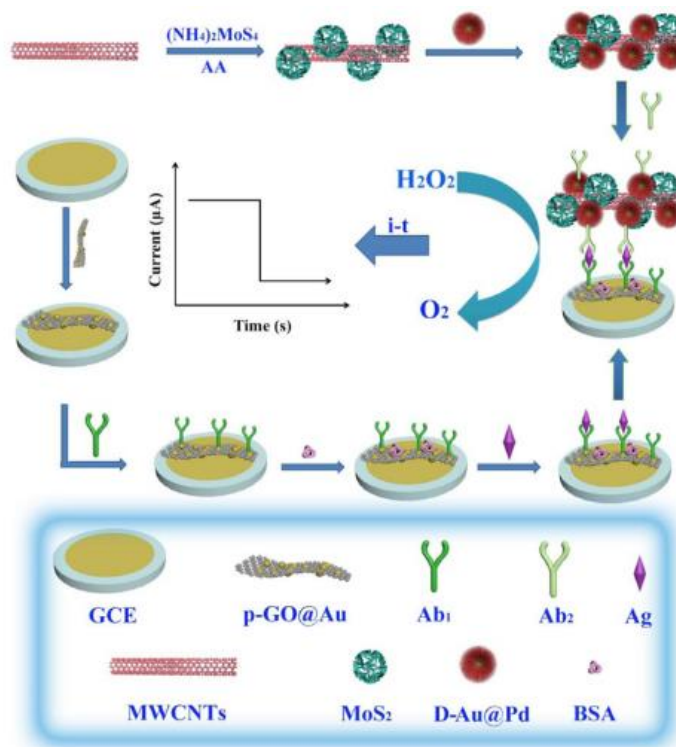


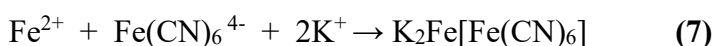
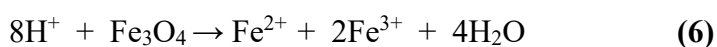
**Figure 4.** Schematic illustration of the components of the sandwich type immunosensor and the measurement by amperometric *i-t* curve in H<sub>2</sub>O<sub>2</sub> (applying -0.6V).

The advantage of using PANI/AuNPs nanostructures as a label in an immunosensor is that PANI acts as a carrier for the AuNPs while providing stability and contributing the electrochemical response since it also shows high redox activity<sup>95</sup>. The sensor for single-cell immunodetection of *Escherichia coli* O157:H7 is based on an indium-tin-oxide (ITO) electrode, where 3- $\mu$ L volume of bacterial suspension is dropped and absorbed on the surface at room temperature. Subsequently, the electrode is immersed in a previously prepared solution containing PANI/AuNPs nanostructures with antibodies immobilised on the surface, for 10 min and electrochemical measurements are carried out with Double Pulse Voltammetry (DPV) in pH 2.5 phosphate buffer. The study showed that in presence of bacteria a strong oxidation peak at + 0.12 V (vs. Ag/AgCl) is generated (when compared to other types of bacteria where tested), which strongly depends on the number of *E. coli* O157:H7 bacteria absorbed on the ITO electrode surface and recognized by the antibodies conjugated to PANI/AuNPs nanostructure. With this biosensor, the authors could detect from single cell to  $10^6$  cells under the tested conditions. Furthermore, real rotten beef samples were tested containing *Aeromonas salmonicida* and *Serratia liquefaciens* (at  $3.0 \times 10^6$  cells  $\text{mL}^{-1}$ ) and no electrochemical response was detected, indicating good selectivity of the sensor. On the other hand, there is a strong correlation between current density and number of cells on the ITO electrode, establishing an LOD of 330 cells  $\text{mL}^{-1}$  (cell density) in buffer spiked with *E. coli* O157:H7. Furthermore,  $0.64 \mu\text{A cm}^{-2}$  was achieved at  $3.3 \times 10^2$  cells  $\text{mL}^{-1}$ , which corresponds to one attached to the electrode, after carrying microscopic observation. However, a better design is needed to improve the detection in solution since other sensors showed lower LOD in terms of cell density, for *E. coli* detection in real food samples<sup>70,102</sup>. In addition, the authors reported that several sample purification steps were carried out to record an electrochemical response, thus, further platform optimization studies are necessary in order to achieve a faster test.

A different type of label are the self-sacrificial labels based on magnetic nanoparticle (MNPs) and Prussian Blue (PB), such as the one developed for detection of the avian influenza virus H5N1, using electrochemical conversion of  $\text{Fe}_3\text{O}_4$  MNPs into an electroactive PB analogue<sup>103</sup>. Conventionally, MNPs have been used in electrochemical biosensors to facilitate mass transport to the sensing surface under magnetic control as well as to separate the target from the sample<sup>104</sup>. However, they are biocompatible and allow electron transfer between redox systems and bulk-electrode materials and also



possess many other advantageous properties for the development of electrochemical biosensors (e.g., high surface energy, large surface area and electron-conducting materials)<sup>105</sup>. Moreover, MNPs have been reported as useful interfaces for electrocatalysis of molecules such as H<sub>2</sub>O<sub>2</sub> or O<sub>2</sub> that are involved in many molecular processes<sup>103–105</sup>. Additionally, they can be used as self-sacrificial labels after applying a chemical or physical treatment that leads to dissolution and release of metal ions which are further taken by an acceptor to amplify the signal<sup>103</sup>. Inorganic compounds such as PB and analogues are very interesting since they present a cubic lattice shape, with many interstitial sites and vacancies where insertion of various ions as counter ions can occur during the redox process of the substance<sup>106</sup>. Compared with platinum, can deliver 1000 times higher electrochemical rate constant for a redox process, increasing the sensitivity of biosensors by generating more current per unit time<sup>107–109</sup>. PB is also known as an artificial peroxidase and very good candidate for the catalysis of H<sub>2</sub>O<sub>2</sub>, therefore, combination with nanomaterials such as MNP is used as a strategy to increase the sensitivity and the analytical performance of biosensors<sup>110</sup>. The immune sandwich assay uses Fe<sub>3</sub>O<sub>4</sub> MNPs as labels, that are decorated with secondary antibodies. As the secondary antibodies recognize the virus, the MNPs undergo through an electrochemical conversion, by a two-step potentiometric process (cyclic voltammetry), where first metal ions are released (**Figure 5**). When the Au electrode with MNPs anchored to the surface (using a magnet), is immersed in 0.4 mM K<sub>4</sub>Fe(CN)<sub>6</sub> and 0.1M K<sub>2</sub>SO<sub>4</sub> solution, a high potential (+1.6 V) is applied to electrode solution, splitting H<sub>2</sub>O to O<sub>2</sub> and H<sup>+</sup>. Subsequently, Fe<sub>3</sub>O<sub>4</sub> is dissolved to continuously release Fe<sup>3+</sup> and Fe<sup>2+</sup> which are immediately electrochemically oxidized to Fe<sup>3+</sup>. The process is followed by the application of a low potential (0 V vs Ag/AgCl) where K<sub>4</sub>Fe(CN)<sub>6</sub> is electrochemically reduced at the electrode surface and combines with reduced Fe<sup>2+</sup> to form ferrous ferrocyanide (K<sub>2</sub>Fe[Fe(CN)<sub>6</sub>]), also known as Prussian white, PW, analogue of PB. The reactions are given in the next **Equations 5-7**:



In CV, the reduction peak that occurs between 0 V and +0.2 V was taken as the analytical signal and was demonstrated to be proportional to the concentration of H1N5 virus. This sensor showed a linear detection range from 0.0025 to 0.16 hemagglutination units (HAU, defined as the amount of virus need to cause the agglutination of red blood cells)<sup>111</sup>, an LOD of 0.0022 HAU, which is ~100 times lower than other biosensors<sup>112–114</sup>. Furthermore, these values were obtained by using only 6  $\mu\text{L}$  of sample, therefore very little volume is needed, a very advantageous characteristic for POC testing. However, this biosensor is a proof-of-concept that still needs to be further investigated to be scalable and implemented in the real world.

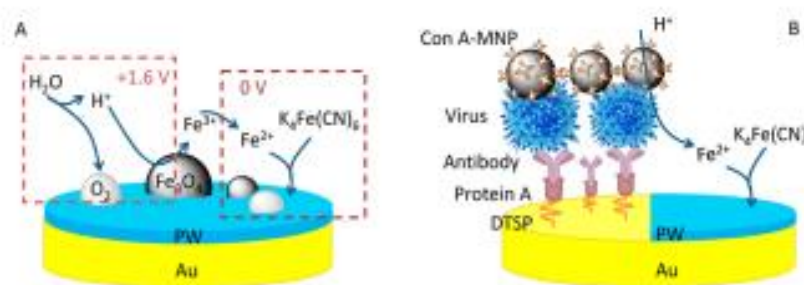


**Figure 5.** Schematic illustration of the immunosensor using  $\text{Fe}_3\text{O}_4$  MNPs as self-sacrificial label. A) Electrochemical conversion of  $\text{Fe}_3\text{O}_4$  MNPs in two-potentiostatic steps (first potential applied, +1.6 V, followed by 0V) for PB analogue production (PW), in a solution containing 0.4 mM  $\text{K}_4\text{Fe}(\text{CN})_6$  and 0.1M  $\text{K}_2\text{SO}_4$ .

### 2.1.3. Electrochemiluminescent labels

Electrochemiluminescence (ECL) can be defined as a process where light is generated through a electrochemical reaction<sup>115</sup>. Luminophores such as Tris(bipyridine) ruthenium (II) or quantum dots, ( $[\text{Ru}(\text{bpy})_3]^{2+}$  and QDs, respectively) are used as labels that can be excited through a reaction involving electrogenerated reactants emitting light as they decay to ground state<sup>116</sup>. The mechanisms how underpinning this process happens are well documented in the literature<sup>117–119</sup>, and they are classified in two categories: i) the annihilation pathway and ii) the co-reactant pathway. The annihilation pathway involves the direct generation of both oxidised and reduced species at an electrode surface, normally through two-directional potential stepping (anodic oxidation and cathodic reduction) to produce the radical ions<sup>120</sup>. Between these species electron-transfer reaction

occurs, generating an excited form that emits light when it decays to the ground state<sup>121</sup>, as in **Figure 6**. In contrast, the co-reactant pathway only a single-potential step is needed for ECL generation. A co-reactant consists of a chemical species e.g., tri-n-propylamine (TrPA), or N-butyldiethanolamine (NBEA) that is reduced or oxidized at the electrode surface, producing intermediates that react with the reduced or oxidized luminophore in the solution to generate the excited state which returns to ground state by emitting light<sup>116</sup>. Therefore, only a single-step potential is needed since the co-reactant reduction or oxidation takes place first, which reacts afterwards with the luminophore<sup>122</sup>. The utilisation of co-reactant systems dominates over its counterpart, since ECL generation is done in single potential step and a wide range of co-reactants are available to choose from<sup>115</sup>. In addition, regeneration of the luminophore allows it to participate in the ECL reaction with an excess of co-reactant which results in the production of many photons per cycle, enhancing the sensitivity of the technique<sup>123</sup>. In **Figure 6** different co-reactant routes are shown for  $[\text{Ru}(\text{bpy})_3]^{2+}$  and TrPA. **Figure 6B** represents the oxidative-reductive pathway where both  $[\text{Ru}(\text{bpy})_3]^{2+}$  and TrPA are simultaneously oxidised at the electrode surface generating  $[\text{Ru}(\text{bpy})_3]^{3+}$  and  $\text{TrPA}^{\bullet+}$ . This last one is deprotonated forming  $\text{TrPA}^{\bullet}$  which reacts with  $[\text{Ru}(\text{bpy})_3]^{3+}$  to form the excited state of the luminophore  $[\text{Ru}(\text{bpy})_3]^{*2+}$ , which rapidly decays to its ground state by emitting light throughout the process. In the catalytic pathway (**Figure 6C**),  $[\text{Ru}(\text{bpy})_3]^{2+}$  is oxidised first to  $[\text{Ru}(\text{bpy})_3]^{3+}$  which reacts with TrPA to generate  $\text{TrPA}^{\bullet+}$ . For the low-potential route (**Figure 6D**), TrPA is oxidised first at the electrode surface, generating  $\text{TrPA}^{\bullet}$  (after deprotonation) and it reacts with  $[\text{Ru}(\text{bpy})_3]^{2+}$ , producing  $[\text{Ru}(\text{bpy})_3]^+$  which is oxidised by  $\text{TrPA}^{\bullet+}$  generating the excited  $[\text{Ru}(\text{bpy})_3]^{*2+}$ . It is still a difficult task to unravel which mechanism is taking place, however, for a typical  $[\text{Ru}(\text{bpy})_3]^{2+}/\text{TrPA}$  system, ECL is dominated by the oxidative-reductive pathway when the concentration of  $[\text{Ru}(\text{bpy})_3]^{2+}$  is  $< 100 \mu\text{M}$ , but above this concentration, catalytic route starts to govern the ECL light generation<sup>124</sup>.

As mentioned above, in terms of biosensing, ECL based assays provide a dark background with a higher signal-to noise ratio since the energy excitation source (electrical) and the detected signal (light) are totally different and separated processes, which leads to achieve higher sensitivity than other electrochemical detection techniques<sup>116</sup>. Furthermore, compared to chemiluminescence, ECL gives excellent control over the time and position of the light generation since it only occurs in the

diffusion layer or the electrode surface if the luminophore is surface confined, providing a better selectivity and reproducibility<sup>123</sup>. Additionally, ECL biosensors also show a broad dynamic range, simplicity in analytical procedures, flexibility due to the wide variety of luminophores and are easy to combine with biological systems<sup>116,125</sup>. Hence, ECL has become a very powerful analytical tool for biosensing in clinical diagnostics, environmental and food monitoring<sup>123</sup>. Therefore, as mentioned above, one of the objectives of this thesis is to study and exploit Ru based dyes as labels for the development of SPR-ECL biosensors.

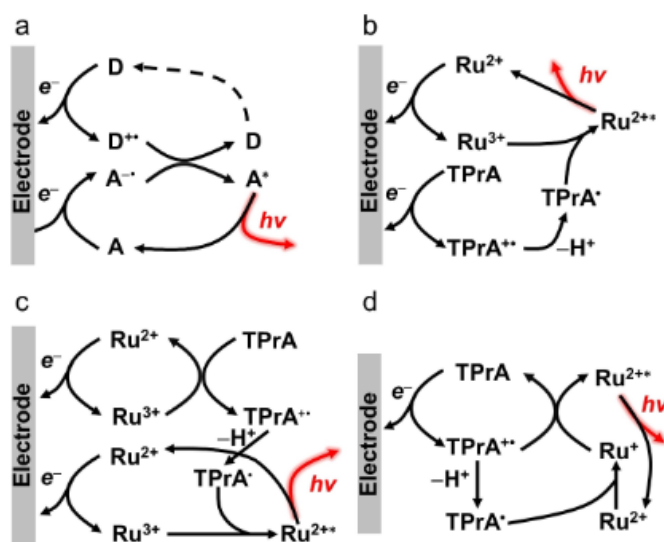


**Figure 6.** Schematic illustration of ECL annihilation and co-reactant pathways<sup>124</sup>. A) Annihilation pathway, B) Oxidative-reductive pathway, C) catalytic pathway and D) low oxidation potential pathway.

In the last twenty years there has been a rapid development of nanomaterials based ECL biosensors and many sensitive, selective and rapid ECL immunoassays and DNA assays have been developed<sup>123</sup>. An example of this is the Faraday cage-type electrochemiluminescence immunosensor based on multi-functionalized graphene oxide (GO) for whole-cell ultrasensitive detection of *Vibrio vulnificus* (marine pathogenic bacteria) in seafood and seawater using chronoamperometry<sup>126</sup>. As opposed to a traditional immunosandwich assay, a Faraday-cage-type immunocomplex is based on a conductive two-dimensional (2D) nanomaterial, functionalized with signal labels and recognition elements, which directly overlaps with the electrode surface and electrons can freely flow from the electrode to the nanomaterial, extending the outer Helmholtz plane (OHP) and having electrochemically effective signal labels (see **Figure 7**)<sup>127</sup>. In

electron kinetics, the OHP is the interfacial region where electronic exchange happens between redox active, solvated ions and the electrode surface, and only an electrochemical reaction occurs if the electrochemical active species are near to the OHP<sup>128</sup>. This region is only a few nanometres or angstroms away from the electrode surface (depending on the ionic concentration) and when a suitable voltage is applied, the OHP potential is altered and activates the ECL labels near to the OHP interface ensuring the initiation of the electrochemical reaction<sup>127</sup>. Therefore, the electron transfer occurs in a fixed distance between the ECL label and the electrode surface and if this distance is increased, the electrochemical reaction cannot take place<sup>127,128</sup>. However, when a label 2D-nanocarrier with a large surface area is introduced in the system, it can be overlaid onto the electrode surface and the electrons can freely flow among the electrode, the carrier and all the luminophores, which all of them become effective and/or available since the OHP has been extended by the presence of functionalized GO layer. In a conventional ECL sandwich immunoassay, the immunocomplex is immobilized “on-electrode”, which restricts the improvement the detection sensitivity, since the distance between luminophore and OHP is going to be potentially larger and not tuneable. The authors of this work built an immunosensor that operates in a co-reactant system (TrPA) using a magnetic glassy carbon electrode, where MNPs conjugated to capture antibodies are deposited after separating the target from liquid samples, and graphene oxide nanosheets functionalized with secondary antibodies and (2,2'-bipyridine) (5-aminophenanthroline) ruthenium (II) ( $[\text{Ru}(\text{bpy})_2(\text{phen})\text{-NH}_2]^{2+}$ ) create a Faraday-type cage ECL model. Ruthenium (II) complexes are among the most studied transition metal-complexes in photochemistry since they show an outstanding combination of stability, redox properties, excited state stability, excited state lifetime and high efficiency in aqueous media, very important characteristics that are key for the development of ECL based analytical tools<sup>129,130</sup>. On the other hand, GO presents a high surface area and shows excellent conductivity, high mechanical strength and good biocompatibility, ideal properties to use it as probe and recognition elements carriers<sup>131,132</sup>. Therefore, in the proposed sensor for *V. vulnificus* detection, GO acts as nanocarrier of (2,2'-bipyridine)(5-aminophenanthroline)ruthenium ( $[\text{Ru}(\text{bpy})_2(\text{phen})\text{-NH}_2]^{2+}$ ) and as nanosemiconductor that accelerates efficiently the electron transfer, achieving a more sensitive ECL sensor<sup>133</sup>. When the bacteria (approximately 1 micrometre of diameter) are introduced on the system and the cells are covered with the multi-functionalized GO nanosheet and the distance between the luminophore and the electrode increases. However, the edge of GO

deposits on the electrode surface directly, extending the OHP of the electrode and having more “effective” luminophores. The biosensor showed a linear range from 4 CFU mL<sup>-1</sup> to 4 × 10<sup>8</sup> CFU mL<sup>-1</sup> and a LOD of 1 CFU mL<sup>-1</sup> under optimal conditions. Comparing with conventional ECL immunosandwich assays, the Faraday-cage model increased the sensitivity about 50-fold<sup>126</sup>. A similar model was built for the detection of *Vibrio parahaemolyticus* in seawater, using ([Ru(bpy)<sub>2</sub>(phen)-NH<sub>2</sub>]<sup>2+</sup> and AgNPs as labels in GO, showing a LOD of 33 CFU mL<sup>-1</sup> using anodic stripping voltammetry as electrochemical technique<sup>134</sup>. These results showed that the Faraday cage structure in combination with ECL labels, improves the accuracy of the biosensor, thus is a powerful tool for pathogen detection<sup>127</sup>.

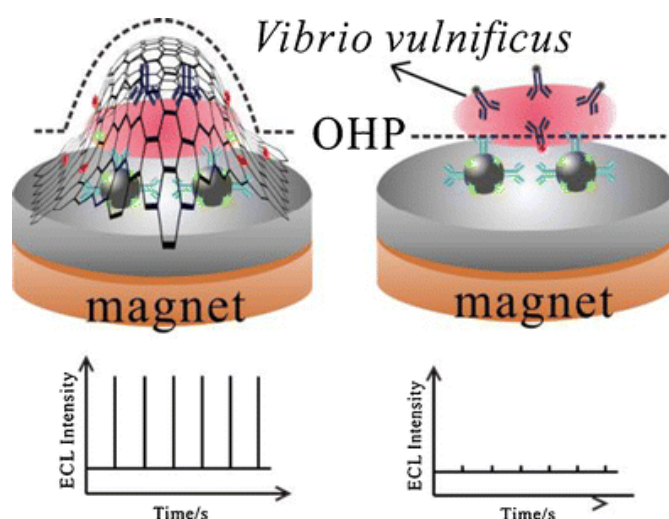


**Figure 7.** Diagram of the Faraday-cage like ECL immunosensor for detection of *Vibrio vulnificus*.

Another example of utilisation of Ru (II) based labels is the recent proof-of concept ECL-DNA sandwich assay using a gold nanocavity array as sensing platform<sup>135</sup>. In this work, ruthenium (II) (2,2'-bipyridyl)-2(4-carboxy phenyl) imidazo (4,5)(1,10) phenanthroline ([Ru(bpy)<sub>2</sub> PIC]<sup>2+</sup>) is used as the DNA probe label. As it has been mentioned above, many efforts have been done to increase the sensitivity and improve the range of applications of ECL labels by combining them with zero-dimensional (0D) nanomaterials, one-dimensional nanomaterials (1D), two-dimensional (2D) nanomaterials, and three-dimensional (3D) nanomaterials<sup>33,136</sup>. Among these materials, 3D metallic nanostructures have been widely used in electrochemical biosensors as electrodes, surfaces for bioreceptor immobilization and scaffolds<sup>101,137–139</sup>. Metals such as gold, are used as

nanostructures since they enhance biosensing properties (e.g., catalytic behaviour, electrochemical and optical properties while increasing the surface area)<sup>140</sup>. Furthermore, different morphologies can be created such as nanocavities, that can provide several advantages in plasmonic biosensing such as possibility of multiplex detection and in general, they have an improved bulk sensitivity<sup>141</sup>. Surface plasmon resonance (SPR) is an optical property of some materials (e.g., gold, silver, zinc or copper) that when they are excited by the incident light, a “cloud” of electrons, also known as plasmon, oscillates on the material surface generating a local electromagnetic field<sup>142</sup>. SPR offers quantitative real-time information about the adsorption of molecules at the surface, whereas ECL provides high sensitivity and selectivity as well as low detection limits, hence, having both systems in the same platform could be very beneficial to track interfacial processes and to improve the analytical performance<sup>143</sup>. Moreover, a fraction of the light generated through ECL can be used to excite the electron oscillation at the nanostructure surface when there is a resonant interaction between the plasmon and the excited state of the luminophores<sup>135,144</sup>. Therefore, materials with optical properties such as gold can be used to influence the light emission process with coupling SPR and ECL enhancing the final light emission<sup>143,144</sup>. As the authors described, a 3D nanocavity array electrode in combination with the label  $[\text{Ru}(\text{bpy})_2 \text{PIC}]^{2+}$  can be used to combine SPR and ECL on a wireless bipolar system<sup>135</sup>. When the DNA probe hybridises to the overhang target DNA of methicillin-resistant *Staphylococcus aureus* on the array surface,  $[\text{Ru}(\text{bpy})_2 \text{PIC}]^{2+}$  emits light at around 610 nm exciting the cavity plasmon and enhancing the ECL intensity of a fraction of the immobilised luminophores. This system shows a linear dynamic range from 10 nM to 30  $\mu\text{M}$  with an LOD of 1  $\mu\text{M}$  and 6 times more analytical sensitivity compared to a planar gold surface under the same conditions. However, further experiments with real samples are needed to test the performance of the sensor for future POC application.

QDs are also often used as ECL labels, as the availability of different sizes, material dependent optical and electrical properties, broad absorption spectra, high quantum yields and the narrow emission spectra makes them very interesting for biosensing applications<sup>34</sup>. In addition, compared to conventional molecular ECL luminophores (e.g.,  $[\text{Ru}(\text{bpy})_3]^{2+}$  and luminol) QDs show good stability, flexible functionality and they are a very low cost effective alternative<sup>145</sup>. Recently, alongside AuNPs, QDs have been extensively used in distance-dependence SPR-enhanced luminescence<sup>143</sup>. An example of

this is the distance-dependent plasmon enhanced DNA sandwich assay based ECL biosensor developed for hepatitis C virus detection using sulphur doped boron nitrogen QDs (S-BN-QDs) and non-metallic plasmonic MoS<sub>2</sub> nanosheets<sup>146</sup> (**Figure 8**). Firstly, the authors demonstrated that using a glassy carbon electrode and cyclic voltammetry, S-BN-QDs showed an ECL peak at -1.75 V, emitting light at 535nm. Subsequently, the optimal distance between S-BN-QDs and MoS<sub>2</sub> nanosheets (on electrode surface) was studied using dsDNA as spacers and results showed that at 19 nm, ECL emission increased 120% over the ECL intensity achieved when distance was 0 nm. When S-BN-QDs are too close to the surface (0 nm), an energy resonance transfer (ERT) optical process happens<sup>147</sup>, in which the excess of energy of an excited molecule (S-BN-QDs), is transferred to an acceptor (MoS<sub>2</sub> nanosheets), quenching the ECL light emitted by S-BN-QDs. However, as the distance increases, the ERT drops and the surface plasma coupling effect is strengthened since MoS<sub>2</sub> nanosheets plasmon is excited by the incident light emitted by QDs, thus ECL is enhanced<sup>146</sup>. The constructed sandwich DNA biosensor for HCV gene detection is based on the utilization of a mixture of two DNA harpins, one fixed on the electrode surface and the second one is conjugated to S-BN-QDs (**Figure 8**). When the target is present, the first harpin opens and hybridizes with the target, exposing a new-single stranded region that is complementary to the second harpin, forming an dsDNA unit at the end designed to be 19 nm long (optimized distance). The sensor displays a linear dynamic range from 0.5 pM to 1 nM with a very good LOD (0.17 pM), comparing with other nucleic acid based biosensors for HCV detection<sup>148,149</sup>. Despite the high sensitivity of the sensor, more experiments are needed with real samples to investigate possible interferences and cross-reactivity events.

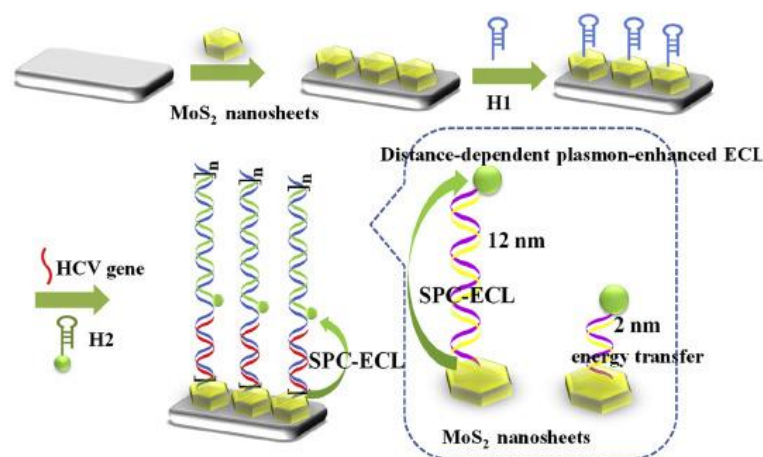




**Figure 8.** Schematic representation of HCV-based sensor and distance-dependent plasmon-enhanced ECL mediated by non-metallic plasmonic MoS<sub>2</sub> nanosheets and QDs.

## 2.2. Label-free electrochemical biosensors

In label-free electrochemical biosensors, the recognition event is directly transduced to an electrical signal and may be preferred over label based since they present several advantages<sup>43</sup>. For instance, they require simpler designs, less processing steps and cost due to the absence of complex labels and they are more easily scaled scalability. However, they often suffer from a lack of sensitivity, cross-reactivity, and may be more prone to non-specific adsorption interference issues<sup>50</sup>. On the other hand, the presence of labels can interfere with kinetics as well as cause nonspecific binding that can lead to systematic errors during the measurements<sup>150</sup>. Furthermore, the sensitivity of label-free biosensors can be improved by modifying the electrode surface with high-functionality materials, enhancing the adsorption properties, increasing the surface area and achieving good biocompatibility<sup>151</sup>. Therefore, label-free electrochemical biosensors, can serve as a powerful POC diagnostic tool, providing real-time single and/or multi-target analyses, with the possibility of development of portable and friendly user devices<sup>5,152</sup>.

### 2.2.1. Electrochemical impedance spectroscopy (EIS)

Among all the electrochemical techniques, impedance spectroscopy (EIS) is the most used in label-free detection since it possess several advantageous characteristics such as being a steady-state technique, small amplitude perturbation of the system and detection of signals over a very wide range of applied frequencies, from 1 mHz to 1 MHz<sup>153</sup>. In terms of biosensing, EIS is a very useful technique to study and understand the interfacial properties and/or changes (capacitance or resistance) in real-time as consequence of selective bio-recognition process<sup>27,153</sup>. One example of EIS POC immunosensor for detection of Zika virus protein is shown in **Figure 9**. The authors used a gold micro electrode (electrode width and electrode gap 10  $\mu\text{m}$ ) modified with antibodies that can recognize and bind to ZIKV-envelope protein<sup>154</sup>. After the biorecognition, a decrease in electron transfer rate of Fe (II)/(III) couple in solution occurs causing an increase in the charge transport resistance measured by EIS. Under optimal conditions, the biosensor

showed a linear detection range from 10 pM to 1 nM and a LOD of 10 pM, i.e., it is highly sensitive. Furthermore, the self-life of the sensor was studied for clinical application, and results demonstrated strong dependence on temperature as it was stable for 30 days only when stored at 4°C. One of the main drawbacks of immunosensors is that the sensitivity of antibodies fluctuates according to parameters such as pH, exposure to light and temperature (typical storage conditions at 4°C), and changes can dramatically affect the antibodies ability to bind to specific targets<sup>155</sup>. Despite the potential of the system for POC detection since it can be integrated in a smartphone, only results under optimal conditions have been reported, therefore further research is needed with real samples for its implementation in clinical diagnostics for ZIKV detection.

Genosensors, or nucleic acid-based biosensors can also be developed on an EIS platform. For instance, the proof-of concept sensor for temperature-enhanced *mcr-1* colistin resistance gene detection from *E. coli* using a gold SPE<sup>156</sup>. This platform is presented as a rapid and cost-efficient way of detection, where hybridization of immobilised specific peptide nucleic acid (PNA) with bacteria plasmid is temperature controlled and enabled by a new flow cell measurement setup. The sensor is highly selective since it allows discrimination of targets containing single nucleotide polymorphisms (SNP) based on a hybridization/dehybridization test over time. It was found that using a temperature of 55 °C for hybridization, followed by a washing step with a buffer, increases the match/mismatch discrimination ratio to 5.7 in comparison with a temperature at 60°C, where the discrimination ratio was 3.4. This behaviour reflects the differences in the temperature dependent hybridisation kinetics between the fully complementary and SNP containing targets. This means that 55°C and the washing step, decreases the signal for the target with SNP, while keeping the perfect match signal for the target without SNP. Further tests were made with heat-denatured *mcr-1 E. coli* and New Delhi metallo-β-lactamase-1 (NDM-1) *E. coli* heat-denatured plasmids (from bacterial cultures) both at a concentration of 4 ng/μL. The results showed that after 30 minutes of hybridization with the PNA on the electrode surface, it was possible to detect *mcr-1* plasmids as well as to discriminate between these different plasmids carrying different resistance genes like NDM-1. However, sample preparation (i.e., cell cultivation and plasmid extraction) is a time-consuming step which should be addressed when new setups are proposed for genosensors development. Furthermore, more data is needed about LOD and dynamic range when used to analyse real samples.

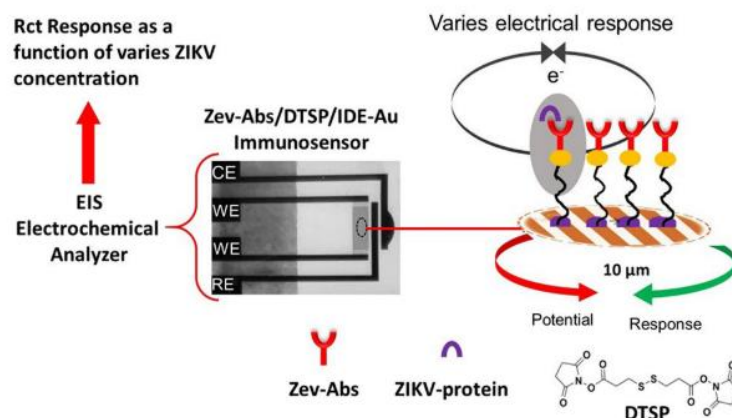


**Figure 9.** Illustration of fabricated EIS immunosensor via immobilization of ZIKV-envelop protein antibody (Zev-Abs) onto self-assembled monolayer (SAM) of dithiobis(succinimidyl propionate) (DTSP) deposited on interdigitated micro-electrode of gold (IDE-Au) array of 10 $\mu\text{m}$ <sup>154</sup>.

### 2.2.2. Detection of enzymes and metabolites released by pathogens

Traditional screening methods, that detect either the whole pathogen, fragments or nucleic acids are very useful for pathogen detection and identification as well as diagnosis of infections. However, they are often expensive and very time-consuming since several sample preparation steps are often needed<sup>157</sup>. Recently, label-free biosensors for direct detection of molecules released by pathogens such as enzymes and quorum sensing molecules (QS molecules), have attracted much attention since their simple design, low cost, and ability to discriminate between alive and dead microorganisms<sup>69</sup>. Therefore, studying and taking advantage of the properties of secreted biomolecules by pathogens can offer multiple alternatives for the development of electrochemical biosensors that indirectly detect the pathogen, or a component. As an example, the enzyme cytochrome c oxidase produced by some bacteria, has been successfully used as a biomarker detection of at carbon microelectrodes using impact electrochemistry technique<sup>158</sup>. Impact or collision electrochemistry, is based on the measurement of an electrical signal arising from the collision of a single entity (e.g., cell, particle, or molecule) on an electrode surface due to its free motion in solution, obtaining a current pulse signal of very short duration ( $\mu\text{s}$  to  $\text{s}$ )<sup>159,160</sup>. With this technique, a label-free approach can be used for bacteria detection, since some of them possess enzymes with redox activity that can generate

currents in contact with the electrode surface<sup>159,161,162</sup>. By employing *N,N,N',N'*-tetramethyl-*para*-phenylene-diamine (TMPD) as redox mediator, the authors were able to establish a dependency of TMPD concentration with bacteria impacts on electrode surface. In this system, cytochrome c oxidase performs the oxidation of TMPD which is regenerated at the electrode surface and a reductive current is generated. Although this technique is a valuable proof of concept, selectivity is the main issue that needs to be addressed for future applications, which could be solved by introducing labelling chemistry<sup>159</sup>.

On the other hand, biosensors for QS molecules detection are very interesting and promising approach, especially for POC applications<sup>163</sup>. By exploiting QS molecules redox activity, such as 4-hydroxyquinoline (HHQ), *Pseudomonas* quinolone signal (PQS) and pyocyanin (PYO), electrochemical sensors have been used for fast, high-throughput detection strategies<sup>69,164</sup>. A successful multiplex detection method of HHQ, PQS and PYO was reported to determine the presence of *Pseudomonas aeruginosa* using a boron diamond doped electrode<sup>165</sup>. Each molecule showed different redox peaks in SWV suggesting it may be possible to detect QS molecules simultaneously. Further tests showed that the LOD of PYO, PQS and HHQ was, 50 nM 250 nM 250 nM, respectively, under optimal conditions. Moreover, *in vitro* experiments with cystic fibrosis sputum samples spiked with  $1 \times 10^5$  cells of *P. aeruginosa* A14 (PA14) and after 11 days of incubation the LODs for PYO, HHQ, and PQS were 2.8  $\mu$ M, 7.2  $\mu$ M, and 10.4  $\mu$ M, respectively, using DPV as electrochemical measurement technique. However, no signals were detected for HHQ and PQS after 3 days of incubation. Additionally, the optimal performance of the biosensor requires pH to be adjusted to 5. Therefore, the suitability of the assay is subjected to the access and availability of equipment to carry out the test, making more difficult near-to patient testing. Nevertheless, the results are very promising and show the potential QS molecules as targets for label-free POC detection in medical environments.

### 3. CONCLUSIONS AND FUTURE PERSPECTIVES

Enhancement of parameters such as sensitivity, specificity, and LOD is pursued for the development of high-performance biosensors. Utilisation of labels for improvement of

these features has proven to be an excellent alternative since they provide good signal amplification, a key feature in biosensors to achieve higher sensitivity and lower detection limits. However, they require more preparation steps which leads to a more complicated and less cost-effective assays. In the literature, label-free biosensors, are presented as low-cost, simple, rapid, and easy to use sensors, where electrochemical impedance spectroscopy (EIS) has been the predominant technique. Moreover, identification of different targets such as QS molecules and enzymes produced by pathogens can be also studied for real-time detection and disease monitorization providing more information about the patient prognosis. Despite all the advantages that label-free technology offers, they often show interference and specificity issues which can negatively affect the final signal readout. Nevertheless, as discussed in this chapter, combination of different materials and techniques constitutes a good approach to improve the analytical performance of electrochemical biosensors for the detection of pathogens. For example, ECL based labels have shown to successfully amplify the signal by keeping a low background noise, improving the sensitivity and the selectivity of the assays. In fact, different luminophores carrying groups such as carbon nanotubes or NPs, can be designed to improve ECL labels efficiency as well as design of SPR-ECL based systems for ECL signal enhancement, and overall, the performance of the biosensor. In addition, advancements in the manufacturing and utilisation of 3D metallic surfaces as electrodes has been shown to provide a larger surface area that can be also further optimized to improve the properties of the sensing platform. Hence, informed by this literature review, there is a strong need for creating robust, sensitive, and cost-effective pathogen biosensors. For this reason, this work focuses on the development of new detection platforms based on ECL, using 3D printed electrodes and, SPR-ECL approach with different ruthenium complexes for its potential use in biosensors for bacteria detection. The objectives of this thesis try to address the issues stated at the beginning of this chapter, focusing on the understanding of electrochemical kinetics and dynamics of the systems proposed in the following chapters, as well as on the optical properties of the materials used in this project. In Chapter 2, a novel 3D printed Ti array electrodes are studied and optimised with a thin layer of AuNPs for their utilisation in ECL co-reactant systems. The unique architecture of these electrodes provides an enhance diffusion as well as a large surface area that can be exploited to immobilise more capture on the surface which can potentially increase the sensitivity of the platform. Moreover, the electrodes prove to provide a tuneable and optimizable surface with AuNPs that improved

the redox properties of the platform, and they can further be functionalized with thiolated biomolecules for future application in bacteria detection.

Separately, in Chapter 3, AuNPs are investigated with spectroscopic and electrochemical techniques, alongside different ruthenium complexes in an aqueous system to elucidate and understand better their interaction, in terms of light enhancement or quenching for application in SPR-ECL sensors. Furthermore, the dye  $[\text{Ru}(\text{bpy})_3\text{-NH}_2]^{2+}$  characterised in Chapter 3 is used for the development of a DNA based ECL assay for UTI causing *Escherichia coli* detection on a GCE coated with a layer of AuNPs. In addition, in Chapter 4 is shown that NBEA as co-reactant is a more suitable co-reactant when compared to TrPA, since higher ECL intensities were which is more advantageous for the development of high sensitive ECL biosensors, Finally in Chapter 5 a novel protocol for the synthesis of  $\text{Fe}_3\text{O}_4$  particles and coating with Au is reported, for their potential used in target separation from sample solution and application in DNA biosensors.

**Chapter 2:**  
**Electrochemical and ECL**  
**characterization of 3D printed Ti**  
**electrodes**

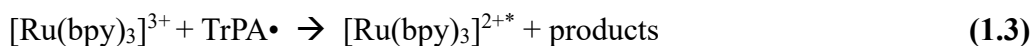
## 1. INTRODUCTION

3D printing for the manufacture of novel electrode structures and other electronic devices has become very popular in recent years<sup>166–169</sup>. 3D printing involves a group of techniques based on the process of adding successive layers of the material to create a three-dimensional object that is previously designed in CAD<sup>170</sup>. These emerging techniques serve as powerful tools for new complex designs that cannot be produced using traditional “subtractive” approaches, e.g., milling that involve removal of material, as well as improve of pre-existing platforms using cheaper materials and simple manufacturing techniques<sup>171,172</sup>. Interest in fabricating 3D printed electrodes is increasing since it provides several advantages for electrochemical analysis and development of electrochemical sensors. Portability, use of low-cost materials, customized shapes, size, conductivity, and precision are some of the characteristics that can be achieved in a very few hours<sup>170,173</sup>. In fact, 3D electrodes have arisen as a potential alternative to overcome the limitations of conventional electrodes and improve electrochemical measurements for detection of biomolecules and/or biological entities<sup>170,174</sup>, e.g., by controlling transport by diffusion or enabling multiple sensors to be made that are free from cross-talk. As the 3D architecture directly impacts the device functionality, e.g., multielectrode arrays, and mass transport of the analyte, different shapes and structures has been studied. Cylindrical electrodes or arrays have attracted much attention due their unique properties i.e., increased surface area, radial diffusion to the tip with linear diffusion to the wall of the cylinders at accessible timescales<sup>175,176</sup>. Therefore, they can provide large diffusion layers compared to planar electrodes<sup>177</sup>. However, to elucidate the real potential of 3D printed arrays, electrochemical characterization is important to understand their mass, electron and ion transport properties for further applications in electrochemical biosensors, electrocatalysis or energy storage<sup>172,178,179</sup>.

While the redox activity of 3D printed electrodes has been widely studied, their application in photonics, has been less explored, e.g., their ability to generate light by an electrochemical reaction, or electrochemiluminescence (ECL). In this scenario, as mentioned above, the 3D architecture as well as the identity and properties of the metal, play important roles in mass transport and electron transfer, dramatically influencing the redox and excited state of the luminophore (e.g.  $[\text{Ru}(\text{bpy})_3]^{2+}$ ) and the production of the co-reactant, as well as the overall kinetics and dynamics of the reaction on to the electrode



surface<sup>175</sup>. Understanding how geometry, size and material affect the ECL process, by enhancing or quenching the electrogenerated light is essential for future applications. For example, the presence of a thick oxide layer on the active electrode surface, can hinder the electron transfer, which usually decreases the current achieved<sup>180,181</sup>. Among all the luminophores, such as luminol, tris(2,2-bipyridyl) ruthenium (II) ([Ru(bpy)<sub>3</sub>]<sup>2+</sup>), lucigenin or quantum dots (QDs), [Ru(bpy)<sub>3</sub>]<sup>2+</sup> has attracted more attention because it presents several advantages e.g., strong luminescence and good solubility in several aqueous and non-aqueous solvents, sensitivity, good ECL efficiency and wide linear range<sup>182</sup>. The most common ECL system where [Ru(bpy)<sub>3</sub>]<sup>2+</sup> has been used is with a co-reactant such as tri-n-propylamine (TrPA). As it is shown in **Equations 1.1-1.4** (simplified version), when applying a potential, an oxidation reaction occurs, where [Ru(bpy)<sub>3</sub>]<sup>2+</sup> is oxidized to [Ru(bpy)<sub>3</sub>]<sup>3+</sup> at the electrode surface. Simultaneously, TrPA is also oxidized, and in a second step a TrPA radical (TrPA•) is generated, which will reduce [Ru(bpy)<sub>3</sub>]<sup>3+</sup> and produce the excited state of ruthenium ([Ru(bpy)<sub>3</sub>]<sup>\*2+</sup>) which then decays to its ground state, emitting red light around 620 nm<sup>183</sup>.



Furthermore, the complex is very stable in both oxidised, [Ru(bpy)<sub>3</sub>]<sup>3+</sup>, and reduced, [Ru(bpy)<sub>3</sub>]<sup>2+</sup> forms<sup>175,182</sup>. Therefore, a combination of 3D printed materials and ECL can provide a high-performance platform for analytical sciences.

In electrochemistry, Selective Laser Melting (SLM) has been used to create 3D electrodes<sup>169,170,182,184</sup>. This technique uses a high-power laser for the successive addition, melting and fusion of thin layers from the chosen metal powder base following a pre-designed pattern, producing near net-shape parts with close to full density<sup>172</sup>. Compared to other techniques such as lithography, SLM provides a fast, cost-effective, and simple manufacture of electrodes with a unique design of micro and macro structures<sup>175</sup>.

Furthermore, SLM generally uses 20–50  $\mu\text{m}$  metal powder particles to print 20–100  $\mu\text{m}$  thick metal layers and the minimum feature size that has been reported ranges from 40–200  $\mu\text{m}$ <sup>185</sup>. However, this relatively new metal printing technology needs further investigation for electrochemical applications, e.g., the fused grain structure can be very rough and even porous, complicating the diffusion profiles. Not many metals have been reported for SLM printing. However, Ni and Ti alloys as well as stainless steel have been successfully used and could be applied in electrochemistry<sup>186</sup>. Ti6Al4V material is the most frequently tested alloy for medical applications because of its biocompatibility with human tissue since an oxide layer is rapidly formed on the surface of the material upon exposure to air, low weight and corrosion resistance<sup>186–189</sup>. This material does not necessarily support fast heterogeneous electron transfer or have good electrocatalytic properties. However, it has interesting redox properties with a specific geometrical structure, and its surface properties can be modified by depositing other materials such as gold. As discussed in the Literature Review, gold has been proven to be useful in the field of biosensors and specially in ECL based detection<sup>190–193</sup>.

This chapter presents 3D Ti electrodes printed with the SLM technique using Ti alloy (Ti-6Al-4V) powder, that show a unique architecture and electrochemical properties. Different techniques such as SEM, cyclic voltammetry and ECL were used to characterize the 3D printed Ti arrays. Furthermore, parameters like surface roughness, diffusion coefficient, heterogeneous electron transfer rate constant, resistance and the properties of the native oxide layer were analysed to provide more information about the characteristics of these novel arrays. The ECL response of the electrodes was analysed through a co-reactant system, by using  $[\text{Ru}(\text{bpy})_3]^{2+}$  as luminophore and tri-n-propylamine (TrPA) as co-reactant. Surface functionalization with gold was also study for surface optimization and potential application for bacteria detection.

## 2. MATERIALS AND METHODOLOGY

### 2.1. Manufacture of 3D printed Ti arrays and workflow

By using the modelling program SolidWorks, the electrode was designed, and metal printing was performed with a Realizer SLM50 metal printer (Realizer, Germany) using Selective-Laser Melting (SLM) technique. The high-energy laser beam fused and linked Ti alloy (Ti-6Al-4V) powder, layer by layer creating an array of 25 vertical round microcylinders (0.015 cm radius, 0.3 cm high) spaced evenly on a 0.48×0.48 cm square base that contained 0.75×0.75 mm holes<sup>175,194</sup>. These electrodes were donated by Prof. Gordon Wallace of the University of Wollongong, Australia. **Figure 1** shows the architecture and wiring of the electrodes with copper wire (99,99% and 0.25 mm) and protected with Teflon tape (12 mm x 0.075mm), so they could be use in a three-electrode electrochemical cell. These electrodes were further modified (mechanically and chemically polished) and functionalized (gold electrodeposition) with the intention of optimizing the surface for biosensing purposes. The uncoated and coated electrodes with gold, they were all wired and protected with Teflon tape as indicated. In order to run the electrochemical experiments, the electrodes were immersed in the solution making sure that all the area of the electrode was in contact with the electrolyte. However, the protected part of the electrode was left outside the solution to avoid corrosion. **Figure 2** shows the workflow followed in this thesis and the characterization of each step.

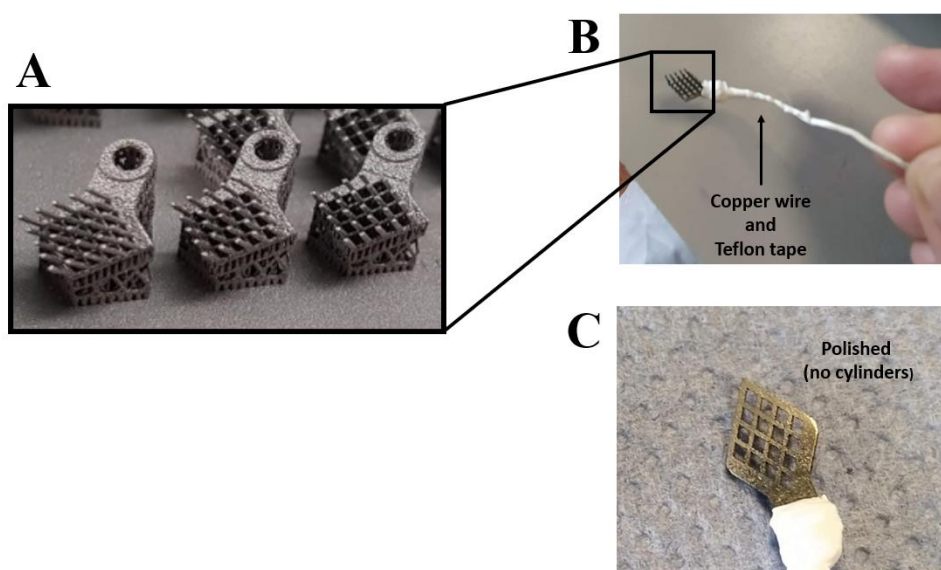


**Figure 1.** Architecture and wiring of electrodes. A) 3D printed Ti electrode. B) Wired 3D printed Ti electrode. C) Mechanically polished 3D printed Ti electrode.

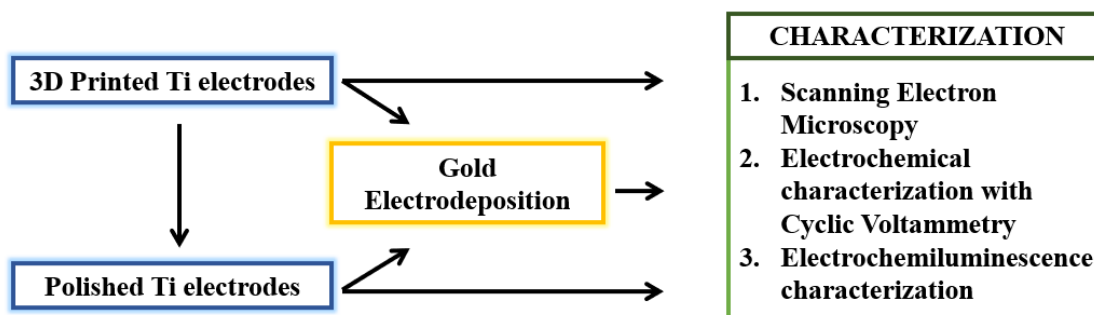


**Figure 2.** Scheme of Chapter 2 workflow.

## 2.2. Characterization of 3D printed Ti electrodes

Structural characterization and surface composition analysis was carried out with Scanning electron microscopy (SEM) (Hitachi S3400n SEM, Tungsten system). For the electrochemical characterization a potentiostat (CH Instrument Model 700E), an Ag/AgCl reference and platinum wire were used (IJ Cambria). The 3D printed electrodes acted as working electrodes. Ferrocenemethanol (FcnMeOH) was tested as redox probe, using lithium perchlorate (LiClO<sub>4</sub>) as supporting electrolyte. All the reagents were purchased from Sigma Aldrich.

Experiments for electrochemiluminescence detection, were performed using a CH Instrument Model 760B workstation, with the 3D printed electrode as working and an Oriol 70680 photomultiplier tube (PMT) biased at  $-850\text{V}$  along with a high-voltage power supply (Oriol, Model 70705) and an amplifier/recorder (Oriol, Model 70701) was used to collect the light emitted as shown in **Figure 3**. In this case, Tris- (2,2'-bipyridyl) dichlororuthenium (II) hexahydrate (Ru[bpy]<sub>3</sub>Cl<sub>2</sub>·6H<sub>2</sub>O) (powder, Sigma Aldrich), tripropylamine (TrPA) ( $\geq 98\%$ , Sigma Aldrich), using LiClO<sub>4</sub> as supporting electrolyte (powder, Sigma Aldrich). All the ECL measurements were performed with the amplifier set at  $10^8$ . This amplifier allows to tune the amplification of the photons emitted during the ECL light generation. This is very important since a high amplification could lead to a saturated signal that can potentially damage the potentiostat. Therefore, the appropriate amplification setting was selected to avoid this issue.

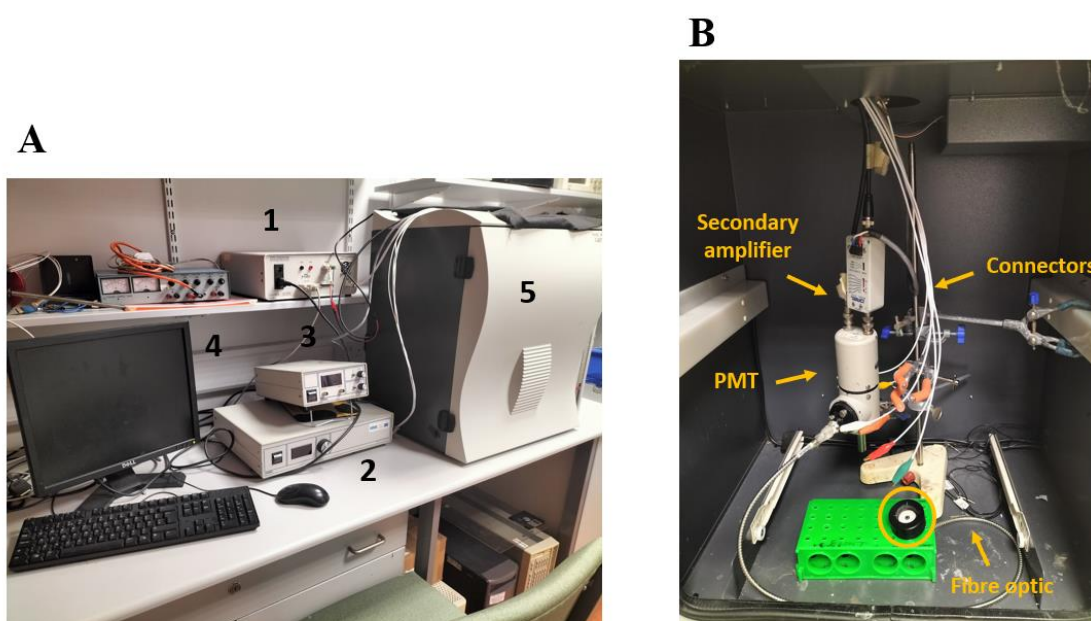


**Figure 3.** ECL signal recording equipment. A) ECL set up: (1) Potentiostat, (2) power-supply, (3) amplifier/recorder, (4) PC desktop for data visualization and (5) dark box. B) Set-up inside dark box: photomultiplier (PMT), secondary amplifier, connectors, and fibre optic for light collection. The circle indicates where the three-electrodes electrochemical cell is placed to record the signal.

### 2.3. Surface treatment and gold electrodeposition

Prior to electrochemical characterization, the electrodes were chemically treated using a protocol developed in this work. The 4-step cleaning protocol involves a mild chemical treatment aimed to remove the oxide layer formed on the surface of the titanium electrodes as well as to remove any other impurities remaining from the printing process. Firstly, electrodes were immersed in boiling deionized water for 30 mins. Subsequently, they were transferred to isopropanol followed by sonication for 30 mins. For the next etching steps, the electrodes were immersed into a boiling solution of 20% v/v HCl, from a 37% v/v stock, in H<sub>2</sub>O (Sigma Aldrich) for 40 minutes and finally transferred to a boiling 10% oxalic acid in H<sub>2</sub>O ( $\geq 99\%$ , Sigma Aldrich) solution for 30 mins, rinsed with deionized water and dried with a stream of nitrogen. Some electrodes were first mechanically cleaned with sandpaper (grit size P1200,  $15.3 \pm 1 \mu\text{m}$ ) and etched afterwards with the cleaning protocol described above.

Electrodeposition of gold onto the surface of Ti electrodes was carried out after chemical etching, using cyclic voltammetry, for 30 cycles (from -0.5 V to -2 V) with a Gold Tank Plating Solution (Spa Plating) using Ag/AgCl as the reference and platinum (Pt) as working electrode. After the electrodeposition the electrodes were rinsed with deionized water and air dried. Before each use, the electrodes were electrochemically cleaned in an aqueous solution 0.1M H<sub>2</sub>SO<sub>4</sub> (Sigma Aldrich) and stored in acid until used.

### 3. RESULTS AND DISCUSSION

#### 3.1. Bare 3D-printed Ti electrodes

##### 3.1.1. Surface characterization

Knowing the structural and/or geometrical features of 3D-printed electrodes is important to understand the overall electrochemical properties of the platform. For example, the size of the individual pins in the array and their separation will influence the mass transport regime and the time/scan rate at which diffusion fields at the individual pins will coalesce. Moreover, surface analysis microscopy techniques can be used to provide information about surface composition, e.g., the presence of oxide layers. Among these techniques, SEM is one of the high-resolution imaging method that helps to monitor size, distribution, formation and morphology at the micro and nanoscale<sup>195</sup>. The images obtained with SEM of the 3D-printed Ti electrodes are shown in **Figure 4A** (not cleaned and not used) **B** (mechanically and chemically polished). These images show that the brand-new unmodified electrode have a significant surface-roughness, providing irregular edges and a somewhat porous surface (**Figure 4A**). The SEM micrographs show how the SLM produces a rough surface that ranges from the nano to 100  $\mu\text{m}$  scale. In SEM, heavier elements produce brighter images since they possess a higher atomic number and a larger number of electrons are scattered out of the sample, therefore, bright regions can be attributed to Ti and darker regions to other components such as oxides or binders from the production process<sup>196</sup>. It is well known that an amorphous oxide layer 1.5-10  $\mu\text{m}$  of thickness is spontaneously formed when titanium is exposed to air or oxygenated conditions at room temperature<sup>197,198</sup>. Furthermore, it has been shown that the oxide layer protects against corrosion and provides high porosity and roughness<sup>199</sup>.

TiO<sub>2</sub> exists in three different crystalline forms: anatase (tetragonal), rutile (tetragonal) and brookite (orthorhombic), and among these three rutile is the most stable and therefore the most likely phase to find, although their occurrence depends on the material, calcinations temperature and deposition method<sup>200</sup>. In order to acquire a smoother and oxide free surface, several methodologies such as mechanical polishing and different etching/chemical treatments have been reported<sup>201</sup>. However, etching often involves the utilisation of highly corrosive chemicals (e.g., hydrofluoric acid, nitric acid, etc.) that are difficult to handle, and for which waste processing is complicated<sup>202</sup>. As an alternative, different combinations of mechanical polishing and etching with acids such as hydrochloric acid (HCl), sulfuric acid (H<sub>2</sub>SO<sub>4</sub>) and/or oxalic acid have been successfully used at high temperatures (~60-100°C) to remove the native oxide layer<sup>203–205</sup>. Although titanium shows an outstanding resistance to corrosion provided by the native oxide layer, this TiO<sub>2</sub> film is not stable in reducing acids or high temperatures where Ti can corrode significantly<sup>206</sup>. In **Figure 4B**, scratches and damage surface are visible after mechanical polishing with sandpaper. However, decrease of the surface roughness and porosity is observed after mechanical and chemical surface treatment.

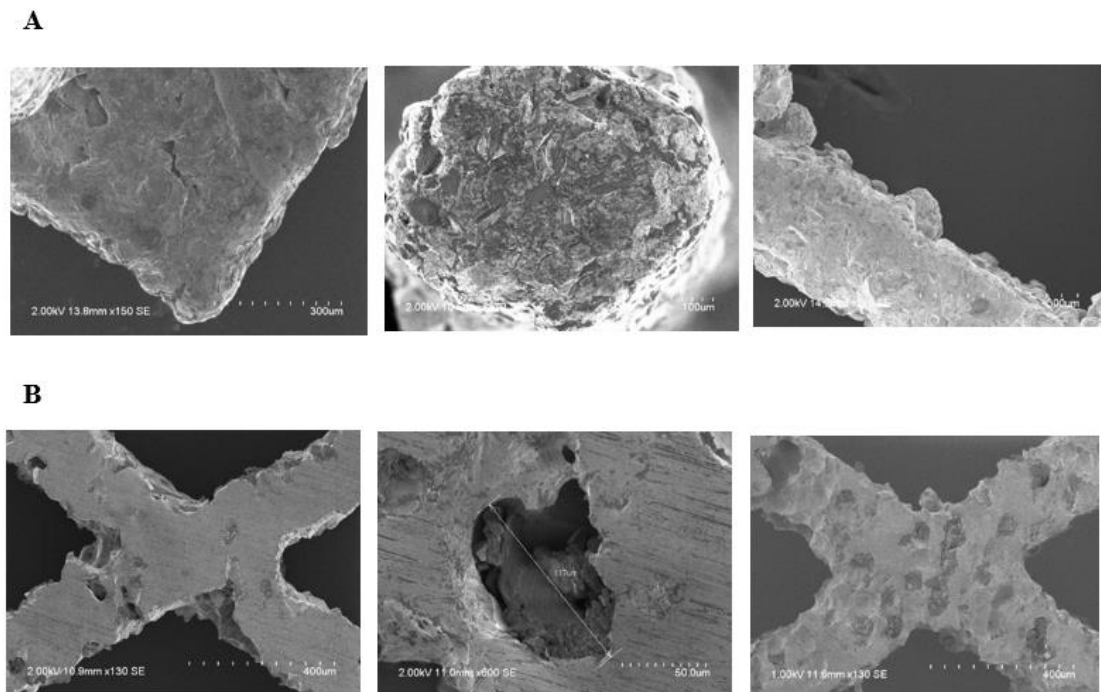
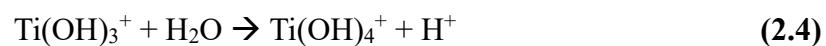
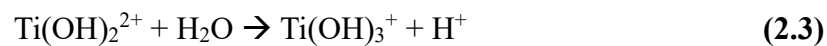
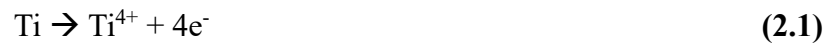


**Figure 4.** SEM images of 3D-printed Ti electrodes using an accelerating voltage that ranges from 1 kV to 2 kV. A) 3D-printed Ti arrays (with cylinders, no etched). Edge, tip of cylinder and base of electrode (from

left to right). Scale bars (left to right): 300  $\mu\text{m}$  B) Base of mechanically polished 3D-printed Ti arrays with sandpaper (no cylinders). Scale bars (left to right): 400  $\mu\text{m}$ , 50  $\mu\text{m}$  and 400  $\mu\text{m}$ .

### 3.1.2. Electrochemical characterization of 3D-printed Ti electrodes

The redox properties of the 3D printed Ti electrodes were determined using cyclic voltammetry. To study the available potential window of the electrodes (with cylinders), a voltammogram was obtained by scanning from -2 V to +2 V in 0.1M LiClO<sub>4</sub> as supporting electrolyte at a scan rate of 0.1 V s<sup>-1</sup> (**Figure 5**). As it is mentioned in the previous section, when titanium is exposed to air, it forms a spontaneous oxide layer, however, this oxide layer can also grow on clean, oxide free titanium surfaces when a positive potential is applied, around +0.2 V to +0.3 V<sup>207</sup>. **Figure 5** shows the onset potential for the spontaneous oxide layer formation is around -0.95 V. The formation of the titanium oxide layer in electrolyte/solution has been often described in acidic conditions<sup>197,208,209</sup>, however, as it is well known that passive layer in different metals is governed by the diffusion of metal ions to the surface and by successive reactions at the interface<sup>210</sup>. In case of titanium, the formation of oxide requires the oxidation of metallic titanium and dissolution of Ti<sup>4+</sup> (**Equation 2.1**). However, Ti<sup>4+</sup> is not stable in water, therefore it immediately hydrolyses producing protons and titanium tetra hydroxide (Ti(OH)<sub>4</sub>) which has been observed to be dominant in aqueous solutions at pH 7.3<sup>211</sup> (see **Equations 2.2-2.4**). Finally, the dehydration Ti(OH)<sub>4</sub> takes place by generating the semi-conductive layer of TiO<sub>2</sub> at the electrode surface (**Equation 2.5**).





Additionally, it has been described that exposing the Ti to anodic potentials (e.g., to oxidise ruthenium trisbipyridyl) ionic conduction processes take place that involve the inward migration of oxygen ions and outward migration of titanium ions ( $\text{Ti}^{4+}$ ) causing the growth of the oxide layer<sup>212</sup> (as described above). Another phenomenon can simultaneously occur, called electronic conduction, where the oxide already formed at the surface produces oxygen evolution at the electrode surface-interface, without contributing to the thickening of the oxide layer<sup>213</sup>. However, the activation of both processes has been shown to be responsible of generating gas bubbles, occluding oxygen within the oxide layer during the anodization of titanium<sup>213</sup> and aluminium-copper alloys<sup>213,214</sup>. Therefore, it could be possible that at more positive potentials (from 0 V to +2 V), the 3D Ti electrode is going through these two processes. Thus, for ECL measurements involving ruthenium trisbipyridyl, it is likely that the luminophore is electrogenerated at an oxide covered electrode surface.

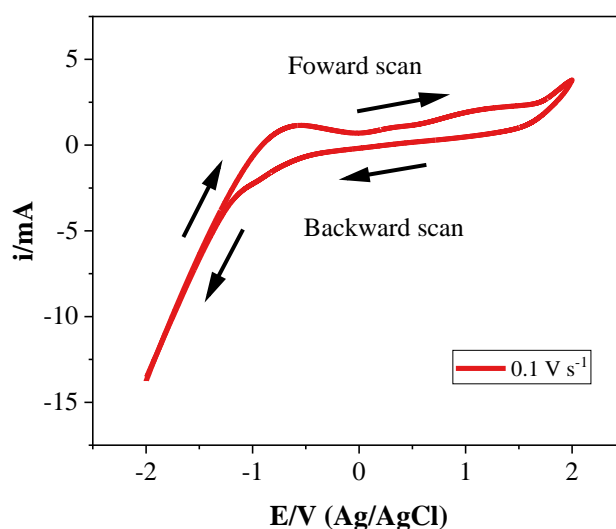


**Figure 5.** Voltammogram of bare 3D printed Ti electrode in 0.1M  $\text{LiClO}_4$  solution as supporting electrolyte. Scan rate at  $0.1 \text{ V s}^{-1}$ .

Further characterization of the electrodes using ferrocene methanol ( $\text{FcMeOH}$ ) as redox probe dissolved in 0.1M  $\text{LiClO}_4$  provided more information about their behaviour. It is important to note that the formal potential of the ferrocene is positive of the oxide formation onset and the electrode is likely to be covered by oxide. As shown in **Figure 6A**, no visible cathodic and anodic peaks are detected with  $\text{FcMeOH}$  at bare titanium

electrodes at any of the scan rates used. On the other hand, for the mechanically polished electrode (**Figure 6B**), Ti quickly forms an oxide layer that will continue to form/thicken under oxidative conditions or exposure to atmospheric oxygen, blocking the electron transfer at the electrode surface. Therefore, the process at approximately +0.25 V and -0.2 V could be the oxidation and reduction of the redox probe, however is being hindered by the presence of the oxide layer (TiO<sub>2</sub>).

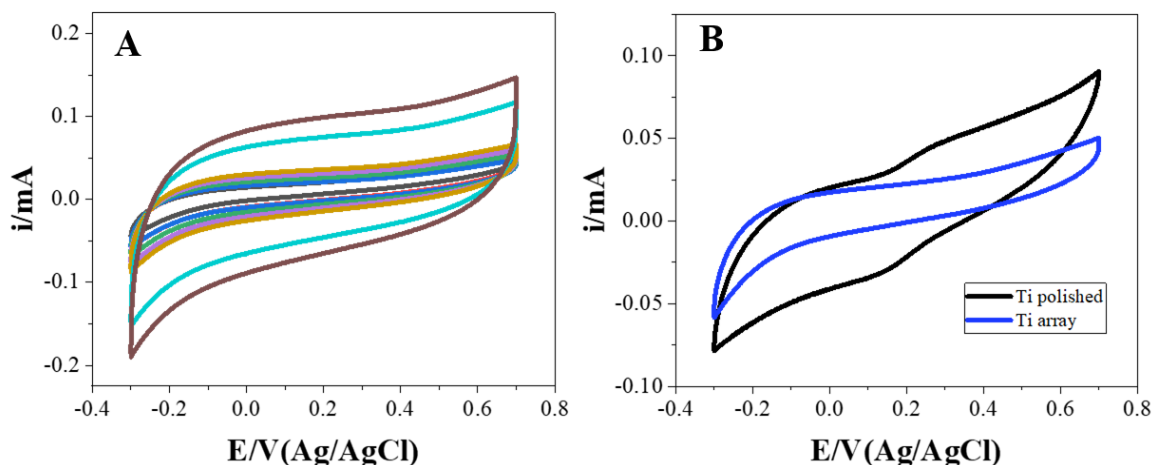


**Figure 6.** Voltammograms in 1 mM FcnMeOH as redox probe and 0.1M LiClO<sub>4</sub> as supporting electrolyte (degassed). A) Bare Ti array. Scan rates: 0.05 V s<sup>-1</sup>, 0.1 V s<sup>-1</sup>, 0.15 V s<sup>-1</sup>, 0.2 V s<sup>-1</sup>, 0.25 V s<sup>-1</sup>, 0.5 V s<sup>-1</sup>, 0.7 V s<sup>-1</sup> and 1 V s<sup>-1</sup>. B) Overlay of bare Ti array and bare polished Ti electrode. Scan rate: 0.1 V s<sup>-1</sup>. Electrodes stored in air.

### 3.1.3. ECL characterization of 3D printed Ti electrodes in co-reactant system

Here the performance of the electrodes using [Ru(bpy)<sub>3</sub>]<sup>2+</sup> as redox probe in presence of the co-reactant TrPA needed for the electrochemiluminescence generation is reported. In brief, TrPA is oxidized at the electrode surface and [Ru(bpy)<sub>3</sub>]<sup>2+</sup> is oxidized to [Ru(bpy)<sub>3</sub>]<sup>3+</sup>. The generated radical cation of TrPA (TrPA<sup>•+</sup>), is deprotonated and reacts with the oxidised ruthenium complex to form the excited state of the ruthenium complex [Ru(bpy)<sub>3</sub>]<sup>\*2+</sup> which rapidly decays to its ground state by emitting a photon at λ<sub>max</sub> at 620 nm<sup>117</sup>. Although other mechanisms have been reported with TrPA and ruthenium (i.e., catalytic route and low potential catalytic route and low potential oxidation route), this “oxidative–reduction route” is the most representative and common one with very bright ECL generation<sup>215</sup>.

In **Figure 7A and B**, the different ECL profiles are shown for each electrode. Both polished and array electrodes showed a similar ECL response, starting around +0.9 V and reaching the maximum light intensity between +1.1 V and +1.2 V. In presence of an oxide layer, as described by Bard and et al.<sup>216</sup>, the direct oxidation of TrPA tends to be inhibited, therefore the first oxidation step that might occur is the oxidation of  $[\text{Ru}(\text{bpy})_3]^{2+}$  where catalytic route dominates (**Chapter 1, Figure 6C**) for the generation of the ECL signal as opposed to the generally most common suggested mechanism, “oxidative-reduction route”. Furthermore, due to the fact that the electrode surface is not very conductive, the electron transfer for TrPA oxidation can be slow<sup>217</sup> so the current response observed is likely to be dominated by the direct oxidation of  $[\text{Ru}(\text{bpy})_2]^{3+}$ . In addition, it has been shown that the ECL intensity can increase if the pH is increased from 6.0 to 8.0 since the deprotonation of the tertiary amine from in more basic pH can accelerate the oxidation of TrPA<sup>218</sup>. The pH of the solution for these experiments was 6.5-7.0 which could explain also the low intensities achieved.

In any case, the response observed suggests that the limitation factor is not the presence or the absence of cylinders, but the generation of a native oxide layer (**Figure 7A and B**). Constant deoxygenation of the solution was not possible for these experiments as opposed to the ones presented in the previous section, therefore rapid formation of  $\text{TiO}_2$  was expected at the scanned potential window (from 0 V to +1.4 V). However, both electrodes showed a steady-state response, weakly dependent on the scan rate. Voltammograms shown in **Figure 7C, and D** suggest that the mechanical polishing of the electrodes decreases the capacitive current of the electrode, but still no distinct faradaic process is observed. Nevertheless, the presence of the oxide layer did not completely block the electron transfer since a small ECL signal was obtained for both polished and unpolished electrodes, showing as well similar intensities across the different scan rates. This result arises from the much higher sensitivity of ECL compared to current detection due to the dark background in ECL whereas there is significant capacitance ( $5.56 \pm 0.88 \times 10^{-4} \text{ F cm}^{-2}$  and  $6.90 \pm 0.60 \times 10^{-5} \text{ F cm}^{-2}$  for Ti array and Ti polished, respectively, using geometric areas) in the CV, making Faradaic currents challenging to quantify.

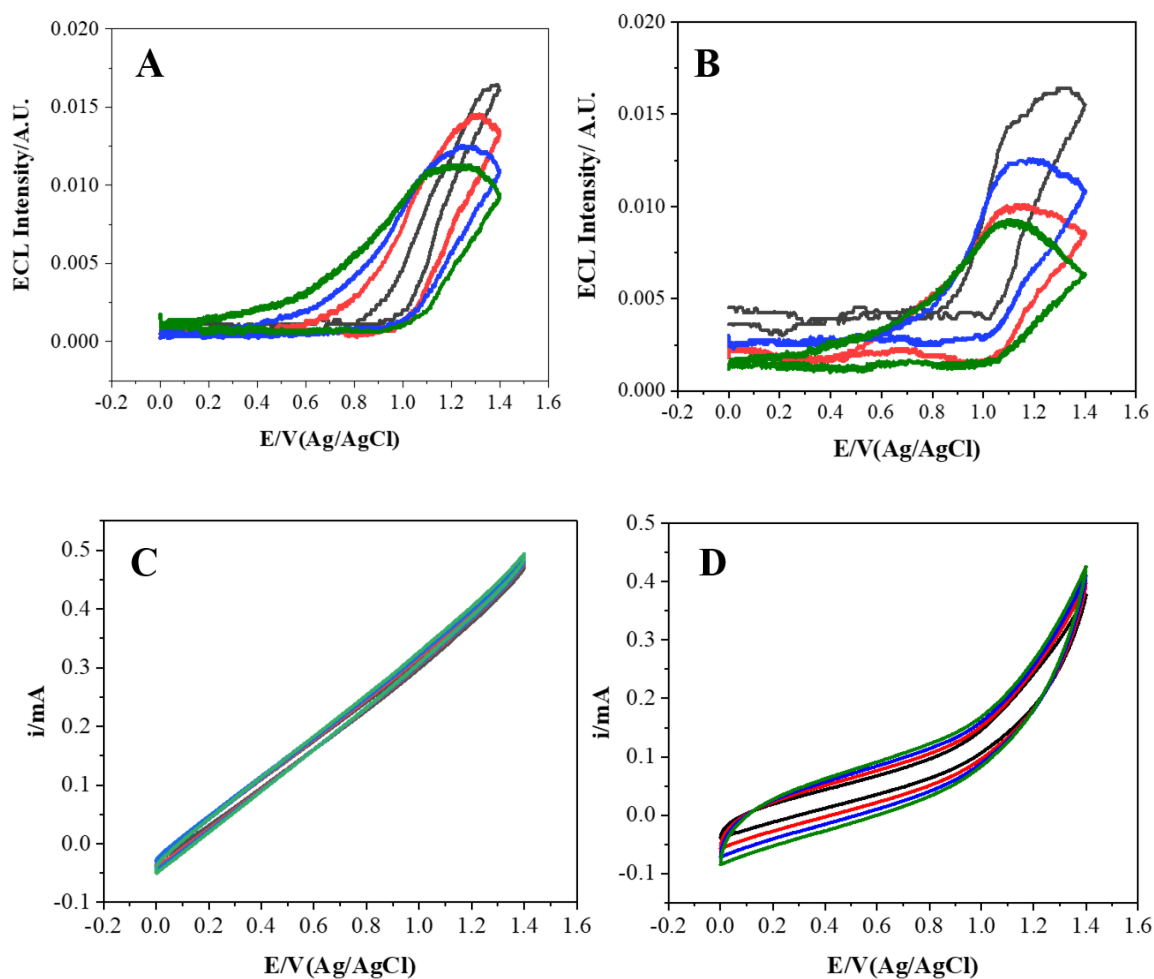


**Figure 7.** ECL response of Ti electrodes using 0.1mM  $[\text{Ru}(\text{bpy})_2]^{+3}$  redox probe, 0.1M TrPA as co-reactant and 0.1M  $\text{LiClO}_4$  as supporting electrolyte. ECL profiles A) Bare Ti array and B) Bare mechanically polished electrode. Voltammograms C) Bare Ti array and D) Bare mechanically polished electrode. Scan rates:  $0.05 \text{ V s}^{-1}$  (black),  $0.1 \text{ V s}^{-1}$  (red),  $0.15 \text{ V s}^{-1}$  (blue),  $0.2 \text{ V s}^{-1}$  (green).

## 3.2. Gold coated Ti electrodes

### 3.2.1. Gold electrodeposition

As observed in the previous section, 3D printed Ti electrodes do not show suitable characteristics for highly sensitive, electrochemiluminescent biosensing applications therefore the electrodes were modified to improve the redox properties of the platform. In this case, gold was deposited since it displays unique characteristics such as biocompatibility for biomolecules immobilization (e.g., antibodies, nucleic acids,

proteins, etc.) via a self-assembled monolayer technique, electrocatalytic properties, high electroactive surface areas, and improves the electrochemical properties and conductivity of the surface<sup>219</sup>. In this way, the ability of SLM to create complex 3D electrode structures is exploited but are combined with the favourable electrochemical and biological properties of gold. Traditionally, chronoamperometry, or pulse current techniques have been used for the electrodeposition of gold on surfaces<sup>175,220</sup>. Chronoamperometry is often chosen as a technique since it provides information about the transient current which allows a higher control of the morphology of the deposits<sup>221,222</sup>. Therefore, chronoamperometry was first attempted to electrodeposit gold and a potential of -0.9 V (for 700 s) was selected as the electrodeposition potential since in the literature it has been reported as the most used potential using a gold salt bath<sup>175,223,224</sup> (**Figure 8A**). The steady-state reduction current observed, -250  $\mu\text{A}$ , at times longer than 50 s, could be attributed to hydrogen evolution (HER), which has been reported when at such negative potential<sup>225</sup>. However, no gold was observed on the electrode surface after the experiment with chronoamperometry. As an alternative, cyclic voltammetry was used for electrodeposition of gold on the 3D Ti electrodes. In fact, Paradowska et al., electrodeposited AuNPs on TiO<sub>2</sub> nanotubes using cyclic voltammetry applying a potential ranging from -0.7 V to -1.25 V<sup>223</sup>. The potential window selected for the electrodeposition was from -0.5 V to -2 V for 28 cycles at 0.1 V s<sup>-1</sup> in order to find out if the appropriate potential was within this potential window since the electrode presents a large surface area as well as poor conductivity due to the presence of the native oxide layer (**Figure 8B**). Cyclic voltammetry is often preferred since it offers multiple benefits such as simplicity, controllability of the electrodeposited layer thickness and monitoring of both oxidation and reduction peaks for dissolution and electrodeposition processes of metals and metallic ions on the electrode surface<sup>219</sup>. During the electrodeposition process, the metallic ions in the solution are reduced to metallic gold nanostructures by accepting the electrons and forming a metallic layer of gold on the electrode surface<sup>226</sup>. Deposition with cyclic voltammetry was successful since the electrodes showed a gold-brown finish and its presence was confirmed after SEM and electrochemical characterization (see **Sections 3.2.2.** and **3.2.3.**, respectively). However, no well-defined reductive or oxidation peaks were observed during the electrodeposition. The commercial bath used in this study contained gold (I) potassium cyanide (KAu(CN)<sub>2</sub>). In the work reported by Elias and et al., gold electrodeposition was monitored using KAu(CN)<sub>2</sub> and CV as electrochemical technique, scanning from -0.6 V

to -1.2 V. They observed that at potentials -0.6 V to -0.9 V, gold deposits were obtained from the reduction of AuCN adsorbed on the cathode surface (see **Equation 3.1-3.3**), however, at more negative potentials (from -0.9 V to -1.3 V, the deposition was governed by direct charge transfer reaction (see **Equation 3.4**), which is also a region governed by HER (water reduction). The shoulder observed in the CV (**Figure 8B**) between -0.9 V and -1.3 V could indicate that both HER and direct charge transfer reaction coexist in this region<sup>225</sup>.



Gold electrodeposition on titanium surfaces through cyclic voltammetry could have been enhanced by the previous etching of the electrodes to remove the native oxide layer. However, the electrodeposition was performed at very negative potentials where reduction of the TiO<sub>2</sub> would be expected. In fact, it has been previously reported that Ti<sup>+3</sup> can be formed at the uppermost monolayer (or multi-layers) of the oxide film (TiO<sub>2</sub>) when scan from 0 V to -1 V<sup>227,228</sup>. There are other ways how the native titanium oxide film can change under reductive conditions, e.g., various stages of oxide reduction up to its dissolution, the adsorption and absorption of hydrogen and etc, however, there is not enough knowledge to determine the transformation of the oxide layer under reductive conditions<sup>206</sup>.

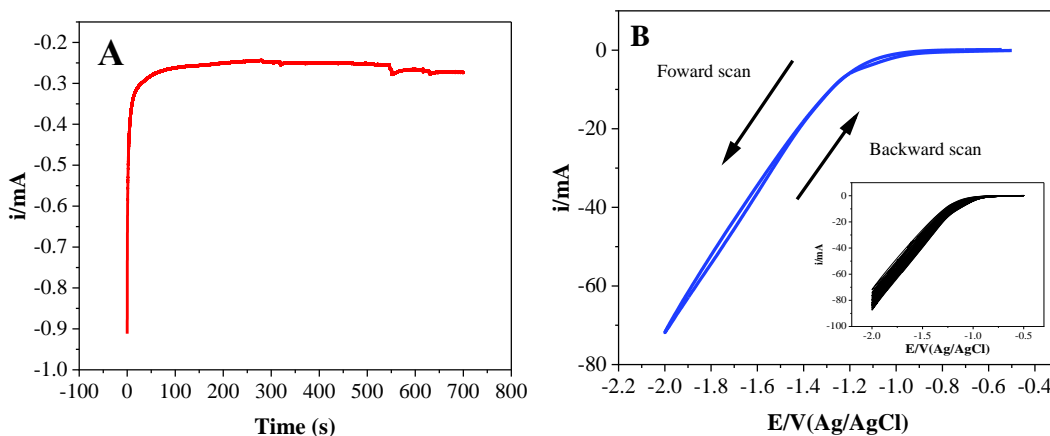


**Figure 8.** Electrodeposition of gold on 3D printed Ti electrode. A) Chronoamperometric  $i$ - $t$  curve, potential applied  $-0.9$  V for 700 s. B) Voltammogram, scanned from  $-0.5$  V to  $-2.0$  V at  $0.1$  V  $s^{-1}$ , first cycle. Inset: voltammogram, 28 cycles.

### 3.2.2. Surface characterization

TiO<sub>2</sub> on the surface electrode cannot meet the sensing requirements (e.g., in sensitivity, detection range and response time) since it decreases the heterogeneous electron transfer, which decreases the analytical sensitivity (less current/light generated per unit time) and raises the limit of detection (dictated by the ratio of the capacitance to Faradaic current response)<sup>229</sup>. Thus, etching the surface to remove the native oxide layer could be an effective strategy to improve the electrochemical properties of the 3D printed Ti electrodes, as well as prior to further modification with deposition of metals such as gold. SEM images (**Figure 9**) show deposits on the electrodes surface after the gold deposition experiments. The brightness of the backscattered electrons achieved after electrodeposition, suggests that electrodeposition was successful, however, this is not enough to conclude that all the deposits are gold. Energy Dispersive X-ray (EDX) microanalysis, could help to elucidate the which elements are present on the surface of the electrode and if the deposits are mostly gold, forming a thin layer of gold. Recently it has been shown that at the gold-rich interface, the gold particles promotes an outward diffusion of titanium ions to react the inward-coming oxygen to form thick oxide layer, which also provides hardness and robustness to the Au-TiO<sub>2</sub> material<sup>230</sup>.

However, it is difficult to establish and/or assess the thickness of the layer since as it is shown in the SEM images, it does not form a continuous layer and the particles observed

are also very heterogeneous. Difference size and shape the gold particles on the electrode surface could a consequence of the application of different potentials with cyclic voltammetry. It has been shown that the size and morphology of the gold deposits can be tuned upon application of different potential windows and more time of electrodeposition<sup>221,231</sup>.

On the other hand, it can be observed that after the etching and electrodeposition process, the electrodes exhibit a very irregular surface compared to the uncoated and untreated Ti array electrode (**Figure 4**). This could be because after characterization of uncoated electrodes, they were further chemically treated again. As it has been mentioned before, chemical treatment of electrodes can seriously damage the surface, since several studies have reported that acid etching of different types of titanium surfaces such as, pure titanium and titanium alloy (Ti-6Al-4V) derivatives causes mass or weight-loss by dissolving the Ti, impacting the morphology and the topography of the surface<sup>232–234</sup>. On the other hand, is possible that the acids removed the oxide by making visible the scale of roughness that it was underneath the native oxide layer. Increasing the roughness of the electrodes could be beneficial by increasing the surface area and therefore, the signal generated since more capture biomolecules can be immobilized on the surface.

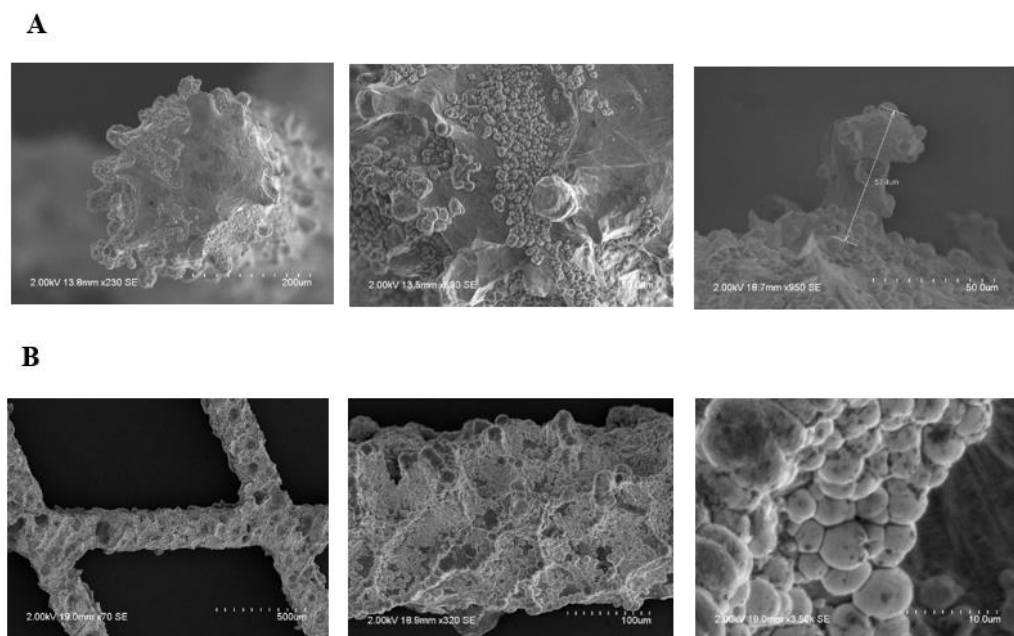


**Figure 9.** SEM images of gold functionalized 3D-printed Ti electrodes, using 2 kV as accelerating voltage. A) Gold functionalized 3D-printed Ti gold arrays (with cylinders, chemically treated). Cylinder, tip of cylinder and edge of cylinder (from left to right). Scale bars (left to right): 200 μm, 50 μm and 50 μm. B)



Mechanically polished gold functionalized 3D-printed Ti arrays with sandpaper (no cylinders, chemically treated). Base of electrode. Scale bars (left to right): 500  $\mu\text{m}$ , 100  $\mu\text{m}$  and 10  $\mu\text{m}$ .

### 3.2.3. Electrochemical characterization of gold coated electrodes

To confirm the presence and determine the electroactive area of the gold on Ti electrodes, cyclic voltammetry measurements were performed in 0.1M of  $\text{H}_2\text{SO}_4$ . As shown in **Figure 10** it can be observed a gold oxidation peak around +1.3V (oxide formation mostly on Au 110 face) and a reduction peak at +0.75V, indicating the reduction of the gold oxide layer<sup>235</sup>. The electroactive area (A) was calculated using the theoretical charge ( $Q_{\text{theo}}$ ) associated with gold ( $390 \mu\text{C cm}^{-2}$ ) and the experimental charge ( $Q_{\text{exp}}$ ) obtained from the voltammograms of the reduction peak observed in **Figure 10** as well as the roughness factor with the geometrical area<sup>236</sup> (see **Equations 4.1-4.2**):

$$\text{Surface area} = \frac{Q_{\text{exp}}}{Q_{\text{theo}}} \quad (4.1)$$

$$\text{Roughness} = \frac{A_{\text{exp}}}{A_{\text{geo}}} \quad (4.2)$$

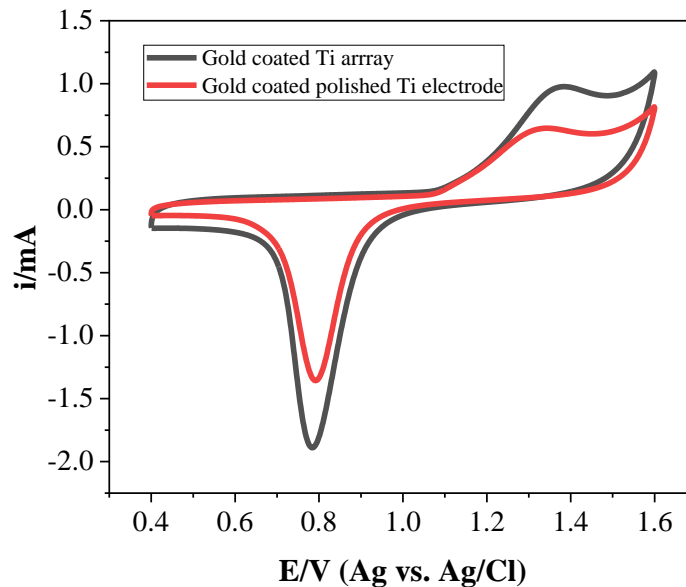


**Figure 10.** Voltammograms of gold coated 3D-printed Ti electrodes in 0.1M  $\text{H}_2\text{SO}_4$  as supporting electrolyte. Scan rate:  $0.2 \text{ V s}^{-1}$ .

The electroactive area obtained for gold modified Ti arrays and gold modified and polished electrodes (no cylinders) were 3.2 and 3.0 cm<sup>2</sup> respectively, which is higher than the geometrical area, and the roughness factor for each electrode was 2.4 and 5.1. However, these values are not as high as expected and it could be due to several factors such as the gold layer is not continuous or that the deposited gold is not all electroactive.

Additionally, further characterization experiments were performed using 1mM FcMeOH as redox probe. Scan rate is a very useful parameter to differentiate if the redox process is diffusion-controlled or if the species is being adsorbed<sup>237</sup>. As it is observed in **Figure 11A and B**, well defined and separated peaks were obtained, where the  $\Delta E_p$  value is larger than 57 mV and increases with the scan rates, indicating a quasi-reversible process as well as characteristics of mass transport controlled by semi-infinite linear diffusion. Additionally, the Randles-Sevcik plot ( $i_p$  versus  $\nu^{1/2}$ ) (**Figure 12**) shows the scan rate dependency since the current increases linearly as a function of the square root of the scan rate, suggesting that is a diffusion-controlled process<sup>238</sup>. Moreover, at fast scan rates, a peak-to-peak separation occurs, where the reaction starts becomes more irreversible, resulting in a trumpet style graph and the peak potentials change linearly with the logarithm of the scan rate<sup>239,240</sup> (**Figure 13**). The reason behind the increase in peak-to-peak separation is possibly due to the ohmic drop which is defined as “*the resistance of the solution during the flow of electrical current through the cell*”<sup>241</sup> and the faster the scan rate, the larger is the drop<sup>238</sup>. This impacts the electrochemical response, by owning higher faradaic currents flowing in the system at fast scan rates<sup>242</sup>. Furthermore, the ohmic-drop is also influenced by the distance between the working and the reference electrode<sup>243</sup>, which was difficult to maintain the same across the experiments to record the triplicates and this might have caused the large standard deviations observed in **Figure 12**. Designing a cell where the distance between the Ti array and the reference electrode could be fixed might help to achieve more reproducible results.

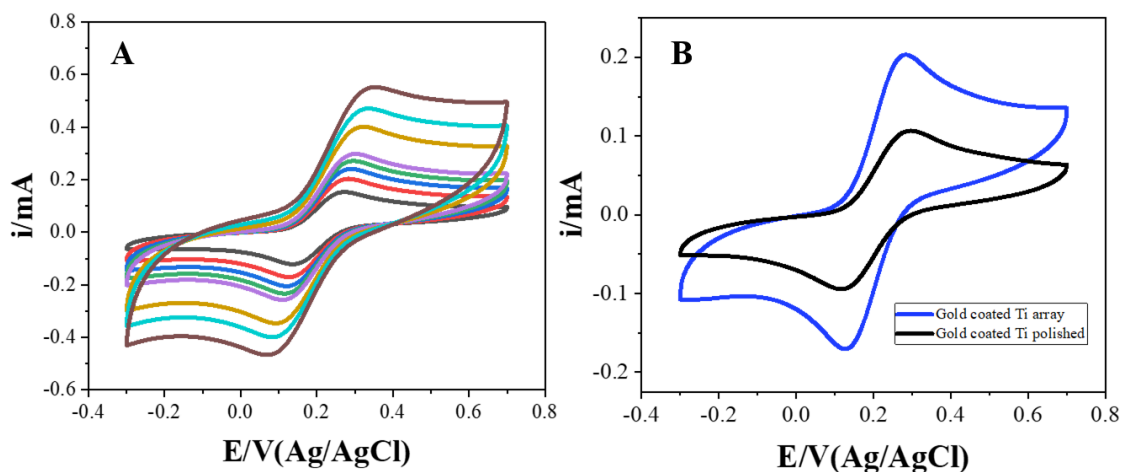


**Figure 11.** Voltammograms in 1 mM FcnMeOH as redox probe and 0.1M LiClO<sub>4</sub> as supporting electrolyte (deaerated). A) Gold coated Ti array. Scan rates: 0.05 V s<sup>-1</sup>, 0.1 V s<sup>-1</sup>, 0.15 V s<sup>-1</sup>, 0.2 V s<sup>-1</sup>, 0.25 V s<sup>-1</sup>, 0.5 V s<sup>-1</sup>, 0.7 V s<sup>-1</sup> and 1 V s<sup>-1</sup>. B) Overlay of gold coated Ti array and gold coated polished Ti electrode. Scan rate 0.1 V s<sup>-1</sup>.

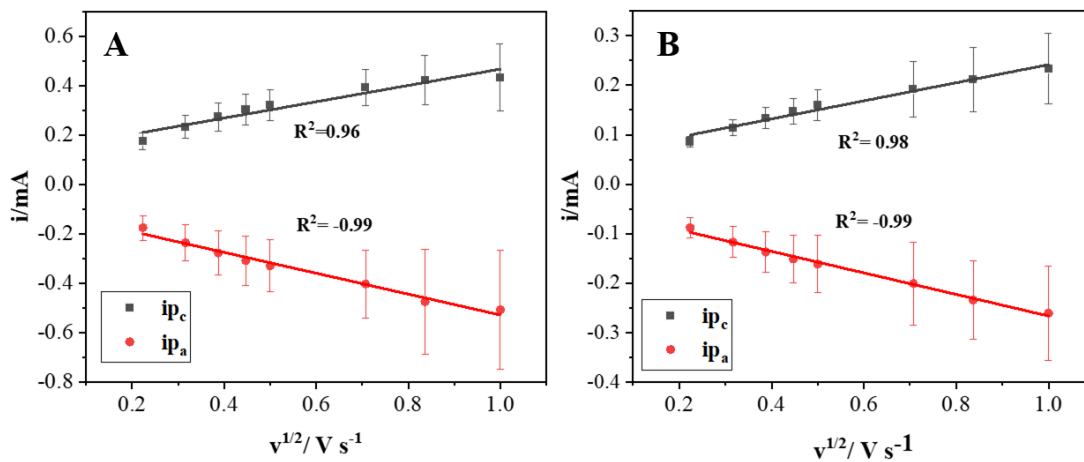


**Figure 12.** Randles-Sevcik plots using 1mM FcnMeOH as redox probe and 0.1M LiClO<sub>4</sub> as supporting electrolyte. Anodic peak current ( $i_{p_a}$ ) and cathodic peak current ( $i_{p_c}$ ). A) Gold coated array and B) gold coated polished electrode. The error bar represents the standard deviation from three independent measurements (same electrode, three independent measurements of same electrode after surface cleaning treatment).

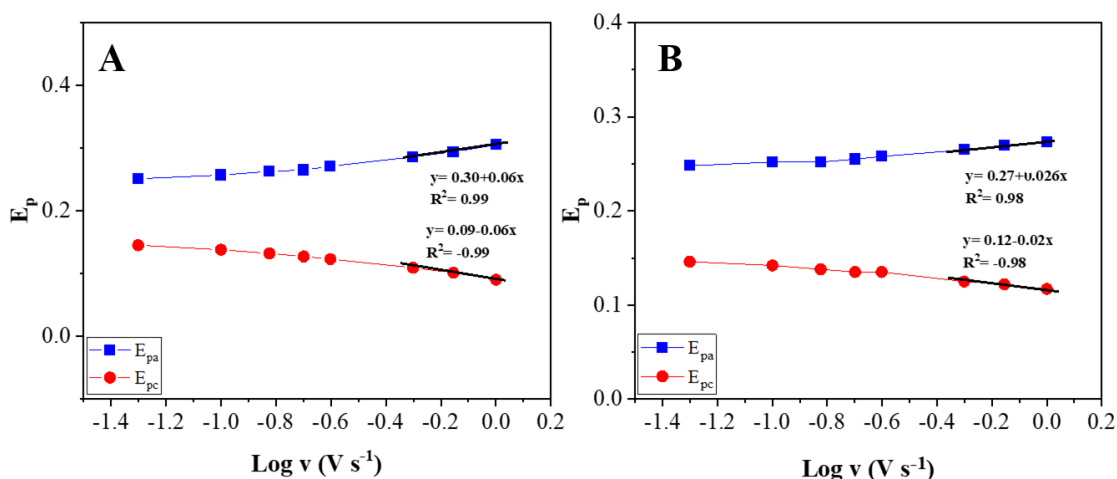


**Figure 13.** Plots of anodic peak potential and cathodic peak potential vs. the logarithm of scan rate. A) Gold coated Ti array. B) Gold coated polished Ti electrode.

In addition, the heterogenous electron transfer rate constant ( $k^0$ ) was calculated for  $0.1 \text{ V s}^{-1}$  following the Kochi and Kingler method for a quasi-reversible reaction, which depends on peak to peak separation<sup>244</sup>, and it requires the calculation of transfer coefficient ( $\alpha$ )<sup>245</sup>. For both equations,  $n$  is the number of electrons,  $v$  the scan rate,  $D$  is the diffusion reported in the literature for ferrocene methanol in solution ( $7.0 \times 10^{-6} \text{ cm}^2 \text{ s}^{-1}$ )<sup>246,247</sup> and other symbols i.e.,  $R$ ,  $T$  and  $F$ , have their usual values (see **Equation 5.1-5.2**):

$$E_p - E_{p/2} = \frac{48 \text{ mV}}{\alpha n} \quad (E_p \text{ and } E_{p/2} \text{ measured in mV}) \quad (5.1)$$

$$k^0 = 2.18 \left( \frac{\alpha D n F v}{RT} \right)^{1/2} \exp \left( \frac{-\alpha^2 n F (E_{pa} - E_{pc})}{RT} \right) \quad (5.2)$$

The values obtained  $2.2 \pm 0.01 \times 10^{-2} \text{ cm s}^{-1}$  (gold coated arrays) and  $1.42 \pm 0.01 \times 10^{-2} \text{ cm s}^{-1}$  (gold coated Ti polished electrodes) are very similar and they are both close the range values for a quasi-reversible reaction ( $10^{-2} > k^0 > 10^{-4} \text{ cm s}^{-1}$ )<sup>248</sup>. On the other hand, the fitting of the voltammograms run in the CH Software using a voltammogram recorded at  $0.1 \text{ V s}^{-1}$  and considering the concentration (1 mM) and the diffusion coefficient ( $7.0 \times 10^{-6} \text{ cm}^2 \text{ s}^{-1}$ ) of the redox probe. The best fit was found at  $k^0 = 2.6 \times 10^{-3} \text{ cm s}^{-1}$  and 2.0

$\times 10^{-3} \text{ cm s}^{-1}$  (gold coated array and gold coated electrode, respectively), indicating as well that the reaction is quasi-reversible reaction. However, they are an order of magnitude bigger than the values obtained with Kingler and Kochi method. The  $k^0$ , gives valuable information about the speed of electron transfer between an electroactive species and the electrode surface as well as whether the electrode material determines the overall electrochemical reaction<sup>249</sup>. However, it has been reported by other researchers<sup>245,250</sup> that the Kohci and Kingler method gives different values obtained by other methods (e.g., Nicholson and Shain or Gileadi) as well as the ones obtained digitally, however, with both methods the values obtained indicate a quasi-reversible reaction. Other tools for the digital simulation of cyclic voltammetry that has gained a lot of attention in the last years is the software COMSOL<sup>251,252</sup>. Although is widely applied in electrochemistry for the theoretical calculation of several parameters in a fast way, undesired errors in the predictions can occur if the electrochemical system is not deeply understood leading to unreliable conclusions<sup>253</sup>.

In any case, the results suggest that following gold deposition, Faradaic currents are achieved for ferrocene methanol and the  $k^0$  values, fit with a semi-infinite linear diffusion model. Parallely, the diffusion layer thickness ( $\delta$ ) (**Equation 6**) was calculated for the gold coated arrays at  $0.1 \text{ V s}^{-1}$  (10 s), ( $\delta = 0.011 \text{ cm}$ ) showing to be smaller than the radius of the cylinder (approximately  $0.015 \text{ cm}$ ), confirming that semi-infinite linear diffusion dominates over radial diffusion<sup>254</sup>. However, at  $0.05 \text{ V s}^{-1}$ , the  $\delta$  calculated equals  $0.016 \text{ cm}$ , which is larger than the radius of the cylinder, therefore, radial diffusion could be expected at timescales slower than  $0.05 \text{ V s}^{-1}$ .

$$\delta = (2Dt)^{1/2} \quad (6)$$

As it is discussed in the literature<sup>175,255,256</sup>, given the dimensions of the cylinders, the contribution of linear diffusion attributed to the main body is expected to be larger than the radial diffusion provided by the tip<sup>175</sup>. In fact, by applying the **Equations 7.1 and 7.2** is possible to calculate the steady state current generated by the cylinder and the tip (respectively)<sup>256</sup> under radial diffusion conditions, respectively, using the cylinder dimensions, the diffusion coefficient,  $\alpha$  and  $\delta$ :

$$i_{ss} = \frac{nFADC}{\alpha \ln(1 + \delta/\alpha)} \quad (7.1)$$

$$i_{ss} = \frac{nFADC}{\delta} \quad (7.2)$$

Using the equations from above and the obtained experimental parameters, it was found that the cylinder's wall current ( $5.41 \times 10^{-5}$  A) was ~13 times higher than the tip ( $4.29 \times 10^{-6}$  A), therefore, theoretically, linear diffusion from the walls predominates over the radial diffusion from the tip, which fits with what has been observed experimentally, a semi-infinite linear diffusion model. Furthermore, recently it has been shown that the larger length of the cylinders have a significant impact on the diffusion mechanisms, where the mass electron transport tends to follow linear diffusion as the length of the cylinder increases<sup>255</sup>. Even though the diffusion layers of each cylinder do not coalesce, the cylinders are large enough, so the system shows a semi-infinite linear diffusion model at the investigated timescale (**Figure 15**). Furthermore, the obtained value for  $\delta$  is smaller than the separation of the cylinders (0.1 cm) (**Figure 14B**), therefore the diffusion layers of each cylinder do not overlap or coalesce under these relatively short timescale conditions, therefore, the diffusion model depends on the experimental timescale. However, it is highly possible that the side of the electrode that does not contain any cylinders (flat with holes), could be also contributing the semi-infinite linear diffusion since this part of the electrode was not insulated. Overall, this set of experiments shows that the thin layer of gold improved the issue of native oxide layer by keeping the structural advantages of the 3D printed electrodes.

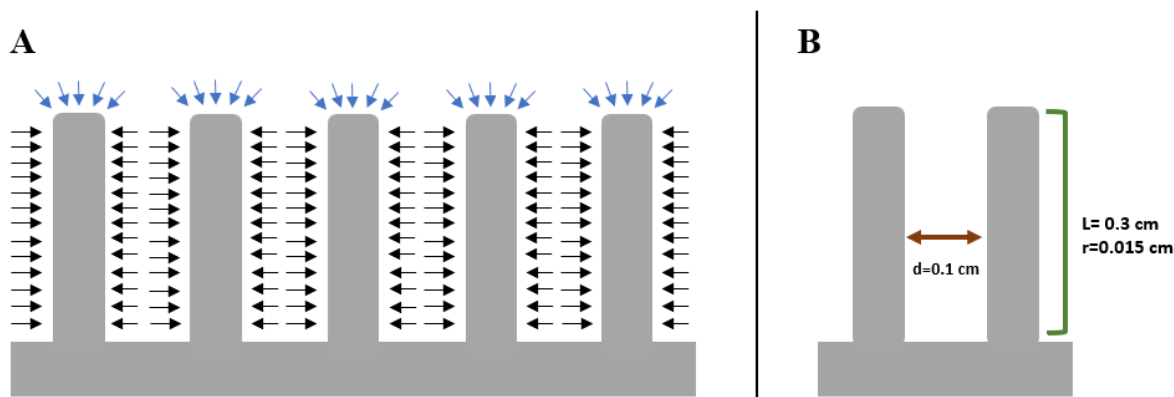


**Figure 14.** Schematic representation of diffusion model of 3D-Printed Ti electrodes. A) Radial diffusion at the tip of cylinders (blue arrows) and linear diffusion (black arrows) at the wall of the cylinders. B) Structural representation of a section of the electrode., d (distance between cylinders), L (cylinder length) and r (cylinder radius).

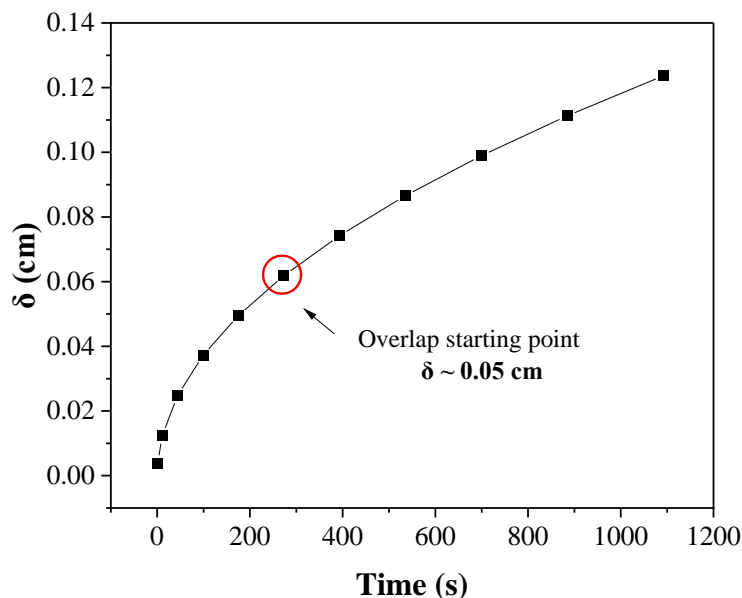


**Figure 15.** Time dependence of the thickness of the diffusion layer ( $\delta$ ) in dimensional variables for diffusion coefficient ( $D= 7.0 \times 10^{-6} \text{ cm}^2 \text{ s}^{-1}$ ).

### 3.2.4. ECL characterization in co-reactant system

As discussed before, since gold enhances the electrochemical properties of the electrode surface, a bigger ECL response could be expected for the gold coated electrodes. Significantly, the achieved intensities are improved when a thin layer of gold was deposited. As shown in **Figure 16A and B**, an increase of  $\sim 90$  and  $\sim 40$  at  $0.1 \text{ V s}^{-1}$  (gold

coated array and gold polished, respectively) in the observed intensities occurs in presence of gold. On the other hand, an oxidation process can be observed at range +0.8 V and +1.0 V for both gold coated electrodes and a reductive reaction between + 0.1 V and + 0.2 V (**Figure 16C and D**) which has been observed before in  $[\text{Ru}(\text{bpy})_3^{2+}]/\text{TrPA}$  systems with gold electrodes<sup>257,258</sup>. The difference in the ECL intensity relies on the material, reflecting the growth of the gold oxide layer, with better catalytical properties.<sup>217</sup> It is possible as well that the ECL signal is enhanced by through the plasmonic effects of the gold nanostructures since it has been demonstrated that they can act as signal boosting antennas as long as there is an spectral overlap between the nanostructures and the luminophore<sup>259</sup>. However it has been reported that electrodeposited AuNPs showed a narrower ECL intensity distribution compared to pre-synthesised AuNPs<sup>260</sup>. Additionally, it has been seen that the anodic currents for the oxidation of TrPA gold can be dissolve gold deposited on the electrode surface<sup>216</sup>. Thus, surface characterisation before and after oxidation of TrPA would be very valuable to elucidate how the surface changes after this process as well as to assess the reproducibility of the platform.

Moreover, an interesting and very defined hysteresis process is noted (**Figure 16A and B**), between the back and forward scan, specifically at the slowest scan-rate ( $0.05 \text{ V s}^{-1}$ ). The return scan crosses over the positive going wave before the intensity rapidly decreases. This is a very complex phenomenon since the electrochemiluminescence reaction can be influenced by many factors (e.g., electron transfer, mass transport the luminophore and the co-reactant, excited state dynamics and etc.,) and any changes of the parameters individually and/or simultaneously can have an impact on the response observed<sup>261,262</sup>.



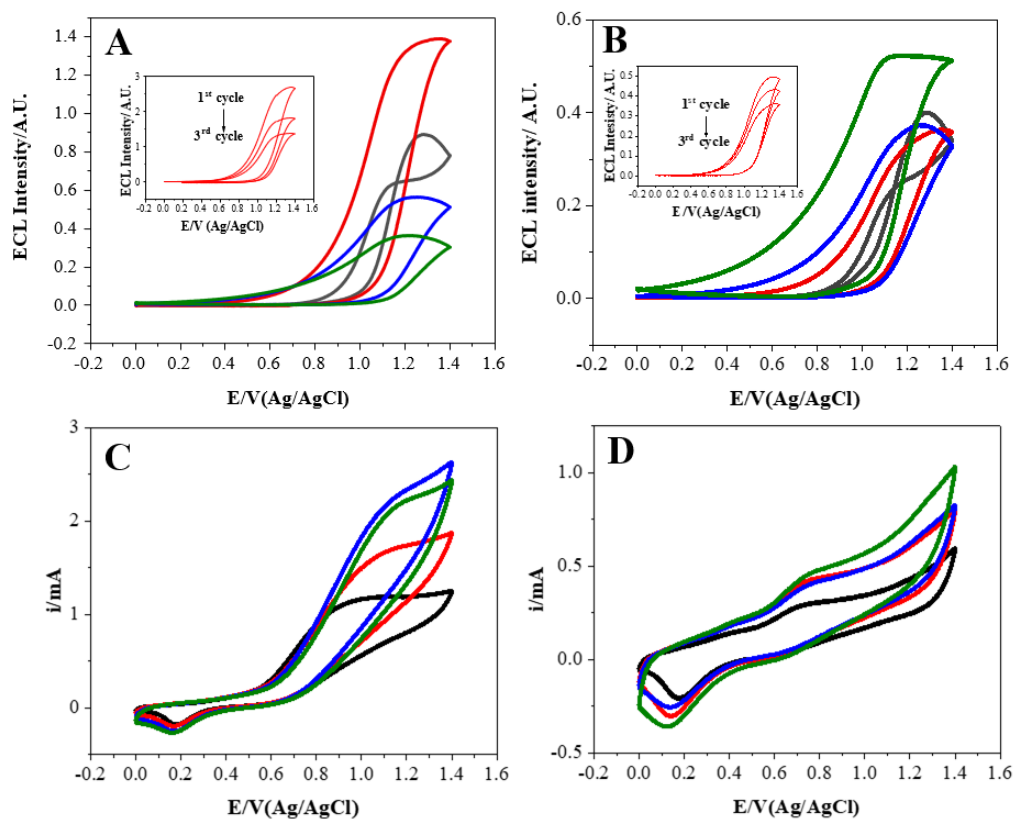


**Figure 16.** ECL response of gold coated Ti electrodes using 0.1mM  $[\text{Ru}(\text{bpy})_2]^{+3}$  redox probe, 0.1M TrPA as co-reactant and 0.1M  $\text{LiClO}_4$  as supporting electrolyte. ECL profiles A) Gold coated Ti array. Inset: ECL response at  $0.1 \text{ V s}^{-1}$  over 3 cycles. B) mechanically polished and gold coated electrode. Inset: ECL response at  $0.1 \text{ V s}^{-1}$  in 3 cycles. Voltammograms C) Gold coated Ti array and E) Gold coated and mechanically polished electrode. Scan rates:  $0.05 \text{ V s}^{-1}$  (black),  $0.1 \text{ V s}^{-1}$  (red),  $0.15 \text{ V s}^{-1}$  (blue),  $0.2 \text{ V s}^{-1}$  (green).

The reproducibility of a gold functionalized 3D Ti printed electrode surface and ECL signal regeneration was investigated under in order to assess its suitability as a biosensing platform. As displayed in the insets of **Figure 16A** and **B**, the ECL intensity decreased upon the 3 electrochemical cycles, probably due to the depletion of the co-reactant at the electrode surface<sup>135</sup>, supported by the RSD values from **Table 1**. Separately, as it is shown in **Figure 17**, different light intensities are achieved for each scan-rate, being  $0.1 \text{ V s}^{-1}$  the scan rate at which more intensity is recorded for the gold coated Ti arrays and  $0.05 \text{ V s}^{-1}$  for the gold coated and polished Ti electrodes. It could be possible that as the scan rate increases, the concentration of the intermediate and/or reduced species increases, due to the electrochemical oxidation of the luminophore provoking and increase of the ECL intensities<sup>263–265</sup>. However, at faster scan rates, regeneration of those species does not

occur since diffusion of the co-reactant from the bulk solution does not take place fast enough to the electrode interface, therefore, a decrease in the ECL intensities is observed upon repeated cycling<sup>266</sup>. Additionally, the difference between the arrays and the polished electrode regarding the optimal scan rate, could be due to the presence of the cylinders on the electrode surface, which might be impacting the diffusion of the species. However, scanning at lower scan rate would be needed in order to elucidate and understand better the nature of this difference. Nevertheless, as mentioned earlier, gold on the surface of the electrode can be dissolved upon oxidation of TrPA, which can lead to changes on the surface and irreproducible results.

**Table 1.** Relative standard deviation (RSD) of 3 consecutive cycles (ECL intensity). Gold coated Ti arrays and gold and polished Ti electrodes.

Scan rate ( $V s^{-1}$ )	RSD (%)	
	Gold coated Ti arrays	Gold coated and polished Ti electrodes
0.05	24	25
0.1	32	16
0.15	31	21
0.2	24	24

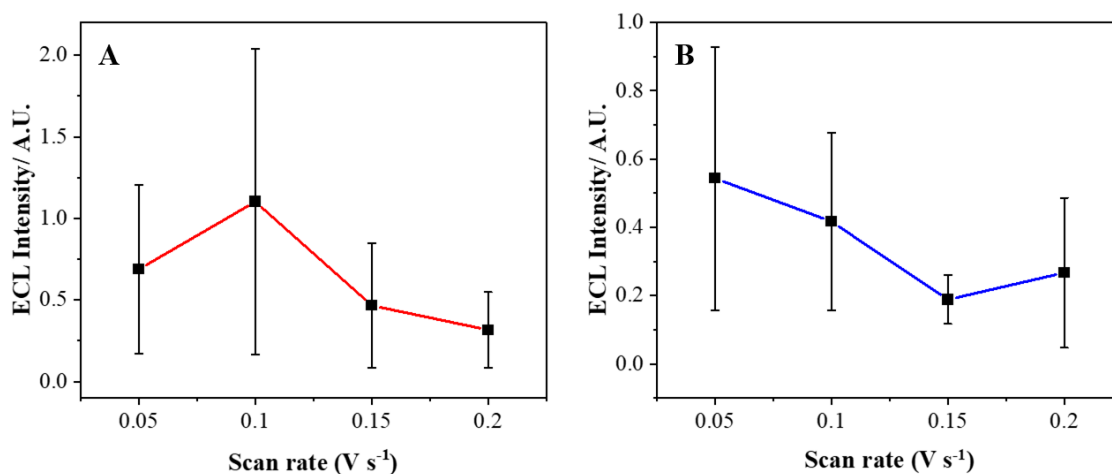


**Figure 17.** Plot of ECL intensity over the scan rate. A) Gold modified Ti array. B) Gold modified and polished Ti electrode. The error bar represents the standard deviation from three independent measurements of one array (n=3).

Moreover, the standard deviation values indicate that there is a large variance around the mean, highlighting the irreproducibility issues of the platform (**Figure 17**). The variability of the solid electrodes presented in here, is highly influenced by the activity, stability, and reproducibility on the electrode surface<sup>267</sup>. For instance, the adsorbed impurities on the surface can hinder the electrochemical response of the electrodes<sup>268</sup>. The co-reactant used in this study, TrPA, is an organic compound that can be easily adsorbed on surfaces and form a film; therefore, its removal is essential to obtain a clean electrode and reproducible results. This can be achieved by polishing the electrodes mechanically as well as by electrochemical cleaning with H<sub>2</sub>SO<sub>4</sub> to smooth and provide an active surface area<sup>267,269</sup>. However, mechanical polishing of the electrodes was not possible since it would have removed the thin layer of gold previously deposited. Thus, electrochemical cleaning was performed with 0.5 M H<sub>2</sub>SO<sub>4</sub> cycling the electrodes from 0 V to +1.6 V until CV became more stable (approximately 20 cycles) to degrade and remove adsorbed impurities by forming a hydrophilic layer of gold oxides on the surface<sup>268,269</sup>. By cycling the electrodes, gold is dissolved as impurities that are stripped during the oxidation process and a partial re-deposition of dissolved gold species happens that leads to the formation of a stable “clean” surface<sup>270</sup>. However, there is a large variability on the stable state of a polished/cleaned gold surface which can impact the electrochemical response and by extension, the ECL response of the electrodes. The variability in the intensities indicates that after every cleaning process, the electrode surface changes, which might be linked to the reactivity of gold and formation of no stable surface states after the electrochemical cleaning of the electrodes<sup>270</sup>. Additionally, as mentioned before, limitations on applying cleaning techniques such as mechanical polishing, also contributes to variability of the surface leading to irreproducible results. Hence, further attempts with other surface treatment strategies would be needed in order to address the irreproducibility issues and optimize the electrode surface for biosensing purposes.

#### **4. CONCLUSION**

This chapter describes the electrochemical properties of 3D printed titanium electrodes as well as their performance in an electrochemiluminescent system. SEM shows that the array surface has significant roughness reflecting the titanium particles used in the

Selective Laser Sintering process. This is potentially an advantage for assay development since a larger area can increase the antibody/DNA capture strand surface coverage increasing the dynamic range and perhaps increasing sensitivity. On the other hand, the aging and growth of oxide on the surface is a challenge for electrochemical and ECL biosensors. However, as it was shown, the redox properties of the electrodes can be significantly improved, especially with respect to  $k^0$ , through functionalization of the surface by electrodeposition of gold. The performance of the electrodes under the co-reactant system with  $[\text{Ru}(\text{bpy})_3]^{2+}$  and TrPA was significantly improved in presence of a thin layer of gold compared to the uncoated electrodes, enhancing ECL signal. Furthermore, the electrochemical characterization of gold coated electrodes with FcnMeOH showed that the reaction is dominated by semi-infinite linear diffusion rather than radial diffusion at scan rates  $> 0.1 \text{ V s}^{-1}$ . This suggests that the contribution of the linear diffusion of the cylinders' walls predominate over the radial diffusion provided by the tips. Overall, these results show that the 3D printed Ti arrays can serve as optimizable platform through modification of materials such as gold that can enhance ECL properties for their potential application in ECL based biosensors. In the future, further modifications of gold-functionalized 3D printed Ti electrodes can be studied for antibody or DNA binding for pathogens and/or biofilms detection. Furthermore, optical properties of  $[\text{Ru}(\text{bpy})_3]^{2+}$  and gold can also be explored to develop plasmonically enhanced ECL sensors.

## **Chapter 3:**

# **Spectroscopic and electrochemical characterization of Ru complexes for SPR-ECL biosensing applications**

## 1. INTRODUCTION

In the last decades, electrochemiluminescence (ECL) has arisen as a powerful analytical technique for biosensing applications<sup>271,272</sup>. Electrochemiluminescence (ECL) is defined as the process where light is emitted by an excited luminophore generated by reactive intermediates at the interface of the electrode and the supporting electrolyte<sup>273</sup>. As explained in **Chapter 1**, signal amplification has been pursued to develop more sensitive platforms. For that, ECL labels coupled to plasmonic materials (e.g., AuNPs, QDs and etc.), have been investigated to develop advanced SPR-ECL systems<sup>37,143</sup>. However, it is fundamental to understand the interaction between luminophores (e.g., ruthenium complexes) and plasmonic materials in order to greatly enhance the signal and reduce the background, especially for their application in solid-surface assays<sup>274</sup>. For that, it is essential to know how each phenomenon, ECL and SPR occurs so they can be implemented in the same system. In the ECL signal generation three steps are involved, starting from a voltage step that produces the reactive intermediate/species of the luminophore. Secondly, an electron transfer occurs between the intermediates leading to the generation of an excited state ( $S_1$ ) of the luminophore. Finally, light is emitted by the luminophore during its relaxation process, decaying to its ground state<sup>273</sup> ( $S_0$ ), where the electrons fill the atomic orbitals with the lowest energy (orbitals are occupied by electron pairs in ground state)<sup>275</sup>. Generally, the energetically-lowest electronic transition happens between the HOMO (highest occupied molecular orbital) and the LUMO (lower unoccupied molecular orbital) and the energy difference between these orbitals is called HOMO-LUMO gap<sup>275</sup>. Note that ECL is a different luminescent process, since as mentioned before, ECL requires a chemical reaction step, e.g., oxidised luminophore and TrPA radical, to create the excited state of the luminophore whereas fluorescence or phosphorescence involves absorption of a photon (**Figure 1A**). In the figure shown in here (**Figure 1B**) an example of ECL generation under a co-reactant system with TrPA and tris(2,2'-bipyridine)ruthenium (II) is displayed, when a positive potential is applied (oxidative-reduction route)<sup>124</sup>.

Since Bard's group<sup>276</sup> reported in 1972 the ECL emission of the luminophore tris(2,2'-bipyridine)ruthenium (II),  $[\text{Ru}(\text{bpy})_3]^{2+}$ , this technique has attracted a lot of attention and now is widely used in chemical and biochemical analysis<sup>277-279</sup>. In photoelectrochemistry, ruthenium based bipyridyl complexes are extensively

investigated due to their unique combination of stability, redox properties, excited state reactivity, light emission, and excited state lifetime<sup>129</sup>.  $[\text{Ru}(\text{bpy})_3]^{2+}$  is used in a wide range of applications such as optoelectronic devices, bio-imaging, bio-analysis, catalysis and nano sciences among others<sup>280</sup>.

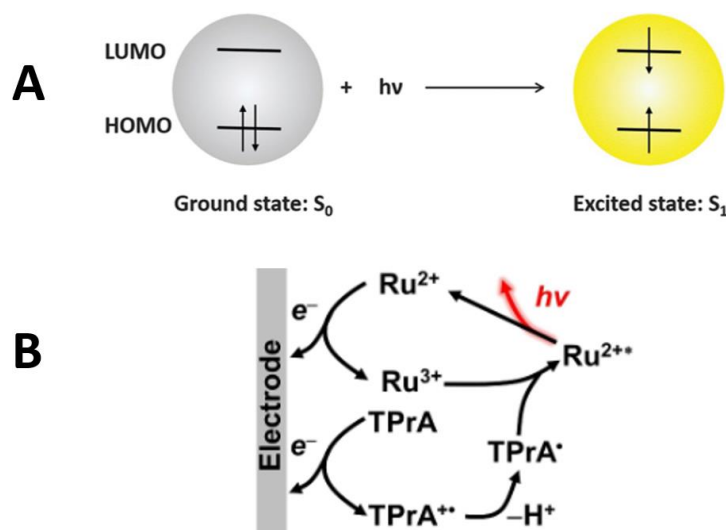


**Figure 1.** Schematic representation of luminescent processes. A) Photoluminescence<sup>275</sup>. B) Electrochemiluminescence generation through oxidative-reductive co-reactant pathway with  $[\text{Ru}(\text{bpy})_3]^{2+}$  as luminophore<sup>2f60</sup>.

ECL a great tool to investigate the photoelectric properties of functional materials and more importantly, is very sensitive to near-field interaction such as localized surface plasmon resonance (LSPR) generated by gold nanoparticles (AuNPs), which can be exploited to tune and optimise the sensitivity of assays<sup>259,281</sup>. AuNPs have been widely investigated due to their unique optical and electronic properties that can be exploited in nanomedicine, biosensing and spectroscopy<sup>282</sup>. Moreover, AuNPs present high chemical and physical stability as well as intrinsic biocompatibility properties that allows them to be used in biological systems, and they can be easily functionalised with biomolecules (e.g., DNA, proteins, antibodies and etc)<sup>283</sup>. Furthermore, their optical characteristics can be strongly enhanced by combining them with different luminophores such as ruthenium complexes<sup>280,284</sup>. As mentioned earlier, for metallic structures such as AuNPs, when the electric field of light at an appropriate wavelength is incident on the material, it can polarize the “plasmon” (collective oscillations of free electrons in metals), provoking the

phenomenon called (LSPR)<sup>285</sup>. As shown in **Figure 2**, the free electrons clouds are dislocated by light (electromagnetic field) by producing uncompensated charges near the particle surface which generates corresponding opposite forces<sup>286</sup>. Several factors can influence the LSPR such as the dielectric environment, temperature, particle size, interparticle distance, particle shape, surface chemical interactions etc<sup>285,286</sup>.

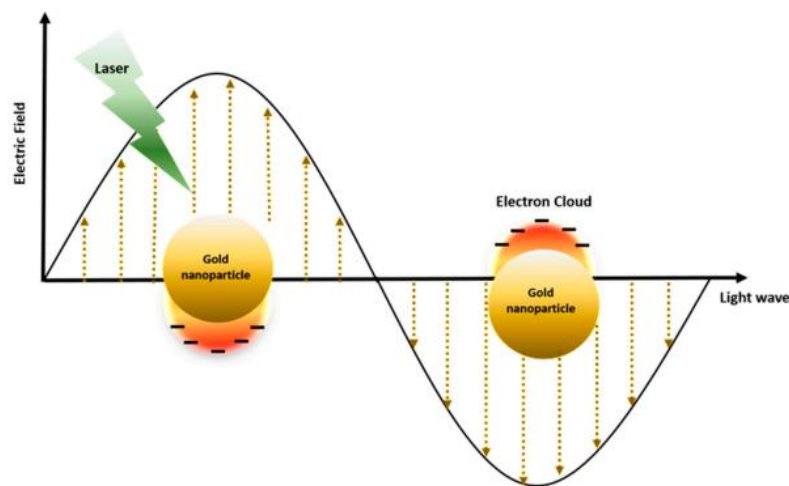


**Figure 2.** Schematic representation of oscillation of collective plasmons (electron cloud) due to applied electric field (incident light)<sup>283</sup>.

Attachment and/or grafting luminophores to nanoparticles such as gold, has recently attracted significant attention<sup>280</sup>. Even though AuNPs labelled with luminophores has been reported, a limitation regarding the luminophore-particle distance exists that can provoke the quenching of the light emitted by the luminophore<sup>287</sup>. According to the literature, the luminophore must be placed at a distance around 10 nm to experience the greatest enhancement, however, at distances shorter than 10 nm, quenching of ECL has been reported due to the energy transfer of the excited state of the luminophore to the metal surface<sup>38</sup>. Therefore, distance of the luminophore to the gold surface as well as the attachment method are key factors that it should be considered when building SPR-ECL platforms using nanoparticles<sup>287</sup>. Ruthenium complexes exhibit excellent redox and luminescent characteristics, therefore, building SPR-ECL units with AuNPs is of great interest for fundamental research but also for potential applications on a wide range of areas such as biosensing and clinical detection of pathogens<sup>38,280,288</sup>. In this sense, DNA can be utilized as an analyte since oligonucleotides can serve as templates than can be



modified with spectroscopically and/or photochemically active metal-centres (i.e., ruthenium complexes) at specific locations<sup>289</sup>. In fact, ruthenium (e.g., 1,10-phenanthroline (phen) or 2,2'-bipyridine (bpy)) labelled DNA show good stability in terms of chemistry, electrochemistry and photophysical behaviour, which make them very suitable for their application in biosensors<sup>290</sup>.

In this chapter, three different ruthenium complexes alongside 10 nm size AuNPs are investigated in aqueous solution to provide a deeper understanding of their interaction and address issues such as quenching and/or enhancement for future application in a SPR-ECL biosensing platform. A tris(2,2'-bipyridine)ruthenium (II) holding an amino group, ( $[\text{Ru}(\text{bpy})_3\text{-NH}_2]^{2+}$ ) already published<sup>291</sup> is characterized by spectroscopic techniques (fluorimetry, UV-Vis) and electrochemical techniques such as Cyclic Voltammetry (CV), and compared to two commercially available dyes, tris(2,2'-bipyridine)ruthenium (II) ( $[\text{Ru}(\text{bpy})_3]^{2+}$ ) and bis(2,2'-bipyridine)-(5-aminophenanthroline)ruthenium bis(hexafluorophosphate) ( $[\text{Ru}(\text{bpy})_2(\text{phen})\text{-NH}_2]^{2+}$ ) to elucidate the suitability of the dye for use in an ECL assay. Separately, a single-stranded DNA (ssDNA) probe was developed and characterised using  $[\text{Ru}(\text{bpy})_3\text{-NH}_2]^{2+}$  and  $[\text{Ru}(\text{bpy})_2(\text{phen})\text{-NH}_2]^{2+}$  for their potential use and/or application on a ECL assay based on DNA detection. Dyes with an amino group were chosen over a carboxyl group for this study since its affinity for gold allows the metal complexes to be in close contact with the gold surfaces providing control over the distance between the two components. Furthermore, it can be successfully used for functionalization of biomolecules avoiding extra steps and/or reagents for their coupling as it would be needed for COOH group (e.g., N-Hydroxysuccinimide/ 1-Ethyl-3-(3-dimethylaminopropyl)carbodiimide)<sup>135,292</sup>. Therefore, the objective of this chapter is to investigate the influence of the plasmon band energy of AuNP and understand how it affects to the metal-to-ligand charge transfer (MLCT) of ruthenium dyes. Finally, the interaction between the luminophores and the conjugated DNA is discussed to elucidate how its presence can alter the optical properties of the dyes.

## 2. MATERIALS AND METHODOLOGY

### 2.1. Chemicals

The AuNPs (NanoXact Gold Nanospheres – Bare (Citrate), size 10 nm) were purchased from nanoComposix (distributed by Generon Ltd, Ireland). Both tris(2,2'-bipyridine) ruthenium (II) ( $\text{Ru}(\text{bpy})_3^{2+}$ ) and bis(2,2'-bipyridine)-(5-aminophenanthroline) ruthenium bis(hexafluorophosphate) ( $\text{Ru}(\text{bpy})_2^{2+}\text{-2PF}_6$ ) were purchased in from Merck (powder) as well as tri-n-propylamine TrPA ( $\geq 98\%$ ) and lithium perchlorate ( $\text{LiClO}_4$ ) (powder). The reagents for dye-DNA conjugation, N, N-Dimethylformamide (DMF), sodium chloride ( $\text{NaCl}$ ), borate buffer saline (powder) and PBS buffer tablets were also purchased from Merck. Nuclease-free  $\text{dH}_2\text{O}$  was purchased from IDT. See ruthenium complexes structures in **Figure 3**.

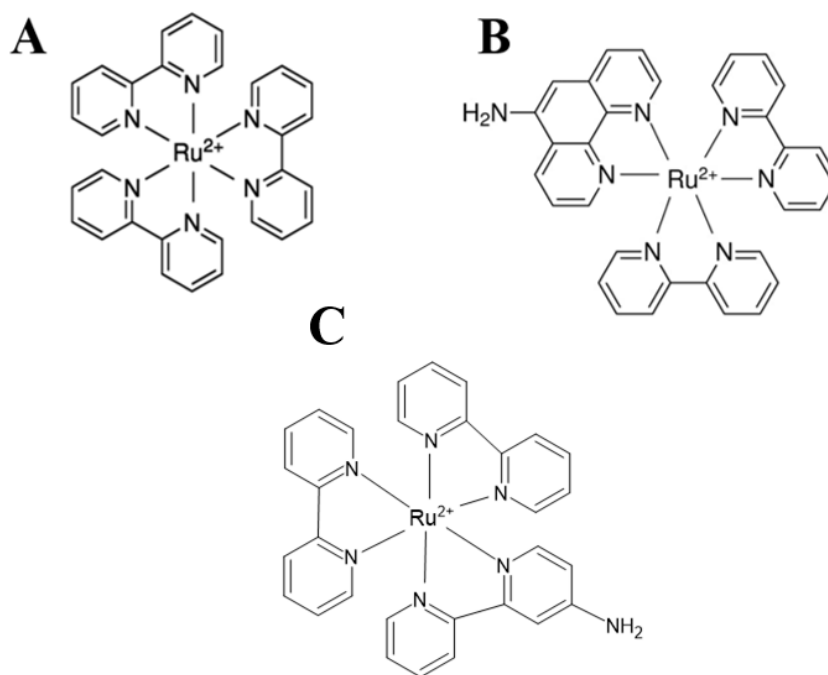


**Figure 3.** Molecular structure of ruthenium complexes studied. A)  $\text{Ru}(\text{bpy})_3 (2\text{Cl}^-) 6\text{H}_2\text{O}$ , B)  $\text{Ru}(\text{bpy})_2(\text{phen-5-NH}_2)(\text{PF}_6)_2$  and C)  $\text{Ru}(\text{bpy})_3\text{-NH}_2$ .

## 2.2. DNA-dye conjugation and purification protocol

The dye-DNA conjugation was carried out using a 30 nucleotides long sequence (purchased from IDT), from *Escherichia coli* (5'-AGACCAACAA CTATAACAGC GATGATTTCC -3'), with a thiol group at 3' and azide ester group (NHS ester) at the 5' end. The conjugation and purification protocol presented in here is based on the work published by Zhou et al.<sup>293</sup>, however, some steps were modified. The  $[\text{Ru}(\text{bpy})_3\text{-NH}_2]^{2+}$  was chosen as label to develop the DNA probe. 50  $\mu\text{L}$  from 1 mM stock solution of  $[\text{Ru}(\text{bpy})_3\text{-NH}_2]^{2+}$  and 50  $\mu\text{L}$  from 100 mM DNA stock solution were mixed in 100  $\mu\text{L}$  of 0.1M borate buffer pH 8.5 with 20mM of DMF. The conjugation reaction was continuously mixed for 12 hours in the dark at room temperature. Subsequently, 20  $\mu\text{L}$  of 2 M NaCl and 500  $\mu\text{L}$  of cold absolute ethanol were added to the mixture, which was place at  $-20^\circ\text{C}$  for 45 minutes. In order to purify the sample, and separate the unbound dye from the DNA, the solution was centrifuged at 14000 rpm for 30 mins. The supernatant was carefully removed, and the pellet was rinse with 1 mL of cold 70% ethanol. After repeating this step three times the pellet was partially air-dried (not to complete dryness) and was then re-dissolved in nuclease free  $\text{dH}_2\text{O}$ . The purified sample was mixed well and stored at  $-20^\circ\text{C}$ .

## 2.3. Spectroscopic characterization

UV-Vis measurements in aqueous solutions were carried out in Shimadzu UV-2600 UV-VIS Spectrometer with UVProbe LabSolutions Software, using  $1 \times 1 \text{ cm}^2$  rectangular quartz cells from Merck. Serial dilutions of samples were carried out to build a concentration curve and subsequently calculate the extinction coefficient ( $\epsilon$ ). Fluorimetry studies were performed using a PerkinElmer LS50B Luminescence Spectrometer and FL WinLab software. Fluorescent lifetimes were recorded in Photoluminescence Spectrometer FLS 1000 (Edinburgh Instruments). Zeta-potential and Dynamic Light Scattering (DLS) measurements of the nanoparticles were measured in Malvern Zetasizer Ultra, using the folded capillary zeta potential cells.

## 2.4. Electrochemiluminescence characterization

Experiments for electrochemiluminescence detection, were carried out CH Instrument Model 760B workstation, an Oriel 70680 photomultiplier tube (PMT) biased at  $-850$  V along with a high-voltage power supply (Oriel, Model 70705) and an amplifier/recorder (Oriel, Model 70701) as shown in **Chapter 2**. An Ag/AgCl and a platinum wire (IJ Cambria) were used as reference and counter electrodes and a glassy-carbon electrode (IJ Cambria) acted as the working electrode. Aqueous  $0.1$  M  $\text{LiClO}_4$  was used as supporting electrolyte and scanning from  $0$  V to  $+1.6$  V, using  $0.1$  mM of the ruthenium dye/luminophore (described above) and  $0.1$  M of TrPA as the co-reactant. A separate experiment was performed with  $0.0254$  mM of  $10$  nm diameter AuNPs using the same concentrations of luminophore and co-reactant.

## 3. RESULTS AND DISCUSSION

### 3.1. Dyes and AuNPs

#### 3.1.1. UV-Vis, Zeta-potential and DLS

As mentioned earlier, one of the objectives of this chapter is to investigate the interaction between the AuNPs and the ruthenium complexes and their effect on the stability, electrochemical, physicochemical and optical properties to inform the development of SPR-ECL platforms. Therefore, UV-Vis and fluorescence spectroscopic techniques were used to get a better insight of AuNPs and dyes interactions in water.  $\text{Ru}(\text{bpy})_3(2\text{Cl}^-)6\text{H}_2\text{O}$  dissolved in water will be referred to as  $[\text{Ru}(\text{bpy})_3]^{2+}$ ,  $\text{Ru}(\text{bpy})_2(\text{phen}-5\text{-NH}_2)(\text{PF}_6)_2$  as  $[\text{Ru}(\text{bpy})_2(\text{phen})\text{-NH}_2]^{2+}$  and  $\text{Ru}(\text{bpy})_3\text{-NH}_2$  as  $[\text{Ru}(\text{bpy})_3\text{-NH}_2]^{2+}$ .

Absorption spectra were recorded of the ruthenium dyes and AuNPs separately, and each of the dyes in the presence of suspended AuNPs. Different concentrations were tested to build a concentration curve and extract the extinction coefficient ( $\epsilon$ ) (applying the Beer-Lambert equation where  $A$  represents absorbance,  $\epsilon$  the extinction coefficient,  $c$  the concentration of the sample and  $l$  the pathlength of the cuvette (**Equation 1**):

$$A = \epsilon cl \quad (1)$$

In **Figure 4** the absorption spectra of each dye are presented. It is observed that the three dyes absorb approximately at the same wavelength ( $\lambda \sim 455$  nm) due to the metal to ligand charge transfer (MLCT) transition (see absorbance values in **Table 1**). This process happens when a photon of light is absorbed by the metal centre of a coordination complex and excites an electron from the metal-based orbital (d) to a ligand-based orbital ( $\pi$ ) (i.e., ligand), generating an excited state of the complex where the metal has lost an electron and the ligand has gained one ( $\pi^*$ ). After this, the excited state relaxes and it decays to its ground state<sup>294,295</sup>. Furthermore, intense bands are observed for the novel dye  $[\text{Ru}(\text{bpy})_3\text{-NH}_2]^{2+}$ , very similar to the ones of the conventional ruthenium dye ( $[\text{Ru}(\text{bpy})_3]^{2+}$ ) around the wavelength 200–300 nm, which has been previously attributed to  $\pi \rightarrow \pi^*$  intraligand transitions from the bipyridine groups<sup>280</sup>. However, for  $[\text{Ru}(\text{bpy})_2(\text{phen})\text{-NH}_2]^{2+}$ , different bands were observed at the same wavelength that might be attributed to  $\pi \rightarrow \pi^*$  intraligand transitions from bipyridine groups to aminophenanthroline ligand. In addition,  $[\text{Ru}(\text{bpy})_3\text{-NH}_2]^{2+}$  and  $[\text{Ru}(\text{bpy})_2(\text{phen})\text{-NH}_2]^{2+}$  present a  $\epsilon$  value  $6.98 \pm 0.0623 \times 10^3$  and  $7.42 \pm 0.0320 \times 10^3$  (respectively) close to the conventional ruthenium dye (**Table 1**) which has been previously reported to be of the order of  $10^4$  range when dissolved in water<sup>296</sup>.

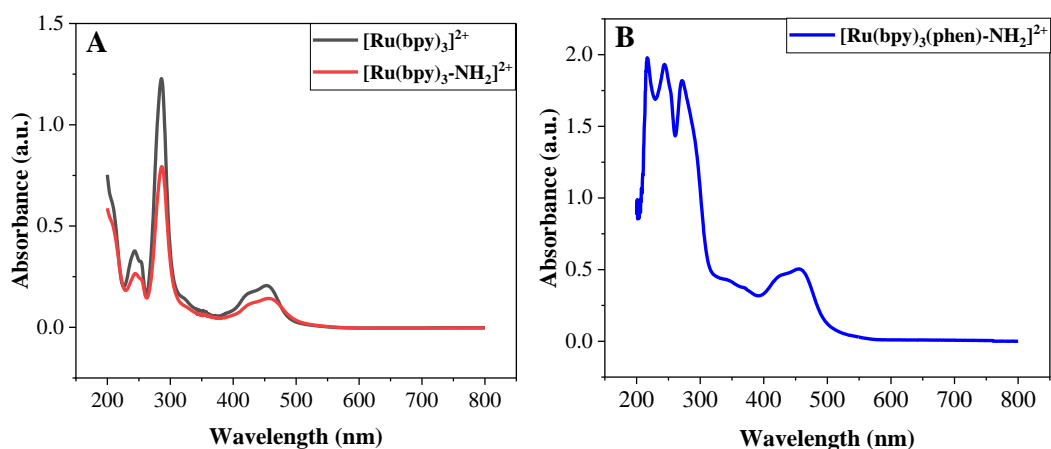


**Figure 4.** Absorption spectra of luminophores (20  $\mu\text{M}$ ) in water. A)  $[\text{Ru}(\text{bpy})_3]^{2+}$  (black) and  $[\text{Ru}(\text{bpy})_3\text{-NH}_2]^{2+}$  (red). B)  $[\text{Ru}(\text{bpy})_2(\text{phen})\text{-NH}_2]^{2+}$ .

The UV-Vis spectra obtained for the commercial AuNPs (see DLS values in **Table 2**) is shown in **Figure 5**, where the surface plasmon band (SPR band) of the AuNPs is observed at 518 nm which is in agreement with the data reported for 10 nm size of AuNPs<sup>297</sup>. However, AuNPs SPR band is shifted band shifted > 80 nm towards blue light region, when mixed with the dyes (**Figure 6**), although the extinction coefficient values of AuNPs fall in the same range as when no combined with dyes (**Table 1**). On the other hand, DLS values from **Table 2** suggest that the shift in the AuNPs band could be due to self-aggregation promoted by the addition of the dyes<sup>288</sup>. When luminophores are mixed with AuNPs, the absorption overlap is relatively limited, therefore, this provides the opportunity to excite each component separately. On the other hand, differences in the zeta-potential values also suggest that the dyes with amino group (-NH<sub>2</sub>) show a significant affinity for gold, with [Ru(bpy)<sub>3</sub>-NH<sub>2</sub>]<sup>2+</sup> causing the larger change in the zeta-potential value of the particles (from negative to positive). In fact, compounds such as amino acids, with an amino group or a thiol group (-SH) have been extensively exploited for AuNPs functionalization<sup>298,299</sup>. Therefore, the dyes with the amino moiety studied in this chapter could be exploited for functionalization of gold surfaces, that can potentially use for the development of biosensors.

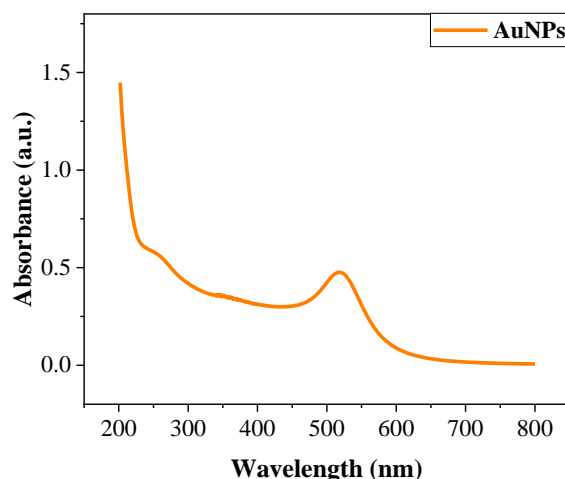


**Figure 5.** Absorption spectrum of 10nm size commercial AuNPs capped with citrate. Solvent: dH<sub>2</sub>O.

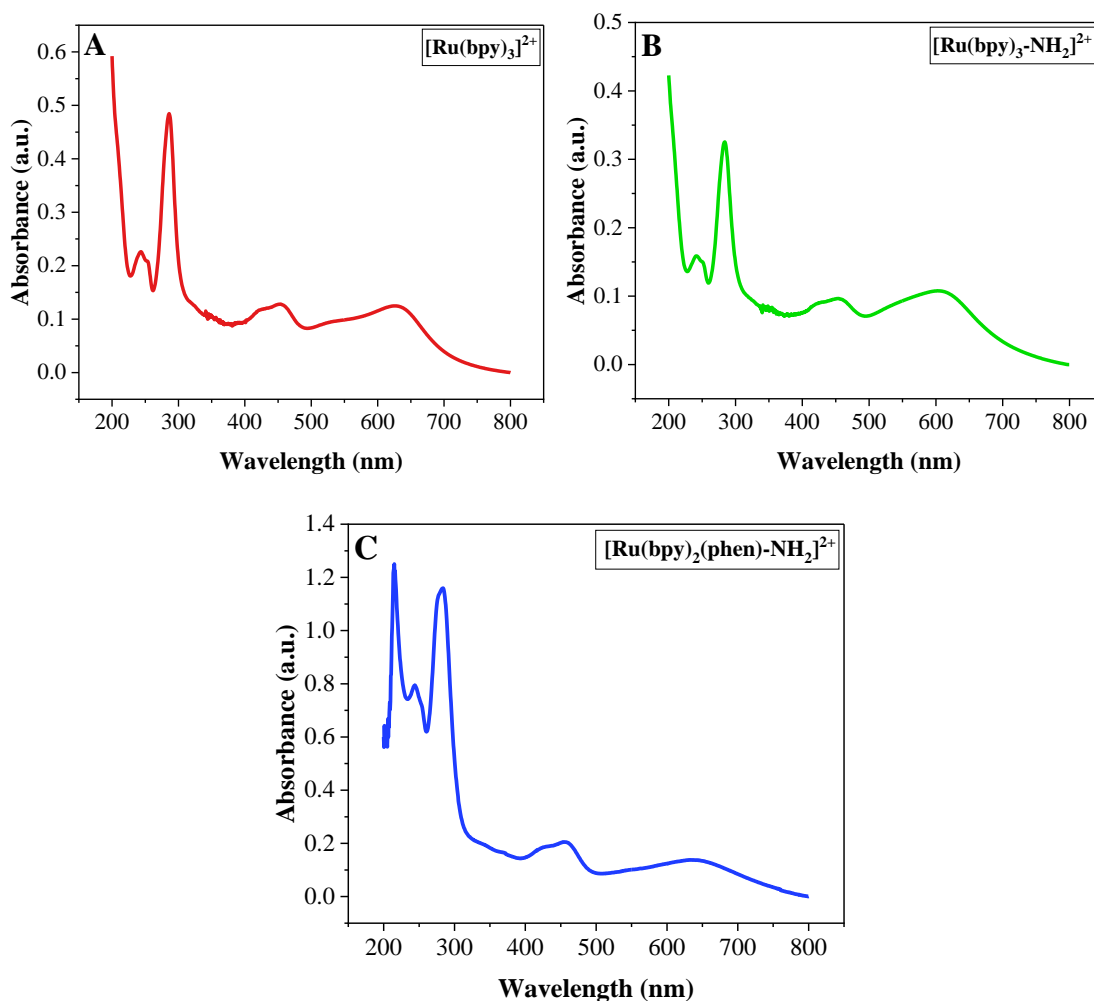


**Figure 6.** Absorption spectra of Ru dyes (20  $\mu\text{M}$ ) mixed with AuNPs (25.4  $\mu\text{M}$ ). A)  $[\text{Ru}(\text{bpy})_3]^{2+}$ , B)  $[\text{Ru}(\text{bpy})_3\text{-NH}_2]^{2+}$  and AuNPs, C)  $[\text{Ru}(\text{bpy})_2(\text{phen})\text{-NH}_2]^{2+}$  and AuNPs. Solvent:  $\text{dH}_2\text{O}$ .

**Table 1.** Absorption and extinction coefficient values extracted from concentration curves from MLCT of dyes and SPR bands of AuNPs.

	Absorbance (nm)	Extinction coefficient ( $\epsilon$ )
<b>AuNPs</b>	518	$2 \pm 0.00 \times 10^8$
<b><math>[\text{Ru}(\text{bpy})_3]^{2+}</math></b>	453	$1.03 \pm 0.0004 \times 10^4$
<b><math>[\text{Ru}(\text{bpy})_3\text{-NH}_2]^{2+}</math></b>	456	$6.98 \pm 0.0623 \times 10^3$
<b><math>[\text{Ru}(\text{bpy})_2(\text{phen})\text{-NH}_2]^{2+}</math></b>	454	$7.42 \pm 0.0320 \times 10^3$
<b><math>[\text{Ru}(\text{bpy})_3]^{2+}</math> + AuNPs</b>	453 and 626	$1.74 \pm 0.21 \times 10^4$ and $2 \pm 0.00 \times 10^8$
<b><math>[\text{Ru}(\text{bpy})_3\text{-NH}_2]^{2+}</math> + AuNPs</b>	453 and 603	$1.63 \pm 0.035 \times 10^4$ and $1 \pm 0.00 \times 10^8$
<b><math>[\text{Ru}(\text{bpy})_2(\text{phen})\text{-NH}_2]^{2+}</math> + AuNPs</b>	454 and 633	$1.64 \pm 0.021 \times 10^4$ and $7 \pm 0.00 \times 10^7$

**Table 2.** Zeta potential and DLS values of AuNPs in water and mixed with dyes.

	Zeta-potential (mV)	DLS (nm)
<b>AuNPs</b>	$-42.82 \pm 0.31$	$16.84 \pm 0.15$
<b><math>[\text{Ru}(\text{bpy})_3]^{2+}</math> + AuNPs</b>	$-26.63 \pm 2.34$	$470.9 \pm 5.53$
<b><math>[\text{Ru}(\text{bpy})_3\text{-NH}_2]^{2+}</math> + AuNPs</b>	$6.16 \pm 2.25$	$765.37 \pm 55.89$
<b><math>[\text{Ru}(\text{bpy})_2(\text{phen})\text{-NH}_2]^{2+}</math> + AuNPs</b>	$-5.07 \pm 0.30$	$773.23 \pm 35.81$

### 3.1.2. Fluorescence: steady state and time-resolved spectroscopy

The fluorescence of dissolved luminophores in water with and without AuNPs was studied. The emission and excitation spectra are shown in **Figure 7** for the three ruthenium complexes. Differences are observed in the emission wavelengths ( $\lambda_{\text{emission}}$ ), especially for the dye  $[\text{Ru}(\text{bpy})_3\text{-NH}_2]^{2+}$ , which emission is slightly shifted ( $\lambda_{\text{emission}} = 628$  nm) compared to commercial dyes (**Table 3**). Furthermore, it also emits less fluorescence than the commercial dyes, being 53% less intense than the standard ruthenium complex (i.e.,  $[\text{Ru}(\text{bpy})_3]^{2+}$ ) at the same concentration. On the other hand,  $[\text{Ru}(\text{bpy})_2(\text{phen})\text{-NH}_2]^{2+}$  show only 6% less intensity than standard ruthenium complex. Many factors can influence the fluorescence intensity of a luminophore, such as fluorophore/luminophore concentration or photobleaching<sup>300</sup>. As the emission intensity depends on the extinction coefficient, it was expected that  $[\text{Ru}(\text{bpy})_3\text{-NH}_2]^{2+}$  showed a similar emission intensity to standard ruthenium. However, as it is not a commercial luminophore, it could be possible that the complex is less stable, especially during the excited lifetime and therefore, more vulnerable to degradation. This can happen due to photon-induced modifications that turn to be permanent, losing their ability to emit fluorescent light (i.e., photobleaching)<sup>301,302</sup>. As the emission experiments were run first this could explain why the excitation spectrum also showed low absorbance. In addition, decomposition of the luminophore can be possible if oxygen is present in the system, specifically caused by a very reactive product called, singlet oxygen ( $^1\text{O}_2$ ), which can cause the photooxidation of the ground-state complex<sup>303</sup>. However, the emission properties can also vary depending on the coordinated ligands and the local environments. Therefore, it could be expected to see some differences in the emission intensities among the ruthenium complexes since they different ligands that can influence the electron donating properties<sup>304</sup>.

On the other hand, the excited state lifetime values were obtained for a better understanding of the dyes. The lifetime values shown in **Table 3**, were obtained by fitting the experimental data. The lifetime value obtained for  $[\text{Ru}(\text{bpy})_3\text{-NH}_2]^{2+}$  ( $\tau_0 = 639$  ns) is slightly shorter than the one obtained for the standard ruthenium,  $\tau_0 = 660$  ns (see **Table 3**). Excited state lifetimes have been reported to be very sensitive to factors such as temperature, solvent pH, concentration, presence of oxygen, binding to macromolecules ion concentration, impurities and etc., thus, changes in the environment can strongly influence the values obtained<sup>300,305</sup>. It was also found that OH vibrations of water have



an impact on energy acceptors by enhancing non-radiative decay for ruthenium bipyridine complexes<sup>280</sup>. That could explain why  $[\text{Ru}(\text{bpy})_2(\text{phen})\text{-NH}_2]^{2+}$  show a longer lifetime decay ( $\tau_0 = 716$  ns), since it only possesses two bipyridine groups and a phenanthroline group, therefore, the way how water impacts on  $[\text{Ru}(\text{bpy})_2(\text{phen})\text{-NH}_2]^{2+}$  lifetime could be different due to the differences in the structural composition of the luminophore. Furthermore, more information about the luminescence of each complex is provided in the next section (see section 3.1.4) in terms of ECL emissions.

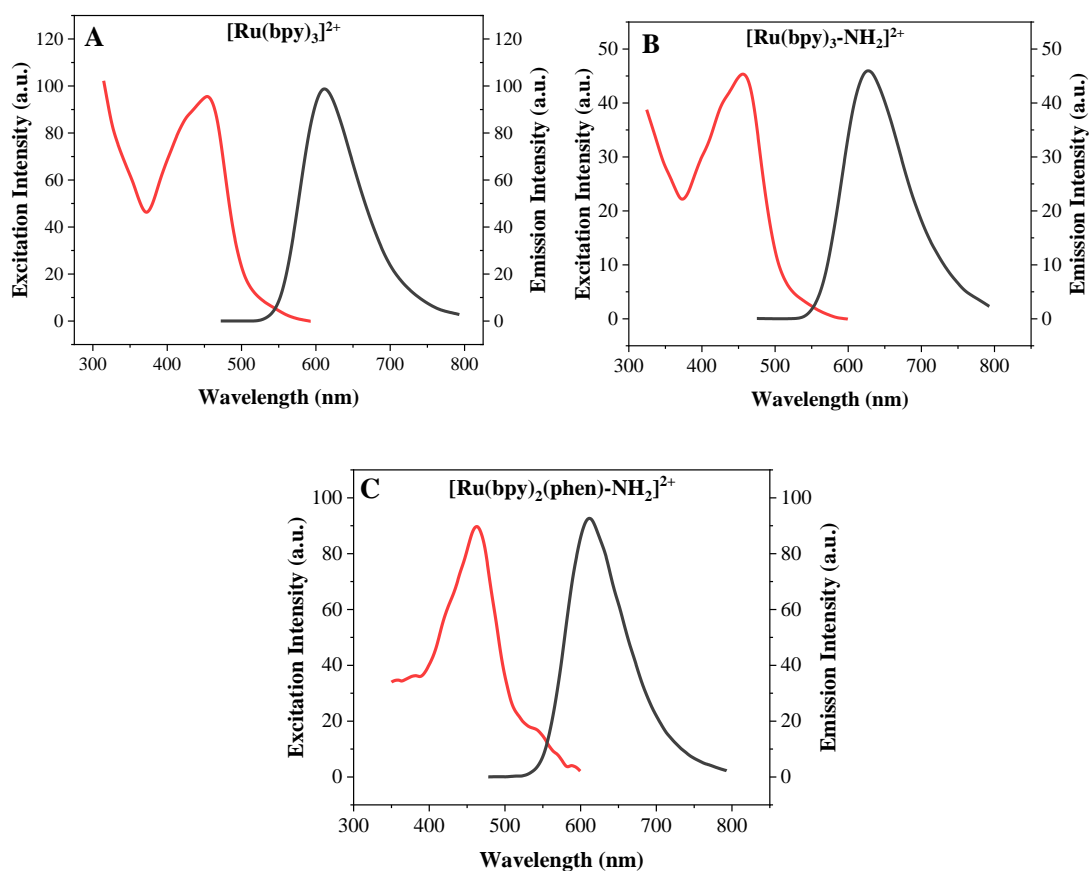


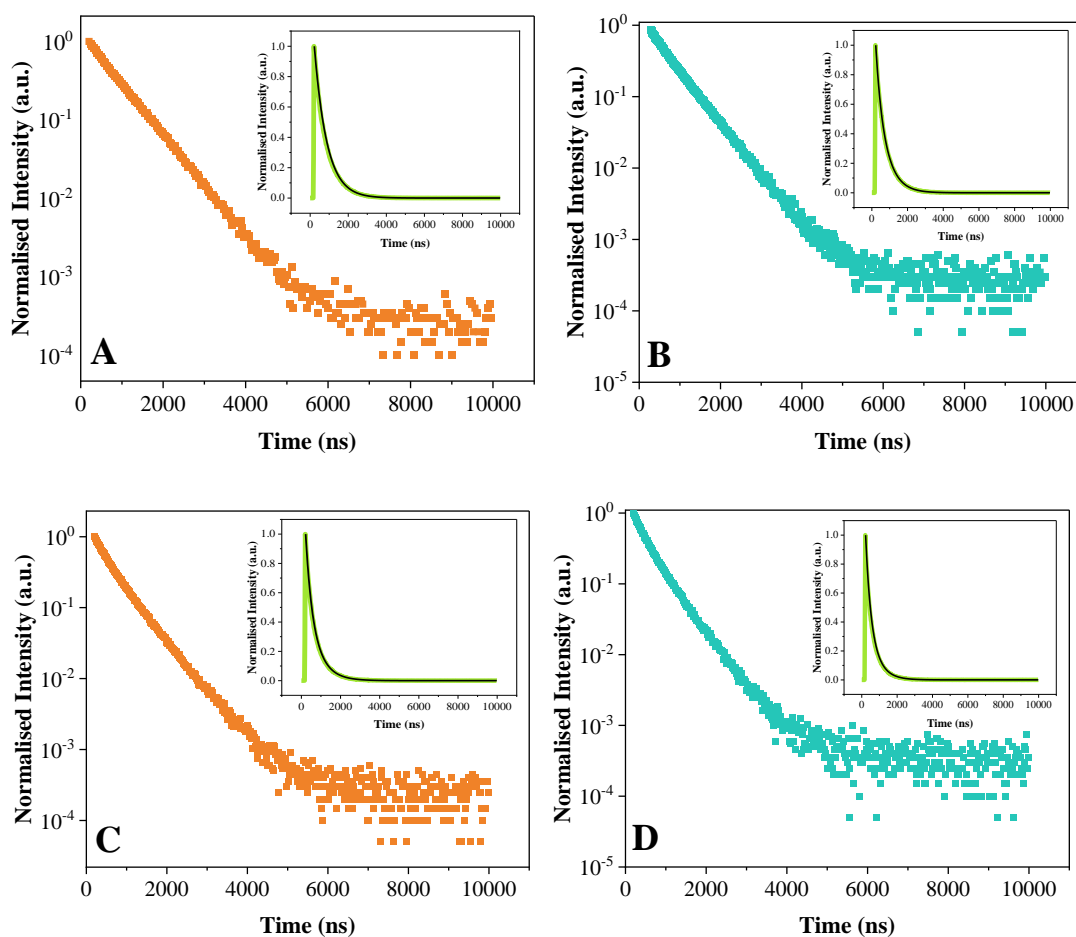
**Figure 7.** Fluorescence spectra (excitation and emission) of luminophores without AuNPs. A)  $[\text{Ru}(\text{bpy})_3]^{2+}$ , B)  $[\text{Ru}(\text{bpy})_3\text{-NH}_2]^{2+}$  and C)  $[\text{Ru}(\text{bpy})_2(\text{phen})\text{-NH}_2]^{2+}$ . Excitation wavelength ( $\lambda=455$  nm).

**Table 3.** Fluorescence data of free ruthenium, life-time values with and without AuNPs and quenching constant ( $K_q$ ) extracted from Stern-Volmer plots. The luminescent lifetimes were fitted with a  $\chi^2$  between 1.0 and 1.6.

	$\lambda_{\text{excitation}}$ (nm)	$\lambda_{\text{emission}}$ (nm)	$\tau_0$ (ns)	$\tau_1$ and $\tau_2$ (ns) with AuNPs	$10^{10} K_q$ ( $\text{L mol}^{-1} \text{s}^{-1}$ )
$[\text{Ru}(\text{bpy})_3]^{2+}$	460	610	660	263 and 608	$2.54 \pm 0.01$
$[\text{Ru}(\text{bpy})_3\text{-NH}_2]^{2+}$	460	628	639	270 and 577	$2.21 \pm 0.05$
$[\text{Ru}(\text{bpy})_2(\text{phen})\text{-NH}_2]^{2+}$	463	611	716	303 and 612	$2.3 \pm 0.03$

In parallel, experiments with AuNPs were also performed to investigate in depth the influence of AuNPs on the luminescence properties of dyes by measuring the lifetime decays when both are present in the sample. The lifetime decays semi-log plots of the luminophores mixed with AuNPs are presented in (**Figure 8**), where differences can be observed. The luminescent lifetimes were achieved fitting the decays with a  $\chi^2$  between 1.0 and 1.6 in the fluorimeter software. The fitting shown in the insets of Figure 8 show  $R^2=0.99$  and it was achieved by fitting the data in OriginLab Software. As it is show in **Table 3**, all the luminophores two lifetimes were achieve when AuNPs were present in the solution, a long one ( $\tau_1 \sim 570$  and  $600$  ns) and a shorter one ( $\tau_2 \sim 260$  and  $303$  ns) (attributed to the intensity signal). The short-lived component for the three samples compromises a lower percentage of the signal, 9.22% for  $[\text{Ru}(\text{bpy})_3]^{2+}$ , 33.82% for  $[\text{Ru}(\text{bpy})_3\text{-NH}_2]^{2+}$  and 19.62%  $[\text{Ru}(\text{bpy})_2(\text{phen})\text{-NH}_2]^{2+}$ . Pramod and et al., using AuNPs functionalised with  $[\text{Ru}(\text{bpy})_3]^{2+}$  dissolved in acetonitrile also obtained a long live component and short-lived component (80% and 20% of the signal, respectively). In their study was suggested that the long-lived component could be attributed to the unquenched luminophore bound to the nanoparticle surface, whereas the short component constitutes the quenched excited state of the luminophore by the AuNP either through an energy or electron transfer process<sup>306</sup>. In another study where different sizes of AuNPs (20 nm to 100 nm diameter) films tested alongside  $[\text{Ru}(\text{bpy})_3]^{2+}$ , it was observed that at the closest separation between luminophore and particle (2 nm spacer) , a significantly shortened lifetime as well as stronger quenching occurred, energy transfer to the NPs, and possibly charge-transfer between the NPs and luminophore was suggested as the cause of obtaining short-lived components<sup>307</sup> agreeing with what reported by Pramod and et al. However, another study using ruthenium metal complexes with different ligands to tune between luminophore and AuNPs, after direct binding onto citrate stabilised AuNPs (>15

nm) observed that the excited state lifetime became longer (e.g., 420 ns to 470 ns), nevertheless, in presence of the AuNPs a short-lived component was also observed (5-20 %) which was attributed to scattering effect<sup>308</sup>. An study investigating transition metal complexes such as ruthenium or iridium bound to macroscopic gold showed that the excited state lifetime value of the ruthenium complex changed upon immobilisation of the complexes onto a gold surface ( $\tau=130$  ns to 210 ns)<sup>309</sup>, promoting a longer lifetime in contrast to what has been reported to smaller surfaces. Therefore, it is plausible that given the results presented in here, and what has been reported in the literature, that the short-lived component is the consequence of the quenching mediated by small AuNPs. In fact, the percentage (%) of the signal could suggest the type or quenching or interaction that occurred between AuNPs and the different luminophores



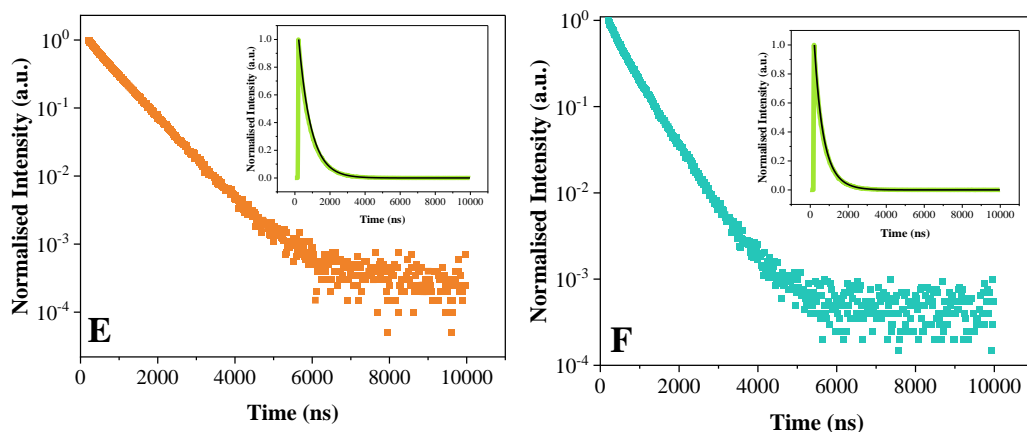


**Figure 8.** Fluorescence life-time decay curves of luminophores (orange) and with AuNPs (blue). A and B)  $[\text{Ru}(\text{bpy})_3]^{2+}$ , C and D)  $[\text{Ru}(\text{bpy})_3\text{-NH}_2]^{2+}$  and E and F)  $[\text{Ru}(\text{bpy})_2(\text{phen})\text{-NH}_2]^{2+}$ . Logarithmic Y-axis vs. time linear. Each decay was normalised to the maximum number of photons obtained for that recording. Inset: Normalised decay experimental curves (green) and fitted curve (black), linear Y-axis vs. time linear. Excitation wavelength of the laser ( $\lambda=375$  nm). Solvent:  $\text{dH}_2\text{O}$ .

Quenching is a phenomenon that happens when a molecule or nanoparticle (quencher) interacts with a fluorophore and the result of that interaction leads to reduce the lifetime or the quantum yield (i.e., fluorescence intensity) of the fluorophore/luminophore<sup>310,311</sup>. Therefore, in this system, AuNPs might be acting as quenchers. It is important to note that as discussed previously, the distance separating the excited state luminophore and the NP will significantly affect this process and this distance is not controlled in suspension. Two main types of quenching exist: static quenching and dynamic/collisional quenching. Static quenching occurs when the quencher and the fluorophore/luminophore form a complex in the ground state that does not emit<sup>312</sup>, whereas in dynamic quenching, the quencher diffuses to the fluorophore during the lifetime of the excited state and upon contact, the fluorophore decays to ground state without emitting a photon<sup>311</sup>. As explained by Alexiev and Farrens<sup>310</sup>, dynamic quenching has an impact on the lifetime fluorescence decay by depopulating the excited state of the fluorophore and as a result, the decay is shorter. However, in static quenching, although it decreases the fluorescence intensity, it has no effect on lifetime fluorescence decay. By observing the lifetime fluorescence decays when AuNPs are added to each ruthenium luminophore, it could be possible to identify the type of quenching that occurs in this system. For the standard ruthenium complex (**Figure 8A**), as discussed earlier, the lifetime decay profile could reveal that the quenching process is predominantly dynamic, whereas for the dye  $[\text{Ru}(\text{bpy})_3\text{-NH}_2]^{2+}$ , the

difference in the decay profile is very small compared to the decay observed without AuNPs, suggesting that AuNPs act as static quenchers. Additionally, the signal percentage of the short-lived component attributed to the quenching of the luminophores by AuNPs, is larger for  $[\text{Ru}(\text{bpy})_3\text{-NH}_2]^{2+}$  than for standard ruthenium (33.82% and 9.22%, respectively) indicating that more  $[\text{Ru}(\text{bpy})_3\text{-NH}_2]^{2+}$  is quenched suggesting that static interaction occurs, in contrast to standard ruthenium, which quenching is more likely to be dynamic. This is in agreement with the zeta-potential values obtained for AuNPs since when  $[\text{Ru}(\text{bpy})_3\text{-NH}_2]^{2+}$  is added, the zeta-potential of the AuNPs changes significantly (from negative to positive), probably due to  $[\text{Ru}(\text{bpy})_3\text{-NH}_2]^{2+}$  binding (covalently or electrostatically) to the nanoparticle surface mediated by the  $\text{-NH}_2$  group, so AuNPs no longer stay separated in suspension. Similar results were reported when a ruthenium (II) complex holding a  $\text{-SH}$  group was added in solution with 13 nm diameter AuNPs<sup>313</sup>. In this study it was suggested that the positive charge of bound ruthenium attracted the negatively charged surfaces of partially coated AuNPs leading to flocculation and posterior aggregation in solution. Other studies also describe the aggregation of AuNPs in solution influenced by the addition of cationic species such as ruthenium complexes<sup>314,315</sup>.

For  $[\text{Ru}(\text{bpy})_2(\text{phen})\text{-NH}_2]^{2+}$  when AuNPs are present, (**Table 3**), and by the non-linear profile of the fluorescence lifetime, both static and dynamic quenching might have occurred. As it also possesses an  $\text{-NH}_2$ , it has the ability to bind to AuNPs surface and therefore change the zeta-potential of the nanoparticles (see **Table 2**). However, the change in AuNPs zeta-potential is not as big as when  $[\text{Ru}(\text{bpy})_3\text{-NH}_2]^{2+}$ . It is possible that less luminophores are bound to the surface and therefore both quenching processes are contributing. Even if quenching processes entail simple reactions which are easy to monitor, their quantitative treatment and data interpretation is not an easy task<sup>312</sup>. For example, sometimes, apparent quenching can happen due to the optical properties of the sample, since high optical densities can increase the turbidity of the sample (as described in the previous section) causing the decrease on the fluorescence intensity<sup>311</sup>.

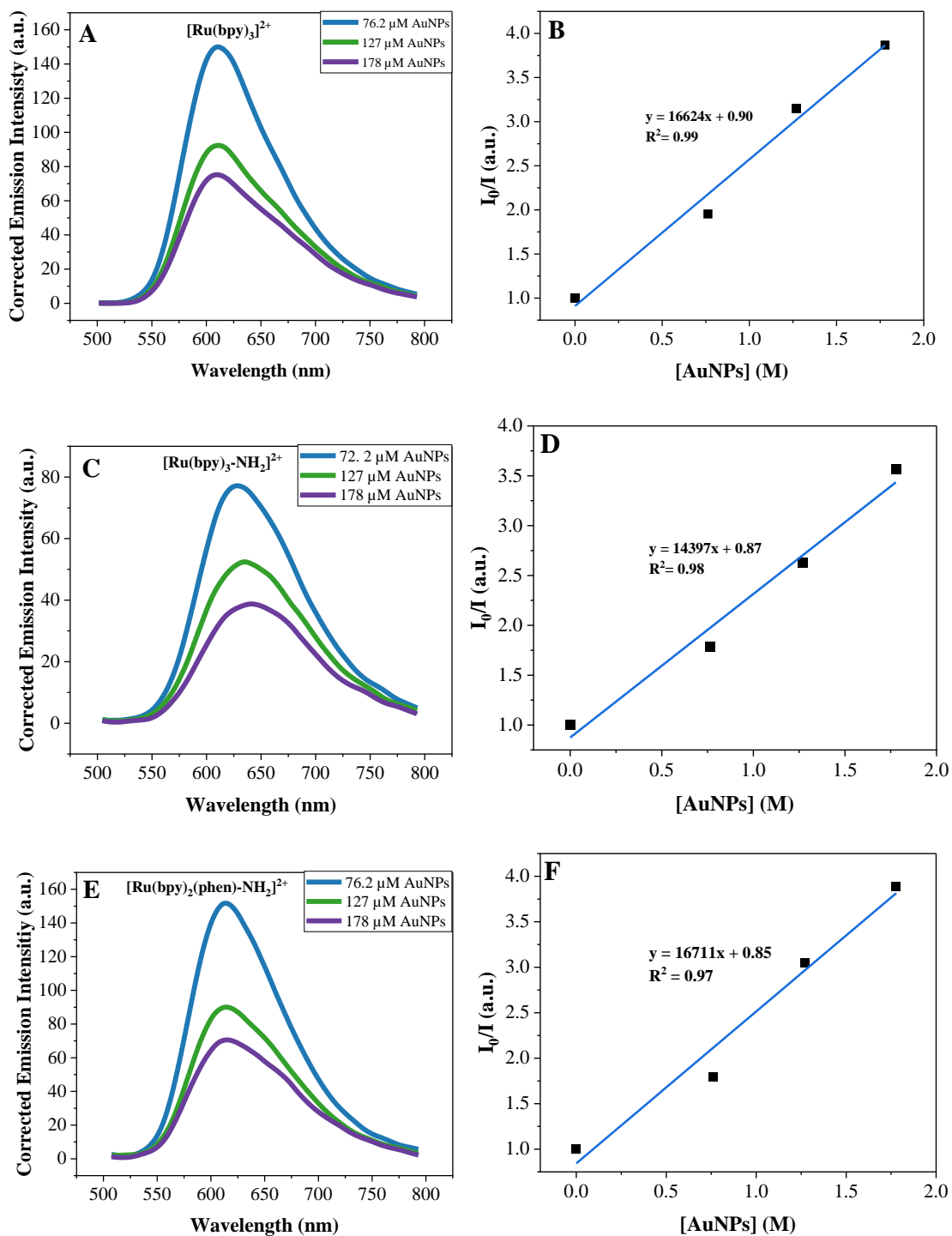


**Figure 9.** Fluorescence emission spectra (corrected for the “inner filter” effect) and corresponding Stern-Volmer plots of luminophores (20 $\mu\text{M}$ ) with different concentrations of AuNPs (76.2  $\mu\text{M}$ , 127  $\mu\text{M}$  and 178  $\mu\text{M}$ ). A to B)  $[\text{Ru}(\text{bpy})_3]^{2+}$ , C to D)  $[\text{Ru}(\text{bpy})_3\text{-NH}_2]^{2+}$  and E to F)  $[\text{Ru}(\text{bpy})_2(\text{phen})\text{-NH}_2]^{2+}$ . (The standard deviations are similar to, or smaller than, the size of the symbols). Excitation wavelength ( $\lambda=455$  nm). Solvent:  $\text{dH}_2\text{O}$ .

However, to better elucidate the quenching phenomenon in the system, steady state fluorescence experiments were carried out at different ruthenium:AuNPs molar ratios. A titration experiment was performed, by keeping the same concentration of the luminophore (20  $\mu\text{M}$ ) and changing the concentration of the nanoparticles (0  $\mu\text{M}$ , 76.2  $\mu\text{M}$ , 127  $\mu\text{M}$  and 178  $\mu\text{M}$ ). **Figure 9** shows that the emission intensity of all the systems decreases with increasing mole ratio of AuNPs. This is also illustrated and quantified as quenching percentage (%) in **Figure 10**. However, the emission intensities shown in **Figure 9** were corrected for the “inner filter” effect that results from the plasmon absorption and emission absorbance. The equation (**Equation 3**) given by Albilson et al.,<sup>316</sup> was applied for the correction of this effect, where  $F_{\text{corr}}$  stands for the fluorescence after the correction,  $F_{\text{obs}}$  is the measured maximum fluorescence intensity,  $A_{\text{ex}}$  and  $A_{\text{em}}$  represents the absorbance at the excitation wavelength ( $\lambda_{\text{ex}}$ ) and maximum emission wavelength ( $\lambda_{\text{em}}$ ), respectively.

$$F_{\text{corr}} = F_{\text{obs}} \times 10^{(A_{\text{ex}} + A_{\text{em}})/2} \quad (3)$$

On the other hand, the Stern-Volmer plots (**Figure 9**) suggest that quenching increases proportionally to the AuNPs concentration. The Stern-Volmer approach is used as a powerful tool to elucidate the quenching phenomenon since it links the steady-state irradiation with the dynamical properties of the excited fluorophore as well as with its diffusional motion and interaction with the quencher molecule<sup>317</sup>. Moreover, the rate of quenching mediated by the quencher, as a function of its concentration in competition with its radiative decay or fluorescence intensity decrease can be studied<sup>318</sup>. The linearity of the plot provides information about the type of quenching that might be taken place. Deviations from linearity indicate a combination between dynamic and static quenching, therefore it can be a useful tool to get a better insight of the quenching process<sup>319</sup>. Applying the **Equations (2.1.-2.2.)** the Stern-Volmer quenching constant ( $K_{\text{SV}}$ ) and the quenching rate constant ( $K_{\text{q}}$ ) can be calculated, between the relative fluorescence intensity ( $I_0/I$ ) with low light excitation and quencher concentration. The fluorescence lifetime of the fluorophore/luminophore ( $\tau_0$ ),  $K_{\text{q}}$  can be calculated as shown below:

$$\frac{I_0}{I} = 1 + K_{SV}[Q] \quad 2.1$$

$$K_{SV} = \tau_0 K_q \quad 2.2$$

The values of  $K_q$  calculated for each luminophore in presence of different concentrations are presented in **Table 3**. The  $K_q$  obtained for the quenching experiments with the luminophores and AuNPs are very similar, however, the best linear relationship was found with the standard ruthenium complex ( $R^2=0.99$ ), suggesting that dynamic quenching had occurred<sup>311</sup>. The other two luminophores,  $[\text{Ru}(\text{bpy})_3\text{-NH}_2]^{2+}$  and  $[\text{Ru}(\text{bpy})_3(\text{phen})\text{-NH}_2]^{2+}$ , showed an inferior linear relationship ( $R^2=0.98$  and  $R^2=0.97$ , respectively), and deviations from the linearity suggested that static quenching is more likely to be occurring. Stern-Volmer approach is used to fit dynamic quenching, since it assumes that the excited state life-time of the luminophore does not change upon the presence of the quencher<sup>320</sup>. In fact, when static quenching occurs, and the relative lifetime ( $\tau_0/\tau$ ) is plotted against the quencher concentration, the relative lifetime value stays the same as the quencher concentration increases, whereas for dynamic quenching, this value linearly increases with the quencher concentration (**Figure 11C and D**)<sup>310</sup>. There have been many attempts have been done to fit static quenching with however during static quenching stoichiometries of the adduct that can be formed which adds a degree of complexity which might be considered to apply a model that considers all the conditions and parameters of the system<sup>312</sup>. In any case, further time-resolved fluorescence experiments testing different absolute concentrations of AuNPs would be needed to determine the type of quenching process occurs in the system. Nevertheless, this set of experiments successfully show the quenching effect of AuNPs in presence of the three luminophores.



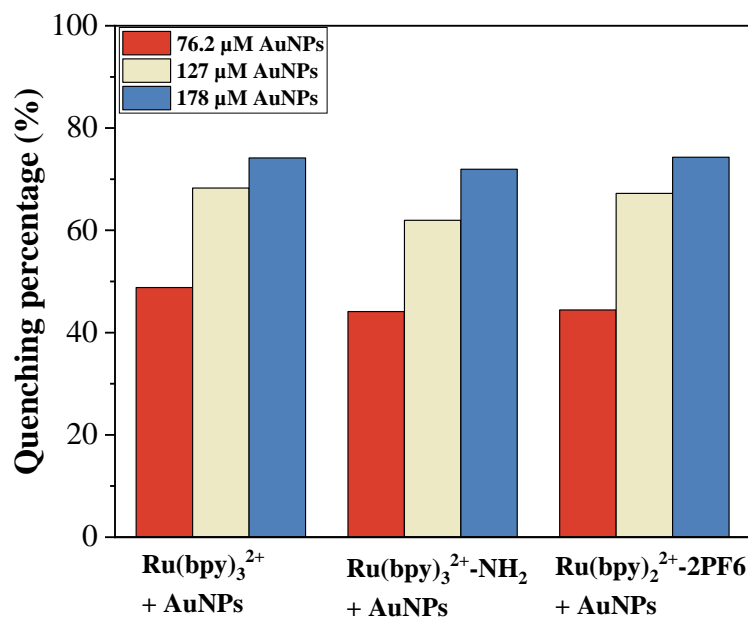


**Figure 10.** Quenching percentage of luminophores according to different concentrations of AuNPs (76.2  $\mu\text{M}$ , 127  $\mu\text{M}$  and 178  $\mu\text{M}$ ).

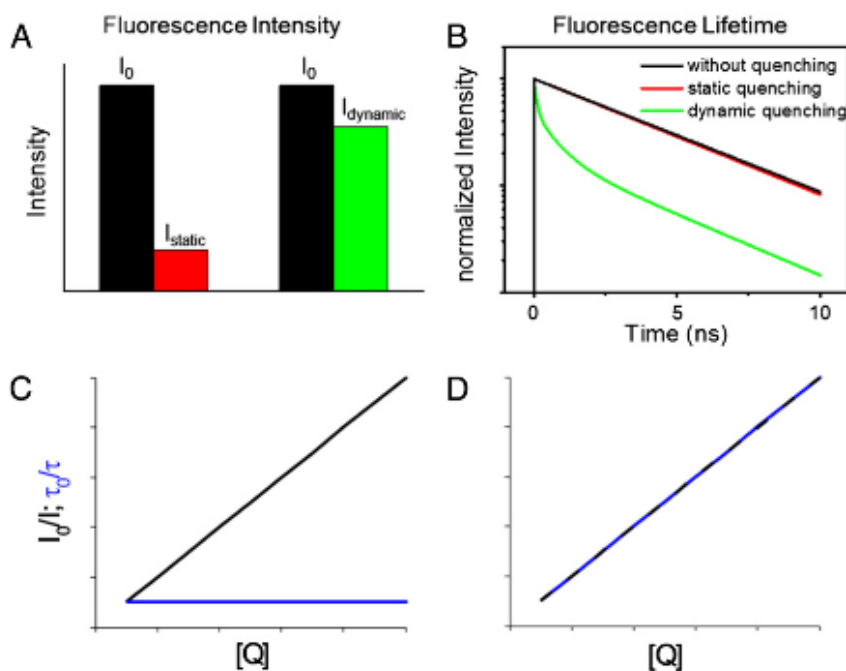
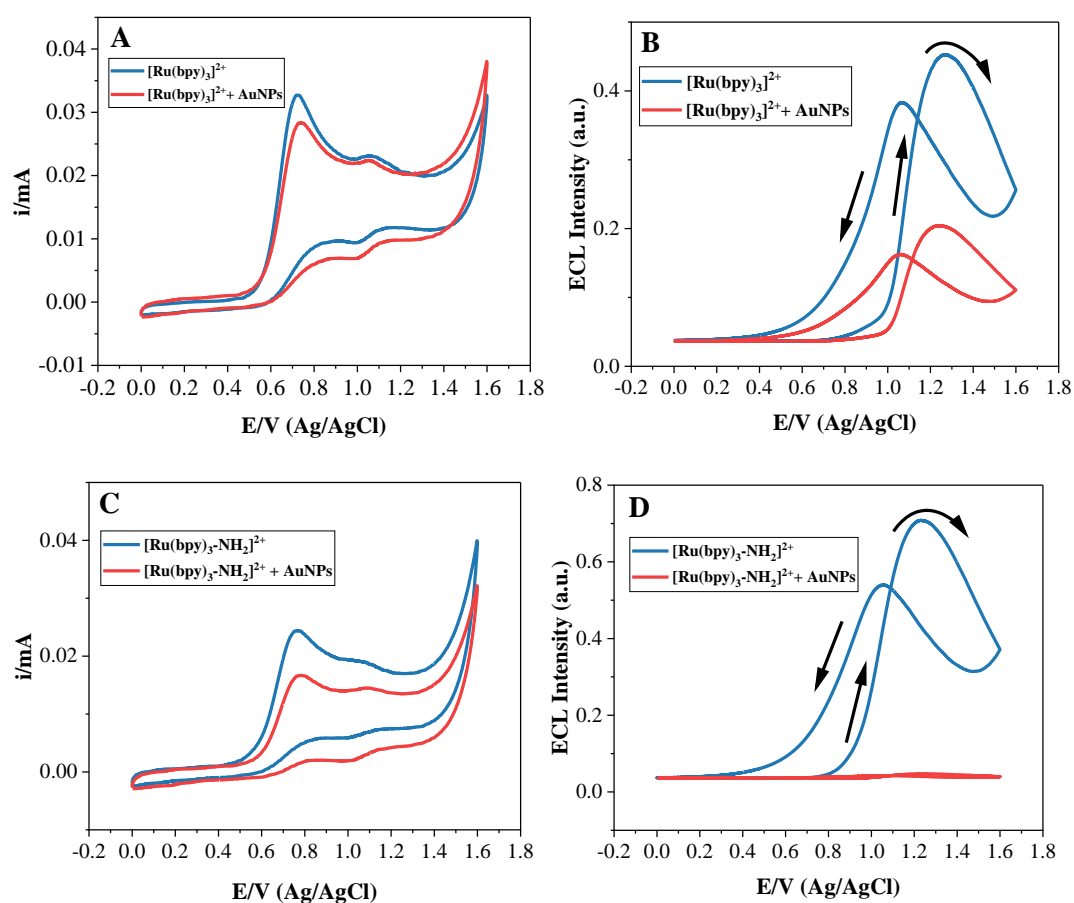


**Figure 11.** Illustration of differences of static and dynamic/collisional quenching by A) steady-state, B) time-resolved fluorescence spectroscopy. C) Stern-Volmer plot for static quenching. D) Stern-Volmer plot for dynamic quenching<sup>310</sup>.

### 3.1.3. ECL characterization

In this section, the ECL characterization of the luminophores is presented and discussed as well as how the AuNPs impact the response for the three ruthenium complexes. As described in **Chapter 2**, in order to generate an ECL signal, tripropylamine (TrPA) was used as a co-reactant. Glassy-carbon electrodes (GCE) were also chosen over other electrode materials since it shows low reactivity, good electrical conductivity and impermeability, characteristics that makes the very suitable for electroanalysis purposes<sup>321</sup>. In addition, lithium perchlorate (LiClO<sub>4</sub>) was chosen as the supporting electrolyte since other supporting electrolytes such as phosphate buffers (PBS) due to their ability to regulate the pH of the system can interfere with the co-reactants protonation and deprotonation process which have been reported to have an impact on the ECL intensities achieve<sup>322–324</sup>. In **Figure 12** it is shown the electrochemical and ECL characterization of the luminophores (scan-rate 0.1 V s<sup>-1</sup>) in the absence and presence of the AuNPs. A significant anodic peak is observed at approximately +0.6 V and +0.8 V, which can be attributed to the oxidation of TrPA on the electrode interface. However, for both standard ruthenium ([Ru(bpy)<sub>3</sub>]<sup>2+</sup>) and the ([Ru(bpy)<sub>3</sub>-NH<sub>2</sub>]<sup>2+</sup>) dye, two small anodic and cathodic peaks are observed around +1.0 V and +1.2V (respectively), which most likely correspond to the oxidation and reduction of the luminophores. The highest ECL light emission peaks were obtained for both complexes (see **Figure 12B and D**), where they also occurred around +1.0V and +1.3V. Although no redox process is observed for [Ru(bpy)<sub>3</sub>(phen)-NH<sub>2</sub>]<sup>2+</sup> in the voltammogram (**Figure 12F**), similar ECL was observed. The ECL emission produced in the systems using ruthenium complexes with TrPA as co-reactant, after applying an oxidative potential, deprotonates TrPA which reacts with e.g., [Ru(bpy)<sub>3</sub>]<sup>2+</sup> or additional [Ru(bpy)<sub>3</sub>]<sup>3+</sup> to form excited-state [Ru(bpy)<sub>3</sub>]<sup>2+\*</sup> (S<sub>1</sub>) which immediately decays to their ground state (S<sub>0</sub>) by emitting light throughout the process<sup>218,325,326</sup>. In addition, a hysteresis process is observed for all the three dyes, where the light emitted in the backward scan is more intense than that emitted at the forward scan. As explained in the previous chapter, hysteresis is a phenomenon that is influenced by many factors (e.g., scan-rate, type of co-reactant, electron transfer and etc), therefore is very difficult to elucidate the cause<sup>192,262</sup>. However, TrPA is not very soluble in LiClO<sub>4</sub>, forming a separate organic layer on top the solution, which might had hindered the ECL signal. For that, addition of phosphoric acid could improve the

solubility of the co-reactant<sup>327</sup>. Furthermore, as mentioned in the previous chapter. pH also plays an important role in the ECL signal enhancement therefore pH could be adjusted to more optimal conditions (pH=7.0-7.4) in order to achieve a higher signal<sup>218</sup>. In addition, the TrPA concentrations should also be considered since different pH levels would be needed to achieve a high a ECL intensity, however as shown by Parveen and et al., that upon high concentrations of TrPA (~0.1 M) side reactions could interfere with the ECL signal following a decrease in the intensity observed<sup>218,327</sup>. Therefore, several factors are influencing the ECL signal under the tested conditions.



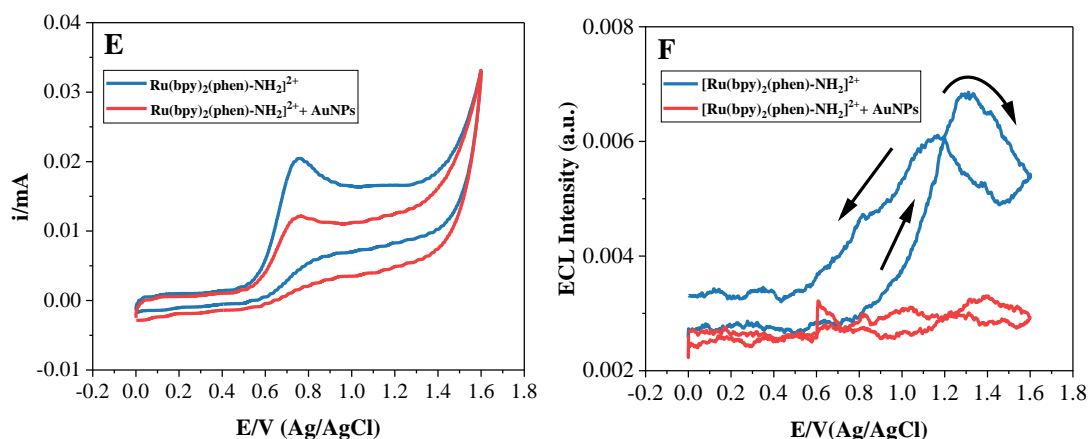


**Figure 12.** ECL characterization of 0.1mM luminophores without (black) and with 0.0254mM AuNPs (red) and 50mM of TrPA in 0.1M LiClO<sub>4</sub> as supporting electrolyte. A to B) [Ru(bpy)<sub>3</sub>]<sup>2+</sup>, C to D) [Ru(bpy)<sub>3</sub>-NH<sub>2</sub>]<sup>2+</sup> and E to F) [Ru(bpy)<sub>2</sub>(phen)-NH<sub>2</sub>]<sup>2+</sup>. Solvent: dH<sub>2</sub>O.

**Table 4.** ECL data of luminophores, relative ECL efficiency and calculated quenching percentage of AuNPs.

	Relative ECL efficiency* (%)	Quenching percentage with AuNPs (%)
[Ru(bpy) <sub>3</sub> ] <sup>2+</sup>	-	55.56
[Ru(bpy) <sub>3</sub> -NH <sub>2</sub> ] <sup>2+</sup>	163.2%	93.29
[Ru(bpy) <sub>2</sub> (phen)-NH <sub>2</sub> ] <sup>2+</sup>	16.59%	7.5

\*Relative ECL efficiencies were calculated taking [Ru(bpy)<sub>3</sub>]<sup>2+</sup> as the standard or reference.

It is important to know the ECL efficiency of each molecule in order to assess which of them is more suitable for the development of an ECL biosensor. Currently, ECL quantum efficiency ( $\Phi_{ECL}$ ) is usually reported relative to emissions obtained with [Ru(bpy)<sub>3</sub>]<sup>2+</sup>, where ECL intensity is integrated as the current (**Equation 3**)<sup>328,329</sup>:

$$\Phi_{ECL x} = \Phi_{ECL st} \frac{\left( \frac{\int ECL dt}{\int current dt} \right)_{st}}{\left( \frac{\int ECL dt}{\int current dt} \right)_x} \quad (3)$$

Bard et al., published in 1973 an absolute efficiency for [Ru(bpy)<sub>3</sub>]<sup>2+</sup>, 5-6%, in the annihilation pathway<sup>330</sup>, which has been accepted by the scientific community as a useful reference value. However, no absolute efficiency has ever been reported for an ECL system where a co-reactant was used<sup>329</sup>. In fact, [Ru(bpy)<sub>3</sub>]<sup>2+</sup> efficiency values are often

used regardless the concentration, type of supporting electrolyte, solution polarity or differences in testing conditions<sup>328,329</sup>. In the study conducted by Bard et al., acetonitrile was used as supporting electrolyte and a rotating ring-disk electrode (RRDE) of 1 mM  $[\text{Ru}(\text{bpy})_3]^{2+}$ , which only had led to poor comparisons and errors in efficiency calculations due to the lack of standardization between relative measurements<sup>328</sup>. Therefore, in this thesis, the results obtained with  $[\text{Ru}(\text{bpy})_3]^{2+}$  and TrPA as co-reactant are used as reference/standard for the calculation of the ECL efficiencies of the novel dye  $[\text{Ru}(\text{bpy})_3\text{-NH}_2]^{2+}$  and the commercial dye  $[\text{Ru}(\text{bpy})_2(\text{phen})\text{-NH}_2]^{2+}$ , since the experiments were carried out under the same conditions (i.e., same type of electrode, redox probe concentrations, supporting electrolyte and equipment.). However, due to the absence of redox peaks in the experiment perform with  $[\text{Ru}(\text{bpy})_2(\text{phen})\text{-NH}_2]^{2+}$ , calculations were carried out only considering the integrated ECL intensities of the luminophores relative to  $[\text{Ru}(\text{bpy})_3]^{2+}$ . The relative efficiencies calculated for each the two of the luminophores are shown **Table 4**. These values revealed that the novel  $[\text{Ru}(\text{bpy})_3\text{-NH}_2]^{2+}$  is 63% more efficient than the standard ruthenium complex, whereas  $[\text{Ru}(\text{bpy})_2(\text{phen})\text{-NH}_2]^{2+}$  is 83% less efficient, as it also comes apparent **Figure 12F**, showing a very low ECL intensity comparing with the other two complexes (**Figure 12B and D**). There are conflicting reports about the role of phenanthroline group in ruthenium complex ECL emission<sup>331</sup>. A study reported that the ECL efficiencies of  $[\text{Ru}(\text{bpy})_3]^{2+}$  with a wide range of co-reactants (N-methylpyridinium, aromatic amine, and quinone compounds) in acetonitrile were greater than for  $[\text{Ru}(\text{phen})_3]^{2+}$  complex<sup>332</sup>. However, in the study conducted by Kim and et al.,<sup>333</sup>, they attributed the intensity increase with the increase number of 1,10-phenanthroline ligands, suggesting that it shows slightly lower donor ability compared to 2,2'-bipyridine, causing the increase in the energy of the MLCT band, thus, reducing the efficiency of radiationless deexcitation processes<sup>331</sup>. Michael and et al., also reported that the ECL intensities of  $[\text{Ru}(\text{bpy})_2(\text{phen})]^{2+}$  and  $[\text{Ru}(\text{phen})_3]^{2+}$  were 253% and 85% of that observed for  $[\text{Ru}(\text{bpy})_3]^{2+}$  using codeine as co-reactant in acetate buffer (pH=4)<sup>334</sup>. Despite there are a large number of studies that report the high ECL emission of  $[\text{Ru}(\text{phen})_3]^{2+}$  and its derivatives for detection of a wide range of analytes<sup>335-338</sup>, they did not report a direct comparison with  $[\text{Ru}(\text{bpy})_3]^{2+}$  under the same conditions. Therefore, more comparative studies are needed to understand how the incorporation of phenanthroline groups affect the ECL emission under different system, since other parameters such as supporting electrolyte, pH of the solution and type of co-reactant play also an important role in the ECL process. Finally, experiments carried out in presence of

AuNPs revealed that ECL intensity emitted by the luminophores decreases as it can be observed in **Figure 12** as well as in the quenching percentage values reported in **Table 4**. It is noticeable that the  $[\text{Ru}(\text{bpy})_3\text{-NH}_2]^{2+}$  complex showed the largest quenching degree (93.26%) followed by  $[\text{Ru}(\text{bpy})_3]^{2+}$  (55.56%). The distance between luminophore and the plasmonic material strongly influences the quenching process in the ECL system. In fact, when the ECL emission sites are physically very close to the surface plasmons, these plasmons can quench the excited state but when somewhat further away (i.e., 10-15 nm) the ECL emission could be enhanced by the plasmonic effect of the AuNPs<sup>258,259,339</sup>. When the distance between an electron donor fluorophore/luminophore and an acceptor plasmonic material is less than 10 nm, a phenomenon called Förster Resonance Energy Transfer (FRET) can occur which can lead to non-radiative energy transfer between an electronically excited donor a ground state acceptor molecule<sup>339,340</sup>. This energy transfer can cause quenching since the excited electron is donated to AuNP<sup>287</sup>. The rate energy transfer is influenced by the spectral overlap of the emission of the donor with the absorption of the acceptor. For example, in this case, ruthenium complexes ( $\lambda_{\text{emission}} \sim 610$  nm) and AuNPs ( $\lambda_{\text{max}}=518$  nm), have a very well defined spectral overlap, which could explain the quenching effect of AuNPs on the luminophores<sup>341,342</sup>. However, as mentioned above, factors such as distance between the two components also have an impact on the rate energy transfer, which can explain the quenching effect observed<sup>342</sup>. Research carried out with metallopolymer  $[\text{Ru}(\text{bpy})_2\text{PVP}_{10}]^{2+}$  and 4-(N, N'-Dimethylamino) pyridine (DMAP) protected AuNPs showed that the ECL emission was not affected by the presence of AuNPs, however at high concentrations of AuNPs, the ECL light was quenched<sup>342</sup>. In that study it was suggested that the presence of DMAP coated AuNPs provides higher conductivity overcoming the quenching effect mediated by the particles, specifically at low AuNPs:Ru molar ratio ( $< 6.0 \times 10^{-3}$ ), for particles with a diameter smaller than 12.5 nm. In the study published by Tejada et al., the ECL quenching effect of tiopronin stabilized AuNPs on  $[\text{Ru}(\text{bpy})_3]^{2+}$  was also investigated. The atomic force microscopy (AFM) results revealed that upon  $[\text{Ru}(\text{bpy})_3]^{2+}$  addition in solution, AuNPs aggregates were formed, increasing the turbidity of the sample, suggesting that it could also hinder the ECL light collection. Additionally, both static and dynamic quenching were also reported as one of the sources of ECL light quenching, however, it is not fully determined at which level both sources might be impacting on the quenching phenomena. Nevertheless the study observed that diluting the concentration of AuNPs ( $> 5 \times 10^{-8}$  M), ECL intensity of the luminophore increased while decreasing

the number of aggregates ( $8.6 \pm 0.9$  nm and  $3.7 \pm 0.6$  nm of diameter for  $8.0 \times 10^{-8}$  M and  $1.0 \times 10^{-8}$  M, respectively)<sup>339</sup>.

The aggregation of AuNPs in presence of the dyes might explain why  $[\text{Ru}(\text{bpy})_3]^{2+}$  shows less quenching degree upon the AuNPs addition, when compared to  $[\text{Ru}(\text{bpy})_3\text{-NH}_2]^{2+}$ , since  $[\text{Ru}(\text{bpy})_3\text{-NH}_2]^{2+}$  seems to show high affinity for gold, forming more complexes/aggregates (see DLS values in **Table 2**), resulting in static quenching. On the other hand,  $[\text{Ru}(\text{bpy})_2(\text{phen})\text{-NH}_2]^{2+}$  showed only a 7.5% of quenching, however, as it was mentioned above, the ECL intensity achieved with the dye was significantly smaller than the other two luminophores therefore, the results obtained were expected. In conclusion, the results obtained in this section agree with what have been previously reported under a ECL different system, and ruthenium (II) complexes, where it have been observed a similar quenching effect mediated by the AuNPs in proximity with the luminophores<sup>287,288,343</sup>. However, further research is needed to understand better the quenching phenomenon (both static and dynamic) on a ECL system in order to design highly sensitive biosensing platforms.

### **3.2. DNA probe conjugation: $[\text{Ru}(\text{bpy})_3\text{-NH}_2]^{2+}$ and $[\text{Ru}(\text{bpy})_2(\text{phen})\text{-NH}_2]^{2+}$**

#### **3.2.1. UV-Vis and fluorescence characterization**

One of the objectives of this thesis is to develop a DNA probe labelled with a ruthenium dye and both  $[\text{Ru}(\text{bpy})_3\text{-NH}_2]^{2+}$  and  $[\text{Ru}(\text{bpy})_2(\text{phen})\text{-NH}_2]^{2+}$  were investigated, by exploiting the amino group for biomolecule conjugation. The luminophores were conjugated according to the protocol explained above and UV-Vis, steady-state and time-resolved emission spectroscopy were performed. First, the UV-Vis results (**Figure 13**) showed that DNA was effectively conjugated to the luminophores, leading to an absorbance peak at 460 nm and 451 nm associated with the binding of  $[\text{Ru}(\text{bpy})_3\text{-NH}_2]^{2+}$  and  $[\text{Ru}(\text{bpy})_2(\text{phen})\text{-NH}_2]^{2+}$ , respectively. These values are slightly shifted compared to the values obtained for the unconjugated luminophores (see **Figure 14**). The emission of the conjugated dyes was also shifted compared to the free dyes (see **Table 3** and **Table 5**). This shift in excitation and emission ( $\sim 8$  and 10 nm), is not significant considering the peak shapes and most likely reflects changes in the local microenvironment of the metal

complex as well as changes in its electron density. Moreover, it is well known that  $[\text{Ru}(\text{bpy})_3]^{2+}$  as a cation, can electrostatically interact and associate with the negatively charged backbone of double-stranded (dsDNA) and single-stranded DNA (dsDNA and ssDNA, respectively) however less efficiently to this last one<sup>129,344</sup>. Therefore, it is possible that the covalently linked metal complex may also interact electrostatically with the negative<sup>345</sup>.

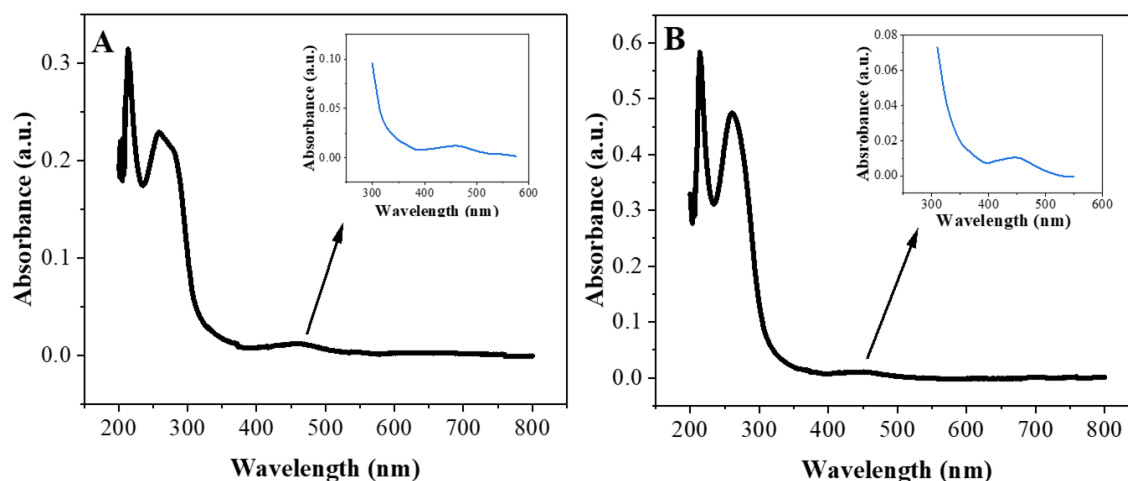


**Figure 13.** Absorbance spectra of Ru luminophores conjugated to DNA (purified samples). A)  $[\text{Ru}(\text{bpy})_3\text{-NH}_2]^{2+}$  and B)  $[\text{Ru}(\text{bpy})_3(\text{phen})\text{-NH}_2]^{2+}$ . Insets represents a close-up from 300 nm to 600 nm. Solvent:  $\text{dH}_2\text{O}$ .

Attempts were made to measure the excited lifetimes of the conjugated luminophores but due to the low optical density of the samples ( $\sim 0.01$  a.u. at  $\lambda_{\text{max}} \sim 450$  nm) this proved impossible. Instead, the crude material (nucleic acid: ruthenium ratio 100:1) prior to purification was used directly without purification and **Figure 15** shows the results obtained. The excited lifetime measure for the conjugated  $[\text{Ru}(\text{bpy})_3\text{-NH}_2]^{2+}$  is shorter ( $\tau_1 = 509$  ns) than the one obtained for the no conjugated luminophore ( $\tau_0 = 639$  ns) (see **Table 3** and **Table 5**) (fitting of the data was performed as described in the previous section, showing a good fit,  $R^2=0.99$ ). Same occurs with the excited lifetime value for conjugated  $[\text{Ru}(\text{bpy})_2(\text{phen})\text{-NH}_2]^{2+}$ , since it was shorter than the one recorded for the luminophore alone ( $\tau_1 = 622$  ns and  $\tau_0 = 716$  ns, respectively (**Figure 15**)). The changes in the optical properties of the luminophores could be explained by the conjugation to ssDNA if all ruthenium molecules were successfully conjugated since DNA was in excess. Nevertheless, a long-lived component was obtained for both conjugated dyes,  $\tau_2$



=1460 ([Ru(bpy)<sub>3</sub>-NH<sub>2</sub>]<sup>2+</sup>) and  $\tau_2$  =1073 ([Ru(bpy)<sub>2</sub>(phen)-NH<sub>2</sub>]<sup>2+</sup>), being the 13.88% and the 10.55% of the signal. The appearance of two separate lifetimes (longer and shorter-lived components) suggest that there's an interaction between the luminophores and the DNA that has been previously attributed to non-covalent binding, i.e., electrostatic interactions and/or intercalation of free luminophore with DNA in case of phenanthroline containing ruthenium (II) complexes<sup>129</sup>. This could suggest that some ruthenium remained “free” in the solution, which could possibly electrostatically interact with the negative backbone of the ssDNA. For example, in the study conducted by Kobayashi and et al., two forms of [Ru(phen)<sub>3</sub>]<sup>2+</sup> were tested with dsDNA, and the long-lived component ( $\tau$  = 1520 ns and 1620 ns) was observed to be > 70% of the signal which was attributed to intercalation of the luminophores in the dsDNA. Therefore, it is possible that a small fraction of unconjugated fraction of ruthenium might have interacted with the ssDNA in solution. It is known that phenanthroline and bipyridine ligands have significantly less intercalation depth than the classic dipyridophenazine (dppz) ligand used in ruthenium (II) complexes as an intercalating agent in dsDNA<sup>289,346–348</sup>, therefore cause of the appearance of a longer second lifetime could be attributed to an electrostatic interaction of “free” [Ru(bpy)<sub>3</sub>-NH<sub>2</sub>]<sup>2+</sup> and [Ru(bpy)<sub>2</sub>(phen)-NH<sub>2</sub>]<sup>2+</sup> with the negative backbone of ssDNA. Even if and -NH<sub>2</sub> provides the advantage of reducing the number of reagents/steps during the labelling process, the conjugation efficiency and the purification of the probe remains a challenge since high control of the pH solution is required. Groups such as -COOH, provide a higher efficiency while preventing the electrostatic interactions between the luminophore and the DNA probe, which would lead to an easier purification of the sample.

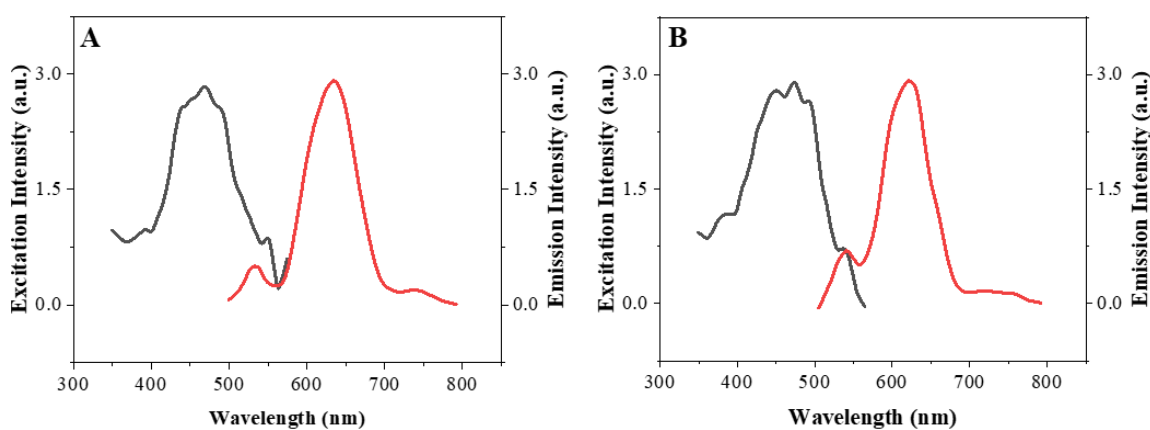


**Figure 14.** Emission spectra of purified and no purified Ru-DNA conjugated probes. A) No purified sample and B) purified sample. Excitation wavelength ( $\lambda=455$  nm). Solvent: dH<sub>2</sub>O.

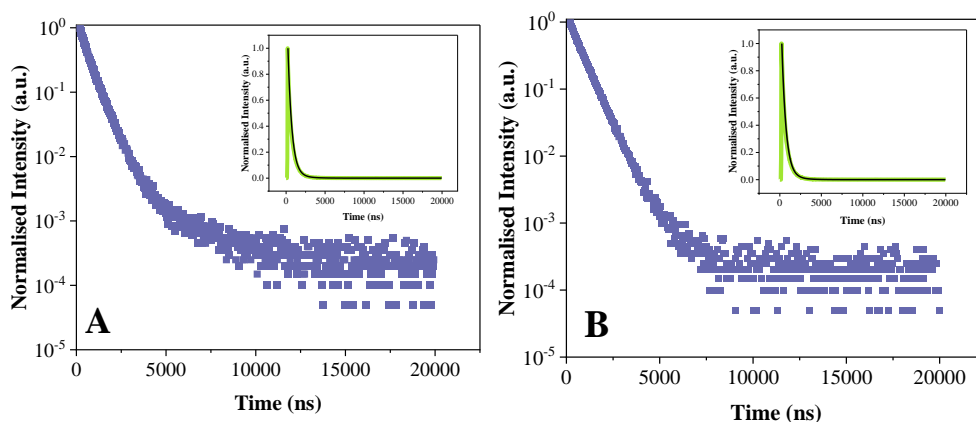


**Figure 15.** Semi-log plots vs. time of the fluorescence life- time of DNA conjugated to [Ru(bpy)<sub>3</sub>-NH<sub>2</sub>]<sup>2+</sup> not purified (A) and DNA conjugated to [Ru(bpy)<sub>3</sub>(phen)-NH<sub>2</sub>]<sup>2+</sup> (B). Logarithmic Y-axis vs. time linear. Each decay was normalised to the maximum number of photons obtained for that recording. Excitation of the laser wavelength ( $\lambda=375$  nm). Solvent: dH<sub>2</sub>O. Inset: Normalised decay experimental curves (green) and fitted curve (black), linear Y-axis vs. time linear.

**Table 5.** Fluorescence data (steady-state and time-resolved spectroscopy) of DNA conjugated luminophores. The luminescent lifetimes were fitted with a  $\chi^2$  between 1.0 and 1.6.

	$\lambda_{\text{excitation}}$ (nm)	$\lambda_{\text{emission}}$ (nm)	$\tau_1$ and $\tau_2$ (ns)*
[Ru(bpy) <sub>3</sub> -NH <sub>2</sub> ] <sup>2+</sup>	468	636	509 and 1406
[Ru(bpy) <sub>2</sub> (phen)-NH <sub>2</sub> ] <sup>2+</sup>	473	623	622 and 1073

\*Excited state lifetime of non-purified samples.

## 4. CONCLUSIONS

In this chapter, three ruthenium (II) complexes were investigated to understand their photophysical properties and to gain insights into their applicability for use in an SPR-ECL biosensing system. Three of the luminophores were optically and electrochemically characterised in AuNPs containing aqueous systems in order to understand more about their interaction and impact on fluorescence and ECL intensities as well as excited state lifetimes. The data suggest that different quenching process (static or dynamic) may predominate depending on the luminophore. According to the zeta-potential values,

luminophores containing an amino moiety ( $[\text{Ru}(\text{bpy})_3\text{-NH}_2]^{2+}$  and  $[\text{Ru}(\text{bpy})_2(\text{phen})\text{-NH}_2]^{2+}$ ) induce a higher AuNPs aggregation, due to its ability to bind to the gold surface. Steady-state fluorescence results, the Stern-Volmer plots and the ECL characterization confirm the effective quenching mediated by the addition of AuNP. This results alongside excited state lifetime values suggest that static quenching is more likely to happen when luminophores containing amino group are used, whereas dynamic quenching is predominant for  $\text{Ru}(\text{bpy})_3^{2+}$ . However, as it was mentioned above, interpretation of quenching data is difficult and more experiments would be needed (i.e., measurement of lifetimes upon different concentrations of AuNP) to fully understand the source of the quenching effect in each system. On the other hand, ECL experiments show that the novel dye,  $[\text{Ru}(\text{bpy})_3\text{-NH}_2]^{2+}$ , is more efficient than the commercial dye  $[\text{Ru}(\text{bpy})_2(\text{phen})\text{-NH}_2]^{2+}$ , which makes it a potential and suitable candidate for the development SPR-ECL biosensor. In fact, both luminophores were effectively conjugated to ssDNA, demonstrating that both could be used as a label. Both dyes emission shifted after conjugation, which suggests that not only covalent binding to NHS-ester terminated DNA occurred, but also possible electrostatic interaction with the negative backbone of the strand might had taken place. Finally, given the obtained results,  $[\text{Ru}(\text{bpy})_3\text{-NH}_2]^{2+}$  seems to display the most optimal properties for the development of a SPR-ECL assay for bacterial DNA as will be shown in the following chapter.

**Chapter 4:**  
**ECL detection of bacterial DNA from  
UTI causing *Escherichia coli* using  
AuNPs deposited on glassy carbon  
electrodes**

## 1. INTRODUCTION

Urinary tract infections (UTIs) are common infections with approximately 400 million cases world-wide annually (2019)<sup>349</sup>, with high social costs and in some cases, they can be life threatening by resulting in acute renal failure in healthy individuals as well as in renal transplant patients<sup>350,351</sup>. Furthermore, it is estimated that 40% of women develop at least one UTI in their lifetime and 11% of women over 18 years old have one infection per year<sup>352</sup>. It has been recently reported that over the 50% of the antibiotics are either incorrectly prescribed or not necessary, which is increasing the incidence of antibiotic resistant bacteria and leading to persistent infections<sup>353,354</sup>. In fact, the wide range of virulence factors present in multi-antibiotic resistant strains provokes the strong pathogenicity and resistance of UTI causing pathogens<sup>355</sup>. This is very concerning, especially in healthcare environments (i.e., hospitals and nursing homes) since catheter-caused UTIs are leading to serious complications such as sepsis, bladder stones and endotoxic shock<sup>356</sup>. In fact, in only 2019, UTIs caused around a quarter of a million deaths, and contributed to 5.2 million disability-adjusted life years worldwide<sup>349</sup>. Therefore, there is a strong motivation to develop systems capable of early detection that can help to control and prevent life-threatening complications caused by UTIs.

Commonly, UTIs are caused by *Escherichia coli* (*E. coli*), which are a group of bacteria commonly found in human and animal microbiota, especially located in digestive tracts<sup>357</sup>. Ureopathogenic *E. coli* (UPEC) are responsible of more than 80% of the UTIs, since they rapidly adapt to the urinary tract and their concentration can reach more than 100,000 CFU/mL<sup>353</sup>. These bacteria's genomes contain a wide range of genes that code for virulence factors that provide pathogenic traits and promote the growth of biofilms causing an infection that is challenging to treat<sup>358</sup>. In the case of a UTI, bacterial attachment to the epithelial cells in the urinary tract is mediated by proteins called adhesins, which bind to host cell receptors<sup>353,359</sup>. This attachment provides mechanical resistance to bacterial cells against the elimination by the flow of urine and bladder emptying, increasing the persistence of the *E. coli*. Among all the adhesins that UPEC strains produce, type 1 fimbriae (FimH protein, encoded by *fimH* gene), is determinant for the tropism for the urinary tract receptors, which are essential for recognition and attachment to urinary tract receptors and allow the biofilm to grow<sup>360</sup>. It has been recently shown that the FimH protein also mediates the adhesion to immune system's predators

such as macrophages, which hampers the elimination of UPEC since they can replicate within the predator and grow a biofilm<sup>361,362</sup> (see **Figure 1**). Type 1 fimbriae accounts for more than 95% of the total *E. coli* virulence factor causing UTIs and is highly conserved in UPEC<sup>363</sup>. Therefore, considering the critical role of *fimH* gene, it could be a useful biomarker for rapid-detection based of UPEC bacteria<sup>360,364</sup>.

The current procedure for the diagnosis of UTIs is based on isolation and quantification of bacteria strains on agar plates followed by their microbial identification, taking between 18 and 30 hours to perform the whole process<sup>365</sup>. Other techniques such as PCR, have also been successfully used, but it requires very expensive equipment and high-qualified personnel which increases the cost significantly<sup>366</sup>. Furthermore, point of care diagnosis could reduce the incidence of antibiotic resistant UTI causing pathogens and rapidly improve the efficacy of the treatments prescribed<sup>367</sup>. Therefore, there is a high demand for the development of cost-effective detection methods to target pathogens in a selective and sensitive way<sup>368</sup>.

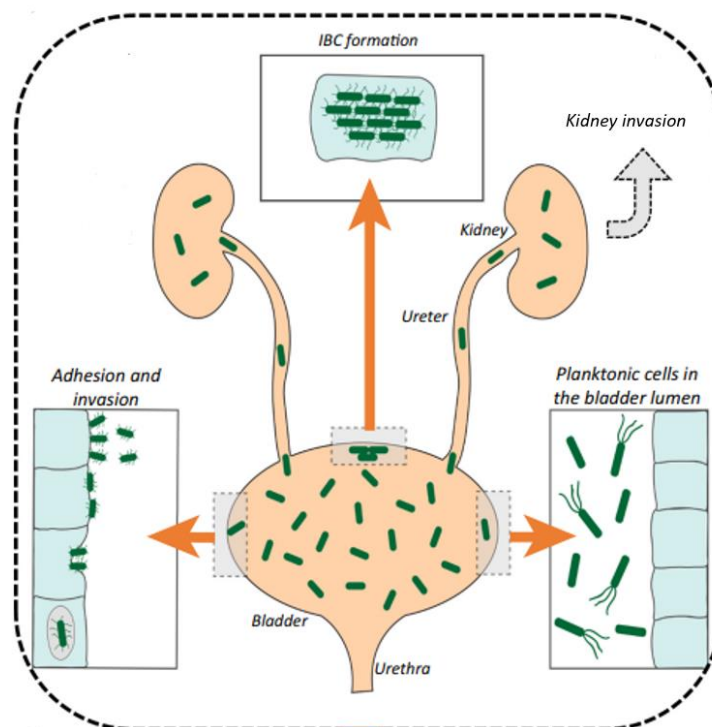


**Figure 1.** Overview of UPEC infection in the urinary tract system. Modified from Lo et al<sup>362</sup>.

Electrochemical biosensors, as reviewed in **Chapter 1**, have become very popular in point of care detection of pathogens since they provide faster detection, low-cost

platforms, they require small sample volumes and minimal pre-treatment<sup>11,368</sup>. Among the different type of biosensors, DNA based electrochemical biosensors are an attractive choice for pathogen detection because of their low detection limits, wide linear dynamic ranges and high reproducibility<sup>369</sup>. Furthermore, nanomaterials such as gold nanoparticles (AuNPs) can be used as a supporting matrix to enhance the signal-to-noise ratio and carry out high-performance electrochemical detection/analysis<sup>8</sup>. Moreover, using gold nanostructures increases the surface area, biocompatibility and stability of the platform<sup>370</sup> and can enhance the analytical performance. AuNPs can be used to optimize platforms such as glassy carbon electrodes (GCE) for biosensing purposes<sup>218</sup>. GC is a sp<sup>2</sup>-hybridized carbon material that has been widely used in electrochemistry as an electrode material<sup>371</sup>. GC meets all the requirements for electrode materials which include favourable redox response to the analyte, fast and reversible electron transport with little fouling, it provides a wide potential window and it's easy to clean among other properties<sup>372</sup>. However, the surface of GCEs needs to be activated/modified if functionalization with biomolecules is required<sup>373</sup>. In this case, AuNPs can act as anchor points for thiolated DNA capture strands and the nanostructures can enhance electrochemical and electrochemiluminescence responses compared to both unmodified GC or Au electrodes. For example, each deposited Au particle can act as a small electrode, which improves transport of the target to the electrode surface by radial diffusion<sup>374</sup>. Furthermore, as discussed in **Chapter 3**, their unique optical properties make them ideal for the development of electrochemiluminescent (ECL) biosensor<sup>375</sup>. In recent years, the combination of surface plasmon resonance (SPR) and ECL in a single instrument has been investigated, which had shown good properties for the improvement of the performance of the biosensors<sup>22,259</sup>. Moreover, AuNPs have been successfully implemented in such systems since their plasmon can be activated by the incident light emitted by luminophores which can enhance the ECL emission, and overall improve the performance of the assay<sup>259,376</sup>.

Here, AuNPs coated GCEs for ECL *fimH* sequence detection of UTI causing *E. coli* are investigated using the amino modified ruthenium complex ( $[\text{Ru}(\text{bpy})_3\text{-NH}_2]^{2+}$ ) for a DNA sandwich assay (capture, target, and probe sequences). A particular focus is on the SPR-ECL effect as a proof-of-concept (**Figure 2**). Also, two different co-reactants are assessed (tri-n-propylamine and N-butyldiethanolamine) to optimise the performance of the bioassay. Cyclic voltammetry (CV) is used as technique for electrodeposition of AuNPs

and both CV and electrochemical impedance spectroscopy (EIS) are used for the characterization of the platform.

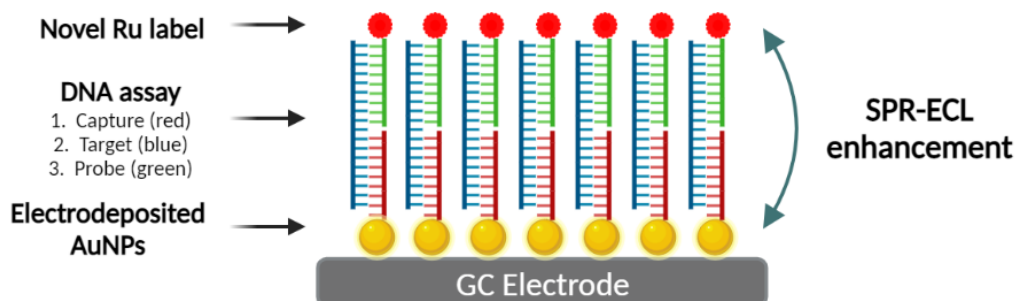


**Figure 2.** Schematic and simplified illustration of the SPR-ECL based biosensor developed for the detection of *fimH* gene of ureopathogenic *E.coli*.

## 2. MATERIALS AND METHODOLOGY

### 2.1. Chemical reagents

The electrochemical characterization was performed using two different supporting electrolytes, lithium perchlorate ( $\text{LiClO}_4$ ) and phosphate buffered saline (PBS). Two redox probes were used, ferrocenemethanol (FcmMeOH) and the redox couple composed of potassium ferricyanide ( $\text{K}_3\text{Fe}(\text{CN})_6$ ) and potassium ferrocyanide ( $\text{K}_4\text{Fe}(\text{CN})_6 \cdot 3\text{H}_2\text{O}$ ), tri-n-propylamine (TrPA) ( $\geq 98\%$ ) and N-butyldiethanolamine (NBEA) ( $\geq 98.6\%$ ) were used for electrochemiluminescent characterization. For the electrodeposition of gold nanoparticles, tetrachloroauric(III) acid ( $\text{HAuCl}_4 \cdot 3\text{H}_2\text{O}$ ) ( $\geq 99.9\%$ ) was used with sodium nitrate ( $\text{NaNO}_3$ ) as supporting electrolyte. All the reagents mentioned above were purchased from Merck. The DNA sequences, the TE buffer and the nuclease free deionized water ( $\text{dH}_2\text{O}$ ) were purchased from Integrated DNA Technologies (IDT). The 6-Mercapto-1-hexanol (MCH) for DNA co-immobilization was purchased from Merck. The amino modified ruthenium (II) complex<sup>291</sup>,  $[\text{Ru}(\text{bpy})_3\text{-NH}_2]^{2+}$  was provided by Dr. Yann Pellegrin of the University of Nantes.



## 2.2. Electrochemical and electrochemiluminescent (ECL) experiments

Glassy-carbon disk electrodes (GCE) and gold disk electrodes were used as working electrodes (3 mm and 2 mm diameter, respectively), Ag/AgCl as reference and platinum wire as counter electrode (all purchased from IJ Cambria). For electrochemical characterization both Cyclic Voltammetry (CV) and Electrochemical Impedance Spectroscopy (EIS) were performed using CH Instrument Model 760E workstation. Separately, experiments for electrochemiluminescence detection, were carried out in CH Instrument Model 760B workstation, an Oriel 70680 photomultiplier tube (PMT) biased at  $-850\text{V}$  along with a high-voltage power supply (Oriel, Model 70705) and an amplifier/recorder (Oriel, Model 70701) as it was shown in previous chapters. PMT gain was set at  $10^9$  for the experiments performed with TrPA and at  $10^8$  for the experiments with NBEA.

## 2.3. Sequence selection

As mentioned previously, the gene *fimH* was selected as candidate for detection of urepathogenic *E. coli*. The *fimH* gene sequence from *Escherichia coli* strain ATCC 35218 was downloaded from Nucleotide RefSeq database<sup>377</sup> in order to choose the target sequence. From a 903 bp coding sequence, 30 bp sequence with a length of  $\sim 10$  nm (each nucleotide has a length of 0.34) was randomly selected. This sequence was plotted in BLAST (a wide genome database where the introduced sequence can be compared with other sequences in the database) and analysed for possible similarities and presence of the same sequence in different bacteria. The output was satisfactory since this sequence was only found in strains of *E. coli*, all ureopathogenic strains. This shows that the gene, and selected sequence are very specific for UTI causing *E. coli*.

## 2.4. Electrode preparation and modification steps

The electrodes were prepared by polishing using  $0.05\ \mu\text{m}$  alumina with Milli-Q water on a polishing microcloth (IJ Cambria). The electrodes were rinsed with water and sonicated in 70% ethanol solution for 10 min to remove any impurities and residual alumina. The

electrodes were rinsed again with Milli-Q and dried under nitrogen at low stream. For AuNPs electrodeposition, the GCE were immersed in a 3 mM H<sub>2</sub>AuCl<sub>4</sub> and 0.1M NaNO<sub>3</sub> solution and cycled for 12 scans (6 cycles) at 0.05 V s<sup>-1</sup> from 0V to +0.9V. The surface activation of the AuNPs on the electrode surface was performed by immersing the electrodes in 0.5 M H<sub>2</sub>SO<sub>4</sub> solution and scanning from 0 V to +1.6 V at 0.1V s<sup>-1</sup> to form, and subsequently remove, an oxide monolayer on the surface of the gold nanoparticles. Then the AuNPs coated electrodes were rinsed with Milli-Q and dried again under nitrogen at low stream.

The capture ssDNA and MCH were co-immobilized on the AuNPs coated GCE. First, 1 μL of 10 mM TCEP stock solution was mixed with 99 μL of 100 μM of capture DNA (**Table 1**) (for SH- activation) and incubated at room temperature (25°C) for 2 hours. For co-immobilization, 10 μL of previous solution were taken and mixed with 5 μL of 10 mM MCH stock solution and 85 μL of TE buffer to achieve 1:5 of DNA/MCH ratio (10 μM and 50 μM, respectively). 10 μL of the DNA/MCH solution was placed as a single drop on the electrode surface and it was incubated for 1 hour and 30 mins at room temperature (25°C). After incubation the electrodes were washed with TE buffer and dried under the nitrogen stream. For the sandwich assay and target sequence electrochemical detection, a 10 μL drop containing 25 μM of ssDNA target (**Table 1**) was place on top of the electrodes and incubated at 37°C for 2 hours. After, the electrodes were wash with buffer and dried again. The ssDNA probe labelled with [Ru(bpy)<sub>3</sub>-NH<sub>2</sub>]<sup>2+</sup> was used for ECL detection of the target. For the development of the probe a shorter sequence (see **Table 1**) was used than the one from the previous chapter, although the labelling protocol was the same (see **Chapter 3**). Purification of the probe was not possible due to the low molecular weight of the DNA sequence and the lack of access to a temperature-controlled centrifuge. As before, 10 μL of the ssDNA probe containing sequence was drop cast on the electrodes and incubated at 37°C for 2 hours, washed with buffer to remove any free ruthenium and unhybridized DNA, and dried under nitrogen stream. The result of each modification step was characterized by CV, EIS and ECL.

**Table 1.** Sequences of single-stranded DNA used in the bioassay for detection of gene *fimH*.

Type	Sequence
Capture ssDNA	5'-TATAGTTGTTGGTCT-SH-3'
Target ssDNA	5'AGACCAACAACACTATAACAGCGATGATTTCC-3'
Probe ssDNA	5'-Azide-GGAAATCATCGCTGT-3'

### 3. RESULTS AND DISCUSSION

#### 3.1. Electrodeposition of AuNPs and electrochemical characterization

Surface modification with metallic particles can bring several benefits such as an increased surface area (larger signal and greater dynamic range), better catalytic and conductive properties, and mass transport enhancement, leading to improved performance for electro and bioanalysis<sup>221</sup>. In **Figure 3A** the voltammogram for the AuNPs electrodeposition on GCE is shown. In the first forward scan (**Figure 3B**), when the cell is switch on at 0.0 V, a large reduction current is observed, which is associated with the reduction of Au (III) to Au (0) (see **Equation 1**)<sup>374</sup>, followed by an oxidation current around +0.7 V which is likely to be oxide formation on the electrodeposited gold. For the backward scan, the reduction current around +0.6 V was observed to be higher than the forward one. Following the thermodynamics principles, this suggest an easier growth of AuNPs is taking place due to the already existent AuNPs on GCE, since AuNPs nucleation on a bare GC surface requires more energy than on gold<sup>378,379</sup>. In the following cycles, this peak is shifted to slightly more positive potentials, which reinforces the hypothesis that AuNPs electrodeposition is occurring on top of the already existing AuNPs<sup>221</sup>.



The protocol for the electrodeposition followed was the same as the one used by Zakaria and et al.,<sup>374</sup>. In their study, different supporting electrolytes were compared to investigate their effect on the morphology and size of the AuNPs deposited via cyclic voltammetry. The study reported that using NaNO<sub>3</sub>, smaller AuNPs (~ 60 nm) are achieved. This is

highly desirable for a NPs based biosensor, since the smaller the size of the particle, the larger is the surface area for a fixed quantity of gold deposited, meaning that more capture biomolecules can be immobilized, and enhance the sensitivity of the platform<sup>380</sup>. Furthermore, it has been previously reported that the presence of NaNO<sub>3</sub>, create a more homogeneous AuNPs films favouring their nucleation and growth, since the presence NO<sub>3</sub><sup>-</sup> avoids the coalescence (aggregation) of particles<sup>221,381</sup>. SEM characterization of the AuNPs coated GCE was attempted, however, due to the small size of the particles no successful images were achieved. This means that the particles were probably smaller than the ones achieved by Zakaria and et al, probably due to the fact that the scan rate use for the electrodeposition of AuNPs on GCE in this thesis was 0.05 Vs<sup>-1</sup> while in their study 0.025 V s<sup>-1</sup> was used. It has been shown that the parameters such as scan rate and number of cycles have an effect on the size and thickness of the AuNPs layer deposited<sup>382,383</sup>.

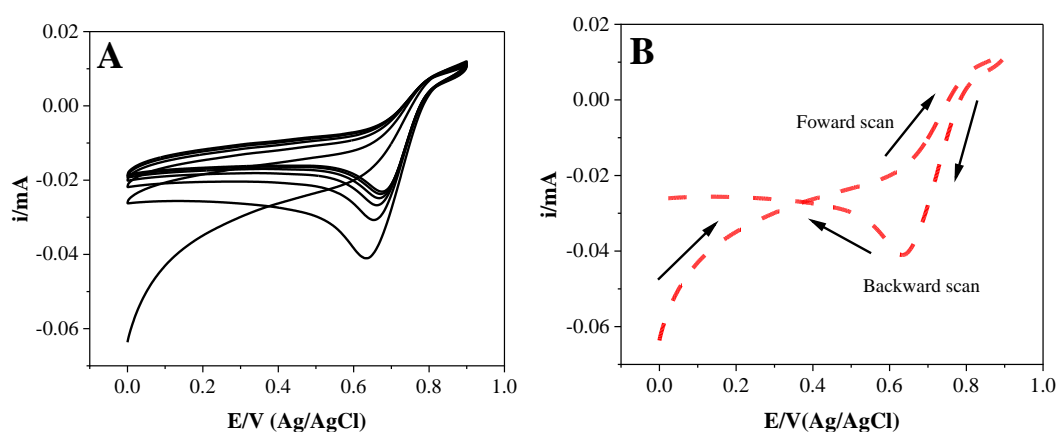


**Figure 3.** Voltammograms of AuNPs electrodeposition using 3 mM HAuCl<sub>4</sub> and 0.1 M NaNO<sub>3</sub> as supporting electrolyte (pH solution ~ 3) using GCE area 0.071 cm<sup>2</sup>. A) Scanning from 0 V to +0.9 V for 6 cycles, scan rate 0.05 V s<sup>-1</sup>. B) First cycle of the electrodeposition process (forward and backward scan).

As a first characterization step, the AuNPs modified GCEs were cycled for surface activation in 0.5 M H<sub>2</sub>SO<sub>4</sub> aqueous solution, scanning from +0 V to +1.6 V at 0.1 V s<sup>-1</sup>. As it can be observed in the voltammogram with 0.1M H<sub>2</sub>SO<sub>4</sub> (**Figure 4**), the modified electrodes show a very similar redox behaviour to a conventional gold disk electrode (2 mm diameter). The several oxidation peaks observed from +1.1 V to +1.3V, when compared to Au electrode (+1.3 V), probably are caused by the presence of different

crystallographic faces<sup>221</sup> and different Au “oxides” due to the complicated sorption process of OH<sup>-</sup> ions onto different. However, the reduction peaks occur at the same potential (+0.82 V), which correspond to the reduction of the oxides formed in previous anodic scan. The electroactive area ( $A$ ) was calculated using the theoretical charge ( $Q_{\text{theo}}$ ) associated with gold ( $390 \mu\text{C cm}^{-2}$ ) and the experimental charge ( $Q_{\text{exp}}$ ) obtained from the voltammograms following the equations from **Chapter 2** (see **Equations 4.1-4.2**). The average electroactive area achieved for AuNPs modified GCE was  $0.21 \pm 0.02 \text{ cm}^2$ , which is nearly 3 times bigger than the electroactive area of polished Au disk electrodes ( $0.07 \pm 0.1 \text{ cm}^2$ ). The percentage of electroactive area was also calculated ( $\%R = A/A_{\text{geo}} \times 100$ )<sup>384</sup>, and for AuNPs modified GCE was 70% and for Au electrode 35%. Furthermore, the electroactive area is bigger than the one achieved in Zakaria and et al., ( $\sim 0.09 \text{ cm}^2$ ) which is probably due to variations in the experimental parameters as mentioned earlier (e.g., speed of the scan rate and the number of cycles). Activation and/or cleaning of the surface also could have an impact, however, even if some concentration of H<sub>2</sub>SO<sub>4</sub> was used (0.5 M), Zakaria and et al., do not report the number of cycles applied.

On the other hand, the charge obtained for the reduction of the AuNPs film in the first scan was  $26.5 \pm 8.2 \mu\text{C}$ , which is very similar to the charge consume in the electroreduction step H<sub>2</sub>AuCl<sub>4</sub> during the first scan ( $22.8 \pm 3.3 \mu\text{C}$ , **Figure 3B**), it could be conclude that Au atoms layer at the AuNPs-solution interface is close to exhaustively oxidized<sup>221</sup>. These results show the benefits of electrodeposition of AuNPs on a platform such as GCE, where large surface electroactive areas can be achieved for subsequent functionalization with thiolated biomolecules.

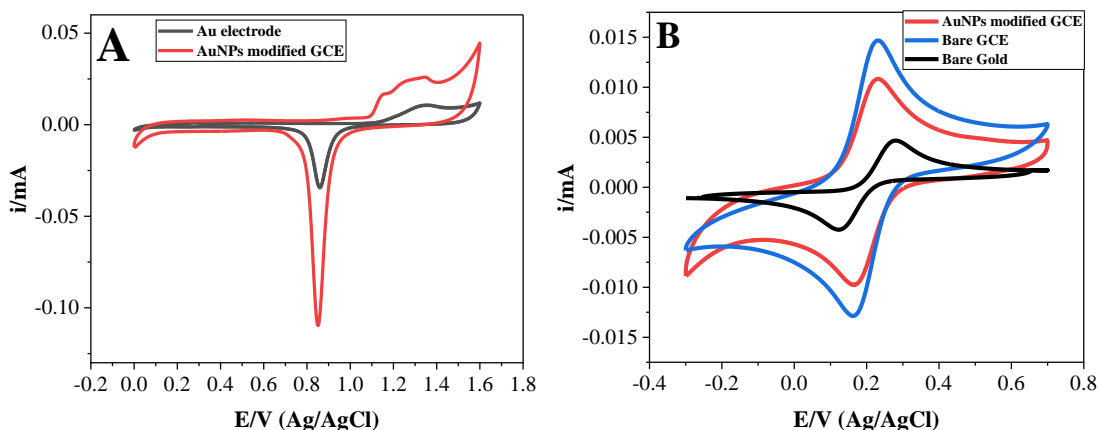
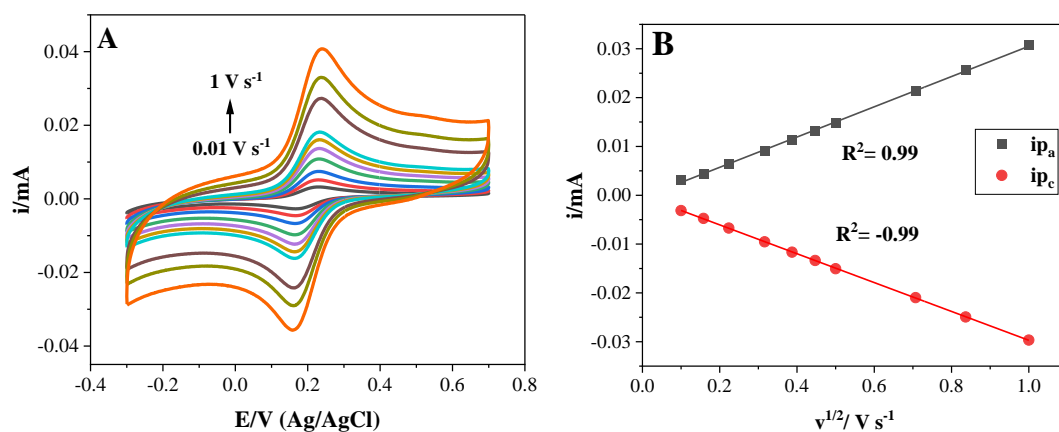


**Figure 4.** Electrochemical characterization. A) Voltammogram of electrodes in 0.1M H<sub>2</sub>SO<sub>4</sub> scanning from 0 V to +1.6V at 0.1 V s<sup>-1</sup>: AuNPs modified GCE (red), conventional Au disk electrode (black). B) Voltammogram of AuNPs modified GCE, bare GCE (blue) and bare Au (black) in 1mM FcnMeOH and 0.1M LiClO<sub>4</sub> as supporting electrolyte at 0.1 M.

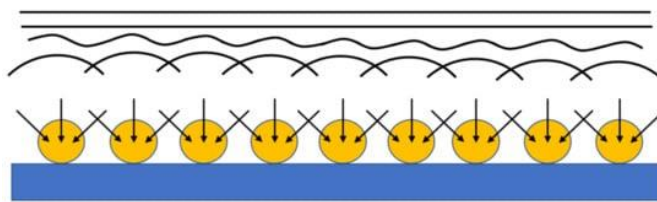
The electrochemical characterization of the modified electrode with 1 mM FcnMeOH in 0.1 M LiClO<sub>4</sub> as well as the results for the scan rate study are shown in both **Figure 4** and **Figure 5**. The reaction is a quasi-reversible both AuNPs coated and bare GCE, since the peak-to-peak separation is  $> 57$  mV. In addition, the Randles-Sevcik plot (**Figure 5B**), shows that the current increases linearly as a function of the square root of the scan rate, suggesting that is a semi-infinite linear diffusion-controlled process<sup>238</sup>. At short time, radial diffusion at the level of single particle could be expected due to them acting like nanoelectrodes due to the small size of the particles (nanoscale level). In this case, each particle would show a three dimensional diffusion field producing a steady-state voltammogram with a very pronounced sigmoidal shape<sup>385</sup>. However, when the distance ( $r$ ) between the electroactive nanostructures is smaller than the thickness of the diffusion layer ( $\delta$ ) (see **Equation 2**), the diffusion layer of each structure converges and mass transport approaches the semi-infinite linear diffusion model<sup>386</sup> as depicted in **Figure 6**. Therefore, according to voltammogram shape and the electroactive area obtained for AuNPs coated GCE, is very likely that the particle density in the surface is high, having a small interparticle distance, leading to the coalescence of the radial diffusion layer of each particle, acting like a flat surface with a semi-infinite linear diffusion model.

$$\delta = (2Dt)^{1/2} \gg r \quad (2)$$

Separately, in order to understand better how the presence of AuNPs affects to the kinetics of the system, the heterogenous electron transfer rate constant ( $k^0$ ) was calculated using the diffusion coefficient value reported in the literature for FcnMeOH ( $7.0 \times 10^{-6} \text{ cm}^2 \text{ s}^{-1}$ )<sup>247</sup>, by performing a digital simulation in the CH Software. For this purpose, a voltammogram recorded at  $0.1 \text{ V s}^{-1}$  was used and the  $k^0$  values obtained for bare and AuNPs coated GCE were  $3.2 \times 10^{-2} \text{ cm s}^{-1}$  and  $3.7 \times 10^{-3} \text{ cm s}^{-1}$  (respectively). Although the values for bare GCE are higher by an order of magnitude, the difference is not very significant since it lies in the quasi-reversible ( $10^{-2} > k^0 > 10^{-4} \text{ cm s}^{-1}$ )<sup>248</sup> as well as the value obtained for AuNPs coated GCE. Thus, these results indicates that the presence of AuNPs decreases the electrode kinetics of system, but it still allows quasi-reversible voltammetric responses to be observed at reasonable scan rates. Moreover, as shown in the following sections, the AuNPs allow the biofunctionalization of the surface for the development of a DNA sensing platform.



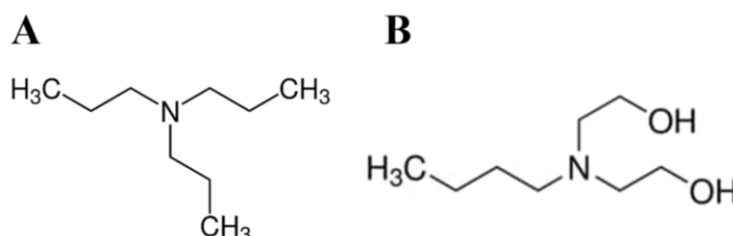
**Figure 5.** Scan rate study of AuNPs modified GCE with 1 mM FcnMeOH in 0.1 M LiClO<sub>4</sub>. A) Voltammogram from 0.01 to 1 V s<sup>-1</sup>. B) Randles-Sevcik plot (the standard deviations are similar to, or smaller than, the size of the symbols).



**Figure 6.** Illustration of convergent diffusion resulting in semi-infinite linear diffusion, when the nanostructure size and interspacing are much smaller than the root mean square of the diffusion length<sup>386</sup>.

### 3.2. ECL characterization and co-reactant study

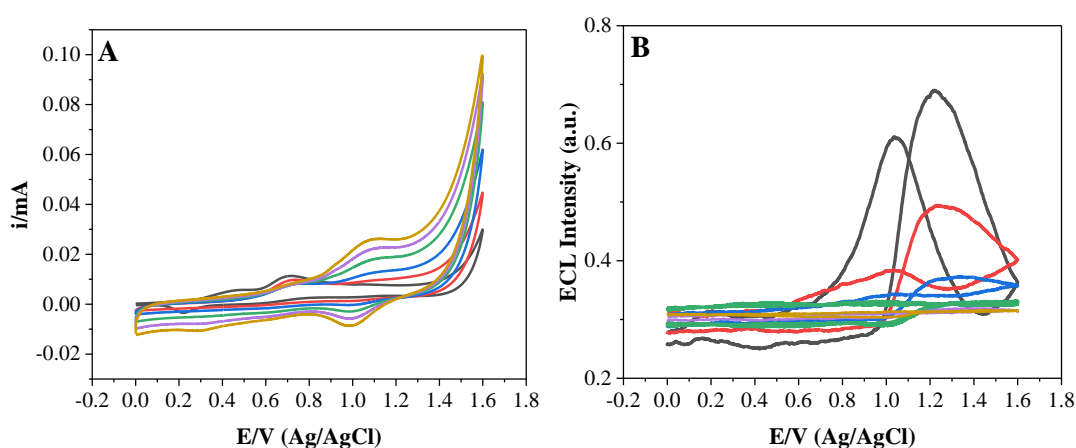
As mentioned above, one objective of this thesis is to develop an ECL assay for the detection of DNA from UTI causing *E. coli* using AuNPs coated GCE as the platform. ECL has arisen as a powerful analytical technique in clinical diagnostics, material science, and environmental monitoring as it combines both electrochemistry and spectroscopy<sup>387,388</sup>. The most common ECL probe used is  $[\text{Ru}(\text{bpy})_3]^{2+}$  which have been successfully applied for drug analysis, nucleic acids and immunoassays due to its easy preparation, low-cost and well-developed technology<sup>389</sup>. Usually, the most common co-reactant used to trigger the ECL reaction is tri-*n*-propylamine (TrPA) alongside ruthenium(II) complexes, however, oxalate, quantum dots, *n*-butyldiethanolamine (NBEA) have been also reported to increase the ECL signal<sup>387,389,390</sup>. In this chapter, the two tertiary amines co-reactants, TrPA and NBEA (see chemical structure in **Figure 7**), were investigated with the dye  $[\text{Ru}(\text{bpy})_3\text{-NH}_2]^{2+}$ , comparing the ECL intensities and determine the suitability of each compound for its application in DNA biosensor and an enhanced bioanalytical performance.



**Figure 7.** Chemical structure of co-reactants tested in this study. A) Tri-*n*-propylamine (TrPA) and B) *N*-butyldiethanolamine (NBEA).



The experiments were performed using AuNPs coated GCE as working electrode, in 0.1 mM of  $[\text{Ru}(\text{bpy})_3\text{-NH}_2]^{2+}$ , 0.1 M of co-reactant and 0.1 M of  $\text{LiClO}_4$  as supporting electrolyte. Results of the co-reactant study are shown in **Figure 8**. For the experiments with TrPA, the voltammogram reveals that TrPA oxidation happens around +0.75 V<sup>391</sup> and this peak is slightly shifted and it becomes less sharp as the scan rate speed increases (**Figure 8A**). Additionally, from a scan rate of 0.05 V s<sup>-1</sup> and higher, an oxidation peak between +1.0 V and +1.2 V appears, which has been attributed in the literature to  $[\text{Ru}(\text{bpy})_3]^{2+}$  oxidation<sup>391,392</sup>. On the other hand, NBEA shows two oxidation peaks (+0.75 V and +1.1 V) when a scan rate of 0.01 V s<sup>-1</sup> is used. However, at faster scan rates, a single peak is observed that ranges from +1.0 V to +1.3 V (**Figure 8C**). It has been previously reported that direct oxidation of NBEA occurs between +0.9 V and +1.2 V<sup>393,394</sup>. Therefore, the observed process is likely to be the deprotonation of the amine group. The higher intensity achieved with NBEA could be due to the two -OH groups that have negative partial charge that the co-reactant carries and this might enable the approach of the positively charged  $[\text{Ru}(\text{bpy})_3\text{-NH}_2]^{2+}$  in close proximity at electrode surface, enhancing the ECL light production<sup>393</sup>. However, the radical cation lifetime of the co-reactants constitutes one of the limiting factors for the ECL signal generation<sup>395</sup>. For example, it has been reported that Di-butyl ethanolamine (DBEA) has a shorter radical lifetime of TrPA which and this could be linked to the differences in ECL intensity. Therefore, it is possible that NBEA as it also shows a shorter radical lifetime promoting a higher intensity<sup>396</sup>.



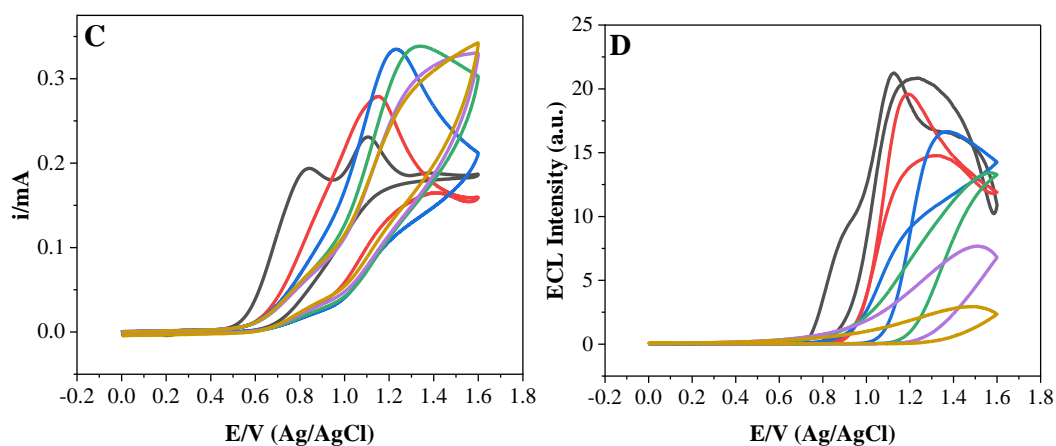


**Figure 8.** Scan rate studies of co-reactants with 0.1mM  $[\text{Ru}(\text{bpy})_3\text{-NH}_2]^{2+}$  in 0.1M  $\text{LiClO}_4$ . A) Voltammogram of 50 mM TrPA and B) ECL characterization of 50mM of TrPA. C) Voltammogram of 10 mM NBEA and D) ECL characterization of 10mM NBEA. Scan rates:  $0.01 \text{ V s}^{-1}$  (black),  $0.025 \text{ V s}^{-1}$  (red),  $0.05 \text{ V s}^{-1}$  (blue),  $0.1 \text{ V s}^{-1}$  (green),  $0.15 \text{ V s}^{-1}$  (purple) and  $0.20 \text{ V s}^{-1}$  (golden). ECL intensity of NBEA was multiplied by a factor of 10 since the gain was changed from  $10^9$  to  $10^8$ .

The reproducibility of the ECL signal across 3 cycles was calculated as the relative standard deviation (RSD), which it is shown in **Table 2**. The RSD values for TrPA decreased with faster scan rates, as opposed to the values for NBEA. This is since TrPA generates lower intensities and at faster scan rates, the ECL values get close to the baseline values, therefore low RSD was expected when the speed of the scans was incremented. On the other hand, for NBEA, RSD values increase as with the increase of speed of the scans. It is possible that at slow scan rates, there is enough time to increase the concentration of the co-reactant intermediate and/or reduced species and diffuse, which enables to achieve higher ECL intensities, however, at fast scan rates, as it occurs for TrPA, is not possible to replenish and diffuse the co-reactant from the bulk solution to the interface of the electrode, causing a decrease on the consecutive cycles<sup>264,397</sup>. This scan rate dependency is portrayed in **Figure 9**, where is shown how the ECL intensity drops as it is scanned faster. For both co-reactants the highest intensity is achieved when scanned at  $0.01 \text{ V s}^{-1}$  and the lowest at the last scan rate applied  $0.2 \text{ V s}^{-1}$ . Furthermore, a difference in the trend is observed between the two co-reactants, where the intensity decreases more linearly for NBEA, whereas for TrPA the decay seems exponential. However, as it was mentioned above, the low intensities achieved at slow scan rates when TrPA was tested, are very close to the baseline values, therefore, no significant changes were expected. On the other hand, as mentioned above, it is likely that the negative charge

of NBEA keeps the positively charged luminophore in proximity, favouring the electron transfer to the tertiary amine<sup>390,393</sup>, but also the radical lifetime, which might explain why the reaction with NBEA is less affected by the speed of the scan rate compared to TrPA. Finally, the utilization of the same solution for the scan-rate study for three consecutive electrodes could also lead to co-reactant depletion, provoking the high standard deviations in ECL intensities achieved for each electrode which could be improved by constant stirring of the solution. Therefore, given the results achieved with the two different co-reactants, NBEA seems to generate higher ECL intensities, being a better alternative as co-reactant for an ECL based assay.

**Table 2.** Relative standard deviation (RSD) of 3 consecutive ECL cycles using TrPA and NBEA as co-reactants.

Scan rate ( $\text{V s}^{-1}$ )	RSD (%)	
	With TrPA	With NBEA
0.01	17	5
0.025	8	10
0.05	3.5	12.5
0.1	2	18.5
0.15	0	20.5
0.2	0	22

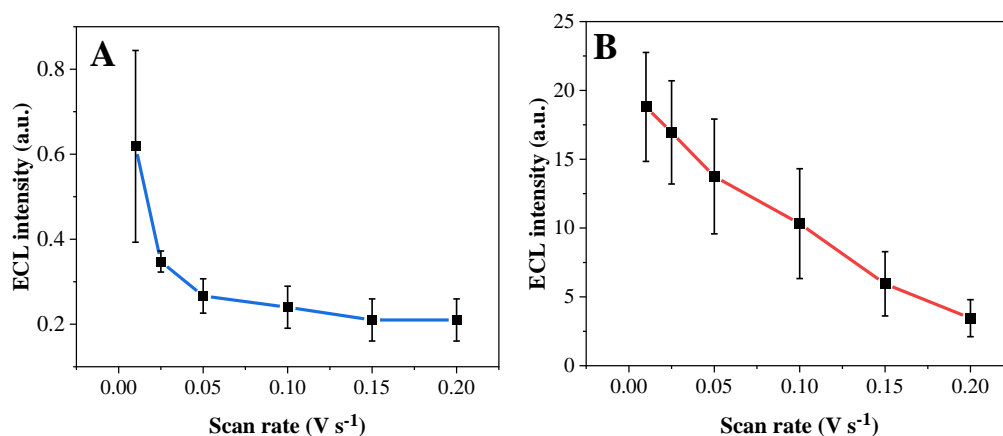


**Figure 9.** Plot of ECL intensity over the scan rate. A) TrPA as co-reactant. B) NBEA as co-reactant. The error bar represents the standard deviation ( $n=3$ ).

### 3.3. Assay development

#### 3.3.1. Surface modification and characterization

For the assay development, every step of AuNPs coated GC electrode modification was characterized using two electrochemical techniques, Cyclic Voltammetry (CV) and Electrochemical Impedance Spectroscopy (EIS), with the redox couple  $\text{Fe}(\text{CN})_6^{4-/3-}$  in 0.1 M PBS buffer as supporting electrolyte. Both capture and probe DNA strands used were 15 nucleotides long (30 nucleotides in total), which both hybridize with a 30 nucleotides long target DNA strand. The length of the strands was chosen to be short since it has been shown that short capture sequences (15-30 nucleotides) are optimal, allowing the hybridisation to occur rapidly. This is recommended since short capture and probes are more effective in fast and stable hybridisation at higher rates than longer sequences, optimising the sensitivity of the platform<sup>398</sup>. On the other hand, co-immobilisation was chosen over a following modification step with MCH. Co-immobilisation of DNA/MCH has been shown to be a better method to control the density of DNA on the surface by having the adequate DNA/MCH ratio, allowing to have sufficient DNA for sensitive detection but also enough space for the correct distribution of the capture strands to avoid steric hindrance<sup>399,400</sup>. As opposed to sequential backfilling with MCH, co-immobilisation provides high control over the spacing among the DNA strands allowing to increase the hybridisation efficiency with the target strand. With sequential blocking, short incubation times are required which often lead to very variable DNA densities on the electrode surface as well as not completely effective removing the non-specifically adsorbed on gold surfaces<sup>401</sup>.

The characterization was first performed by CV and **Figure 10A** shows that at every modification step the current associated with the ferro/ferri cyanide redox reaction drops significantly, especially, when the capture DNA strand and the MCH are covalently co-immobilized on the surface. This occurs because electron transfer is hindered by the negatively charged phosphoric acid groups of the ssDNA backbone as well as by the presence of MCH since it is a non-conductive molecule<sup>79,402</sup>. Furthermore, the peak-to-peak separation ( $\Delta E_p$ ) for the unmodified AuNPs coated GCE is 0.217 V whereas, when DNA/MCH are added,  $\Delta E_p$  0.322 V and in presence of 25  $\mu\text{M}$  of target, the separation becomes bigger ( $\Delta E_p=0.405$  V). This is a result of the redox peaks shifting due to slower rates of heterogeneous electron transfer when the surface is modified (**Table 3**), and the reaction becoming more irreversible, probably due to the ohmic drop that is influence by the speed of the scan rate<sup>242</sup>. The current also slightly dropped in presence of the target, due to the electrostatic repulsion of dsDNA, which further impairs the diffusion of

$\text{Fe}(\text{CN})_6^{4-/3-}$  onto the electrode interface<sup>79</sup>. CV results were further verified by using EIS as a second characterization technique, and results are shown in **Figure 10B**. All the curves were recorded applying a DC potential of +0.2 V, an AC amplitude of 0.025 V over a frequency range of 0.1 Hz-100 Hz. The EIS were fitted with a simplified Randles equivalent circuit using ZView 4 software. The model for the fitting consists of the resistance solution ( $R_s$ ), the constant phase element (CPE), which represents the capacitance of the electrode interface, the charge transfer rate of the redox probe at the interface of the electrode ( $R_{ct}$ ) and the Warburg element (W) that represents the diffusion process in dielectric spectroscopy<sup>403</sup>. CPE was chosen over a capacitor, since experimentally, the perfect capacitor does not exist, and the application of CPE helps to model the behaviour of a non-ideal capacitance. The surface roughness, surface heterogeneity and porosity are the main reasons why this can occur<sup>153</sup>. In fact, several studies used CPE to model the capacitance of DNA modified electrodes, since it showed to improve the goodness of the fit<sup>404-407</sup>.

Bare unmodified AuNPs coated GCE showed a  $R_{ct}$  value of 77.96  $\Omega$ , and CPE of 16.23  $\mu\text{F}\Omega^{-1} \text{cm}^{-2} \text{s}^n$ . Values on the same order of magnitude have been reported for a conventional and clean gold disk electrode using the same redox probe<sup>408-410</sup>. On the other hand, when capture DNA/MCH were immobilised,  $R_{ct}$  values dramatically changed as well as after the addition of the target sequence ( $R_{ct}=2120 \Omega$ ) (**Table 3**). This suggests the correct modification of the electrodes and successful hybridisation of the target after its incubation (for 2 hours). The gradual increase in the  $R_{ct}$  values obtained, as the modification steps proceed, indicate that the electron transfer is hindered due to the formation of a thick layer that impairs the electron transfer at the electrode surface, especially when dsDNA is present. As expected, the impedance results are in agreement with the results obtained with CV technique, showing the successful modification of the electrode surface.

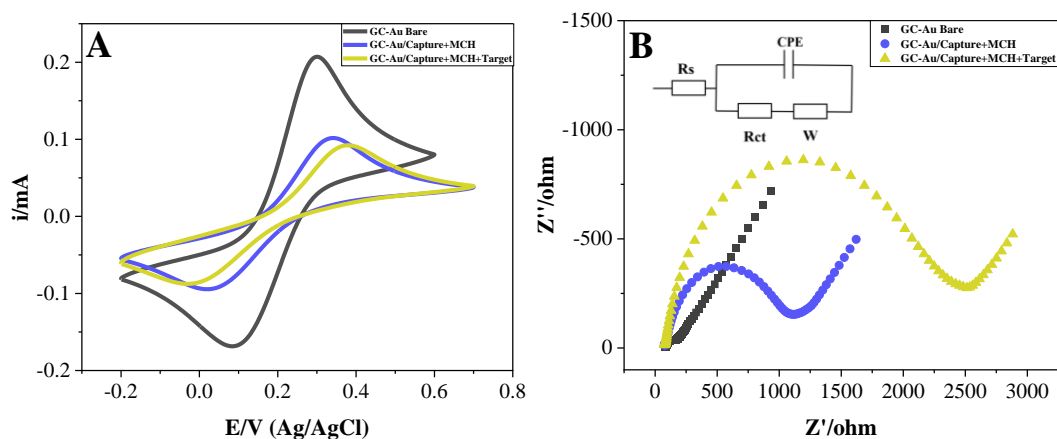


**Figure 10.** The voltammogram at  $0.1 \text{ V s}^{-1}$  (A) and EIS curves (B) of GCE-Au bare (black), modified GCE-Au with capture DNA/MCH (blue) and modified GCE-Au with capture DNA/MCH hybridized with  $25 \mu\text{M}$  of DNA target after incubation. Work solution: Work solution:  $0.01 \text{ M}$  phosphate buffer ( $\text{pH } 7.4$ ) containing  $5 \text{ mM Fe}(\text{CN})_6^{4-/3-}$ . Inset: simplified Randles equivalent circuit.

**Table 3.** The values from the redox probe oxidation ( $E_{\text{pa}}$ ) and reduction ( $E_{\text{pc}}$ ), separation peak ( $\Delta E_{\text{p}}$ ), constant phase element (CPE) and charge transfer resistance ( $R_{\text{ct}}$ ).

	$E_{\text{pa}}$ (V)	$E_{\text{pc}}$ (V)	$\Delta E_{\text{p}}$ (V)	$R_{\text{ct}}$ ( $\Omega$ )	CPE ( $\mu\text{F}\Omega^{-1} \text{cm}^{-2} \text{s}^n$ )
<b>AuNPs coated GCE</b>	0.3	0.083	0.217	77.96	16.23
<b>AuNPs/Capture/MCH</b>	0.314	0.019	0.322	962.80	5.02
<b>AuNPs/Capture/MCH/Target</b>	0.378	-0.027	0.405	2120.0	3.56

### 3.3.2. ECL detection of gene *fimH* from UTI causing *E.coli*

As mentioned before, the objective of this chapter is to develop and ECL based biosensor for DNA detection of UTI causing *E. coli*. As a proof-of-concept, an assay was developed for detection of *fimH* gene using the ruthenium (II) complex,  $[\text{Ru}(\text{bpy})_3\text{-NH}_2]^{2+}$ , as a label for the ssDNA probe. In the **Figure 11A**, it is shown the results obtained for the ECL characterization of the assay at every step of modification. The unmodified AuNPs coated electrode produced a small signal in the presence of  $0.1 \text{ M}$  of NBEA, which was observed across all the independent measurements. Nevertheless, this background signal is very weak, and so the level of interference with the results achieved for the next steps is very small. On the other hand, characterization of the electrodes coated with the capture ssDNA/MCH monolayer show very low ECL signal (**Figure 11B**) (close to the baseline values) preventing the electron transfer and therefore, the strong oxidation of the co-

reactant that might have led to low ECL background generation as for previously mentioned unmodified electrodes.

To further evaluate the performance of the sensor, 25  $\mu\text{M}$  probe Ru-labelled probe ssDNA was incubated to test non-specific interactions/binding of the probe. Separately, 25  $\mu\text{M}$  of target ssDNA complementary to the ssDNA capture were incubated, followed by the addition and the incubation of Ru-labelled probe ssDNA in order to investigate if detection was possible under the developed ECL system. As shown **Figure 11A**, in both scenarios, the ECL emission begins around +0.75 V, reaching its maximum emission around +1.3 V, which is consistent with the emission generated by  $[\text{Ru}(\text{bpy})_3\text{-NH}_2]^{3+}$ . Additionally, a hysteresis process is observed, which as shown in this thesis, is a common phenomenon for ruthenium (II) based complexes. The highest intensities achieved are in the presence of the target, which indicates the successful hybridisation with the capture and probe strands. However, a high ECL background was observed when capture/MCH monolayers were incubated with Ru-labelled probe. This suggests that non-specific interactions/binding events occurred. In fact, as mentioned above, the probe utilized was not purified, due to the low molecular weight of the strand. As described in **Chapter 3**, the positively charged  $[\text{Ru}(\text{bpy})_3\text{-NH}_2]^{2+}$  can interact electrostatically with the negative backbone of the ssDNA and dsDNA, which might have caused the high ECL background shown in **Figure 11**. This is not ideal since this has a direct negative effect on the sensitivity of the sensor. On the other hand, purification of the labelled probe with techniques such as HPLC, could help to remove any unreacted ruthenium from the sample and therefore, minimize the non-specific interactions by achieving a lower background signal.

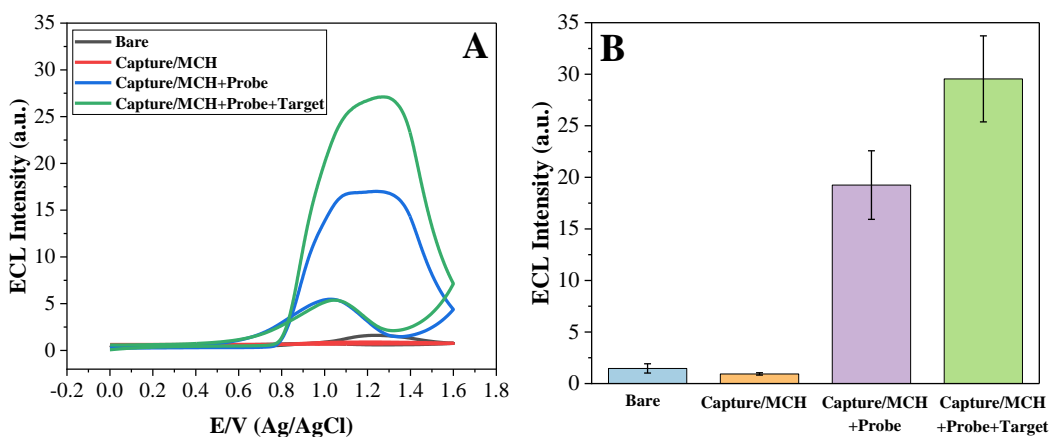


**Figure 11.** ECL characterization of the assay at every step of modification. A) Plot of ECL characterization at 0.01 V s<sup>-1</sup> and 0.1 M of NBEA in 0.1M of LiClO<sub>4</sub> as supporting electrolyte. B) Quantification of ECL emission intensity for independent measurements. Standard deviation is represented as error bars.

Despite non-specific interactions of the Ru label, the target was successfully detected. A second objective for the AuNPs, beyond increasing the electrode area and acting as anchor points for the capture DNA, was to investigate the possibility of the ECL enhancement based on localized surface plasmon resonance (LSPR). LSPR refers to the collective oscillation of the electrons on the NPs surface that have been excited by incident light, in this case, the ECL light emitted by the luminophore triggered by the presence of the co-reactant<sup>259</sup>. This feature can be tuned by controlling key parameters such as the distance between the luminophore and the plasmonic particle to achieve an enhanced performance of the assay<sup>411</sup>. For example, in this study, the chosen assay length (capture, target and probe DNA) is 10 nm long, which has been previously reported to be the optimal distance to achieve the greatest LSPR-ECL enhancement, on the order to 3- to-6 fold using plasmonic materials such as AuNPs<sup>39,271,412</sup>. However, at distances shorter than 10 nm, quenching of ECL has been observed due to energy transfer from the excited state of the luminophore into the surface of the plasmonic material<sup>22</sup>. However, LSPR-ECL phenomenon of Au particles is not only sensitive to the distance between the luminophore and the metal surface, it also sensitive to size and shape of particles, interparticle distance, type of luminophore and the surrounding solvent which can contribute to quenching or enhancement of the luminophore<sup>259,413-415</sup>. Therefore, in order to elucidate which is the optimal distance to achieve the higher ECL enhancement on the electrodeposited AuNPs, future experiments would be needed using different lengths of DNA. However, for the building of a DNA assay, the steric hindrance mediated by the formation of dsDNA after hybridisation of capture, target and probe are key, since it can inhibit further hybridisation of target molecules, leading to poor sensitivity<sup>39</sup>. Thus, testing different concentrations of DNA capture molecules in order to avoid steric hindrance and optimize the assay are required. Additionally, for real samples testing, the steps for bacterial DNA retrieving should be optimised. In this sense, urine samples from patients with a potential UTI would be taken and bacterial DNA extraction would be performed by utilisation of kit intended for urine, such as the Genomic DNA Extraction Kit from Cephan Life Sciences or AMPIXTRACT® Urine DNA Isolation Kit from Enzo



Life Sciences. After this extraction, the obtained DNA could be incubated with the already modified electrode and perform the detection of the target after addition and incubation with the ruthenium labelled probe.

#### 4. CONCLUSIONS

In summary, a SPR-ECL biosensor for *fimH* gene detection was designed as a proof of concept utilising a novel ruthenium complex as a label and AuNPs as plasmonic material. AuNPs were successfully electrodeposited on the GCEs using CV, achieving a large surface area and slightly improved diffusion when compared to bare GCE. The presence of AuNPs on the electrode surface also facilitated the immobilisation of capture ssDNA which was confirmed with CV and EIS as well as the hybridisation of target ssDNA with the capture strand, resulting in a drop of the current (voltammogram) and an increase of  $R_{ct}$  values (EIS). On the other hand, the ruthenium label was characterised with two different co-reactants, TrPA and NBEA in order to determine their suitability for an ECL assay. Results showed that NBEA alongside  $[Ru(bpy)_3-NH_2]^{2+}$  is more effective than the conventional TrPA as co-reactant, probably due to the direct and fast oxidation of the two hydroxyethyl groups of the NBEA, increments significantly the ECL intensities. Therefore, NBEA was determine as the most optimal co-reactant for the development of the ECL based DNA assay. ECL characterisation of the DNA assay, showed that the target could be detected at a concentration of 25  $\mu$ M, however, it also revealed a strong background when ssDNA capture was incubated with the  $[Ru(bpy)_3-NH_2]^{2+}$  labelled ssDNA probe. These results indicate that non-specific interactions occurred due the high affinity of free  $[Ru(bpy)_3-NH_2]^{2+}$  for gold surfaces and the negative backbone of both dsDNA and ssDNA, impacting significantly on the sensitivity of the assay. Therefore, further experiments are needed by testing better purification methods such as HPLC to reduce the background noise. In addition, testing different lengths of DNA also could help to elucidate the optimal distance between the electrodeposited AuNPs and the  $[Ru(bpy)_3-NH_2]^{2+}$  label and understand better the characteristics of the platform, and overall, improve the performance of the assay. Nevertheless, this work showed that the designed DNA sandwich assay can be utilized for the detection of the presence of the *fimH* gene, which codifies a virulence factor that is key for the growth of biofilms of ureopathogenic *E. coli* in the urinary tract of humans.



# **Chapter 5:**

## **Synthesis and characterization of Fe<sub>3</sub>O<sub>4</sub> core/Au shell particles using the thermal decomposition method**

### **1. INTRODUCTION**

Nanoscience is one of the most important and impactful research fields of modern science and many researchers are achieving important developments in healthcare such as disease diagnosis by the utilisation of nanotechnology<sup>416</sup>. The interest in magnetic nanoparticles (MNPs) is growing rapidly since they possess excellent performance and unique properties, e.g., the ability to preconcentrate biomarkers, high surface area, paramagnetism, ferromagnetism, electromagnetism, coercivity, and etc<sup>104,417</sup>. Additionally, MNPs can be functionalized with biomolecules (e.g., antibodies, nucleic acid, proteins), e.g., by first coating with other materials such as gold, thus allowing advanced diagnostic biosensors to be developed<sup>418</sup>. Magnetic particles has been the focus of many researchers since the efficiency of separation directly impacts on the amount of sample extracted<sup>419</sup>. Magnetic beads are available commercially and their size can range from 0.02–350  $\mu\text{m}$  diameter depending on their application<sup>420</sup>. Larger particles (micron

range) are meant for cell isolation while diameters in the nano range are used for smaller biomolecules such antibodies or nucleic acid. However, larger particles provide a faster separation time than smaller sizes<sup>421</sup>, therefore, the right diameter has to be chosen considering both target molecule and the desired time separation.

Superparamagnetic magnetite ( $\text{Fe}_3\text{O}_4$ ) is the most commonly used iron oxide NP since it displays high biocompatibility and low toxicity, a characteristic that makes them very suitable for biosensing applications<sup>422</sup>. Moreover, due to their ferromagnetic properties they facilitate sample preconcentration and washing steps of biomolecules or cells, essential for sample purification by preventing any cross reactions during the detection process<sup>423</sup>. Numerous techniques have been used for the synthesis of  $\text{Fe}_3\text{O}_4$  NPs such as electrodeposition, microemulsion, coprecipitation, hydrothermal and etc<sup>424</sup>. Among these methods, thermal decomposition is one of the most innovative physical methods to synthesize MNPs since it is less polluting, less time-consuming, with less likelihood of aggregates and agglomeration of particles compared to other methods and it tends to form monodispersed and stable particles<sup>425</sup>. For all these reasons, this method has become popular.

The synthesis of the MNPs typically involves two steps: first the synthesis of the metallic core itself, and secondly, the modification/stabilization of the surface<sup>426</sup>. Utilization of organometallic compounds (precursors) and surfactants (capping agents) is very common in order to produce monodispersed and highly crystalline particles<sup>427</sup>. Oleic acid (**Figure 1A**) has been widely used as a long-chain fatty acid modifier of  $\text{Fe}_3\text{O}_4$  NPs by generating a protective and waterproof shield around the particles by binding to the surface through its carboxyl group<sup>426,428–430</sup>. Additionally, oleyl amine (an unsaturated fatty amine acid) (**Figure 1B**) also has been successfully used as a capping agent of iron based nanoparticles, which interaction is based on the presence of its amine groups,  $-\text{NH}_2$  which has a strong affinity for metallic surfaces<sup>431–433</sup>. Furthermore, both oleyl amine and oleic acid have been reported as a versatile ligand pair in the synthesis of metallic nanoparticles to obtain more monodisperse particles during the synthesis and post-synthesis processes<sup>434</sup>.

However, despite the enormous potential of MNPs, these materials are not ideal as active elements for sensing applications due to their low electrical conductivity and limited optical properties<sup>435</sup>. One approach to address this issue is to coat MNPs with gold

since it provides higher conductivity, enhanced optical properties such as localized surface plasmon resonance, the possibility of biofunctionalization through amine/thiol terminal groups as well as protection of the MNPs from corrosion and oxidation<sup>435-437</sup>. Coating MNPs with a noble metal also provides other advantages such as higher stability, which allows their utilization under conditions where MNPs with no shell would degrade rapidly<sup>438</sup>.

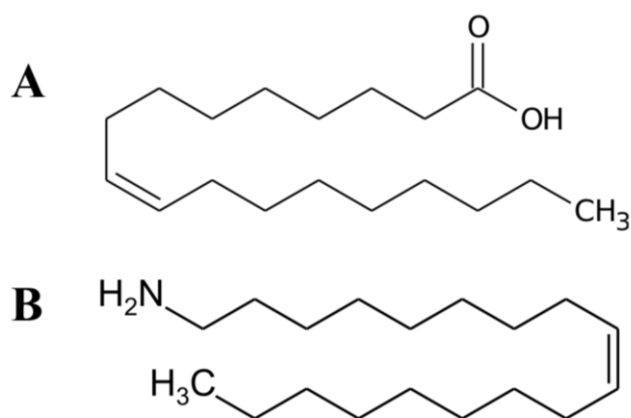


**Figure 1.** Chemical structure of (A) oleic acid and (B) oleyl amine.

This chapter describes the synthesis of Fe<sub>3</sub>O<sub>4</sub> core-Au shell particles through a novel thermal decomposition method using the oleyl amine/oleic acid ligand pair as capping agents. Additionally, phase transfer of the particles to aqueous suspension was performed by exchanging the pair of capping agents by citrate, which will potentially allow the biofunctionalization of the particles with thiolated DNA. This work was performed in collaboration with the group of Prof. Carmen Blanco from the University of Oviedo (Spain) as a proof-of concept for the application of the synthesized particles on a biosensing platform for bacterial DNA detection. This collaboration arose within the Break Biofilms Training Network (H2020-MSCA-ITN), with the aim to develop platforms/biosensors for the detection of biofilm-forming bacteria. The academic secondment length was 1 month in the hosting university (University of Oviedo), where the magnetic particles were synthesized and coated with gold. The characterisation (UV-Vis, FT-IR, SEM and TEM) of the samples was performed in Dublin City University with the goal to investigate the application of Fe<sub>3</sub>O<sub>4</sub>/Au particles on a SPR-ECL DNA sandwich assay for target separation and DNA preconcentration.

## 2. MATERIALS AND METHODOLOGY

### 2.1. Chemical reagents

The following chemicals were used for the synthesis and gold coating of particles: Iron (III) acetylacetonate ([Fe(acac)], 99%), hydrogen tetrachloroaurate(III) trihydrate (HAuCl<sub>4</sub>·3H<sub>2</sub>O, ≥99.9%, Au 48.5–50.25%), oleylamine (80%)(ACROS), 1-hexadecanol (96%) (ACROS), oleic acid (90%), 1-methyl- 2-pyrrolidinone (NMP, ≥99.0%) (Alfa Aesar) and anhydrous toluene (99.8%) (Sigma Aldrich). For phase exchange, Tetramethylammonium hydroxide (TMAOH) (Sigma Aldrich) tri-Sodium citrate dihydrate (Sigma Aldrich) were used.

### 2.2. Synthesis of Fe<sub>3</sub>O<sub>4</sub> core/Au shell particles

#### 2.2.1. Synthesis Fe<sub>3</sub>O<sub>4</sub> core via the thermal decomposition method

Two solutions were prepared, solution (A) and solution B. For solution (A) 2.652g of 1-hexadecanol was added to a three-neck round-bottom flask, 3RB, (100 mL) followed by 35 ml of deoxygenated N-Methyl-2-pyrrolidone, NMP. Then 3.71 mL of oleic acid was injected, and the solution was ultrasonicated for 1 minute. Finally, 4.318 mL of oleyl amine were added. Separately, solution (B) was prepared by weighing 535.1 mg of [Fe(acac)<sub>3</sub>] (precursor) in 10 mL of deoxygenated NMP.

Afterwards, the set up for the synthesis of particles was prepared (see **Figure 2**). A silicon bath was prepared where the 3-RB flask was placed to maintain the desired temperature during the synthesis. When the temperature of the bath reached 50°C, the 3-RB flask was introduced, and argon gas was bubbled through the solution for 15 minutes via a syringe to remove oxygen. Then the temperature was slowly increased until it reached the desired temperature, 190°C. At this point, a turn valve was placed at the top of the condenser and a balloon filled with argon connected, then the second solution (B) was injected quickly and stirred for 1 h. Afterwards, to speed up the cooling process, the solution was cooled

down by using a hair dryer in cool mode. Finally, the solution was left stirring overnight under low oxygen conditions. The argon is denser than air and it displaced any oxygen.

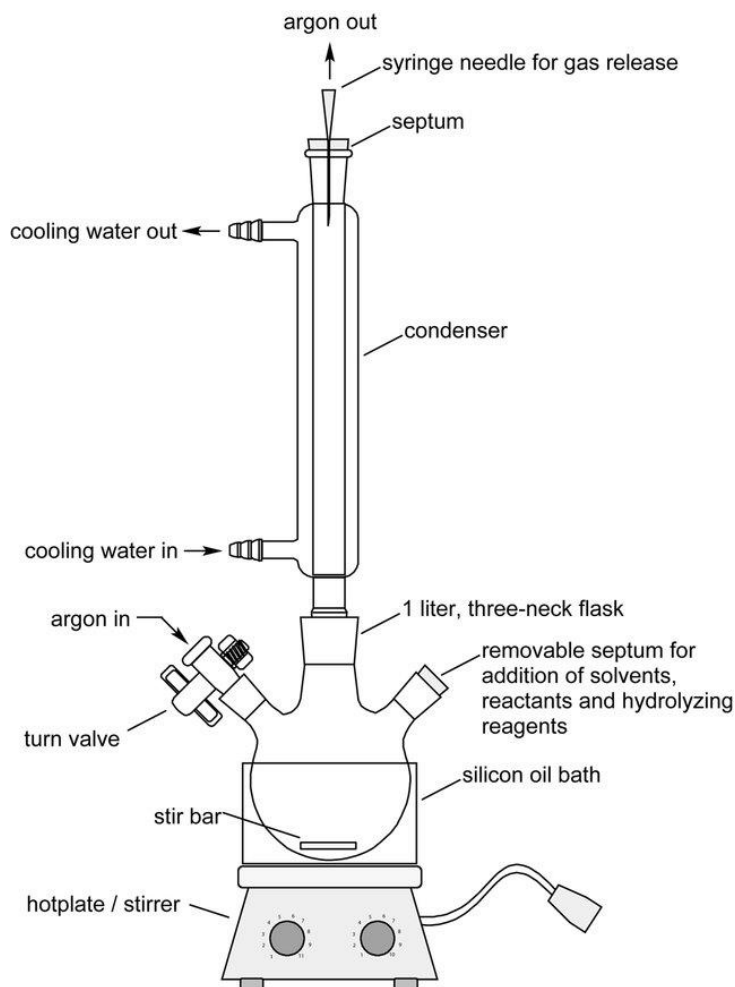


**Figure 2.** Schematic representation of set-up for synthesis of magnetic particles by thermal decomposition method<sup>439</sup>.

### 2.2.2. Washing of synthesized Fe<sub>3</sub>O<sub>4</sub> particles

After synthesis, the product was washed using 50 mL of ethanol that were added to the solution in the 3-RB flask and stirred for 1 h. The solution was then transferred to another flask, and particles were collected by placing a magnet under the flask and decanting the solution. After the supernatant was removed, another 50 ml of ethanol was added, and the mixture was stirred with a glass stirrer. Washing with ethanol was performed another two times until the colour of the supernatant was clear. After each washing step, the particles were isolated using a magnet and finally transferred to 5 ml of anhydrous toluene.

### 2.2.3. Au coating of Fe<sub>3</sub>O<sub>4</sub> particles

For Au coating of the particles, two solutions were prepared, solution (A) and solution (B). For solution (A), 1.25 mL of Fe<sub>3</sub>O<sub>4</sub> MNPs was placed in a 3-RB flask (250 mL) and 20 mL of anhydrous toluene added followed by stirring for 5 minutes. Separately in a different flask, solution (B) was prepared by adding 0.34232 g of H<sub>2</sub>AuCl<sub>4</sub>·3H<sub>2</sub>O (a ratio 1:7 of Fe<sub>3</sub>O<sub>4</sub>: Au to produce a thickness of gold ~70-80 nm). Secondly, 7.07 mL of oleyl amine (capping agent) were injected. Then, a similar set-up to the one previously described was prepared for the coating of MNPs. First, the silicon bath was heated up 80 °C, and the 3-RB flask containing the solution (A) was placed in the bath. When the temperature of bath reached 100 °C, solution (B) was added slowly (35 mL) over 35 minutes (drop by drop) by utilising a glass syringe in order to avoid any reaction of toluene with plastic and to prevent contamination. After finishing the injection of solution (B), the whole the system was covered with aluminium foil and stirred for 1 h at 100 °C. During this time a colour change was observed from dark brown to dark red/wine colour after adding solution (B), suggesting a successful coating of the MNPs with gold.

### 2.2.4. Washing step and phase transfer

After cooling the system to room temperature, 85 mL of ethanol were added in order to precipitate the resulting Au coated MNPs. For the first washing step, the solution was transferred to a beaker and a magnet was placed under the flask in order to collect the particles (**Figure 3**). Then, in single step, the supernatant was carefully removed, and 5 mL of ethanol was added for a second washing round. After 3x washing, the ethanol was removed, and 10 mL of anhydrous toluene was added to disperse the particles. The colour of the solution changed back to red dark wine. This solution was then transferred to another beaker for further washing.

Subsequently, in order to have the particles in an aqueous phase, which is more suitable for biofunctionalization, the protocol published by Robinson et al.<sup>440</sup> was followed. A two-step phase transfer of Fe<sub>3</sub>O<sub>4</sub> core/Au shell particles was used, using TMAOH and citrate for functionalization. As a first step, the particles in ethanol were collected using



a magnet and redispersed in 1 M TMAOH solution, followed by the addition of 0.04 g of sodium citrate. Then the pH was adjusted to pH ~ 6.5 and the solution was sonicated for 15 minutes and collected again with a magnet and finally dispersed in 5 ml of deionized water.

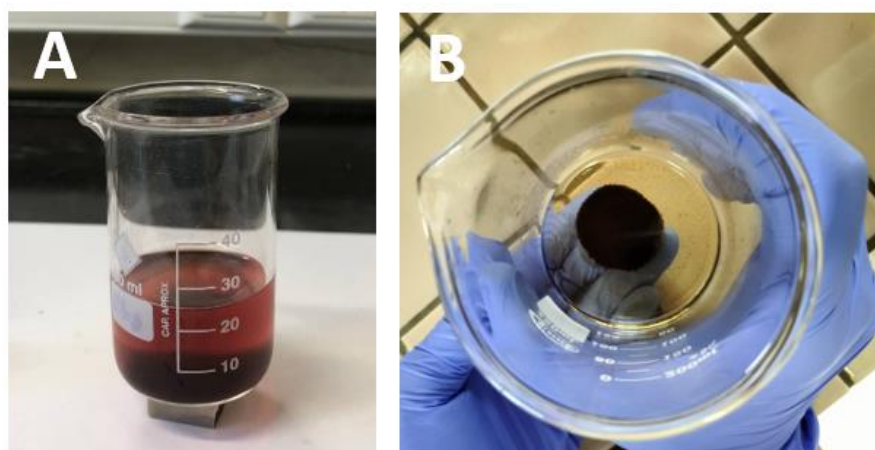


**Figure 3.** Synthesized Fe<sub>3</sub>O<sub>4</sub> core/Au shell particles. A) Particles in anhydrous toluene, collected using a magnet. B) Isolated particles (without solvent).

### 2.3. Characterization of Fe<sub>3</sub>O<sub>4</sub> core/Au shell particles

Surface characterization of synthesized particles was done using Transmission Electron Microscopy (TEM) and Scanning Electron Microscopy (SEM) modes of the Electron Microscopy Labs Hitachi S5500 Field Emission. Spectroscopic characterization of the particles, such as UV-Vis measurements, was performed in Shimadzu UV-2600 UV-VIS Spectrometer with UVProbe LabSolutions Software, using 1 cm quartz cells from Merck. FT-IR measurements were carried in the using a PerkinElmer Spectrum Two FT-IR spectrometer and zeta-potential was measured Malvern Zetasizer Ultra using Universal Dip Cell and a quartz cuvette.

### 3. RESULTS AND DISCUSSION

#### 3.1. Fe<sub>3</sub>O<sub>4</sub> core/Au shell particles characterization

##### 3.1.1. SEM and TEM images

The product, ideally, Fe<sub>3</sub>O<sub>4</sub> core/Au shell particles, was first characterized using SEM. **Figure 4** shows SEM images that show very large sized particles, with very heterogenous shapes. TEM (**Figure 5**) indicates that the intrinsic particle size is around 200 nm in diameter, but these are highly aggregated. Furthermore, **Figure 5** also shows smaller particles (magnetic cores) within a matrix which is most likely to be gold, forming a cluster or aggregates of Fe<sub>3</sub>O<sub>4</sub> cores/Au shell instead of individual magnetic particles coated with gold, as it was intended.

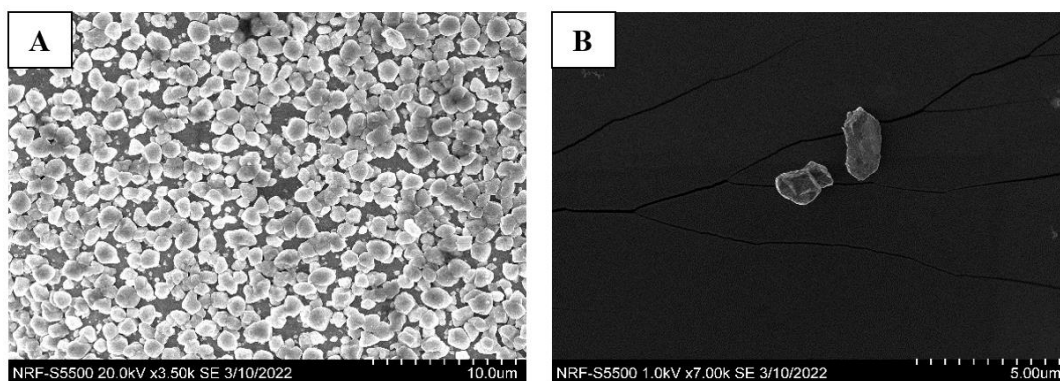


**Figure 4.** SEM images of Fe<sub>3</sub>O<sub>4</sub> core/Au shell synthesised particles. A) Image taken using an acceleration voltage of 20.0kV. Scale bar 10μm. b) Image taken using an acceleration voltage of 1.0 kV. Scale bar 5μm.

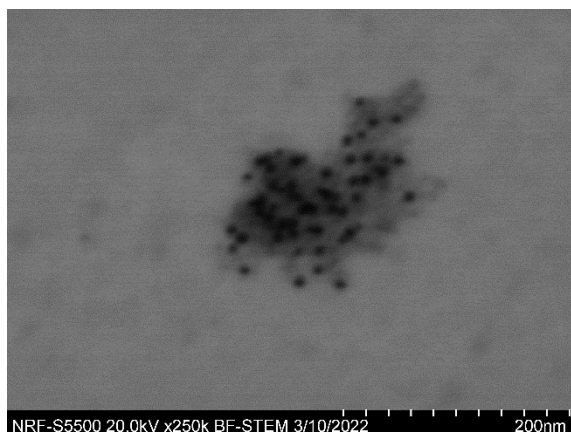


**Figure 5.** TEM image of a single Fe<sub>3</sub>O<sub>4</sub> core/Au shell particle using 20 kV acceleration voltage. Scale bar 200nm.

Both SEM and TEM images were analysed using the software ImageJ in order to calculate the average diameter of the particles ( $D$ , nm). The particles/aggregates from **Figure 4**, show an average diameter of 900 nm. However, analysis of the particles under the TEM (**Figure 5**), revealed that, the magnetic cores show an approximate diameter of 8 nm (as expected), but they seem to be in aggregated and entrapped within a matrix of gold. The coating method used in this study is based on a direct coating with gold, where the oleic acid and the oleyl amine (capping agents of bare MNPs) are intended to be desorbed due to thermal activation and the gold reduced directly onto the surface of individual particles<sup>441</sup>. After this step, the gold coated MNPs are then intended to be re-encapsulated with oleyl amine/oleic acid. The main advantage of this method is that the production of a gold shell can be controlled through the capping agents. Despite this, ensuring the magnetic cores are individually coated remains a challenge of this coating method<sup>427</sup>. Normally, aggregation is prevented by tuning the mole ratio of magnetic cores to Au<sup>3+</sup> in solution, or the ratio of gold precursor to reducing and capping agents (i.e., oleyl amine and oleic acid), however, very often many experimental attempts are required to find the optimal parameters<sup>427</sup>. Finally, characterization of the particles as synthesised and subsequently coated may also constitute a challenge, since they tend to form aggregates during sample preparation, which leads to very unclear results when TEM and SEM techniques are used<sup>427</sup>.

### 3.1.2. UV-Vis measurements

Further characterization experiments were carried out using UV-Vis in order to confirm the presence of gold. **Figure 6** shows a peak absorbance around  $\lambda_{\max} = 530$  nm, which suggests that the particles are in fact coated with gold. For gold nanoparticles synthesized in toluene and with oleyl amine as capping agent, it has been shown that when absorbance  $\lambda_{\max} = 535$  nm is recorded, the gold thickness is  $\geq 80$  nm of diameter<sup>442</sup>. It is possible that in this solvent, the particles are more disperse, but remain in clusters of gold of a size of  $\geq 80$  nm. Therefore, is still very difficult elucidate the real size of the particles. However, given the results achieved with UV-Vis spectroscopy and considering what has been reported in the literature in regards the absorbance of Au particles<sup>442-444</sup>, the Fe<sub>3</sub>O<sub>4</sub> core/Au shell particles synthesized with the method presented in this study show a small core (8 nm diameter) that embedded/aggregated in thick shell of Au reaching a thickness around  $\sim 80$  nm in the organic solvent. Therefore, further efforts would be needed to achieve monodisperse, individually coated magnetic cores that are stable towards aggregation by optimising the parameters of the coating step such as magnetic core to gold ratio as well as the gold to capping agent's ratio.

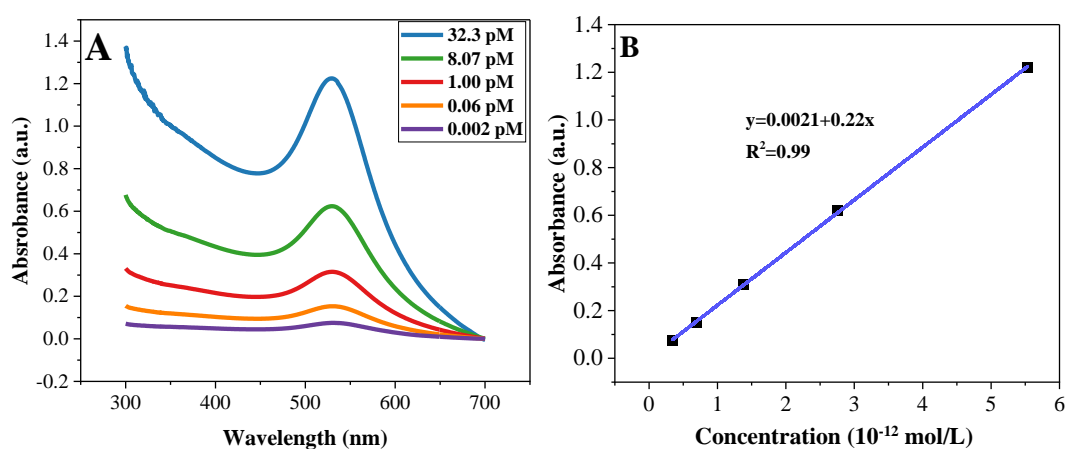


**Figure 6.** UV-Vis spectroscopy results. A) Absorbance spectra of serial dilutions of Fe<sub>3</sub>O<sub>4</sub> core/Au shell particles, using toluene as solvent. B) Beer's law calibration curve.

Nevertheless, these results could be used to estimate the number of particles per mL ( $N_{\text{seed}}$ ), following the **Equation 1** presented by Leng et al., (2015)<sup>445</sup>, assuming a spherical shape of the aggregates, and a diameter of 80 nm ( $d$ ), where  $\rho$  is the density for gold (19.3 g/cm<sup>3</sup>),  $M$  stands for atomic weight of gold (197 g/mol) and known initial

concentration of gold ( $C_{Au}$ ) added to the solution assuming a reaction yield of 100%. On the other hand, to calculate the extinction coefficient, molar the molar concentration of particles needs to be calculated. For that, first, the average number of gold atoms ( $N$ ) must be calculated using the **Equation 2**<sup>446</sup>, where  $\rho$ ,  $d$  and  $M$  have the same values as for the previous equation.

$$N_{seed} = \frac{6 \times 10^{21} C_{Au} M}{\pi \rho_{Au} d^3} \quad (1)$$

$$N = \frac{\pi \rho d^3}{6 M} \quad (2)$$

As described by Liu et al., (2006)<sup>446</sup>, this information can further be used to determine the molar concentration of the particles in solution. This can be done by using the **Equation 3**, where the total number of gold atoms ( $N_{total}$ , equivalent to the initial amount of gold salt added to the solution) is divided by the average number of gold atoms per sphere ( $N$ ), where  $V$  represents volume of the solution in litre,  $N_A$  represents Avogadro's constant and  $C$ , the concentration of particles in solution. It is assumed that all the gold salt added to the solution reacted 100%.

$$C = \frac{N_{total}}{NVN_A} \quad (3)$$

According to the equations above, a concentration of  $3.81 \times 10^{13}$  particles/mL was achieved or an initial molar concentration of  $6.46 \times 10^{-11}$  M. As mentioned above, this data was used to calculate the extinction coefficient, according to Lambert-Beer law (see **Equation 4**). The absorbance recorded at 530 nm was plotted against the concentration of the solution and the extinction coefficient was obtained from the slope of the linear region of the absorbance–concentration curve<sup>446</sup>. The extinction coefficient value achieved was  $4.33 \times 10^{10} \text{ M}^{-1} \text{ cm}^{-1}$ . In **Figure 6B** the linear fitting of the curve absorbance-concentration of the sample shows a good correlation coefficient. The

theoretical value achieved for the extinction coefficient of the Fe<sub>3</sub>O<sub>4</sub> core/Au shell particles assuming a size of 80 nm agrees with the values reported in the literature for spheric particles with a diameter between 60 and 80 nm for absorbances observed at 530-550 nm<sup>447-449</sup>, although those measurements were performed in water.

$$A = \varepsilon \times l \times C \quad (4)$$

### 3.2. Citrate capped Fe<sub>3</sub>O<sub>4</sub> core/Au shell particles characterization: FT-IR and UV-Vis

As the goal is to use these particles in biosensing platforms by immobilising thiolated DNA capture on their surface, the synthesized Fe<sub>3</sub>O<sub>4</sub> core/Au shell particles were transferred from toluene to water following a protocol described in **Section 2**, using citrate as capping agent. Sodium citrate is a very common chemical used for capping of AuNPs since is cheap, nontoxic and its negatively charged carboxylate groups are responsible for the charge stabilization of the particles<sup>450</sup>. FT-IR results of citrate capped Fe<sub>3</sub>O<sub>4</sub> core/Au shell particles are shown in **Figure 7**, using water as solvent. The broad band observed between 3500 and 3000 cm<sup>-1</sup> is attributed is C-OH stretching vibration, but the peaks observed from 1400 to 1300 cm<sup>-1</sup> are related to the asymmetric stretching vibration of carboxylate groups (COO<sup>-</sup>), thus, this could indicate the anchoring/adsorption of citrate on the surface of the Au shell<sup>451,452</sup>.

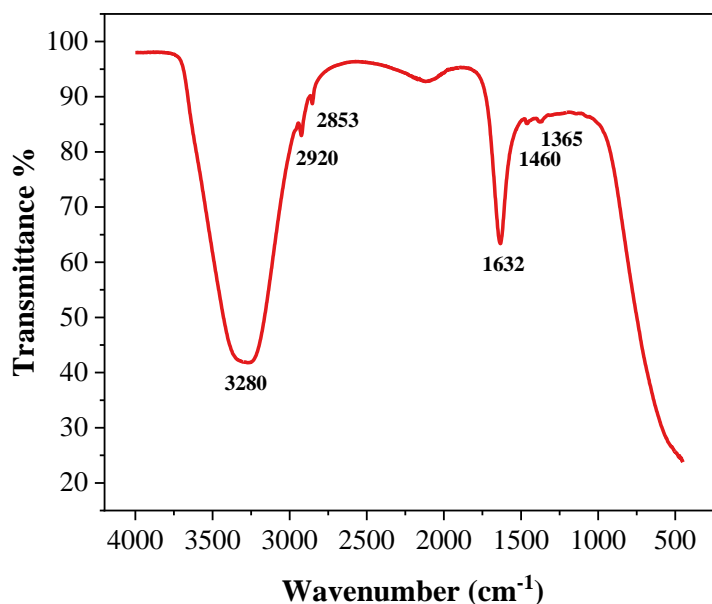


**Figure 7.** FT-IR spectra of citrate capped Fe<sub>3</sub>O<sub>4</sub>/Au shell aggregates in water.

Further characterization of the particles was performed using UV-Vis spectroscopy. **Figure 8** shows that after the phase transfer and capping with citrate, two absorption peaks were achieved, at  $\lambda_{\text{max}} = 580 \text{ nm}$  and  $\lambda_{\text{max}} = 697 \text{ nm}$ . The observation of these two peaks indicates aggregation of the Fe<sub>3</sub>O<sub>4</sub>/Au shell aggregates<sup>453,454</sup>. As particles could not remain dispersed in the solution, the interparticle distance becomes shorter causing aggregation, which enables plasmon coupling that leads to absorption at longer wavelengths<sup>442</sup>. It could be possible that citrate to particles ratio was very low, which can lead to poor capping and therefore, poor stability of the particles. Thus, further experiments are needed to optimize the citrate capping protocol in order to prevent aggregation and achieve high stability of the particles for posterior modification with thiolated DNA and utilisation in the development of a biosensor.

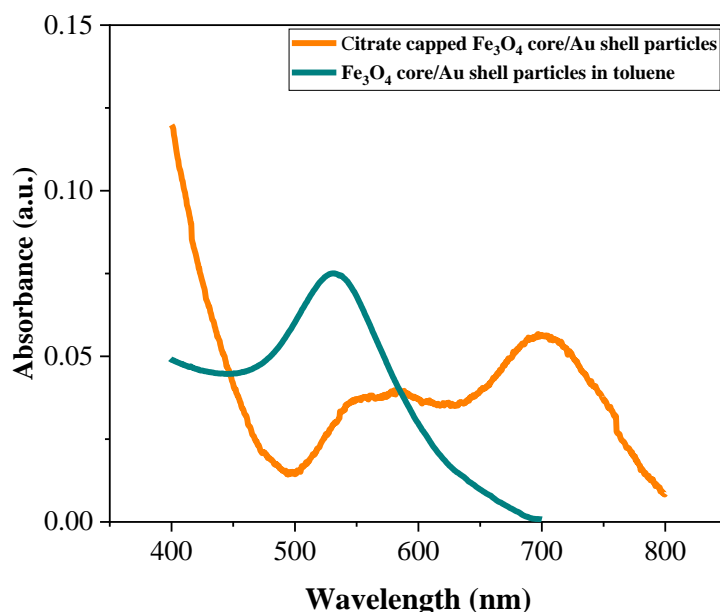


**Figure 8.** Absorbance spectra of citrate capped Fe<sub>3</sub>O<sub>4</sub> core/Au shell aggregates (in water) and Fe<sub>3</sub>O<sub>4</sub> core/Au shell particles (in toluene).

### 3.3. Theoretical DNA loading on Fe<sub>3</sub>O<sub>4</sub>/Au shell particles

As mentioned above, the objective of this chapter was to synthesize Fe<sub>3</sub>O<sub>4</sub> core/Au shell particles that could be used to develop a biosensor for bacterial DNA detection by exploiting the high affinity of the thiol groups for gold surfaces to modify citrate stabilized Au particles with thiolated DNA molecules. **Figure 9** shows an example of a possible applications of gold coated Fe<sub>3</sub>O<sub>4</sub> particles for single stranded DNA (ssDNA) detection on a ECL system. The gold coated electrodes could be further functionalized with capture ssDNA and incubated with target DNA for magnetic separation. Subsequently, the collected particles with hybridized target can be incubated with the DNA probe labelled with a ruthenium complex and a second magnetic separation step would remove all the not unhybridized probe strands. The last step would be to deposit the particles onto the electrode surface with the help of a magnet and ECL detection would then be performed.



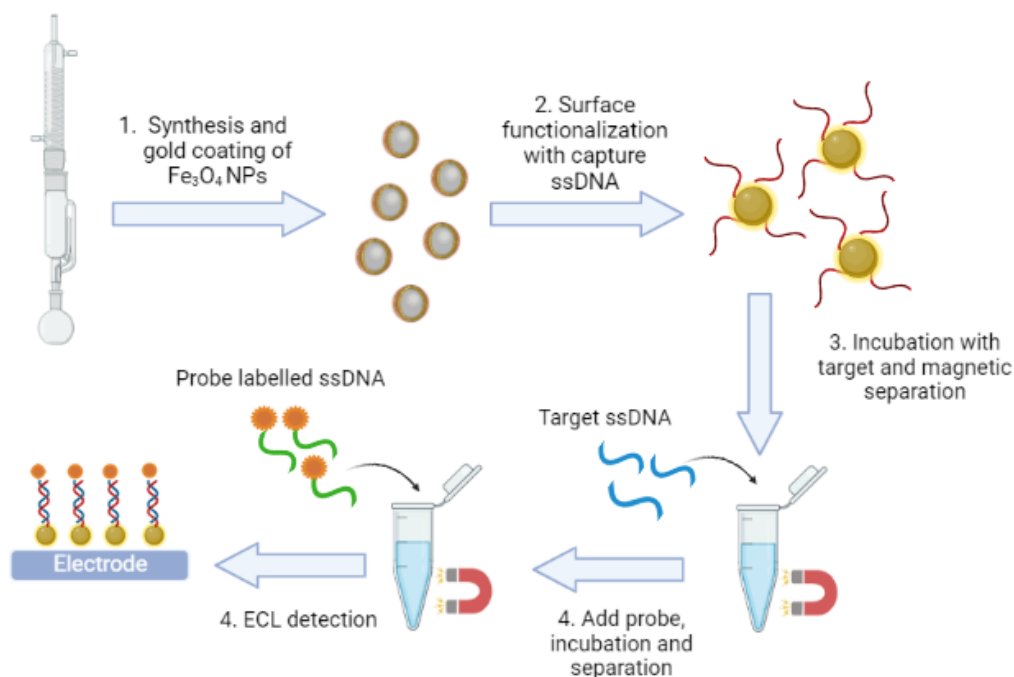


**Figure 9.** Schematic representation of the application of Fe<sub>3</sub>O<sub>4</sub> core/Au shell particles on a ECL platform for nucleic acids detection. Created in BioRender.com.

The aim of this section is to elucidate the optimal parameters according to size of Au particles for DNA immobilisation and potential application is biosensors. There are several parameters that need to be considered since they have significant influence on Au-DNA conjugates, that will directly impact on the hybridisation efficiency of the target DNA, such as surface coverage on the particle which affects the configuration of the attached capture strands, as well as nonspecific binding<sup>455,456</sup>. In order to develop an assay, is very important to obtain the optimal coverage of the particles. For that, calculating the possible maximum number of double stranded DNA molecules (dsDNA) on a particle surface can be useful. In this case, dsDNA is considered instead of single stranded DNA (ssDNA) since capture-target hybridisation must occurred for the detection. Thus, the total area occupied by dsDNA can be calculated by modelling the nucleic acid molecules as spheres, considering that the diameter of the double helix ranges from 2.6-2.9 nm<sup>457,458</sup>. Assuming, the packing density of the DNA molecules is 0.907, the average diameter of dsDNA molecule is 2.75, and the diameter of the particles, the **Equation 5**<sup>457</sup> can be used to calculate the maximum number of dsDNA molecules can be immobilised on a gold particle.

$$\text{Number of dsDNA molecule} = 0.907 \times \frac{\text{Surface area of particle}}{\text{Surface area occupied by dsDNA molecule}} \quad (5)$$

In **Figure 10** a model of DNA loading as a function of nanoparticle size is presented. As it can be observed, as the nanoparticle size increases (from 10 nm to 100 nm) the number of dsDNA molecules increases by two orders of magnitude. The estimated number of dsDNA molecules for maximum coverage of 80 nm diameter spherical particles (such as the ones presented in this chapter) is 768 per particle. The number of target molecules hybridising with the capture also can be calculated by assuming that on average, two target molecules out of four bind to the specific capture<sup>459,460</sup>. Considering also the previously calculated concentration of Fe<sub>3</sub>O<sub>4</sub> core/Au shell particles is 3.81 x 10<sup>13</sup> particles/mL, the estimated hybridised number of target molecules is 1.6 x 10<sup>16</sup> per mL (384 molecules per particle). All these calculations assume that there is an excess of both capture and target added to the sample, since the values showed in here can only be achieved under those specific conditions. On the other hand, curvature of sphere is another factor that could be considered since it has been shown that for nanoparticles with diameter > 60 nm, the nucleic acid coverage values are closer to the ones obtained for a flat gold surface, and smaller diameters are desirable since they present a larger surface curvature that promotes a better molecule spacing by preventing steric interactions<sup>461</sup>. However, as mentioned earlier, for the calculations presented above, the packing density of DNA molecules was considered according to the circle density limit<sup>462</sup>, where DNA molecules are modelled as spheres and their arrangement on given surface occurs without any overlap<sup>457</sup>. Therefore, different factors can be considered in order to build mathematical models for a better understanding and optimization of the experimental parameters with the aim to improve the analytical performance of systems/platforms.

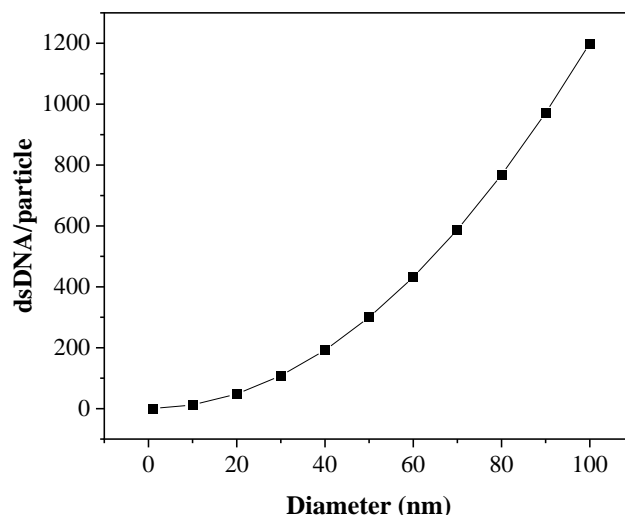


**Figure 10.** Model of dsDNA loading as a function of nanoparticle (from 1 nm to 100 nm diameter).

#### 4. CONCLUSIONS

In this Chapter, a new thermal decomposition method using both oleyl amine and oleic acid as capping agents for synthesis the synthesis  $\text{Fe}_3\text{O}_4$  particles as well as subsequent coating with gold, was described. Successful coating of the particles with gold would provide the possibility of functionalization with biomolecules such as DNA and develop a platform for bacteria detection. The results obtained under the SEM and TEM were unclear regarding to the size of the particles, however, the diameter of the magnetic core seemed to be approximately 8 nm, as expected. However, the particles are not size monodisperse and appear to be agglomerated and subsequently coated by gold. The spectroscopic analysis with UV-Vis suggests that the average diameter of the gold particles (possibly containing several magnetic cores), could be around 80 nm. Therefore, optimisation of the magnetic core to gold ratio could be key to achieve individually coated particles in future experiments. In addition, sample preparation of the particles for characterization under both SEM and TEM, requires drying steps which can compromise the sample and lead to more aggregation. This could be prevented by optimising the protocol for a better coverage of the particles with the capping agents. Furthermore, the phase transfer to aqueous solvent through exchanging the oleyl amine/oleic acid for citrate also revealed that optimisation of gold coated particle and capping agent ratio remains a challenge for a full coverage of the particles and avoid aggregates formation.

Thus, further experiments are needed to improve their stability and solubility for future application in biosensing platforms.

# **Chapter 6:**

## **Final remarks and future research work**

## 1. FINAL REMARKS

In this chapter, a brief overview of the main conclusions is provided as well as an outline of the future research opportunities for improving ECL systems and their application in biosensors. The research carried out for this project, has examined, and addressed a wide range of gold-based 2D and 3D platforms for ECL. This effort has focused on the understanding of the electrochemical properties of novel systems, as well as on the optical properties of the materials.

Firstly, the thesis presented a novel 3D printed Ti electrode array and explored its possible use as an ECL biosensing platform. The SEM characterization revealed a high roughness of the surface, and alongside their unique design (25 microcylinders on a porous square base), this provides a large surface area that could potentially increase the dynamic range and perhaps sensitivity of the platform by immobilising a larger number of capture molecules. Electrochemical characterization of the bare 3D printed Ti electrode array show that a thick layer of oxide forms spontaneously when titanium is exposed to air which inhibits electron transfer at the electrode surface. Therefore, is not possible to observe a well-defined faradaic process for a solution phase redox probe such as ferrocene methanol. In order to improve this situation, a thin layer of gold was electrodeposited using cyclic voltammetry. Successful electrodeposition was proven by SEM micrographs, which revealed the presence of deposited gold, as well as by characterization of the electrodes in 0.1M H<sub>2</sub>SO<sub>4</sub> showing the formation and reduction of gold oxide +1.4 V and +0.8 V, respectively. The electrochemical and ECL properties of the modified electrodes were further investigated. As opposed to bare 3D Ti electrodes, a faradaic process was observed when the FcnMeOH was tested as redox probe, and the current increased linearly with increasing scan rate. Significantly, ECL results showed that the performance of the gold coated arrays was superior to the bare 3D Ti electrodes in the co-reactant ECL system of [Ru(bpy)<sub>3</sub>]<sup>2+</sup> and TrPA. Therefore, gold coated 3D Ti electrodes could perhaps be further optimized to improve their catalytic and optical properties to maximise the benefits of their unique architecture for better analytical performance.

Secondly, due to the optical properties of AuNPs and their potential to be implemented in ECL systems, gold nanoparticles, 10 nm diameter AuNP, were analysed spectroscopically and electrochemically alongside different ruthenium (II) complexes to

better understand their interaction and elucidate key processes such as quenching and/or enhancement for future application in a SPR-ECL biosensing platforms. Two commercial ruthenium dyes ( $[\text{Ru}(\text{bpy})_3]^{2+}$  and  $[\text{Ru}(\text{bpy})_2(\text{phen})\text{-NH}_2]^{2+}$ ) were compared to a novel dye ( $[\text{Ru}(\text{bpy})_3\text{-NH}_2]^{2+}$ ). Both ECL and fluorescence results showed that upon addition of AuNPs quenching of the ruthenium-based emission occurs. Significantly, the zeta-potential values of AuNPs changed in the presence of the dyes that have an  $\text{-NH}_2$  functionality, ( $[\text{Ru}(\text{bpy})_3\text{-NH}_2]^{2+}$  and  $[\text{Ru}(\text{bpy})_2\text{-2PF}_6]^{2+}$ ). This arises because of the high affinity of the amine groups for gold suggesting that the possible mechanism of quenching for these dyes is predominantly static, rather than dynamic, quenching. Additionally, it was observed that the dye  $[\text{Ru}(\text{bpy})_3\text{-NH}_2]^{2+}$  shows higher ECL intensity as well as the highest ECL efficiency, compared to the commercial dyes, which makes it more suitable for ECL based biosensors. Therefore,  $[\text{Ru}(\text{bpy})_3\text{-NH}_2]^{2+}$  was used to label ssDNA probe strands and then used for the detection of *fimH* gene of urepathogenic *Escherichia coli*. Here, the first proof-of- concept ECL biosensor detecting *fimH* gene was reported, using glassy carbon electrodes coated with gold nanoparticles electrodeposited using cyclic voltammetry. Additionally, two co-reactants TrPA and NBEA were compared and ECL results show that NBEA gives a substantial increase in the ECL signal of  $[\text{Ru}(\text{bpy})_3\text{-NH}_2]^{2+}$  compared to the traditional TPrA, therefore, it was chosen as the optimal co-reactant for the development of the ECL biosensor. Cyclic voltammetry and electrochemical impedance spectroscopy (EIS) showed the successful co-immobilisation of ssDNA capture/MCH as well as hybridisation with the target. The developed biosensor could effectively detect the target, however, a high ECL background was observed when the probe was incubated with the capture strand. This probably arises because the Ru-labelled probe ssDNA could not be sufficiently purified due to the lack of sufficiently high G, temperature-controlled centrifuge.

Finally, as the focus of the thesis was to develop gold-based systems for their application in ECL biosensors and detection of bacteria, gold coated magnetic particles were investigated for the extraction and preconcentration of DNA based biomarkers. Thus, in the last chapter, a novel thermal decomposition method for the synthesis and of  $\text{Fe}_3\text{O}_4$  particles followed by the coating with a shell of gold was investigated, using oleyl amine and oleic acid as capping and/or stabilizing agents. The SEM and TEM revealed that 8 nm diameter magnetic cores were effectively synthesized, however, heterogeneous, and collective gold coating of magnetic particles was observed, indicating that aggregation

had occurred during the gold coating process. The plasmon peak observed with UV-Vis suggests that in solution (toluene), showed the presence of gold, however, it is belief that aggregation was still present. Therefore, further attempts are needed to find the best magnetic core to gold ratio as well as to achieve the optimal resistance to aggregation by tuning the concentration of the capping agents.

## 2. FUTURE RESEARCH WORK

In this thesis gold was investigated as suitable material for developing novel ECL based biosensors/platforms. In this regard, novel 3D Ti printed electrodes functionalised with a thin layer of gold served to improve the redox and ECL properties of the electrodes surface. Furthermore, this leads to the possibility of further functionalization through self-assembled monolayer (SAMs) of biomolecules such as antibodies which could be used for the detection of protein-based biomarkers or detection of whole-cell bacteria. In addition, as mentioned earlier, the unique architecture of the electrodes provides a larger surface area and therefore, a larger number of capture biomolecules can be immobilised improving the sensitivity of the assay. However, there are still some challenges to overcome such as generation of a homogeneous and identical layer of gold at every electrode, to achieve the highest reproducibility in the signal. Developing the optimal surface treatment before (to effectively remove the passive layer) and after electrodeposition of gold (to remove any residual impurities and activate the gold layer) is essential to achieve this goal.

Due to the excellent optical properties of AuNPs further experiments can be performed to understand better the quenching/enhancement mechanisms upon the interaction between the particles and the novel ruthenium dye,  $[\text{Ru}(\text{bpy})_3\text{-NH}_2]^{2+}$ . For that, dsDNA can be used as spacer, and different lengths could be tested to control the distance between luminophore and particle. In addition, these experiments could help to find the optimal distance to achieve the highest ECL signal enhancement which can be useful for the development of an SPR-ECL sensor for bacterial DNA detection. These studies could be performed in solution or a platform like the one presented in **Chapter 4**, however, as mentioned above, optimisation of the purification protocol for the Ru labelled DNA probes is needed to achieve the best results. This could also help to improve the assay



presented in this thesis for the detection of *fimH* gene from ureopathogenic *Escherichia coli* detection. Additionally, the same system could be transferred to different platforms containing Au particles, with the goal of point-of-care detection and diagnosis of bacterial infections. In this sense, the biodegradable and carbon-based screen-printed electrodes (SPCE) containing gold particles (such as the ones developed in our research group) could be potentially used for this purpose. The gold particles from the surface could serve as islands for immobilisation of biomolecules such as DNA capture strands. Here, the preliminary data obtained after the electrochemical and ECL characterization of SPCE electrodes containing gold spheres is presented (**Figure 1**), to demonstrate their potential as platforms for sensing applications. This SPCE are made of carbon-based inks, consisting of carbon particles with polymer binders, solvents and additives<sup>463</sup>. For the working electrode (3 mm diameter), this ink was mixed with 500 nm Au particles powder. Separately, a carbon counter and pseudo Ag/AgCl reference were manufacture in house on a single substrate. The electrodes were screen-printed using a DEK-248 semi-automatic screen-printer.

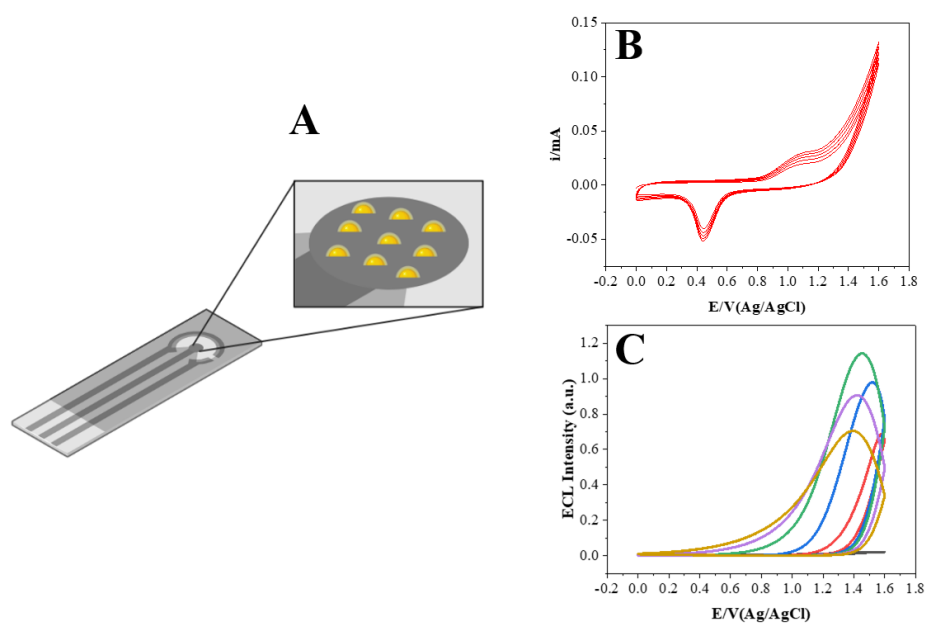


**Figure 1.** A) Schematic illustration of SPCE containing gold spheres. B) Voltammogram of SPCE containing gold spheres in 0.1M H<sub>2</sub>SO<sub>6</sub> (6 cycles). C) ECL intensities achieved with the electrodes in 0.1 mM [Ru(bpy)<sub>3</sub>]<sup>2+</sup> and 0.1 M TrPA using PBS as supporting electrolyte (scan rate study).

Further experiments could be carried out using different sizes of gold particles within the ink in order to in a ECL system in order to develop a SPR-ECL sensor with an amplified

signal. In addition to the advantages of ECL detection, it is scalable and it could be easily combine with SPEs in a cost-effective way for their application in POC systems for real on-site an real-time detection of diseases. On the other hand, 3D printing arises as a potential technology to develop platforms with unique and complex geometries with the aim of improving the mechanical and electrochemical properties of electrodes. In this sense, further shapes and structures could be investigated for their potential application in the biosensing field.

### 3. APPLICATIONS OUTSIDE SENSORS

As mentioned earlier, the focus of this thesis was to investigate different platforms and materials for their potential application in the biosensing field. However, the results obtained suggest that some of these platforms could have other applications outside the sensing area. For example, the 3D printed Ti electrodes presented in this work, showed to have a thick and semiconductive TiO<sub>2</sub> layer that could be exploited to develop systems for carbon dioxide (CO<sub>2</sub>) reduction through photocatalytic water splitting reaction<sup>464</sup>. CO<sub>2</sub> is one of the most produced greenhouse gases by the usage of the fossil fuel and its excessive emission to the atmosphere has been responsible of the global warming<sup>465</sup>. Therefore, many efforts have been put in the development of systems for the capture CO<sub>2</sub> from the atmosphere and produce hydrocarbons which can be used as a non-fossil energy source. In this sense, TiO<sub>2</sub> could be an excellent material since it is cheap, non-toxic, inert, highly stable, active and proven to be not very sensitive to extreme pH, which are desirable properties for photocatalytic applications<sup>466,467</sup>. Very little research has been done with 3D structures, however the data reported shown that 3D ordered nanostructures of TiO<sub>2</sub> enhanced the photocatalytic activity for the reduction of CO<sub>2</sub> with H<sub>2</sub>O<sup>468-471</sup>. Another application of 3D structure TiO<sub>2</sub> materials to solve environmental issues is the photoelectrochemical and photocatalytic production of hydrogen as clean-burning fuel since it combustion generates almost zero carbon emission with water and heat being the major combustion by-products. In fact, several studies have been recently publish using 3D printed TiO<sub>2</sub> microelectrodes for the production of hydrogen through water splitting<sup>472-474</sup>. Overall, synthesis and printing of 3D structures provides a promising

outlook by taking advantage of customisable designs that aim to develop systems with improved the photocatalytic and photoelectrochemical properties <sup>475</sup>.

In the field of photocatalysis, other types of materials/sensitisers can be investigated such as ruthenium (II) based complexes due to their unique photochemical properties. Ruthenium (II) and nanostructures TiO<sub>2</sub> has been shown to be an excellent combination for photocatalytic hydrogen evolution from water splitting<sup>476-479</sup> as well as photosensitizers for the development and application in dye-sensitized solar cells, for light harvesting and solar energy conversion<sup>480-483</sup>. In this sense, 3D printed TiO<sub>2</sub> platforms could be studied for their application in dye-sensitized solar cells alongside ruthenium dyes to improve the characteristics of this system. In conclusion, the materials investigated in this thesis could be applied in the biosensing field with aim of a fast detection of diseases, however, they are also transferrable to other fields. In this case, the photocatalytic and photoelectrochemical properties of ruthenium (II) complexes and TiO<sub>2</sub> can be exploited to develop systems that allows the production of clean/green energy in order to replace fossil fuels.

## BIBLIOGRAPHY

1. Samson R, Navale GR, Dharne MS. Biosensors: frontiers in rapid detection of COVID-19. *3 Biotech.* 2020;10(9):1-9. doi:10.1007/S13205-020-02369-0/FIGURES/4
2. Rasmi Y, Li X, Khan J, Ozer T, Choi JR. Emerging point-of-care biosensors for rapid diagnosis of COVID-19: current progress, challenges, and future prospects. *Anal Bioanal Chem.* 2021;413(16):4137-4159. doi:10.1007/S00216-021-03377-6/TABLES/2
3. Reynoso EC, Laschi S, Palchetti I, Torres E. Advances in Antimicrobial Resistance Monitoring Using Sensors and Biosensors: A Review. *Chemosens 2021, Vol 9, Page 232.* 2021;9(8):232. doi:10.3390/CHEMOSENSORS9080232
4. Rentschler S, Kaiser L, Deigner HP. Emerging Options for the Diagnosis of Bacterial Infections and the Characterization of Antimicrobial Resistance. *Int J Mol Sci 2021, Vol 22, Page 456.* 2021;22(1):456. doi:10.3390/IJMS22010456
5. Kaya HO, Cetin AE, Azimzadeh M, Topkaya SN. Pathogen detection with electrochemical biosensors: Advantages, challenges and future perspectives. *J Electroanal Chem.* 2021;882:114989. doi:10.1016/J.JELECHEM.2021.114989
6. Huang F, Zhang Y, Lin J, Liu Y. Biosensors Coupled with Signal Amplification Technology for the Detection of Pathogenic Bacteria: A Review. *Biosens 2021, Vol 11, Page 190.* 2021;11(6):190. doi:10.3390/BIOS11060190
7. Karbelkar AA, Furst AL. Electrochemical Diagnostics for Bacterial Infectious Diseases. *ACS Infect Dis.* 2020;6(7):1567-1571. doi:10.1021/ACSINFECDIS.0C00342
8. Cho IH, Kim DH, Park S. Electrochemical biosensors: perspective on functional nanomaterials for on-site analysis. *Biomater Res 2020 241.* 2020;24(1):1-12. doi:10.1186/S40824-019-0181-Y
9. Singh A, Sharma A, Ahmed A, et al. Recent Advances in Electrochemical Biosensors: Applications, Challenges, and Future Scope. *Biosens 2021, Vol 11, Page 336.* 2021;11(9):336. doi:10.3390/BIOS11090336

10. Banakar M, Hamidi M, Khurshid Z, et al. Electrochemical Biosensors for Pathogen Detection: An Updated Review. *Biosens 2022, Vol 12, Page 927*. 2022;12(11):927. doi:10.3390/BIOS12110927
11. Cesewski E, Johnson BN. Electrochemical biosensors for pathogen detection. *Biosens Bioelectron*. 2020;159:112214. doi:10.1016/J.BIOS.2020.112214
12. Ronkainen NJ, Halsall HB, Heineman WR. Electrochemical biosensors. *Chem Soc Rev*. 2010;39(5):1747-1763. doi:10.1039/b714449k
13. Marin M, Nikolic MV, Vidic J. Rapid point-of-need detection of bacteria and their toxins in food using gold nanoparticles. *Compr Rev Food Sci Food Saf*. 2021;20(6):5880-5900. doi:10.1111/1541-4337.12839
14. Omar MH, Razak KA, Ab Wahab MN, Hamzah HH. Recent progress of conductive 3D-printed electrodes based upon polymers/carbon nanomaterials using a fused deposition modelling (FDM) method as emerging electrochemical sensing devices. *RSC Adv*. 2021;11(27):16557-16571. doi:10.1039/D1RA01987B
15. Liyarita BR, Ambrosi A, Pumera M. 3D-printed Electrodes for Sensing of Biologically Active Molecules. *Electroanalysis*. 2018;30(7):1319-1326. doi:10.1002/ELAN.201700828
16. Remaggi G, Zaccarelli A, Elviri L. 3D Printing Technologies in Biosensors Production: Recent Developments. *Chemosensors*. 2022;10(2):65. doi:10.3390/CHEMOSENSORS10020065/S1
17. Tang Z, Jia S, Zhou C, Li B. 3D Printing of Highly Sensitive and Large-Measurement-Range Flexible Pressure Sensors with a Positive Piezoresistive Effect. *ACS Appl Mater Interfaces*. 2020;12(25):28669-28680. doi:10.1021/ACSAMI.0C06977/SUPPL\_FILE/AM0C06977\_SI\_001.PDF
18. Abdalla A, Patel BA. 3D-printed electrochemical sensors: A new horizon for measurement of biomolecules. *Curr Opin Electrochem*. 2020;20:78-81. <https://doi.org/10.1016/j.coelec.2020.04.009>
19. Huang F, Zhang Y, Lin J, Liu Y. Biosensors Coupled with Signal Amplification Technology for the Detection of Pathogenic Bacteria: A Review. *Biosens 2021, Vol 11, Page 190*. 2021;11(6):190. doi:10.3390/BIOS11060190

20. Mittal S, Kaur H, Gautam N, Mantha AK. Biosensors for breast cancer diagnosis: A review of bioreceptors, biotransducers and signal amplification strategies. *Biosens Bioelectron.* 2017;88:217-231. doi:10.1016/J.BIOS.2016.08.028
21. Wang Y, Li B, Tian T, Liu Y, Zhang J, Qian K. Advanced on-site and in vitro signal amplification biosensors for biomolecule analysis. *TrAC Trends Anal Chem.* 2022;149:116565. doi:10.1016/J.TRAC.2022.116565
22. Dinel MP, Tartaggia S, Wallace GQ, Boudreau D, Masson JF, Polo F. The Fundamentals of Real-Time Surface Plasmon Resonance/Electrogenerated Chemiluminescence. *Angew Chemie Int Ed.* 2019;58(50):18202-18206. doi:10.1002/ANIE.201909806
23. Ma C, Zhang Z, Tan T, Zhu JJ. Recent Progress in Plasmonic based Electrochemiluminescence Biosensors: A Review. *Biosens 2023, Vol 13, Page 200.* 2023;13(2):200. doi:10.3390/BIOS13020200
24. Wang Q, Ren ZH, Zhao WM, et al. Research advances on surface plasmon resonance biosensors. *Nanoscale.* 2022;14(3):564-591. doi:10.1039/D1NR05400G
25. Sin ML, Mach KE, Wong PK, Liao JC. Advances and challenges in biosensor-based diagnosis of infectious diseases. <https://doi.org/10.1586/147371592014888313>. 2014;14(2):225-244. doi:10.1586/14737159.2014.888313
26. Wang L, Lin J. Recent advances on magnetic nanobead based biosensors: From separation to detection. *TrAC Trends Anal Chem.* 2020;128:115915. doi:10.1016/J.TRAC.2020.115915
27. de Eguilaz MR, Cumba LR, Forster RJ. Electrochemical detection of viruses and antibodies: A mini review. *Electrochem commun.* 2020;116:106762. doi:10.1016/J.ELECOM.2020.106762
28. Monteil S, Casson AJ, Jones ST. Electronic and electrochemical viral detection for point-of-care use: A systematic review. *PLoS One.* 2021;16(9):e0258002. doi:10.1371/JOURNAL.PONE.0258002
29. Suhito IR, Koo KM, Kim TH. Recent Advances in Electrochemical Sensors for

- the Detection of Biomolecules and Whole Cells. *Biomed 2021, Vol 9, Page 15*. 2020;9(1):15. doi:10.3390/BIOMEDICINES9010015
30. Divya, Dkhar DS, Kumari R, Mahapatra S, Kumar R, Chandra P. Ultrasensitive Aptasensors for the Detection of Viruses Based on Opto-Electrochemical Readout Systems. *Biosens 2022, Vol 12, Page 81*. 2022;12(2):81. doi:10.3390/BIOS12020081
  31. Thapa K, Liu W, Wang R. Nucleic acid-based electrochemical biosensor: Recent advances in probe immobilization and signal amplification strategies. *Wiley Interdiscip Rev Nanomedicine Nanobiotechnology*. 2022;14(1):e1765. doi:10.1002/WNAN.1765
  32. Huo XL, Lu HJ, Xu JJ, Zhou H, Chen HY. Recent advances of ratiometric electrochemiluminescence biosensors. *J Mater Chem B*. 2019;7(42):6469-6475. doi:10.1039/C9TB01823A
  33. Shi Z, Li G, Hu Y. Progress on the application of electrochemiluminescence biosensor based on nanomaterials. *Chinese Chem Lett*. 2019;30(9):1600-1606. doi:10.1016/J.CCLET.2019.04.066
  34. Chen Y, Zhou S, Li L, Zhu J jie. Nanomaterials-based sensitive electrochemiluminescence biosensing. *Nano Today*. 2017;12:98-115. doi:10.1016/J.NANTOD.2016.12.013
  35. Adhikari J, Rizwan M, Keasberry NA, Ahmed MU. Current progresses and trends in carbon nanomaterials-based electrochemical and electrochemiluminescence biosensors. *J Chinese Chem Soc*. 2020;67(6):937-960. doi:10.1002/JCCS.201900417
  36. Yoo SM, Jeon YM, Heo SY. Electrochemiluminescence Systems for the Detection of Biomarkers: Strategical and Technological Advances. *Biosens 2022, Vol 12, Page 738*. 2022;12(9):738. doi:10.3390/BIOS12090738
  37. Wang Q, Ren ZH, Zhao WM, et al. Research advances on surface plasmon resonance biosensors. *Nanoscale*. 2022;14(3):564-591. doi:10.1039/D1NR05400G
  38. Dinel M-P, Tartaggia S, Wallace GQ, Boudreau D, Masson J-F, Polo F. The

- Fundamentals of Real-Time Surface Plasmon Resonance/Electrogenerated Chemiluminescence. *Angew Chemie.* 2019;131(50):18370-18374. doi:10.1002/ANGE.201909806
39. Li MX, Zhao W, Qian GS, Feng QM, Xu JJ, Chen HY. Distance mediated electrochemiluminescence enhancement of CdS thin films induced by the plasmon coupling of gold nanoparticle dimers. *Chem Commun.* 2016;52(99):14230-14233. doi:10.1039/C6CC08441A
  40. Yarakı MT, Tan YN. Metal Nanoparticles-Enhanced Biosensors: Synthesis, Design and Applications in Fluorescence Enhancement and Surface-enhanced Raman Scattering. *Chem – An Asian J.* 2020;15(20):3180-3208. doi:10.1002/ASIA.202000847
  41. Purohit B, Vernekar PR, Shetti NP, Chandra P. Biosensor nanoengineering: Design, operation, and implementation for biomolecular analysis. *Sensors Int.* 2020;1:100040. doi:10.1016/J.SINTL.2020.100040
  42. Carpenter AC, Paulsen IT, Williams TC. Blueprints for Biosensors: Design, Limitations, and Applications. doi:10.3390/genes9080375
  43. Vidic J, Manzano M. Electrochemical biosensors for rapid pathogen detection. *Curr Opin Electrochem.* 2021;29:100750. doi:10.1016/J.COEELEC.2021.100750
  44. Ahmed A, Rushworth J V, Hirst NA, Millner PA. Biosensors for Whole-Cell Bacterial Detection. Published online 2014. doi:10.1128/CMR.00120-13
  45. Zhang S, Li X, Wu J, et al. Molecular Methods for Pathogenic Bacteria Detection and Recent Advances in Wastewater Analysis. *Water 2021, Vol 13, Page 3551.* 2021;13(24):3551. doi:10.3390/W13243551
  46. Menon S, Mathew MR, Sam S, Keerthi K, Kumar KG. Recent advances and challenges in electrochemical biosensors for emerging and re-emerging infectious diseases. *J Electroanal Chem.* 2020;878:114596. doi:10.1016/J.JELECHEMA.2020.114596
  47. Koyappayil A, Lee MH. Ultrasensitive Materials for Electrochemical Biosensor Labels. *Sensors 2021, Vol 21, Page 89.* 2020;21(1):89. doi:10.3390/S21010089
  48. Syahir A, Usui K, Tomizaki K, Kajikawa K, Mihara H. Label and Label-Free



- Detection Techniques for Protein Microarrays. *Microarrays 2015, Vol 4, Pages 228-244*. 2015;4(2):228-244. doi:10.3390/MICROARRAYS4020228
49. Liu Y, Liu Y, Qiao L, Liu Y, Liu B. Advances in signal amplification strategies for electrochemical biosensing. *Curr Opin Electrochem*. 2018;12:5-12. doi:10.1016/J.COEELEC.2018.05.001
  50. Koyappayil A, Lee MH. Ultrasensitive Materials for Electrochemical Biosensor Labels. *Sensors (Basel)*. 2021;21(1):1-19. doi:10.3390/S21010089
  51. Li H, Han Y, Zhao H, Jafri H, Tian B. Dyes as Labels in Biosensing. *Dye Pigment - Nov Appl Waste Treat*. Published online March 1, 2021. doi:10.5772/INTECHOPEN.96540
  52. Kokkinos C. Electrochemical DNA Biosensors Based on Labeling with Nanoparticles. *Nanomater 2019, Vol 9, Page 1361*. 2019;9(10):1361. doi:10.3390/NANO9101361
  53. Prodromidis MI, Economou A. New Trends in Antibody-Based Electrochemical Biosensors. *Compr Anal Chem*. 2017;77:55-100. doi:10.1016/BS.COAC.2017.05.001
  54. Yang H. Enzyme-based ultrasensitive electrochemical biosensors. *Curr Opin Chem Biol*. 2012;16(3-4):422-428. doi:10.1016/J.CBPA.2012.03.015
  55. Sang S, Wang Y, Feng Q, Wei Y, Ji J, Zhang W. Progress of new label-free techniques for biosensors: a review. <http://dx.doi.org/10.3109/073885512014991270>. 2015;36(3):465-481. doi:10.3109/07388551.2014.991270
  56. Mahato K, Kumar S, Srivastava A, Maurya PK, Singh R, Chandra P. Electrochemical Immunosensors: Fundamentals and Applications in Clinical Diagnostics. *Handb Immunoass Technol Approaches, Performances, Appl*. Published online January 1, 2018:359-414. doi:10.1016/B978-0-12-811762-0.00014-1
  57. Silva NFD, Neves MMPS, Magalhães JMCS, Freire C, Delerue-Matos C. Electrochemical immunosensor towards invasion-associated protein p60: An alternative strategy for *Listeria monocytogenes* screening in food. *Talanta*.

- 2020;216:120976. doi:10.1016/J.TALANTA.2020.120976
58. He H, Sun T, Liu W, et al. Highly sensitive detection of salbutamol by ALP-mediated plasmonic ELISA based on controlled growth of AgNPs. *Microchem J.* 2020;156. doi:10.1016/J.MICROC.2020.104804
  59. Liu Y, Pan M, Wang W, et al. Plasmonic and Photothermal Immunoassay via Enzyme-Triggered Crystal Growth on Gold Nanostars. *Anal Chem.* 2019;91(3):2086-2092. doi:10.1021/ACS.ANALCHEM.8B04517/ASSET/IMAGES/LARGE/AC-2018-045175\_0006.JPEG
  60. Mazzei F, Botrè F, Montilla S, Pilloton R, Podestà E, Botrè C. Alkaline phosphatase inhibition based electrochemical sensors for the detection of pesticides. *J Electroanal Chem.* 2004;574(1):95-100. doi:10.1016/J.JELECHEM.2004.08.004
  61. Eissa S, Zourob M. Ultrasensitive peptide-based multiplexed electrochemical biosensor for the simultaneous detection of *Listeria monocytogenes* and *Staphylococcus aureus*. *Microchim Acta.* 2020;187(9):1-11. doi:10.1007/S00604-020-04423-3/FIGURES/5
  62. Li F, Ye Q, Chen M, et al. An ultrasensitive CRISPR/Cas12a based electrochemical biosensor for *Listeria monocytogenes* detection. *Biosens Bioelectron.* 2021;179:113073. doi:10.1016/J.BIOS.2021.113073
  63. Han J-H, Lee D, Chew CHC, Kim T, Pak JJ. A multi-virus detectable microfluidic electrochemical immunosensor for simultaneous detection of H1N1, H5N1, and H7N9 virus using {ZnO} nanorods for sensitivity enhancement. 228:36-42. doi:10.1016/j.snb.2015.07.068
  64. Napi MLM, Sultan SM, Ismail R, How KW, Ahmad MK. Electrochemical-Based Biosensors on Different Zinc Oxide Nanostructures: A Review. *Materials (Basel).* 2019;12(18). doi:10.3390/MA12182985
  65. Bukkitgar SD, Kumar S, Pratibha, et al. Functional nanostructured metal oxides and its hybrid electrodes – Recent advancements in electrochemical biosensing applications. *Microchem J.* 2020;159:105522.

doi:10.1016/J.MICROC.2020.105522

66. Lee T, Park SY, Jang H, et al. Fabrication of electrochemical biosensor consisted of multi-functional DNA structure/porous au nanoparticle for avian influenza virus (H5N1) in chicken serum. *Mater Sci Eng C*. 2019;99:511-519. doi:10.1016/J.MSEC.2019.02.001
67. Kwon J, Lee Y, Lee T, Ahn JH. Aptamer-Based Field-Effect Transistor for Detection of Avian Influenza Virus in Chicken Serum. *Anal Chem*. 2020;92(7):5524-5531. doi:10.1021/ACS.ANALCHEM.0C00348/ASSET/IMAGES/LARGE/AC0C00348\_0005.JPEG
68. Oliver ZT, Hogan M, Albats E. Bridging the Knowledge and Business Ecosystems: Resources and Mechanisms for Regional Entrepreneurial Development. *Triple Helix J*. 2020;1(aop):1-39. doi:10.1163/21971927-bja10008
69. Forster RJ, De Eguilaz MR, Barhoum A, Cumba LR. Electrochemical (Bio)Sensors for Bacteria and Biofilms. *Ref Modul Biomed Sci*. Published online January 1, 2022. doi:10.1016/B978-0-12-822548-6.00117-5
70. Shoaie N, Forouzandeh M, Omidfar K. Voltammetric determination of the Escherichia coli DNA using a screen-printed carbon electrode modified with polyaniline and gold nanoparticles. *Microchim Acta*. 2018;185(4):1-9. doi:10.1007/S00604-018-2749-Y/TABLES/1
71. Paniel N, Baudart J. Colorimetric and electrochemical genosensors for the detection of Escherichia coli DNA without amplification in seawater. *Talanta*. 2013;115:133-142. doi:10.1016/J.TALANTA.2013.04.050
72. Pandey R, Chang D, Smieja M, Hoare T, Li Y, Soleymani L. Integrating programmable DNazymes with electrical readout for rapid and culture-free bacterial detection using a handheld platform. *Nat Chem* 2021 139. 2021;13(9):895-901. doi:10.1038/s41557-021-00718-x
73. Pandey R, Lu Y, Osman E, et al. DNazyme-Immobilizing Microgel Magnetic Beads Enable Rapid, Specific, Culture-Free, and Wash-Free Electrochemical Quantification of Bacteria in Untreated Urine. *ACS Sensors*. 2022;7(4):985-994.

doi:10.1021/ACSSENSORS.1C02440

74. Toyos-Rodríguez C, García-Alonso FJ, de la Escosura-Muñiz A. Electrochemical Biosensors Based on Nanomaterials for Early Detection of Alzheimer's Disease. *Sensors* 2020, Vol 20, Page 4748. 2020;20(17):4748. doi:10.3390/S20174748
75. Liu L, Deng D, Sun W, Yang X, Yang S, He S. ELECTROCHEMICAL SCIENCE Electrochemical Biosensors with Electrocatalysts Based on Metallic Nanomaterials as Signal Labels. *Int J Electrochem Sci*. 2018;13:10496-10513. doi:10.20964/2018.11.47
76. Bonnet R, Farre C, Valera L, et al. Highly labeled methylene blue-ds DNA silica nanoparticles for signal enhancement of immunoassays: application to the sensitive detection of bacteria in human platelet concentrates. *Analyst*. 2018;143(10):2293-2303. doi:10.1039/C8AN00165K
77. Imran M, Ehrhardt CJ, Bertino MF, Shah MR, Yadavalli VK. Chitosan Stabilized Silver Nanoparticles for the Electrochemical Detection of Lipopolysaccharide: A Facile Biosensing Approach for Gram-Negative Bacteria. *Micromachines* 2020, Vol 11, Page 413. 2020;11(4):413. doi:10.3390/MI11040413
78. Lee CW, Chang HY, Wu JK, Tseng FG. Ultra-sensitive electrochemical detection of bacteremia enabled by redox-active gold nanoparticles (raGNPs) in a nano-sieving microfluidic system (NS-MFS). *Biosens Bioelectron*. 2019;133:215-222. doi:10.1016/J.BIOS.2019.03.040
79. Chen Y, Guo S, Zhao M, et al. Amperometric DNA biosensor for Mycobacterium tuberculosis detection using flower-like carbon nanotubes-polyaniline nanohybrid and enzyme-assisted signal amplification strategy. *Biosens Bioelectron*. 2018;119:215-220. doi:10.1016/J.BIOS.2018.08.023
80. Ang WL, Seah XY, Koh PC, Caroline C, Bonanni A. Electrochemical Polymerase Chain Reaction Using Electroactive Graphene Oxide Nanoparticles as Detection Labels. *ACS Appl Nano Mater*. 2020;3(6):5489-5498. doi:10.1021/ACSANM.0C00797/ASSET/IMAGES/LARGE/AN0C00797\_0006.JPEG
81. Vigneshvar S, Sudhakumari CC, Senthilkumaran B, Prakash H. Recent advances

- in biosensor technology for potential applications - an overview. *Front Bioeng Biotechnol.* 2016;4(FEB):11. doi:10.3389/FBIOE.2016.00011/BIBTEX
82. Gao Z, Li Y, Zhang X, et al. Ultrasensitive electrochemical immunosensor for quantitative detection of {HBeAg} using Au@Pd/{MoS}<sub>2</sub>@{MWCNTs} nanocomposite as enzyme-mimetic labels. 102:189-195. doi:10.1016/j.bios.2017.11.032
  83. Oliveira TMBF, Morais S. New Generation of Electrochemical Sensors Based on Multi-Walled Carbon Nanotubes. *Appl Sci* 2018, Vol 8, Page 1925. 2018;8(10):1925. doi:10.3390/APP8101925
  84. Cho I-H, Kim DH, Park S. Electrochemical biosensors: perspective on functional nanomaterials for on-site analysis. doi:10.1186/s40824-019-0181-y
  85. Kannan P, Maduraiveeran G. Bimetallic Nanomaterials-Based Electrochemical Biosensor Platforms for Clinical Applications. *Micromachines* 2022, Vol 13, Page 76. 2021;13(1):76. doi:10.3390/MI13010076
  86. Bruno L, Scuderi M, Priolo F, Falciola L, Mirabella S. Enlightening the bimetallic effect of Au@Pd nanoparticles on Ni oxide nanostructures with enhanced catalytic activity. Published online 123AD. doi:10.1038/s41598-023-29679-6
  87. Huang Y, Ferhan AR, Dandapat A, et al. A Strategy for the Formation of Gold-Palladium Supra-Nanoparticles from Gold Nanoparticles of Various Shapes and Their Application to High-Performance H<sub>2</sub>O<sub>2</sub> Sensing. *J Phys Chem C.* 2015;119(46):26164-26170. doi:10.1021/ACS.JPCC.5B08423/ASSET/IMAGES/LARGE/JP-2015-08423B\_0007.JPEG
  88. Vilian ATE, Dinesh B, Kang SM, Krishnan UM, Huh YS, Han YK. Recent advances in molybdenum disulfide-based electrode materials for electroanalytical applications. *Microchim Acta.* 2019;186(3):1-29. doi:10.1007/S00604-019-3287-Y/FIGURES/7
  89. Wang T, Du K, Liu W, Zhang J, Li M. Electrochemical Sensors Based on Molybdenum Disulfide Nanomaterials. *Electroanalysis.* 2015;27(9):2091-2097. doi:10.1002/ELAN.201500117

90. Rajan AG, Mark J, Martirez P, Carter EA. Coupled Effects of Temperature, Pressure, and pH on Water Oxidation Thermodynamics and Kinetics. Published online 2021. doi:10.1021/acscatal.1c02428
91. McHugh PJ, Stergiou AD, Symes MD. Decoupled Electrochemical Water Splitting: From Fundamentals to Applications. *Adv Energy Mater.* 2020;10(44):2002453. doi:10.1002/AENM.202002453
92. Wei C, Rao RR, Peng J, et al. Recommended Practices and Benchmark Activity for Hydrogen and Oxygen Electrocatalysis in Water Splitting and Fuel Cells. *Adv Mater.* 2019;31(31):1806296. doi:10.1002/ADMA.201806296
93. Rogers JK, Taylor ND, Church GM. Biosensor-based engineering of biosynthetic pathways. *Curr Opin Biotechnol.* 2016;42:84-91. doi:10.1016/J.COPBIO.2016.03.005
94. Wei B, Zhang J, Ou X, Lou X, Xia F, Vallée-Bélisle A. Engineering Biosensors with Dual Programmable Dynamic Ranges. *Anal Chem.* 2018;90(3):1506-1510. doi:10.1021/ACS.ANALCHEM.7B04852/ASSET/IMAGES/LARGE/AC-2017-04852W\_0004.JPEG
95. Nguyen DQ, Ishiki K, Shiigi H. Single cell immunodetection of Escherichia coli O157:H7 on an indium-tin-oxide electrode by using an electrochemical label with an organic-inorganic nanostructure. *Microchim Acta.* 2018;185(10):1-8. doi:10.1007/S00604-018-3001-5/TABLES/2
96. Kucherenko IS, Soldatkin OO, Kucherenko DY, Soldatkina O V., Dzyadevych S V. Advances in nanomaterial application in enzyme-based electrochemical biosensors: a review. *Nanoscale Adv.* 2019;1(12):4560-4577. doi:10.1039/C9NA00491B
97. Majdinasab M, Mitsubayashi K, Marty JL. Optical and Electrochemical Sensors and Biosensors for the Detection of Quinolones. *Trends Biotechnol.* 2019;37(8):898-915. doi:10.1016/J.TIBTECH.2019.01.004
98. Shoaie N, Daneshpour M, Azimzadeh M, et al. Electrochemical sensors and biosensors based on the use of polyaniline and its nanocomposites: a review on recent advances. *Microchim Acta 2019 1867.* 2019;186(7):1-29.

doi:10.1007/S00604-019-3588-1

99. Luong JHT, Narayan T, Solanki S, Malhotra BD. Recent Advances of Conducting Polymers and Their Composites for Electrochemical Biosensing Applications. *J Funct Biomater* 2020, Vol 11, Page 71. 2020;11(4):71. doi:10.3390/JFB11040071
100. El-Said WA, Abdelshakour M, Choi JH, Choi JW. Application of Conducting Polymer Nanostructures to Electrochemical Biosensors. *Mol* 2020, Vol 25, Page 307. 2020;25(2):307. doi:10.3390/MOLECULES25020307
101. Wongkaew N, Simsek M, Griesche C, Baeumner AJ. Functional Nanomaterials and Nanostructures Enhancing Electrochemical Biosensors and Lab-on-a-Chip Performances: Recent Progress, Applications, and Future Perspective. *Chem Rev.* 2019;119(1):120-194.  
doi:10.1021/ACS.CHEMREV.8B00172/ASSET/IMAGES/MEDIUM/CR-2018-00172J\_0046.GIF
102. Shahrokhian S, Ranjbar S. Aptamer immobilization on amino-functionalized metal–organic frameworks: an ultrasensitive platform for the electrochemical diagnostic of Escherichia coli O157:H7. *Analyst.* 2018;143(13):3191-3201. doi:10.1039/C8AN00725J
103. Zhang Q, Li L, Qiao Z, et al. Electrochemical Conversion of Fe<sub>3</sub>O<sub>4</sub> Magnetic Nanoparticles to Electroactive Prussian Blue Analogues for Self-Sacrificial Label Biosensing of Avian Influenza Virus H5N1. 89(22):12145-12151. doi:10.1021/acs.analchem.7b02784
104. Mollarasouli F, Zor E, Ozcelikay G, Ozkan SA. Magnetic nanoparticles in developing electrochemical sensors for pharmaceutical and biomedical applications. *Talanta.* 2021;226:122108. doi:10.1016/J.TALANTA.2021.122108
105. Hasanzadeh M, Shadjou N, de la Guardia M. Iron and iron-oxide magnetic nanoparticles as signal-amplification elements in electrochemical biosensing. *TrAC Trends Anal Chem.* 2015;72:1-9. doi:10.1016/J.TRAC.2015.03.016
106. Estelrich J, Busquets MA. Prussian Blue: A Safe Pigment with Zeolitic-Like Activity. *Int J Mol Sci.* 2021;22(2):1-14. doi:10.3390/IJMS22020780
107. Ivanov VD. Four decades of electrochemical investigation of Prussian blue. *Ionics*

- 2019 262. 2019;26(2):531-547. doi:10.1007/S11581-019-03292-Y
108. Komkova MA, Andreev EA, Ibragimova OA, Karyakin AA. Prussian Blue based flow-through (bio)sensors in power generation mode: New horizons for electrochemical analyzers. *Sensors Actuators B Chem.* 2019;292:284-288. doi:10.1016/J.SNB.2019.04.134
  109. Koncki R. Chemical Sensors and Biosensors Based on Prussian Blues. <http://dx.doi.org/101080/10408340290765452>. 2010;32(1):79-96. doi:10.1080/10408340290765452
  110. Jerez-Masaquiza MD, Fernández L, González G, Montero-Jiménez M, Espinoza-Montero PJ. Electrochemical Sensor Based on Prussian Blue Electrochemically Deposited at ZrO<sub>2</sub> Doped Carbon Nanotubes Glassy Carbon Modified Electrode. *Nanomater (Basel, Switzerland)*. 2020;10(7):1-21. doi:10.3390/NANO10071328
  111. Kaufmann L, Syedbasha M, Vogt D, et al. An Optimized Hemagglutination Inhibition (HI) Assay to Quantify Influenza-specific Antibody Titers. *J Vis Exp.* 2017;2017(130):55833. doi:10.3791/55833
  112. Xu L, Wang R, Kelso LC, Ying Y, Li Y. A target-responsive and size-dependent hydrogel aptasensor embedded with QD fluorescent reporters for rapid detection of avian influenza virus H5N1. *Sensors Actuators B Chem.* 2016;234:98-108. doi:10.1016/J.SNB.2016.04.156
  113. Lum J, Wang R, Hargis B, et al. An Impedance Aptasensor with Microfluidic Chips for Specific Detection of H5N1 Avian Influenza Virus. *Sensors 2015, Vol 15, Pages 18565-18578*. 2015;15(8):18565-18578. doi:10.3390/S150818565
  114. Bai H, Wang R, Hargis B, Lu H, Li Y. A SPR aptasensor for detection of avian influenza virus H5N1. *Sensors (Basel)*. 2012;12(9):12506-12518. doi:10.3390/S120912506
  115. Rizwan M, Mohd-Naim NF, Ahmed MU. Trends and Advances in Electrochemiluminescence Nanobiosensors. *Sensors 2018, Vol 18, Page 166*. 2018;18(1):166. doi:10.3390/S18010166
  116. Martínez-Periñán E, Gutiérrez-Sánchez C, García-Mendiola T, Lorenzo E. Electrochemiluminescence Biosensors Using Screen-Printed Electrodes. *Biosens*



117. Zu Y, Bard AJ. Electrogenenerated chemiluminescence. 66. The role of direct coreactant oxidation in the ruthenium tris(2,2')bipyridyl/triethylamine system and the effect of halide ions on the emission intensity. *Anal Chem.* 2000;72(14):3223-3232. doi:10.1021/AC000199Y
118. Wallace WL, Bard AJ, Wallace WL, Bard AJ. *Electrogenenerated Chemiluminescence. 35. Temperature Dependence of the ECL Efficiency of Ru(Bpy)<sub>3</sub><sup>2+</sup> in Acetonitrile and Evidence for Very High Excited State Yields from Electron Transfer Reactions.* Vol 83.; 1979.
119. Forster RJ, Bertonecello P, Keyes TE. Electrogenenerated Chemiluminescence. Published online 2009. doi:10.1146/annurev-anchem-060908-155305
120. Kerr E, Doeven EH, Barbante GJ, et al. New perspectives on the annihilation electrogenerated chemiluminescence of mixed metal complexes in solution. *Chem Sci.* 2016;7(8):5271-5279. doi:10.1039/C6SC01570K
121. Richter MM. Electrochemiluminescence (ECL). *Chem Rev.* 2004;104(6):3003-3036.  
doi:10.1021/CR020373D/ASSET/IMAGES/LARGE/CR020373DF00025.JPEG
122. Irkham, Watanabe T, Fiorani A, Valenti G, Paolucci F, Einaga Y. Co-reactant-on-Demand ECL: Electrogenenerated Chemiluminescence by the in Situ Production of S<sub>2</sub>O<sub>8</sub><sup>2-</sup> at Boron-Doped Diamond Electrodes. *J Am Chem Soc.* 2016;138(48):15636-15641.  
doi:10.1021/JACS.6B09020/ASSET/IMAGES/LARGE/JA-2016-09020C\_0007.JPEG
123. Babamiri B, Bahari D, Salimi A. Highly sensitive bioaffinity electrochemiluminescence sensors: Recent advances and future directions. *Biosens Bioelectron.* 2019;142:111530. doi:10.1016/J.BIOS.2019.111530
124. Wang Y, Su B. Deciphering the Mechanisms of Electrochemiluminescence by Spatially Resolved Measurements. *Anal Sens.* 2021;1(4):148-155.  
doi:10.1002/ANSE.202100037
125. Fiorani A, Merino JP, Zanutt A, et al. Advanced carbon nanomaterials for

- electrochemiluminescent biosensor applications. *Curr Opin Electrochem.* 2019;16:66-74. doi:10.1016/J.COEELEC.2019.04.018
126. Guo Z, Sha Y, Hu Y, et al. Faraday cage-type electrochemiluminescence immunosensor for ultrasensitive detection of *Vibrio vulnificus* based on multi-functionalized graphene oxide. *Anal Bioanal Chem.* 2016;408(25):7203-7211. doi:10.1007/S00216-016-9851-Y/TABLES/2
127. Kannan P, Chen J, Su F, Guo Z, Huang Y. Faraday-Cage-Type Electrochemiluminescence Immunoassay: A Rise of Advanced Biosensing Strategy. *Anal Chem.* 2019;91(23):14792-14802. doi:10.1021/ACS.ANALCHEM.9B04503/ASSET/IMAGES/LARGE/AC9B04503\_0010.JPEG
128. Shao H, Lu J, Zhang Q, Hu Y, Wang S, Guo Z. Ruthenium-based metal organic framework (Ru-MOF)-derived novel Faraday-cage electrochemiluminescence biosensor for ultrasensitive detection of miRNA-141. *Sensors Actuators B Chem.* 2018;268:39-46. doi:10.1016/J.SNB.2018.04.088
129. Kobayashi N, Minami H, Nakamura K. Photonics of DNA/ruthenium(II) complexes. *Nanophotonics.* 2018;7(8):1373-1385. doi:10.1515/NANOPH-2018-0029/ASSET/GRAPHIC/J\_NANOPH-2018-0029\_FIG\_017.JPG
130. Lv W, Ye H, Yuan Z, Liu X, Chen X, Yang W. Recent advances in electrochemiluminescence-based simultaneous detection of multiple targets. *TrAC Trends Anal Chem.* 2020;123:115767. doi:10.1016/J.TRAC.2019.115767
131. Su Y, Lv Y. Graphene and graphene oxides: recent advances in chemiluminescence and electrochemiluminescence. Published online 2014. doi:10.1039/c4ra03598d
132. Dong YP, Zhou Y, Wang J, Zhu JJ. Electrogenerated Chemiluminescence Resonance Energy Transfer between Ru(bpy)<sub>3</sub><sup>2+</sup> Electrogenerated Chemiluminescence and Gold Nanoparticles/Graphene Oxide Nanocomposites with Graphene Oxide as Coreactant and Its Sensing Application. *Anal Chem.* 2016;88(10):5469-5475. doi:10.1021/ACS.ANALCHEM.6B00921/ASSET/IMAGES/LARGE/AC-2016-009219\_0009.JPEG

133. Guo Z, Sha Y, Hu Y, et al. Faraday cage-type electrochemiluminescence immunosensor for ultrasensitive detection of *Vibrio vulnificus* based on multi-functionalized graphene oxide. *Anal Bioanal Chem* 2016 40825. 2016;408(25):7203-7211. doi:10.1007/S00216-016-9851-Y
134. Wang T, Song X, Lin H, et al. A Faraday cage-type immunosensor for dual-modal detection of *Vibrio parahaemolyticus* by electrochemiluminescence and anodic stripping voltammetry. *Anal Chim Acta.* 2019;1062:124-130. doi:10.1016/J.ACA.2019.02.032
135. Cumba L, Pellegrin Y, Melinato F, Forster RJ. Enhanced Electrochemiluminescence from 3D Nanocavity Electrode Arrays. *Sensors and Actuators Reports.* 2022;4:100082. doi:10.1016/J.SNR.2022.100082
136. Zhou J, Li Y, Wang W, Tan X, Lu Z, Han H. Metal-organic frameworks-based sensitive electrochemiluminescence biosensing. *Biosens Bioelectron.* 2020;164:112332. doi:10.1016/J.BIOS.2020.112332
137. Dipalo M, Messina GC, Amin H, et al. 3D plasmonic nanoantennas integrated with MEA biosensors. *Nanoscale.* 2015;7(8):3703-3711. doi:10.1039/C4NR05578K
138. Li C, Li Z, Li S, et al. LSPR optical fiber biosensor based on a 3D composite structure of gold nanoparticles and multilayer graphene films. *Opt Express, Vol 28, Issue 5, pp 6071-6083.* 2020;28(5):6071-6083. doi:10.1364/OE.385128
139. Chen JB, Yousefi H, Nemr CR, et al. Nanostructured Architectures for Biomolecular Detection inside and outside the Cell. *Adv Funct Mater.* 2020;30(37):1907701. doi:10.1002/ADFM.201907701
140. Del Real Mata C, Siavash Moakhar R, Hosseini II, Jalali M, Mahshid S. A nanostructured microfluidic device for plasmon-assisted electrochemical detection of hydrogen peroxide released from cancer cells. *Nanoscale.* 2021;13(34):14316-14329. doi:10.1039/D0NR07608B
141. Beiderman M, Ashkenazy A, Segal E, et al. Optimization of Gold Nanorod Features for the Enhanced Performance of Plasmonic Nanocavity Arrays. *ACS Omega.* 2021;6(43):29071-29077. doi:10.1021/ACSOMEGA.1C04301/ASSET/IMAGES/LARGE/AO1C04301\_00

05.JPEG

142. Foroutan S, Dizaji HZ, Riahi A. Plasmon resonance-enhanced photocathode by light trapping in periodic concentric circular nanocavities on gold surface. *Optik (Stuttg)*. 2017;138:223-228. doi:10.1016/J.IJLEO.2017.03.033
143. Dinel MP, Tartaggia S, Wallace GQ, Boudreau D, Masson JF, Polo F. The Fundamentals of Real-Time Surface Plasmon Resonance/Electrogenerated Chemiluminescence. *Angew Chemie - Int Ed*. 2019;58(50):18202-18206. doi:10.1002/anie.201909806
144. Zhang J, Gryczynski Z, Lakowicz JR. First observation of surface plasmon-coupled electrochemiluminescence. *Chem Phys Lett*. 2004;393(4-6):483-487. doi:10.1016/J.CPLETT.2004.06.050
145. Chen X, Liu Y, Ma Q. Recent advances in quantum dot-based electrochemiluminescence sensors. *J Mater Chem C*. 2018;6(5):942-959. doi:10.1039/C7TC05474B
146. Liu Y, Nie Y, Wang M, Zhang Q, Ma Q. Distance-dependent plasmon-enhanced electrochemiluminescence biosensor based on MoS<sub>2</sub> nanosheets. *Biosens Bioelectron*. 2020;148:111823. doi:10.1016/J.BIOS.2019.111823
147. Calçada M, Lunardi JT, Manzoni LA, Monteiro W, Pereira M. A distributional approach for the one-dimensional hydrogen atom. *Front Phys*. 2019;7(JULY):100. doi:10.3389/FPHY.2019.00100/BIBTEX
148. Donmez S, Arslan F, Arslan H. Sequence-specific label-free nucleic acid biosensor for the detection of the hepatitis C virus genotype 1a using a disposable pencil graphite electrode. <https://doi.org/10.3109/216914012014998831>. 2015;44(3):912-917. doi:10.3109/21691401.2014.998831
149. Donmez S, Arslan F, Arslan H. A nucleic acid biosensor for detection of hepatitis c virus genotype 1a using poly(L-Glutamic acid)-modified electrode. *Appl Biochem Biotechnol*. 2015;176(5):1431-1444. doi:10.1007/S12010-015-1655-6/FIGURES/8
150. Khristunova E, Dorozhko E, Korotkova E, Kratochvil B, Vyskocil V, Barek J. Label-Free Electrochemical Biosensors for the Determination of Flaviviruses:

- Dengue, Zika, and Japanese Encephalitis. *Sensors* 2020, Vol 20, Page 4600. 2020;20(16):4600. doi:10.3390/S20164600
151. Hai X, Li Y, Zhu C, Song W, Cao J, Bi S. DNA-based label-free electrochemical biosensors: From principles to applications. *TrAC Trends Anal Chem.* 2020;133:116098. doi:10.1016/J.TRAC.2020.116098
  152. Poghossian A, Schöning MJ. Label-Free Sensing of Biomolecules with Field-Effect Devices for Clinical Applications. *Electroanalysis.* 2014;26(6):1197-1213. doi:10.1002/ELAN.201400073
  153. Magar HS, Hassan RYA, Mulchandani A. Electrochemical Impedance Spectroscopy (EIS): Principles, Construction, and Biosensing Applications. *Sensors (Basel).* 2021;21(19). doi:10.3390/S21196578
  154. Kaushik A, Yndart A, Kumar S, et al. A sensitive electrochemical immunosensor for label-free detection of Zika-virus protein. 8(1):9700. doi:10.1038/s41598-018-28035-3
  155. Singh A, Pasha SK, Manickam P, Bhansali S. Single-domain antibody based thermally stable electrochemical immunosensor. *Biosens Bioelectron.* 2016;83:162-168. doi:10.1016/J.BIOS.2016.04.054
  156. Schulze H, Arnott A, Libori A, Obaje EA, Bachmann TT. Temperature-Enhanced mcr-1 Colistin Resistance Gene Detection with Electrochemical Impedance Spectroscopy Biosensors. *Anal Chem.* 2021;93(15):6025-6033. doi:10.1021/ACS.ANALCHEM.0C00666/SUPPL\_FILE/AC0C00666\_SI\_001.PDF
  157. Kuss S, Amin HMA, Compton RG. Electrochemical Detection of Pathogenic Bacteria—Recent Strategies, Advances and Challenges. *Chem - An Asian J.* 2018;13(19):2758-2769. doi:10.1002/asia.201800798
  158. Couto RAS, Chen L, Kuss S, Compton RG. Detection of Escherichia coli bacteria by impact electrochemistry. *Analyst.* 2018;143(20):4840-4843. doi:10.1039/C8AN01675E
  159. Sekretareva A. Single-entity electrochemistry of collision in sensing applications. *Sensors and Actuators Reports.* 2021;3:100037. doi:10.1016/J.SNR.2021.100037

160. Kanokkanchana K, Saw EN, Tschulik K. Nano Impact Electrochemistry: Effects of Electronic Filtering on Peak Height, Duration and Area. *ChemElectroChem*. 2018;5(20):3000-3005. doi:10.1002/CELC.201800738
161. Gao G, Wang D, Brocenschi R, Zhi J, Mirkin M V. Toward the Detection and Identification of Single Bacteria by Electrochemical Collision Technique. *Anal Chem*. 2018;90(20):12123-12130. doi:10.1021/ACS.ANALCHEM.8B03043/ASSET/IMAGES/LARGE/AC-2018-03043N\_0006.JPEG
162. Chen Y, Wang D, Liu Y, Gao G, Zhi J. Redox activity of single bacteria revealed by electrochemical collision technique. *Biosens Bioelectron*. 2021;176:112914. doi:10.1016/J.BIOS.2020.112914
163. Miller C, Gilmore J. Detection of Quorum-Sensing Molecules for Pathogenic Molecules Using Cell-Based and Cell-Free Biosensors. *Antibiotics*. 2020;9(5):259. doi:10.3390/antibiotics9050259
164. Alatraktchi FA, Svendsen WE, Molin S. Electrochemical Detection of Pyocyanin as a Biomarker for *Pseudomonas aeruginosa*: A Focused Review. *Sensors*. 2020;20(18):5218. doi:10.3390/s20185218
165. Buzid A, Shang F, Reen FJ, et al. Molecular Signature of *Pseudomonas aeruginosa* with Simultaneous Nanomolar Detection of Quorum Sensing Signaling Molecules at a Boron-Doped Diamond Electrode. *Sci Rep*. 2016;6(1):1-9. doi:10.1038/srep30001
166. Stefano JS, Kalinke C, Da Rocha RG, et al. Electrochemical (Bio)Sensors Enabled by Fused Deposition Modeling-Based 3D Printing: A Guide to Selecting Designs, Printing Parameters, and Post-Treatment Protocols. *Anal Chem*. 2022;94(17):6417-6429. doi:10.1021/ACS.ANALCHEM.1C05523/ASSET/IMAGES/LARGE/AC1C05523\_0008.JPEG
167. Zeng L, Li P, Yao Y, Niu B, Niu S, Xu B. Recent progresses of 3D printing technologies for structural energy storage devices. *Mater Today Nano*. 2020;12:100094. doi:10.1016/J.MTNANO.2020.100094

168. Park YG, Yun I, Chung WG, Park W, Lee DH, Park JU. High-Resolution 3D Printing for Electronics. *Adv Sci.* 2022;9(8):2104623. doi:10.1002/ADVS.202104623
169. Lee CY, Taylor AC, Nattestad A, Beirne S, Wallace GG. 3D Printing for Electrocatalytic Applications. *Joule.* 2019;3(8):1835-1849. doi:10.1016/J.JOULE.2019.06.010
170. Liyarita BR, Ambrosi A, Pumera M. 3D-printed Electrodes for Sensing of Biologically Active Molecules. *Electroanalysis.* 2018;30(7):1319-1326. doi:10.1002/ELAN.201700828
171. Chu T, Park S, Fu K (Kelvin). 3D printing-enabled advanced electrode architecture design. *Carbon Energy.* 2021;3(3):424-439. doi:10.1002/CEY2.114
172. Zhu C, Liu T, Qian F, et al. 3D printed functional nanomaterials for electrochemical energy storage. *Nano Today.* 2017;15:107-120. doi:10.1016/J.NANTOD.2017.06.007
173. Kadimisetty K, Mosa IM, Malla S, et al. 3D-printed supercapacitor-powered electrochemiluminescent protein immunoarray. *Biosens Bioelectron.* 2016;77:188-193. doi:10.1016/J.BIOS.2015.09.017
174. Abdalla A, Patel BA. 3D-printed electrochemical sensors: A new horizon for measurement of biomolecules. *Curr Opin Electrochem.* 2020;20:78-81. doi:10.1016/J.COELEC.2020.04.009
175. Douman SF, De Eguilaz MR, Cumba LR, et al. Electrochemiluminescence at 3D Printed Titanium Electrodes. *Front Chem.* 2021;0:279. doi:10.3389/FCHEM.2021.662810
176. Cennamo N, Saitta L, Tosto C, et al. Microstructured Surface Plasmon Resonance Sensor Based on Inkjet 3D Printing Using Photocurable Resins with Tailored Refractive Index. *Polym 2021, Vol 13, Page 2518.* 2021;13(15):2518. doi:10.3390/POLYM13152518
177. Mitsudo K, Kurimoto Y, Yoshioka K, Suga S. Miniaturization and Combinatorial Approach in Organic Electrochemistry. *Chem Rev.* 2018;118(12):5985-5999. doi:10.1021/ACS.CHEMREV.7B00532

178. Fu K, Kwon S-R, Han D, Bohn PW. Single Entity Electrochemistry in Nanopore Electrode Arrays: Ion Transport Meets Electron Transfer in Confined Geometries. Published online 2020. doi:10.1021/acs.accounts.9b00543
179. Lee C-Y, Taylor AC, Nattestad A, Beirne S, Wallace GG. 3D Printing for Electrocatalytic Applications. *Joule*. 2019;3:1835-1849. doi:10.1016/j.joule.2019.06.010
180. Chang HK, Choe B-H, Lee JK. Influence of titanium oxide films on copper nucleation during electrodeposition. *Mater Sci Eng A*. 2005;409:317-328. doi:10.1016/j.msea.2005.03.114
181. Nelut,a N, Ibris,a ~, Ibris,a I, Claudia J, Rosca M. EIS study of Ti and its alloys in biological media. Accessed June 2, 2023. www.scioncorp.com.
182. Huang B, Zhou X, Xue Z, Lu X. Electrochemiluminescence quenching of tris(2,2'-bipyridyl)ruthenium. *TrAC Trends Anal Chem*. 2013;51:107-116. doi:10.1016/J.TRAC.2013.06.012
183. Wei H, Wang E. Electrochemiluminescence of tris(2,2'-bipyridyl)ruthenium and its applications in bioanalysis: A review. *Luminescence*. 2011;26(2):77-85. doi:10.1002/bio.1279
184. Quinton D, Galtayries A, Prima F, Griveau S. Functionalization of titanium surfaces with a simple electrochemical strategy. *Surf Coatings Technol*. 2012;206(8-9):2302-2307. doi:10.1016/j.surfcoat.2011.10.008
185. Chin SY, Dikshit V, Priyadarshini BM, Zhang Y. Powder-Based 3D Printing for the Fabrication of Device with Micro and Mesoscale Features. *Micromachines*. 2020;11(7). doi:10.3390/MI11070658
186. Karolewska K, Ligaj B. Comparison analysis of titanium alloy Ti6Al4V produced by metallurgical and 3D printing method. *AIP Conf Proc*. 2019;2077(1):020025. doi:10.1063/1.5091886
187. Leese R, Ivanov A. Comparison of polarisation curves and chronoamperometry experiments of titanium with and without ultrasonic vibrations of the electrolyte. *Spec Issue Artic Adv Mech Eng*. 2016;8(3):2016. doi:10.1177/1687814016637984
188. Berbel LO, Banczek E do P, Karousis IK, Kotsakis GA, Costa I. Determinants of



- corrosion resistance of Ti-6Al-4V alloy dental implants in an In Vitro model of peri-implant inflammation. Riveiro Rodríguez A, ed. *PLoS One*. 2019;14(1):e0210530. doi:10.1371/journal.pone.0210530
189. Döner A. Comparison of Corrosion Behaviors of Bare Ti and TiO<sub>2</sub>. *Emerg Sci J*. 2019;3(4):235-240. doi:10.28991/esj-2019-01185
190. Zhao Y, Li L, Hu L, et al. An electrochemiluminescence immunosensor for the N-terminal brain natriuretic peptide based on the high quenching ability of polydopamine. *Microchim Acta*. 2019;186(9). doi:10.1007/S00604-019-3709-X
191. Dai P, Ke J, Xie C, et al. An off–on electrochemiluminescence detection for microRNAs based on TiO<sub>2</sub> nanotubes sensitized with gold nanoparticles as enhanced emitters. *Anal Bioanal Chem* 2020 41223. 2020;412(23):5779-5787. doi:10.1007/S00216-020-02800-8
192. Douman SF, Collins D, Cumba LR, et al. Wireless electrochemiluminescence at functionalised gold microparticles using 3D titanium electrode arrays. *Chem Commun*. 2021;57(38):4642-4645. doi:10.1039/D1CC01010G
193. Huang X, Deng X, Su K, Qi W. Enhanced electrochemiluminescence of Au–Ag bimetallic nanocluster@CNTs–TiO<sub>2</sub> nanocomposite and its use in ultra-sensitive immunosensing for CEA. *New J Chem*. 2021;45(29):13064-13069. doi:10.1039/D1NJ01409A
194. Zhao C, Wang C, Gorkin R, Beirne S, Shu K, Wallace GG. Three dimensional (3D) printed electrodes for interdigitated supercapacitors. *Electrochem commun*. 2014;41:20-23. doi:10.1016/j.elecom.2014.01.013
195. Mansoureh G, Parisa V. Synthesis of metal nanoparticles using laser ablation technique. *Emerg Appl Nanoparticles Archit Nanostructures Curr Prospect Futur Trends*. Published online January 1, 2018:575-596. doi:10.1016/B978-0-323-51254-1.00019-1
196. Henini M. Scanning electron microscopy: an introduction. *III-Vs Rev*. 2000;13(4):40-44. doi:10.1016/S0961-1290(00)80006-X
197. Sul YT, Johansson CB, Jeong Y, Albrektsson T. The electrochemical oxide growth behaviour on titanium in acid and alkaline electrolytes. *Med Eng Phys*.

- 2001;23(5):329-346. doi:10.1016/S1350-4533(01)00050-9
198. Williamson RS, Disegi J, Janorkar A V., Griggs JA, Roach MD. Effect of duty cycle on the crystallinity, pore size, surface roughness and corrosion resistance of the anodized surface on titanium. *Surf Coatings Technol.* 2015;277:278-288. doi:10.1016/J.SURFCOAT.2015.07.020
199. Wheelis SE, Gindri IM, Valderrama P, Wilson TG, Huang J, Rodrigues DC. Effects of decontamination solutions on the surface of titanium: investigation of surface morphology, composition, and roughness. *Clin Oral Implants Res.* 2016;27(3):329-340. doi:10.1111/CLR.12545
200. Horprathum M, Kaewkhao J, Eiamchai P, Chindaudom P, Limsuwan P. Investigation of Inhomogeneity of TiO<sub>2</sub> Thin Films Using Spectroscopic Ellipsometry. *J Phys Conf Ser.* 2013;417(1):012007. doi:10.1088/1742-6596/417/1/012007
201. Ji R, Wang H, Wang B, et al. Removing loose oxide layer and producing dense  $\alpha$ -phase layer simultaneously to improve corrosion resistance of Ti-6Al-4V titanium alloy by coupling electrical pulse and ultrasonic treatment. *Surf Coatings Technol.* 2020;384:125329. doi:10.1016/J.SURFCOAT.2019.125329
202. Say WC, Tsai YY. Surface characterization of cast Ti-6Al-4V in hydrofluoric-nitric pickling solutions. *Surf Coatings Technol.* 2004;176(3):337-343. doi:10.1016/S0257-8972(03)00747-3
203. Zhang F, Zhang CF, Yin M nv, Ren LF, Lin H sheng, Shi G sheng. Effect of heat treatment on H<sub>2</sub>O<sub>2</sub>/HCl etched pure titanium dental implant: An in vitro study. *Med Sci Monit.* 2012;18(7):BR265. doi:10.12659/MSM.883204
204. Hung KY, Lin YC, Feng HP. The Effects of Acid Etching on the Nanomorphological Surface Characteristics and Activation Energy of Titanium Medical Materials. *Mater (Basel, Switzerland).* 2017;10(10). doi:10.3390/MA10101164
205. Juodzbalys G, Sapragoniene -Phd M, Wennerberg -Phd A, Sapragoniene M, Wennerberg A. New Acid Etched Titanium Dental Implant Surface. *Balt Dent Maxillofac J.* 2003;5:101-105.

206. de Souza KA, Robin A. Influence of concentration and temperature on the corrosion behavior of titanium, titanium-20 and 40% tantalum alloys and tantalum in sulfuric acid solutions. *Mater Chem Phys*. 2007;103(2-3):351-360. doi:10.1016/j.matchemphys.2007.02.026
207. Burrelv MC, Armstrong NR. Oxides Formed on Polycrystalline Titanium Thin-Film Surfaces: Rates of Formation and Composition of Oxides Formed at Low and High O<sub>2</sub> Partial Pressures. *Langmuir*. 1986;2:30-36. Accessed January 25, 2022. <https://pubs.acs.org/sharingguidelines>
208. Yu H, Chen J, Zhang S, Yu Y, Wang S, Ye M. Effects of electrolyte composition on the growth and properties of titanium oxide nanotubes. *Electrochem Commun*. 2022;135:107217. doi:10.1016/J.ELECOM.2022.107217
209. Diamanti M V., Pedferri MP. Effect of anodic oxidation parameters on the titanium oxides formation. *Corros Sci*. 2007;49(2):939-948. doi:10.1016/J.CORSCI.2006.04.002
210. Asserghine A, Filotás D, Németh B, Nagy L, Nagy G. Potentiometric scanning electrochemical microscopy for monitoring the pH distribution during the self-healing of passive titanium dioxide layer on titanium dental root implant exposed to physiological buffered (PBS) medium. *Electrochem Commun*. 2018;95:1-4. doi:10.1016/J.ELECOM.2018.08.008
211. Fovet Y, Gal JY, Toumelin-Chemla F. Influence of pH and fluoride concentration on titanium passivating layer: stability of titanium dioxide. *Talanta*. 2001;53(5):1053-1063. doi:10.1016/S0039-9140(00)00592-0
212. Mazzarolo A, Curioni M, Vincenzo A, Skeldon P, Thompson GE. Anodic growth of titanium oxide: Electrochemical behaviour and morphological evolution. *Electrochim Acta*. 2012;75:288-295. doi:10.1016/J.ELECTACTA.2012.04.114
213. Habazaki H, Uozumi M, Konno H, Shimizu K, Skeldon P, Thompson GE. Crystallization of anodic titania on titanium and its alloys. *Corros Sci*. 2003;45(9):2063-2073. doi:10.1016/S0010-938X(03)00040-4
214. Iglesias-Rubianes L, Garcia-Vergara SJ, Skeldon P, Thompson GE, Ferguson J, Beneke M. Cyclic oxidation processes during anodizing of Al–Cu alloys.

- Electrochim Acta.* 2007;52(24):7148-7157.  
doi:10.1016/J.ELECTACTA.2007.05.052
215. Gou X, Xing Z, Ma C, Zhu J-J. A Close Look at Mechanism, Application, and Opportunities of Electrochemiluminescence Microscopy. Published online 2019.  
doi:10.1021/cbmi.2c00007
216. Zu Y, Bard AJ. Electrogenated chemiluminescence. 66. The role of direct coreactant oxidation in the ruthenium tris(2,2')bipyridyl/tripropylamine system and the effect of halide ions on the emission intensity. *Anal Chem.* 2000;72(14):3223-3232.  
doi:10.1021/AC000199Y/SUPPL\_FILE/AC000199Y\_S.PDF
217. Valenti G, Fiorani A, Li H, Sojic N, Paolucci F. Essential Role of Electrode Materials in Electrochemiluminescence Applications. *ChemElectroChem.* 2016;3(12):1990-1997. doi:10.1002/CELC.201600602
218. Parveen S, Chen Y, Yuan Y, et al. Electrochemiluminescence of [Ru(bpy)<sub>3</sub>]<sup>2+</sup>/tripropylamine at glassy carbon, platinum, and palladium electrodes. *Sensors and Actuators Reports.* 2021;3.  
doi:10.1016/J.SNR.2021.100062
219. Zakaria ND, Omar MH, Ahmad Kamal NN, et al. Effect of Supporting Background Electrolytes on the Nanostructure Morphologies and Electrochemical Behaviors of Electrodeposited Gold Nanoparticles on Glassy Carbon Electrode Surfaces. *ACS Omega.* 2021;6(38):24419-24431.  
doi:10.1021/ACSOMEGA.1C02670/ASSET/IMAGES/LARGE/AO1C02670\_0011.JPEG
220. Low CTJ, Wills RGA, Walsh FC. Electrodeposition of composite coatings containing nanoparticles in a metal deposit. *Surf Coatings Technol.* 2006;201(1-2):371-383. doi:10.1016/J.SURFCOAT.2005.11.123
221. Hezard T, Fajerweg K, Evrard D, Collire V, Behra P, Gros P. Gold nanoparticles electrodeposited on glassy carbon using cyclic voltammetry: Application to Hg(II) trace analysis. *J Electroanal Chem.* 2012;664:46-52.  
doi:10.1016/J.JELECHEMA.2011.10.014

222. Siampour H, Abbasian S, Moshaii A, Omidfar K, Sedghi M, Naderi-Manesh H. Seed-mediated Electrochemically Developed Au Nanostructures with Boosted Sensing Properties: An Implication for Non-enzymatic Glucose Detection. *Sci Reports* 2020 101. 2020;10(1):1-11. doi:10.1038/s41598-020-64082-5
223. Paradowska E, Arkusz K, Pijanowska DG. Comparison of Gold Nanoparticles Deposition Methods and Their Influence on Electrochemical and Adsorption Properties of Titanium Dioxide Nanotubes. *Materials (Basel)*. 2020;13(19). doi:10.3390/MA13194269
224. Zheng H, Almeida RM, Rivera T, Ravaine S. Fabrication of broadband omnidirectional non-reflective gold surfaces by electrodeposition. <http://dx.doi.org/101179/2055031614Y0000000003>. 2014;1(1):11-16. doi:10.1179/2055031614Y.0000000003
225. Elias J, Gizowska M, Brodard P, et al. Electrodeposition of gold thin films with controlled morphologies and their applications in electrocatalysis and SERS. *Nanotechnology*. 2012;23(25). doi:10.1088/0957-4484/23/25/255705
226. Liu F, Huang L, Duan X, et al. A facile method to prepare noble metal nanoparticles modified Self-Assembly (SAM) electrode. <https://doi.org/101080/1745808020171373202>. 2017;13(1):1-10. doi:10.1080/17458080.2017.1373202
227. Kim J Do, Pyun S Il, Seo M. Effect of hydrogen on stresses in anodic oxide film on titanium. *Electrochim Acta*. 2003;48(9):1123-1130. doi:10.1016/S0013-4686(02)00823-X
228. Baez VB, Graves JE, Pletcher D. The reduction of oxygen on titanium oxide electrodes. *J Electroanal Chem*. 1992;340(1-2):273-286. doi:10.1016/0022-0728(92)80303-L
229. Bai J, Zhou B. Titanium dioxide nanomaterials for sensor applications. *Chem Rev*. 2014;114(19):10131-10176. doi:10.1021/CR400625J/ASSET/IMAGES/LARGE/CR-2013-00625J\_0002.JPEG
230. Zhang Z, Yu H, Li X, Dong H. Impact of the Amount of the Gold Layer on the

- Tribological Performance of the Ceramic Conversion Treated CP-Titanium. *Tribol Lett.* 2023;71(2):1-12. doi:10.1007/S11249-023-01711-W/FIGURES/13
231. Mohd Zaki MH, Mohd Y, Chin LY. Surface Properties of Nanostructured Gold Coatings Electrodeposited at Different Potentials. *Int J Electrochem Sci.* 2020;15(11):11401-11415. doi:10.20964/2020.11.41
  232. Nazarov D, Rudakova A, Borisov E, Popovich A. Surface Modification of Additively Manufactured Nitinol by Wet Chemical Etching. *Mater 2021, Vol 14, Page 7683.* 2021;14(24):7683. doi:10.3390/MA14247683
  233. KY H, YC L, HP F. The Effects of Acid Etching on the Nanomorphological Surface Characteristics and Activation Energy of Titanium Medical Materials. *Mater (Basel, Switzerland).* 2017;10(10). doi:10.3390/MA10101164
  234. Ban S, Iwaya Y, Kono H, Sato H. Surface modification of titanium by etching in concentrated sulfuric acid. *Dent Mater.* 2006;22(12):1115-1120. doi:10.1016/j.dental.2005.09.007
  235. Burke LD, Nugent PF. The Electrochemistry of Gold: I The Redox Behaviour of the Metal in Aqueous Media.
  236. Trasatti S, Petrii OA. International Union of Pure and Applied Chemistry Physical Chemistry Division Commission on Electrochemistry: Real Surface Area Measurements in Electrochemistry. *Pure Appl Chem.* 1991;63(5):711-734. doi:10.1351/PAC199163050711/MACHINEREADABLECITATION/RIS
  237. Zuaznabar-Gardona JC, Fragoso A. Electrochemical characterisation of the adsorption of ferrocenemethanol on carbon nano-onion modified electrodes. *J Electroanal Chem.* 2020;871:114314. doi:10.1016/J.JELECHEM.2020.114314
  238. Elgrishi N, Rountree KJ, McCarthy BD, Rountree ES, Eisenhart TT, Dempsey JL. A Practical Beginner's Guide to Cyclic Voltammetry. *J Chem Educ.* 2018;95(2):197-206. doi:10.1021/acs.jchemed.7b00361
  239. Laviron E. General expression of the linear potential sweep voltammogram in the case of diffusionless electrochemical systems. *J Electroanal Chem Interfacial Electrochem.* 1979;101(1):19-28. doi:10.1016/S0022-0728(79)80075-3
  240. Steentjes T, Jonkheijm P, Huskens J. Electron Transfer Processes in Ferrocene-

- Modified Poly(ethylene glycol) Monolayers on Electrodes. Published online 2017. doi:10.1021/acs.langmuir.7b02160
241. Trasatti S. ELECTROCHEMICAL THEORY | Electrokinetics. *Encycl Electrochem Power Sources*. Published online January 1, 2009:23-31. doi:10.1016/B978-044452745-5.00021-6
242. Veloso WB, Paixão TRLC, Meloni GN. 3D printed electrodes design and voltammetric response. *Electrochim Acta*. 2023;449:142166. doi:10.1016/J.ELECTACTA.2023.142166
243. Anantharaj S, Noda S. iR drop correction in electrocatalysis: everything one needs to know! *J Mater Chem A*. 2022;10(17):9348-9354. doi:10.1039/D2TA01393B
244. Klingler RJ, Kochi JK. Heterogeneous Rates of Electron Transfer. Application of Cyclic Voltammetric Techniques to Irreversible Electrochemical Processes. *J Am Chem Soc*. 1980;102(14):4790-4798. doi:10.1021/JA00534A036/ASSET/JA00534A036.FP.PNG\_V03
245. Muhammad H, Tahiri IA, Muhammad M, et al. A comprehensive heterogeneous electron transfer rate constant evaluation of dissolved oxygen in DMSO at glassy carbon electrode measured by different electrochemical methods. *J Electroanal Chem*. 2016;775:157-162. doi:10.1016/J.JELECHEM.2016.05.049
246. Cannes C, Kanoufi F, Bard AJ. Cyclic voltammetry and scanning electrochemical microscopy of ferrocenemethanol at monolayer and bilayer-modified gold electrodes. *J Electroanal Chem*. 2003;547(1):83-91. doi:10.1016/S0022-0728(03)00192-X
247. Mishyn V, Aspermair P, Leroux Y, et al. "Click" Chemistry on Gold Electrodes Modified with Reduced Graphene Oxide by Electrophoretic Deposition. *Surfaces 2019, Vol 2, Pages 193-204*. 2019;2(1):193-204. doi:10.3390/SURFACES2010015
248. Liu CY, Liu ZY, Peng R, Zhong ZC. Quasireversible Process of Dopamine on Copper-Nickel Hydroxide Composite/Nitrogen Doped Graphene/Nafion Modified GCE and Its Electrochemical Application. *J Anal Methods Chem*. 2014;2014. doi:10.1155/2014/724538

249. Randviir EP. A cross examination of electron transfer rate constants for carbon screen-printed electrodes using Electrochemical Impedance Spectroscopy and cyclic voltammetry. *Electrochim Acta*. 2018;286:179-186. doi:10.1016/J.ELECTACTA.2018.08.021
250. Bhatti NK, Subhani MS, Khan AY, Qureshi R, Rahman A. Heterogeneous electron transfer rate constants of viologen monocations at a platinum disk electrode. *Turkish J Chem*. 2006;30(2):165-180.
251. Lavacchi A, Bardi U, Borri C, Caporali S, Fossati A, Perissi I. Cyclic voltammetry simulation at microelectrode arrays with COMSOL Multiphysics®. *J Appl Electrochem*. 2009;39(11):2159-2163. doi:10.1007/S10800-009-9797-2/FIGURES/6
252. Dickinson E, Ekström H, Fontes E. COMSOL Multiphysics®: Finite element software for electrochemical analysis. A mini-review. *Electrochem Commun*. 2014;40:71-74. doi:10.1016/J.ELECOM.2013.12.020
253. Klymenko O V., Svir I, Amatore C. A New Approach for the Simulation of Electrochemiluminescence (ECL). *ChemPhysChem*. 2013;14(10):2237-2250. doi:10.1002/CPHC.201300126
254. Zoski CG, Wijesinghe M. Electrochemistry at Ultramicroelectrode Arrays and Nanoelectrode Ensembles of Macro- and Ultramicroelectrode Dimensions. *Isr J Chem*. 2010;50(3):347-359. doi:10.1002/IJCH.201000025
255. Le H, Kätelhön E, Compton RG. Characterising the nature of diffusion via a new indicator: Microcylinder and microring electrodes. *J Electroanal Chem*. 2019;855:113602. doi:10.1016/J.JELECHEM.2019.113602
256. Fang YM, Sun JJ, Chen GN. A Simple Approach to the Solution of the Diffusion Equation at the Microcylinder Electrode—an Inspiration from the Film Projector. *ChemPhysChem*. 2009;10(14):2393-2396. doi:10.1002/CPHC.200900404
257. Ding J, Zhou P, Guo W, Su B. Confined Electrochemiluminescence Generation at Ultra-High-Density Gold Microwell Electrodes. *Front Chem*. 2021;8:1278. doi:10.3389/FCHEM.2020.630246/BIBTEX
258. Wang D, Guo L, Huang R, Qiu B, Lin Z, Chen G. Surface Enhanced



- Electrochemiluminescence of Ru(bpy)<sub>3</sub><sup>2+</sup>. *Sci Reports* 2015 51. 2015;5(1):1-7. doi:10.1038/srep07954
259. Ma C, Zhang Z, Tan T, Zhu JJ. Recent Progress in Plasmonic based Electrochemiluminescence Biosensors: A Review. *Biosensors*. 2023;13(2). doi:10.3390/BIOS13020200
260. Wei Y, Zhang Y, Pan J, et al. Plasmon-Enhanced Electrochemiluminescence at the Single-Nanoparticle Level. *Angew Chemie*. 2023;135(2):e202214103. doi:10.1002/ANGE.202214103
261. Douman SF, De Eguilaz MR, Cumba LR, et al. Electrochemiluminescence at 3D Printed Titanium Electrodes. *Front Chem*. 2021;9:662810. doi:10.3389/fchem.2021.662810
262. Guo W, Zhou P, Sun L, Ding H, Su B. Microtube Electrodes for Imaging the Electrochemiluminescence Layer and Deciphering the Reaction Mechanism. *Angew Chemie - Int Ed*. 2021;60(4):2089-2093. doi:10.1002/ANIE.202012340
263. Liu X, Qi W, Gao W, et al. Remarkable increase in luminol electrochemiluminescence by sequential electroreduction and electrooxidation. *Chem Commun*. 2014;50(93):14662-14665. doi:10.1039/C4CC06633B
264. Niu H, Yang X, Wang Y, et al. Electrochemiluminescence Detection of Sunset Yellow by Graphene Quantum Dots. *Front Chem*. 2020;8:505. doi:10.3389/FCHEM.2020.00505/BIBTEX
265. Han H, You Z, Liang J, Sheng Z. Electrogenated chemiluminescence of CdSe quantum dots dispersed in aqueous solution. *Front Biosci*. 2007;12(6):2352-2357. doi:10.2741/2237/PDF
266. Kamyabi MA, Alipour Z, Moharramnezhad M. An enzyme-free electrochemiluminescence insulin probe based on the regular attachment of ZnO nanoparticles on a 3-D nickel foam and H<sub>2</sub>O<sub>2</sub> as an efficient co-reactant. *Anal Methods*. 2021;13(8):1003-1012. doi:10.1039/D0AY02071K
267. Carvalhal RF, Freire RS, Kubota LT. Polycrystalline Gold Electrodes: A Comparative Study of Pretreatment Procedures Used for Cleaning and Thiol Self-Assembly Monolayer Formation. *Electroanalysis*. 2005;17(14):1251-1259.

doi:10.1002/ELAN.200403224

268. Hoogvliet JC, Dijkema M, Kamp B, Van Bennekom WP. Electrochemical pretreatment of polycrystalline gold electrodes to produce a reproducible surface roughness for self-assembly: A study in phosphate buffer pH 7.4. *Anal Chem.* 2000;72(9):2016-2021.  
doi:10.1021/AC991215Y/ASSET/IMAGES/LARGE/AC991215YF00006.JPEG
269. Fischer LM, Tenje M, Heiskanen AR, et al. Gold cleaning methods for electrochemical detection applications. *Microelectron Eng.* 2009;86(4-6):1282-1285. doi:10.1016/J.MEE.2008.11.045
270. Chinnaiah J, Kasian O, Dekshinamoorthy A, et al. Tuning the Anodic and Cathodic Dissolution of Gold by Varying the Surface Roughness. *ChemElectroChem.* 2021;8(8):1524-1530. doi:10.1002/CELC.202100366
271. Wang D, Guo L, Huang R, Qiu B, Lin Z, Chen G. Surface Enhanced Electrochemiluminescence of Ru(bpy)<sub>3</sub><sup>2+</sup>. *Sci Reports 2015 51.* 2015;5(1):1-7. doi:10.1038/srep07954
272. Zanut A, Fiorani A, Canola S, et al. Insights into the mechanism of coreactant electrochemiluminescence facilitating enhanced bioanalytical performance. *Nat Commun 2020 111.* 2020;11(1):1-9. doi:10.1038/s41467-020-16476-2
273. Raju CV, Sornambigai M, Kumar SS, Raju CV, Sornambigai M, Kumar SS. Ruthenium-Tris-Bipyridine Derivatives as a Divine Complex for Electrochemiluminescence Based Biosensor Applications. *Ruthenium - An Element Loved by Res.* Published online May 21, 2021. doi:10.5772/INTECHOPEN.96819
274. Su Q, Jiang C, Gou D, Long Y. Surface Plasmon-Assisted Fluorescence Enhancing and Quenching: From Theory to Application. *ACS Appl Bio Mater.* 2021;4(6):4684-4705.  
doi:10.1021/ACSABM.1C00320/ASSET/IMAGES/LARGE/MT1C00320\_0017.JPEG
275. Bouffier L, Sojic N. Chapter 1: Introduction and Overview of Electrogenated Chemiluminescence. In: *RSC Detection Science.* Vol 2020-January. Royal Society of Chemistry; 2020:1-28. doi:10.1039/9781788015776-00001

276. Tokel NE, Bard AJ. Electrogenerated Chemiluminescence. IX. Electrochemistry and Emission from Systems Containing Tris(2,2'-bipyridine)ruthenium(II) Dichloride. *J Am Chem Soc.* 1972;94(8):2862-2863. doi:10.1021/JA00763A056/ASSET/JA00763A056.FP.PNG\_V03
277. Li MJ, Chen Z, Zhu N, Yam VWW, Zu Y. Electrochemiluminescence of ruthenium(II) complexes functionalized with crown ether pendants and effects of cation binding. *Inorg Chem.* 2008;47(3):1218-1223. doi:10.1021/IC7019582/SUPPL\_FILE/IC7019582-FILE001.CIF
278. Rhyne PW, Wong OT, Zhang YJ, Weiner RS. Electrochemiluminescence in bioanalysis. *Bioanalysis.* 2009;1(5):919-935. doi:10.4155/BIO.09.80
279. Qi H, Zhang C. Electrogenerated chemiluminescence biosensing. *Anal Chem.* 2020;92(1):524-534. doi:10.1021/ACS.ANALCHEM.9B03425/ASSET/IMAGES/LARGE/AC9B03425\_0004.JPEG
280. Dumur F, Guerlin A, Lehoux A, et al. Mutual influence of gold and silver nanoparticles on Tris-(2,2'bipyridine)-Ru(II) core complexes: Post-functionalization processes, optical and electrochemical investigations. *Appl Surf Sci.* 2020;499:143847. doi:10.1016/J.APSUSC.2019.143847
281. Wang P, Liang Z, Zhao J, Nie Y, Xu S, Ma Q. A polarization-resolved ECL strategy based on the surface plasmon coupling effect of orientational Au nanobipyramids patterned structures. *Chem Eng J.* 2022;448:137630. doi:10.1016/J.CEJ.2022.137630
282. Gellé A, Moores A. Plasmonic nanoparticles: Photocatalysts with a bright future. *Curr Opin Green Sustain Chem.* 2019;15:60-66. doi:10.1016/J.COGSC.2018.10.002
283. Kim HS, Lee DY. Near-Infrared-Responsive Cancer Photothermal and Photodynamic Therapy Using Gold Nanoparticles. Published online 2018. doi:10.3390/polym10090961
284. Huang X, El-Sayed MA. Gold nanoparticles: Optical properties and implementations in cancer diagnosis and photothermal therapy. *J Adv Res.*

- 2010;1(1):13-28. doi:10.1016/J.JARE.2010.02.002
285. Amendola V, Pilot R, Frascioni M, Maragò OM, Iati MA. Surface plasmon resonance in gold nanoparticles: a review. *J Phys Condens Matter*. 2017;29(20):203002. doi:10.1088/1361-648X/AA60F3
286. Sadrolhosseini AR, Noor ASM, Moxsin MM, Sadrolhosseini AR, Noor ASM, Moxsin MM. Application of Surface Plasmon Resonance Based on a Metal Nanoparticle. *Plasmon - Princ Appl*. Published online October 24, 2012. doi:10.5772/51219
287. Osborne SAM, Pikramenou Z. Highly luminescent gold nanoparticles: effect of ruthenium distance for nanoprobe with enhanced lifetimes. *Faraday Discuss*. 2015;185(0):219-231. doi:10.1039/C5FD00108K
288. Perez-Tejeda P, Grueso E, Marin-Gordillo A, Torres-Marquez C, Giraidez-Pérezpérez RM. Aqueous Gold Nanoparticle Solutions for Improved Efficiency in Electrogenated Chemiluminescent Reactions. Published online 2018. doi:10.1021/acsanm.8b01323
289. Flamme M, Clarke E, Gasser G, Hollenstein M. Applications of Ruthenium Complexes Covalently Linked to Nucleic Acid Derivatives. doi:10.3390/molecules23071515
290. Halid NIA, Hasbullah SA, Ahmad H, Heng LY, Karim NHA, Harun SN. Electrochemical DNA biosensor for detection of porcine oligonucleotides using ruthenium(II) complex as intercalator label redox. *AIP Conf Proc*. 2015;1614(1):313. doi:10.1063/1.4895214
291. Ashford DL, Stewart DJ, Glasson CR, et al. An amide-linked chromophore-catalyst assembly for water oxidation. *Inorg Chem*. 2012;51(12):6428-6430. doi:10.1021/IC300061U/SUPPL\_FILE/IC300061U\_SI\_001.PDF
292. Zhou M, Li L, Dan N. Enhanced electrochemiluminescence immunoassay: 1. Wisely using an electronically neutral ruthenium complex luminophore. *J Electroanal Chem*. 2022;919:116511. doi:10.1016/J.JELECHEM.2022.116511
293. Zhou X, Zhu D, Liao Y, et al. Synthesis, labeling and bioanalytical applications of a tris(2,2'-bipyridyl)ruthenium(II)-based electrochemiluminescence probe. *Nat*

*Protoc* 2014 95. 2014;9(5):1146-1159. doi:10.1038/nprot.2014.060

294. Zhou J-Y, Luo T, She W-L, et al. Metal-to-Ligand Charge Transfer Spectra for Transition Metal Complexes of Chelated Aromatic Ligands: Theory and Experiment. *Laser Forsch und Tech / Laser Res Eng*. Published online 1996:168-170. doi:10.1007/978-3-642-80263-8\_38
295. Thompson DW, Ito A, Meyer TJ. [Ru(bpy)<sub>3</sub>]<sup>2+</sup> and other remarkable metal-to-ligand charge transfer (MLCT) excited states. *Pure Appl Chem*. 2013;85(7):1257-1305. doi:10.1351/PAC-CON-13-03-04/PDF
296. Kalyanasundaram K. Photophysics, photochemistry and solar energy conversion with tris(bipyridyl)ruthenium(II) and its analogues. *Coord Chem Rev*. 1982;46(C):159-244. doi:10.1016/0010-8545(82)85003-0
297. Memon AG, Channa IA, Shaikh AA, et al. Citrate-Capped AuNP Fabrication, Characterization and Comparison with Commercially Produced Nanoparticles. *Cryst* 2022, Vol 12, Page 1747. 2022;12(12):1747. doi:10.3390/CRYST12121747
298. Mocanu A, Cernica I, Tomoaia G, Bobos LD, Horovitz O, Tomoaia-Cotisel M. Self-assembly characteristics of gold nanoparticles in the presence of cysteine. *Colloids Surfaces A Physicochem Eng Asp*. 2009;338(1-3):93-101. doi:10.1016/J.COLSURFA.2008.12.041
299. Rajeshwari A, Garg K, Elavarasi M, Chandrasekaran N, Mukherjee A. Interaction of Citrate-Capped Gold Nanoparticles with the Selected Amino Thiols for Sensing Applications. *Proc Natl Acad Sci India Sect B - Biol Sci*. 2017;87(1):23-30. doi:10.1007/S40011-015-0567-0/FIGURES/10
300. Zhong W, Urayama P, Mycek MA. Imaging fluorescence lifetime modulation of a ruthenium-based dye in living cells: the potential for oxygen sensing. *J Phys D Appl Phys*. 2003;36(14):1689. doi:10.1088/0022-3727/36/14/306
301. Vanheusden M, Vitale R, Camacho R, et al. Fluorescence Photobleaching as an Intrinsic Tool to Quantify the 3D Expansion Factor of Biological Samples in Expansion Microscopy. *ACS Omega*. 2020;5(12):6792-6799. doi:10.1021/ACSOMEGA.0C00118/ASSET/IMAGES/LARGE/AO0C00118\_0005.JPEG

302. Adams F, Barbante C. Spectroscopic Imaging. *Compr Anal Chem.* 2015;69:339-384. doi:10.1016/B978-0-444-63439-9.00009-8
303. Fuller ZJ, Bare WD, Kneas KA, Xu WY, Demas JN, DeGraff BA. Photostability of Luminescent Ruthenium(II) Complexes in Polymers and in Solution. *Anal Chem.* 2003;75(11):2670-2677. doi:10.1021/AC0261707
304. Rashid A, Mondal S, Ghosh P. Development and Application of Ruthenium(II) and Iridium(III) Based Complexes for Anion Sensing. *Mol 2023, Vol 28, Page 1231.* 2023;28(3):1231. doi:10.3390/MOLECULES28031231
305. Palo K, Brand L, Eggeling C, Jäger S, Kask P, Gall K. Fluorescence Intensity and Lifetime Distribution Analysis: Toward Higher Accuracy in Fluorescence Fluctuation Spectroscopy. *Biophys J.* 2002;83(2):605-618. doi:10.1016/S0006-3495(02)75195-3
306. Pramod P, Sudeep PK, Thomas KG, Kamat P V. Photochemistry of ruthenium trisbipyridine functionalized on gold nanoparticles. *J Phys Chem B.* 2006;110(42):20737-20741. doi:10.1021/JP064878
307. Kedem O, Wohlleben W, Rubinstein I. Distance-dependent fluorescence of tris(bipyridine)ruthenium(II) on supported plasmonic gold nanoparticle ensembles. *Nanoscale.* 2014;6(24):15134-15143. doi:10.1039/C4NR04237A
308. Osborne SAM, Pikramenou Z. Highly luminescent gold nanoparticles: effect of ruthenium distance for nanoprobe with enhanced lifetimes. *Faraday Discuss.* 2015;185(0):219-231. doi:10.1039/C5FD00108K
309. Adams SJ, Lewis DJ, Preece JA, Pikramenou Z. Luminescent gold surfaces for sensing and imaging: Patterning of transition metal probes. *ACS Appl Mater Interfaces.* 2014;6(14):11598-11608. doi:10.1021/AM502347C/SUPPL\_FILE/AM502347C\_SI\_001.PDF
310. Alexiev U, Farrens DL. Fluorescence spectroscopy of rhodopsins: Insights and approaches. *Biochim Biophys Acta - Bioenerg.* 2014;1837(5):694-709. doi:10.1016/J.BBABIO.2013.10.008
311. Lakowicz JR. Principles of fluorescence spectroscopy. *Princ Fluoresc Spectrosc.* Published online 2006:1-954. doi:10.1007/978-0-387-46312-4/COVER

312. Genovese D, Cingolani M, Rampazzo E, Prodi L, Zaccheroni N. Static quenching upon adduct formation: a treatment without shortcuts and approximations. *Chem Soc Rev.* 2021;50(15):8414-8427. doi:10.1039/D1CS00422K
313. Rogers NJ. The development of gold nanoparticles labelled with transition metal complexes for imaging applications. Published online 2014.
314. Yang Y, Matsubara S, Nogami M, Shi J. Controlling the aggregation behavior of gold nanoparticles. *Mater Sci Eng B.* 2007;140:172-176. doi:10.1016/j.mseb.2007.03.021
315. De Oliveira KM, Dos Santos TCC, Dinelli LR, Marinho JZ, Lima RC, Bogado AL. Aggregates of gold nanoparticles with complexes containing ruthenium as modifiers in carbon paste electrodes. *Polyhedron.* 2013;50(1):410-417. doi:10.1016/J.POLY.2012.11.014
316. Kubista M, Sjöback R, Eriksson S, Albinsson B. Experimental correction for the inner-filter effect in fluorescence spectra. *Analyst.* 1994;119(3):417-419. doi:10.1039/AN9941900417
317. Gehlen MH. The centenary of the Stern-Volmer equation of fluorescence quenching: From the single line plot to the SV quenching map. *J Photochem Photobiol C Photochem Rev.* 2020;42:100338. doi:10.1016/J.JPHOTOCHEMREV.2019.100338
318. Gentleman AS, Lawson T, Ellis MG, et al. Stern–Volmer analysis of photocatalyst fluorescence quenching within hollow-core photonic crystal fibre microreactors. *Chem Commun.* 2022;58(75):10548-10551. doi:10.1039/D2CC03996F
319. Banerjee R, Sinha R, Purkayastha P.  $\beta$ -Cyclodextrin Encapsulated Coumarin 6 on Graphene Oxide Nanosheets: Impact on Ground-State Electron Transfer and Excited-State Energy Transfer. *ACS Omega.* 2019;4(14):16153-16158. doi:10.1021/ACSOMEGA.9B02335/ASSET/IMAGES/LARGE/AO9B02335\_0008.JPEG
320. Siegel R, Glazier S. TNT Sensor: Stern-Volmer Analysis of Luminescence Quenching of Ruthenium Bipyridine. *J Chem Educ.* 2021;98(8):2643-2648. doi:10.1021/ACS.JCHEMED.0C01221/ASSET/IMAGES/MEDIUM/ED0C0122

1\_M017.GIF

321. Yi Y, Weinberg G, Prenzel M, et al. Electrochemical corrosion of a glassy carbon electrode. *Catal Today*. 2017;295:32-40. doi:10.1016/J.CATTOD.2017.07.013
322. Yin X, Sha B, He X. Electrochemiluminescence from tris(2,2'-bipyridyl)ruthenium (II) in the presence of aminocarboxylic acid co-reactants. *Sci China, Ser B Chem*. 2009;52(9):1394-1401. doi:10.1007/S11426-009-0136-6/METRICAL
323. Daviddi E, Oleinick A, Svir I, Valenti G, Paolucci F, Amatore C. Theory and Simulation for Optimising Electrogenenerated Chemiluminescence from Tris(2,2'-bipyridine)-ruthenium(II)-Doped Silica Nanoparticles and Tripropylamine. *ChemElectroChem*. 2017;4(7):1719-1730. doi:10.1002/CELC.201600892
324. Kebede N, Francis PS, Barbante GJ, Hogan CF. Electrogenenerated chemiluminescence of tris(2,2' bipyridine)ruthenium(II) using common biological buffers as co-reactant, pH buffer and supporting electrolyte. *Analyst*. 2015;140(21):7142-7145. doi:10.1039/C5AN01216C
325. Wang H, Xu G, Dong S. Electrochemistry and electrochemiluminescence of stable tris(2,2'-bipyridyl)ruthenium(II) monolayer assembled on benzene sulfonic acid modified glassy carbon electrode. *Talanta*. 2001;55(1):61-67. doi:10.1016/S0039-9140(01)00406-4
326. Guo Z, Shen Y, Wang M, Zhao F, Dong S. Electrochemistry and Electrogenenerated Chemiluminescence of SiO<sub>2</sub> Nanoparticles/Tris(2,2'-bipyridyl)ruthenium(II) Multilayer Films on Indium Tin Oxide Electrodes. *Anal Chem*. 2004;76(1):184-191.  
doi:10.1021/AC034759F/ASSET/IMAGES/LARGE/AC034759FF00011.JPEG
327. Fiorani A, Valenti G, Irkham, Paolucci F, Einaga Y. Quantification of electrogenerated chemiluminescence from tris(bipyridine)ruthenium(II) and hydroxyl ions. *Phys Chem Chem Phys*. 2020;22(27):15413-15417. doi:10.1039/D0CP02005B
328. Adsetts JR, Chu K, Hesari M, Ma J, Ding Z. Absolute Electrochemiluminescence Efficiency Quantification Strategy Exemplified with Ru(bpy)<sub>3</sub><sup>2+</sup> in the Annihilation Pathway. *Anal Chem*. 2021;93(33):11626-11633.



doi:10.1021/ACS.ANALCHEM.1C02403/ASSET/IMAGES/MEDIUM/AC1C02403\_M008.GIF

329. Chu K, Adsetts JR, Ma J, et al. Physical Strategy to Determine Absolute Electrochemiluminescence Quantum Efficiencies of Coreactant Systems Using a Photon-Counting Photomultiplier Device. *J Phys Chem C*. 2021;125(40):22274-22282.  
doi:10.1021/ACS.JPCC.1C06342/ASSET/IMAGES/LARGE/JP1C06342\_0008.JPEG
330. Tokel-Takvoryan NE, Hemingway RE, Bard AJ. Electrogenerated Chemiluminescence. XIII. Electrochemical and Electrogenerated Chemiluminescence Studiesm of Ruthenium Chelates. *J Am Chem Soc*. 1973;95(20):6582-6589.  
doi:10.1021/JA00801A011/ASSET/JA00801A011.FP.PNG\_V03
331. Cooke MM, Doeven EH, Hogan CF, et al. Comparison of homoleptic and heteroleptic 2,2'-bipyridine and 1,10-phenanthroline ruthenium complexes as chemiluminescence and electrochemiluminescence reagents in aqueous solution. *Anal Chim Acta*. 2009;635(1):94-101. doi:10.1016/J.ACA.2008.12.042
332. Kapturkiewicz A, Szrebowaty P. Electrochemically generated chemiluminescence of tris(2,2'-bipyridine)ruthenium(II), tris(1,10-phenanthroline)ruthenium(II) and tris(4,7-diphenyl-1,10-phenanthroline)ruthenium(II) complexes. *J Chem Soc Dalton Trans*. 2002;(16):3219-3225. doi:10.1039/B202012B
333. Kim BH, Lee DN, Park HJ, et al. Synthesis and characterization of electrochemiluminescent ruthenium(II) complexes containing o-phenanthroline and various  $\alpha$ -diimine ligands. *Talanta*. 2004;62(3):595-602. doi:10.1016/j.talanta.2003.09.001
334. Michel PE, Fiaccabrino GC, De Rooij NF, Koudelka-Hep M. Integrated sensor for continuous flow electrochemiluminescent measurements of codeine with different ruthenium complexes. *Anal Chim Acta*. 1999;392(2-3):95-103. doi:10.1016/S0003-2670(99)00251-2
335. Xi J, Shi B, Ai X, He Z. Chemiluminescence detection of isoniazid using Ru(phen)<sub>3</sub><sup>2+</sup>-isoniazid-Ce(IV) system. *J Pharm Biomed Anal*. 2004;36(1):237-

241. doi:10.1016/J.JPBA.2004.05.021
336. Han HY, He ZK, Zeng YE. Chemiluminescence method for the determination of glutathione in human serum using the Ru(phen)<sub>3</sub><sup>2+</sup> - KMnO<sub>4</sub> system. *Microchim Acta*. 2006;155(3-4):431-434. doi:10.1007/S00604-006-0513-1
337. He Z, Wu F, Meng H, Yuan L, Luo Q, Zeng Y. Chemiluminescence Determination of Sulfur Dioxide in Air Using Tris(1,10-Phenanthroline)Ruthenium–KIO<sub>4</sub> System. <http://dx.doi.org/10.1080/00032719908542828>. 2008;32(2):401-410. doi:10.1080/00032719908542828
338. Wu F, He Z, Luo Q, Zeng Y. High-Performance Liquid Chromatographic Determination of Oxalic Acid in Tea Using Tris(1,10-phenanthroline)-ruthenium(II) Chemiluminescence. *Anal Sci*. 1998;14(5):971-973. doi:10.2116/ANALSCI.14.971/METRICS
339. Perez-Tejeda P, Martínez-Delgado A, Grueso E, Giráldez-Pérez RM. Measuring nanoparticle-induced resonance energy transfer effect by electrogenerated chemiluminescent reactions. *RSC Adv*. 2020;10(7):3861-3871. doi:10.1039/C9RA08857A
340. Aissaoui N, Moth-Poulsen K, Käll M, Johansson P, Wilhelmsson LM, Albinsson B. FRET enhancement close to gold nanoparticles positioned in DNA origami constructs. *Nanoscale*. 2017;9(2):673-683. doi:10.1039/C6NR04852H
341. Gai QQ, Wang DM, Huang RF, Liang XX, Wu HL, Tao XY. Distance-dependent quenching and enhancing of electrochemiluminescence from tris(2, 2'-bipyridine) ruthenium (II)/tripropylamine system by gold nanoparticles and its sensing applications. *Biosens Bioelectron*. 2018;118:80-87. doi:10.1016/j.bios.2018.07.023
342. Anitha Devadoss Supervisors Robert Forster Tia E Keyes AJ. COLLOIDAL GOLD NANOPARTICLES FOR HIGH SENSITIVITY ECL BIOSENSORS: EFFECT OF SIZE AND SHAPE. Published online 2011.
343. Estalayo-Adrián S, McManus GJ, Dalton HL, Savyasachi AJ, Kelly JM, Gunnlaugsson T. Functionalisation of gold nanoparticles with ruthenium(II) polypyridyl complexes for their application in cellular imaging. *Dalt Trans*.

- 2020;49(40):14158-14168. doi:10.1039/D0DT02754E
344. Vernet G, Mullet WM, Lai EPC, et al. Single-Mismatch Position-Sensitive Detection of DNA Based on a Bifunctional Ruthenium Complex. *Anal Chem.* 2007;80(1):77-84. doi:10.1021/AC071095R
345. Ghosh A, Mandoli A, Kumar DK, et al. DNA binding and cleavage properties of a newly synthesised Ru(II)-polypyridyl complex. *Dalt Trans.* 2009;(42):9312-9321. doi:10.1039/B906756F
346. Lincoln P, Nordén B. DNA binding geometries of ruthenium(II) complexes with 1,10-phenanthroline and 2,2'-bipyridine ligands studied with linear dichroism spectroscopy. Borderline cases of intercalation. *J Phys Chem B.* 1998;102(47):9583-9594.  
doi:10.1021/JP9824914/ASSET/IMAGES/LARGE/JP9824914F00006.JPEG
347. Barton JK, Goldberg JM, Kumar C V., Turro NJ. Binding Modes and Base Specificity of Tris(phenanthroline)ruthenium(II) Enantiomers with Nucleic Acids: Tuning the Stereoselectivity. *J Am Chem Soc.* 1986;108(8):2081-2088.  
doi:10.1021/JA00268A057/ASSET/JA00268A057.FP.PNG\_V03
348. Kumar C V., Barton JK, Turro NJ. Photophysics of Ruthenium Complexes Bound to Double Helical DNA. *J Am Chem Soc.* 1985;107(19):5518-5523.  
doi:10.1021/JA00305A032/ASSET/JA00305A032.FP.PNG\_V03
349. Zeng Z, Zhan J, Zhang K, Chen H, Cheng S. Global, regional, and national burden of urinary tract infections from 1990 to 2019: an analysis of the global burden of disease study 2019. *World J Urol.* 2022;40(3):755-763. doi:10.1007/S00345-021-03913-0/FIGURES/4
350. Schulz WA. Uropathogenic bacteria leave a mark. *Lab Investig.* 2011;91:816-818.  
doi:10.1038/labinvest.2011.51
351. Bien J, Sokolova O, Bozko P. Role of Uropathogenic Escherichia coli Virulence Factors in Development of Urinary Tract Infection and Kidney Damage. *Int J Nephrol.* 2012;2012:15. doi:10.1155/2012/681473
352. Rossen JWA, Cruz-Córdova A, Maffei ME, Terlizzi ME, Gribaudo G. UroPathogenic Escherichia coli (UPEC) Infections: Virulence Factors, Bladder

- Responses, Antibiotic, and Non-antibiotic Antimicrobial Strategies. *Front Microbiol* | [www.frontiersin.org](http://www.frontiersin.org). 2017;1:1566. doi:10.3389/fmicb.2017.01566
353. Vendeville J-B, Kyriakides MJ, Takebayashi Y, et al. Fast Identification and Quantification of Uropathogenic *E. coli* through Cluster Analysis. Published online 2021. doi:10.1021/acsbio.1c00732
  354. Van Driel AA, Notermans & DW, Meima & A, et al. Antibiotic resistance of *Escherichia coli* isolated from uncomplicated UTI in general practice patients over a 10-year period. *Eur J Clin Microbiol Infect Dis*. 2019;38:2151-2158. doi:10.1007/s10096-019-03655-3
  355. Yang X, Chen H, Zheng Y, Qu S, Wang H, Yi F. Disease burden and long-term trends of urinary tract infections: A worldwide report. *Front Public Heal*. 2022;10. doi:10.3389/FPUBH.2022.888205/FULL
  356. Call ZD, Jang I, Geiss BJ, Dandy DS, Henry CS. Progress toward a Simplified UTI Diagnostic: Pump-Free Magnetophoresis for *E. coli* Detection. *Anal Chem*. 2022;94(21):7545-7550. doi:10.1021/ACS.ANALCHEM.2C00316/SUPPL\_FILE/AC2C00316\_SI\_003.M P4
  357. Martinson JN V., Walk ST. *Escherichia coli* residency in the gut of healthy human adults. *EcoSal Plus*. 2020;9(1). doi:10.1128/ECOSALPLUS.ESP-0003-2020
  358. Sarowska J, Futoma-Koloch B, Jama-Kmiecik A, et al. Virulence factors, prevalence and potential transmission of extraintestinal pathogenic *Escherichia coli* isolated from different sources: recent reports Gut Pathogens. *Gut Pathog*. doi:10.1186/s13099-019-0290-0
  359. Flores-Mireles AL, Walker JN, Caparon M, Hultgren SJ. Urinary tract infections: epidemiology, mechanisms of infection and treatment options. Published online 2015. doi:10.1038/nrmicro3432
  360. Hojati Z, Zamanzad B, Hashemzadeh M, Molaie R, Gholipour A. The FimH Gene in Uropathogenic *Escherichia coli* Strains Isolated From Patients With Urinary Tract Infection. *Jundishapur J Microbiol*. 2015;8(2):17520. doi:10.5812/JJM.17520

361. Avalos Vizcarra I, Hosseini V, Kollmannsberger P, et al. How type 1 fimbriae help *Escherichia coli* to evade extracellular antibiotics OPEN. *Nat Publ Gr*. Published online 2015. doi:10.1038/srep18109
362. Lo AW, Moriel DG, Phan MD, et al. ‘Omic’ Approaches to Study Uropathogenic *Escherichia coli* Virulence. *Trends Microbiol*. 2017;25(9):729-740. doi:10.1016/J.TIM.2017.04.006
363. Tchesnokova V, Aprikian P, Kisiela D, et al. Type 1 Fimbrial Adhesin FimH Elicits an Immune Response That Enhances Cell Adhesion of *Escherichia coli*. *Infect Immun*. 2011;79(10):3895. doi:10.1128/IAI.05169-11
364. Hasan RN, Jasim SA, Ali YH. Detection of fimH, kpsMTII, hlyA, and traT genes in *Escherichia coli* isolated from Iraqi patients with cystitis. *Gene Reports*. 2022;26:101468. doi:10.1016/J.GENREP.2021.101468
365. Velican AM, Lumini,ta L, Măru,tescu M, et al. Rapid Detection and Antibiotic Susceptibility of Uropathogenic *Escherichia coli* by Flow Cytometry. *Microorganisms*. 2022;8:1233. doi:10.3390/microorganisms8081233
366. Nair S, Gomez-Cruz J, Manjarrez-Hernandez Á, Ascanio G, Sabat RG, Escobedo C. Selective Uropathogenic *E. coli* Detection Using Crossed Surface-Relief Gratings. *Sensors* 2018, Vol 18, Page 3634. 2018;18(11):3634. doi:10.3390/S18113634
367. Sharma A, Agrawal A, Awasthi KK, Awasthi K, Awasthi A. Biosensors for diagnosis of urinary tract infections: Advances and future challenges. *Mater Lett X*. 2021;10:100077. doi:10.1016/J.MLBLUX.2021.100077
368. Campuzano S, Yáñez-Sedeño P, Manuel Pingarrón J. Molecular Biosensors for Electrochemical Detection of Infectious Pathogens in Liquid Biopsies: Current Trends and Challenges. doi:10.3390/s17112533
369. Wu Q, Zhang Y, Yang Q, Yuan N, Zhang W. Review of Electrochemical DNA Biosensors for Detecting Food Borne Pathogens. doi:10.3390/s19224916
370. Gutiérrez-Gálvez L, del Caño R, Menéndez-Luque I, et al. Electrochemiluminescent nanostructured DNA biosensor for SARS-CoV-2 detection. *Talanta*. 2022;240:123203. doi:10.1016/J.TALANTA.2021.123203

371. Cao Z, Su B. Light enhanced electrochemistry and electrochemiluminescence of luminol at glassy carbon electrodes. *Electrochem commun.* 2019;98:47-52. doi:10.1016/J.ELECOM.2018.11.016
372. Uskoković V. A historical review of glassy carbon: Synthesis, structure, properties and applications. *Carbon Trends.* 2021;5. doi:10.1016/J.CARTRE.2021.100116
373. Sharma S. Glassy Carbon: A Promising Material for Micro- and Nanomanufacturing. *Materials (Basel).* 2018;11(10). doi:10.3390/MA11101857
374. Zakaria ND, Omar MH, Ahmad Kamal NN, et al. Effect of Supporting Background Electrolytes on the Nanostructure Morphologies and Electrochemical Behaviors of Electrodeposited Gold Nanoparticles on Glassy Carbon Electrode Surfaces. *ACS Omega.* 2021;6(38):24419-24431. doi:10.1021/ACSOMEGA.1C02670/ASSET/IMAGES/LARGE/AO1C02670\_0011.JPEG
375. Zhao C, Niu L, Wang X, Sun W. Electrochemiluminescence of gold nanoparticles and gold nanoparticle-labelled antibodies as co-reactants. *RSC Adv.* 2018;8(63):36219-36222. doi:10.1039/C8RA07429A
376. Bezuneh TT, Fereja TH, Kitte SA, Li H, Jin Y. Gold nanoparticle-based signal amplified electrochemiluminescence for biosensing applications. *Talanta.* 2022;248. doi:10.1016/J.TALANTA.2022.123611
377. Pruitt KD, Tatusova T, Maglott DR. NCBI reference sequences (RefSeq): a curated non-redundant sequence database of genomes, transcripts and proteins. *Nucleic Acids Res.* 2007;35(Database issue). doi:10.1093/NAR/GKL842
378. Gunawardena G, Hills G, Montenegro I, Scharifker B. Electrochemical nucleation: Part I. General considerations. *J Electroanal Chem Interfacial Electrochem.* 1982;138(2):225-239. doi:10.1016/0022-0728(82)85080-8
379. Grujicic D, Pesic B. Electrodeposition of copper: the nucleation mechanisms. *Electrochim Acta.* 2002;47(18):2901-2912. doi:10.1016/S0013-4686(02)00161-5
380. Špringer T, Ermini ML, Špačková B, Jabloňků J, Homola J. Enhancing sensitivity of surface plasmon resonance biosensors by functionalized gold nanoparticles: Size matters. *Anal Chem.* 2014;86(20):10350-10356.

doi:10.1021/AC502637U/SUPPL\_FILE/AC502637U\_SI\_001.PDF

381. Gotti G, Fajerweg K, Evrard D, Gros P. Electrodeposited gold nanoparticles on glassy carbon: Correlation between nanoparticles characteristics and oxygen reduction kinetics in neutral media. *Electrochim Acta*. 2014;128:412-419. doi:10.1016/J.ELECTACTA.2013.10.172
382. Chiang HC, Wang Y, Zhang Q, Levon K. Optimization of the Electrodeposition of Gold Nanoparticles for the Application of Highly Sensitive, Label-Free Biosensor. *Biosens* 2019, Vol 9, Page 50. 2019;9(2):50. doi:10.3390/BIOS9020050
383. Etesami M, Mohamed N. Catalytic Application of Gold Nanoparticles Electrodeposited by Fast Scan Cyclic Voltammetry to Glycerol Electrooxidation in Alkaline Electrolyte. *Int J Electrochem Sci*. 2011;6(10):4676-4689. doi:10.1016/S1452-3981(23)18357-X
384. Trachioti MG, Lazanas AC, Prodromidis MI. Shedding light on the calculation of electrode electroactive area and heterogeneous electron transfer rate constants at graphite screen-printed electrodes. *Microchim Acta*. 2023;190(7):1-14. doi:10.1007/S00604-023-05832-W/FIGURES/9
385. Arrigan DWM. Nanoelectrodes, nanoelectrode arrays and their applications. *Analyst*. 2004;129(12):1157-1165. doi:10.1039/B415395M
386. Scandurra A, Iacono V, Boscarino S, Scalese S, Grimaldi MG, Ruffino F. Model of Chronoamperometric Response towards Glucose Sensing by Arrays of Gold Nanostructures Obtained by Laser, Thermal and Wet Processes. *Nanomater* 2023, Vol 13, Page 1163. 2023;13(7):1163. doi:10.3390/NANO13071163
387. Raju CV, Kumar SS. Co-reactant-free self-enhanced solid-state electrochemiluminescence platform based on poly(luminol)-gold nanocomposite for signal-on detection of mercury ion. *Sci Reports* 2021 111. 2021;11(1):1-11. doi:10.1038/s41598-021-86195-1
388. Zhuo Y, Wang HJ, Lei YM, et al. Electrochemiluminescence biosensing based on different modes of switching signals. *Analyst*. 2018;143(14):3230-3248. doi:10.1039/c8an00276b

389. Zhao C, Niu L, Wang X, Sun W. Electrochemiluminescence of gold nanoparticles and gold nanoparticle-labelled antibodies as co-reactants. Published online 2018. doi:10.1039/c8ra07429a
390. Kirschbaum-Harriman S, Duerkop A, Baeumner AJ. Improving ruthenium-based ECL through nonionic surfactants and tertiary amines. *Analyst*. 2017;142(14):2648-2653. doi:10.1039/C7AN00197E
391. Zhou M, Robertson GP, Roovers J. Comparative study of ruthenium(II) tris(bipyridine) derivatives for electrochemiluminescence application. *Inorg Chem*. 2005;44(23):8317-8325. doi:10.1021/IC0510112/SUPPL\_FILE/IC0510112SI20050621\_035054.PDF
392. Troian-Gautier L, Moucheron C. Ruthenium(II) Complexes bearing Fused Polycyclic Ligands: From Fundamental Aspects to Potential Applications. *Mol* 2014, Vol 19, Pages 5028-5087. 2014;19(4):5028-5087. doi:10.3390/MOLECULES19045028
393. Kirschbaum-Harriman S, Mayer M, Duerkop A, Hirsch T, Baeumner AJ. Signal enhancement and low oxidation potentials for miniaturized ECL biosensors via N-butyl-diethanolamine. *Analyst*. 2017;142(13):2469-2474. doi:10.1039/C7AN00261K
394. Han S, Niu W, Li H, Hu L, Yuan Y, Xu G. Effect of hydroxyl and amino groups on electrochemiluminescence activity of tertiary amines at low tris(2,2'-bipyridyl)ruthenium(II) concentrations. *Talanta*. 2010;81(1-2):44-47. doi:10.1016/J.TALANTA.2009.11.037
395. Rebecani S, Zanut A, Santo CI, Valenti G, Paolucci F. A Guide Inside Electrochemiluminescent Microscopy Mechanisms for Analytical Performance Improvement. *Anal Chem*. 2022;94(1):336-348. doi:10.1021/ACS.ANALCHEM.1C05065/ASSET/IMAGES/LARGE/AC1C05065\_0014.JPEG
396. Zhang X, Lu W, Ma C, et al. Insights into electrochemiluminescence dynamics by synchronizing real-time electrical, luminescence, and mass spectrometric measurements †. *Chem Sci*. 2022;13. doi:10.1039/d2sc01317g



397. Kamyabi MA, Alipour Z, Moharramnezhad M. An enzyme-free electrochemiluminescence insulin probe based on the regular attachment of ZnO nanoparticles on a 3-D nickel foam and H<sub>2</sub>O<sub>2</sub> as an efficient co-reactant †. Published online 2021. doi:10.1039/d0ay02071k
398. Hlongwane GN, Dodoo-Arhin D, Wamwangi D, Daramola MO, Moothi K, Iyuke SE. DNA hybridisation sensors for product authentication and tracing: State of the art and challenges. *South African J Chem Eng.* 2019;27:16-34. doi:10.1016/J.SAJCE.2018.11.002
399. Oberhaus F V., Frense D, Beckmann D. Immobilization Techniques for Aptamers on Gold Electrodes for the Electrochemical Detection of Proteins: A Review. *Biosens 2020, Vol 10, Page 45.* 2020;10(5):45. doi:10.3390/BIOS10050045
400. Zhang L, Li Z, Zhou X, et al. Hybridization performance of DNA/mercaptohexanol mixed monolayers on electrodeposited nanoAu and rough Au surfaces. *J Electroanal Chem.* 2015;757:203-209. doi:10.1016/J.JELECHEM.2015.09.032
401. Keighley SD, Li P, Estrela P, Migliorato P. Optimization of DNA immobilization on gold electrodes for label-free detection by electrochemical impedance spectroscopy. *Biosens Bioelectron.* 2008;23(8):1291-1297. doi:10.1016/J.BIOS.2007.11.012
402. Uehara TM, De Aguiar HB, Bergamaski K, Miranda PB. Adsorption of alkylthiol self-assembled monolayers on gold and the effect of substrate roughness: A comparative study using scanning tunneling microscopy, cyclic voltammetry, second-harmonic generation, and sum-frequency generation. *J Phys Chem C.* 2014;118(35):20374-20382. doi:10.1021/JP5054919/ASSET/IMAGES/LARGE/JP-2014-054919\_0006.JPEG
403. Barhoum A, J. Forster R. Label-free electrochemical immunosensor for picomolar detection of the cervical cancer biomarker MCM5. *Anal Chim Acta.* 2022;1225:340226. doi:10.1016/J.ACA.2022.340226
404. Peng H, Soeller C, Travas-Sejdic J. Novel conducting polymers for DNA sensing. *Macromolecules.* 2007;40(4):909-914. doi:10.1021/MA062060G/SUPPL\_FILE/MA062060GSI20061205\_051102.PDF

405. Yang Z, Castrignanò E, Estrela P, Frost CG, Kasprzyk-Hordern B. Community Sewage Sensors towards Evaluation of Drug Use Trends: Detection of Cocaine in Wastewater with DNA-Directed Immobilization Aptamer Sensors. *Sci Reports* 2016 61. 2016;6(1):1-10. doi:10.1038/srep21024
406. Butterworth A, Blues E, Williamson P, Cardona M, Gray L, Corrigan DK. SAM Composition and Electrode Roughness Affect Performance of a DNA Biosensor for Antibiotic Resistance. *Biosens* 2019, Vol 9, Page 22. 2019;9(1):22. doi:10.3390/BIOS9010022
407. Zheng H, Ma X, Chen L, et al. Label-free electrochemical impedance biosensor for sequence-specific recognition of double-stranded DNA. *Anal Methods*. 2013;5(19):5005-5009. doi:10.1039/C3AY40972D
408. Gou D, Xie G, Li Y, Zhang X, Chen H. Voltammetric immunoassay for Mycobacterium tuberculosis secretory protein MPT64 based on a synergistic amplification strategy using rolling circle amplification and a gold electrode modified with graphene oxide, Fe<sub>3</sub>O<sub>4</sub> and Pt nanoparticles. *Microchim Acta*. 2018;185(9):1-9. doi:10.1007/S00604-018-2972-6/FIGURES/4
409. Malinowska N, Białobrzaska W, Łęga T, et al. Antibody Modified Gold Electrode as an Impedimetric Biosensor for the Detection of Streptococcus pyogenes. *Sensors* 2020, Vol 20, Page 5324. 2020;20(18):5324. doi:10.3390/S20185324
410. Park BW, Yoon DY, Kim DS. Formation and modification of a binary self-assembled monolayer on a nano-structured gold electrode and its structural characterization by electrochemical impedance spectroscopy. *J Electroanal Chem*. 2011;661(2):329-335. doi:10.1016/J.JELECHEM.2011.08.013
411. Sui M, Kunwar S, Pandey P, Lee J. Strongly confined localized surface plasmon resonance (LSPR) bands of Pt, AgPt, AgAuPt nanoparticles. *Sci Reports* 2019 91. 2019;9(1):1-14. doi:10.1038/s41598-019-53292-1
412. Li MX, Zhang N, Zhao W, Luo XL, Chen HY, Xu JJ. Ultrasensitive detection of microRNA-21 based on plasmon-coupling-induced electrochemiluminescence enhancement. *Electrochem commun.* 2018;94:36-40. doi:10.1016/J.ELECOM.2018.08.003

413. Pan S, Li X, Yadav J. Single-nanoparticle spectroelectrochemistry studies enabled by localized surface plasmon resonance. *Phys Chem Chem Phys*. 2021;23(35):19120-19129. doi:10.1039/D1CP02801D
414. Manchon D, Lermé J, Zhang T, et al. Plasmonic coupling with most of the transition metals: a new family of broad band and near infrared nanoantennas. *Nanoscale*. 2014;7(3):1181-1192. doi:10.1039/C4NR05383D
415. Hong YA, Ha JW. Enhanced refractive index sensitivity of localized surface plasmon resonance inflection points in single hollow gold nanospheres with inner cavity. *Sci Reports 2022 121*. 2022;12(1):1-9. doi:10.1038/s41598-022-11197-6
416. Majidi S, Sehrig Z, Farkhani SM, et al. Current methods for synthesis of magnetic nanoparticles. *Nanomedicine, Biotechnol.* 2016;44(2):722-734. doi:10.3109/21691401.2014.982802
417. Mehta R V. Synthesis of magnetic nanoparticles and their dispersions with special reference to applications in biomedicine and biotechnology. *Mater Sci Eng C*. 2017;79:901-916. doi:10.1016/J.MSEC.2017.05.135
418. Chen YT, Kolhatkar AG, Zenasni O, Xu S, Lee TR. Biosensing Using Magnetic Particle Detection Techniques. *Sensors 2017, Vol 17, Page 2300*. 2017;17(10):2300. doi:10.3390/S17102300
419. Zhu Y, Zhang B, Gu J, Li S. Magnetic beads separation characteristics of a microfluidic bioseparation chip based on magnetophoresis with lattice-distributed soft magnets. *J Magn Magn Mater*. 2020;501:166485. doi:10.1016/J.JMMM.2020.166485
420. Henken RL, Chantiwas R, Gilman SD. Influence of Immobilized Biomolecules on Magnetic Bead Plug Formation and Retention in Capillary Electrophoresis. *Electrophoresis*. 2012;33(5):827. doi:10.1002/ELPS.201100353
421. Witte K, Müller K, Grüttner C, Westphal F, Johansson C. Particle size- and concentration-dependent separation of magnetic nanoparticles. Published online 2016. doi:10.1016/j.jmmm.2016.11.006
422. Ali A, Shah T, Ullah R, et al. Review on Recent Progress in Magnetic Nanoparticles: Synthesis, Characterization, and Diverse Applications. *Front*

*Chem.* 2021;9:548. doi:10.3389/FCHEM.2021.629054/BIBTEX

423. Bezinge L, Suea-Ngam A, Demello AJ, Shih CJ. Nanomaterials for molecular signal amplification in electrochemical nucleic acid biosensing: recent advances and future prospects for point-of-care diagnostics. *Mol Syst Des Eng.* 2020;5(1):49-66. doi:10.1039/C9ME00135B
424. Liu S, Yu B, Wang S, Shen Y, Cong H. Preparation, surface functionalization and application of Fe<sub>3</sub>O<sub>4</sub> magnetic nanoparticles. *Adv Colloid Interface Sci.* 2020;281:102165. doi:10.1016/J.CIS.2020.102165
425. Odularu AT. Metal Nanoparticles: Thermal Decomposition, Biomedical Applications to Cancer Treatment, and Future Perspectives. Published online 2018. doi:10.1155/2018/9354708
426. Ye L, Zhou L, Lu Y. Direct Continuous Synthesis of Oleic Acid-Modified Fe<sub>3</sub>O<sub>4</sub>Nanoparticles in a Microflow System. *Ind Eng Chem Res.* 2022;61(12):4320-4328. doi:10.1021/ACS.IECR.2C00028/ASSET/IMAGES/LARGE/IE2C00028\_0012.JPEG
427. Silva SM, Tavallaie R, Sandiford L, Tilley RD, Gooding JJ. Gold coated magnetic nanoparticles: from preparation to surface modification for analytical and biomedical applications. 7528 | *Chem Commun.* 2016;52:7528. doi:10.1039/c6cc03225g
428. Cai J, Miao YQ, Yu BZ, Ma P, Li L, Fan HM. Large-Scale, Facile Transfer of Oleic Acid-Stabilized Iron Oxide Nanoparticles to the Aqueous Phase for Biological Applications. *Langmuir.* 2017;33(7):1662-1669. doi:10.1021/ACS.LANGMUIR.6B03360/ASSET/IMAGES/LARGE/LA-2016-033607\_0005.JPEG
429. Jadhav N V., Prasad AI, Kumar A, et al. Synthesis of oleic acid functionalized Fe<sub>3</sub>O<sub>4</sub> magnetic nanoparticles and studying their interaction with tumor cells for potential hyperthermia applications. *Colloids Surf B Biointerfaces.* 2013;108:158-168. doi:10.1016/J.COLSURFB.2013.02.035
430. Cai J, Miao YQ, Yu BZ, Ma P, Li L, Fan HM. Large-Scale, Facile Transfer of

- Oleic Acid-Stabilized Iron Oxide Nanoparticles to the Aqueous Phase for Biological Applications. *Langmuir*. 2017;33(7):1662-1669. doi:10.1021/ACS.LANGMUIR.6B03360/ASSET/IMAGES/LARGE/LA-2016-033607\_0005.JPEG
431. Peng S, Wang C, Xie J, Sun S. Synthesis and stabilization of monodisperse Fe nanoparticles. *J Am Chem Soc*. 2006;128(33):10676-10677. doi:10.1021/JA063969H
432. Ansari SM, Sinha BB, Sen D, Sastry PU, Kolekar YD, Ramana C V. Effect of Oleylamine on the Surface Chemistry, Morphology, Electronic Structure, and Magnetic Properties of Cobalt Ferrite Nanoparticles. *Nanomaterials*. 2022;12(17):3015. doi:10.3390/NANO12173015/S1
433. Mbewana-Ntshanka NG, Moloto MJ, Mubiayi PK. Role of the amine and phosphine groups in oleylamine and trioctylphosphine in the synthesis of copper chalcogenide nanoparticles. *Heliyon*. 2020;6(11):e05130. doi:10.1016/J.HELIYON.2020.E05130
434. Mourdikoudis S, Menelaou M, Fiuza-Maneiro N, et al. Oleic acid/oleylamine ligand pair: a versatile combination in the synthesis of colloidal nanoparticles. *Nanoscale Horizons*. 2022;7(9):941-1015. doi:10.1039/D2NH00111J
435. Moraes Silva S, Tavallaie R, Sandiford L, Tilley RD, Gooding JJ. Gold coated magnetic nanoparticles: from preparation to surface modification for analytical and biomedical applications. *Chem Commun*. 2016;52(48):7528-7540. doi:10.1039/C6CC03225G
436. Nassireslami E, Ajdarzade M. Gold Coated Superparamagnetic Iron Oxide Nanoparticles as Effective Nanoparticles to Eradicate Breast Cancer Cells via Photothermal Therapy. *Adv Pharm Bull*. 2018;8(2):201. doi:10.15171/APB.2018.024
437. León Félix L, Sanz B, Sebastián V, et al. Gold-decorated magnetic nanoparticles design for hyperthermia applications and as a potential platform for their surface-functionalization. *Sci Reports* 2019 91. 2019;9(1):1-11. doi:10.1038/s41598-019-40769-2

438. Katz E. Synthesis, Properties and Applications of Magnetic Nanoparticles and Nanowires-A Brief Introduction. 2019;5:61. doi:10.3390/magnetochemistry5040061
439. DeAngelis MT, Rondinone AJ, Pawel MD, Labotka TC, Anovitz LM. Sol-gel synthesis of nanocrystalline fayalite ( $\text{Fe}_2\text{SiO}_4$ ). *Am Mineral*. 2012;97(4):653-656. doi:10.2138/AM.2012.3899
440. Robinson I, Tung LD, Maenosono S, Wälti C, Thanh NTK. Synthesis of core-shell gold coated magnetic nanoparticles and their interaction with thiolated DNA. *Nanoscale*. 2010;2(12):2624-2630. doi:10.1039/C0NR00621A
441. Wang L, Luo J, Fan Q, et al. Monodispersed core-shell  $\text{Fe}_3\text{O}_4@Au$  nanoparticles. *J Phys Chem B*. 2005;109(46):21593-21601. doi:10.1021/JP0543429
442. Stanglmair C, Scheeler SP, Pacholski C. Seeding growth approach to gold nanoparticles with diameters ranging from 10 to 80 nanometers in organic solvent. *Eur J Inorg Chem*. 2014;(23):3633-3637. doi:10.1002/EJIC.201402467
443. Niu J, Zhu T, Liu Z. One-step seed-mediated growth of 30–150 nm quasispherical gold nanoparticles with 2-mercaptopropionic acid as a new reducing agent. *Nanotechnology*. 2007;18(32):325607. doi:10.1088/0957-4484/18/32/325607
444. Klein S, Petersen S, Taylor U, Rath D, Barcikowski S. Quantitative visualization of colloidal and intracellular gold nanoparticles by confocal microscopy. <https://doi.org/10.1117/1.3461170>. 2010;15(3):036015. doi:10.1117/1.3461170
445. Leng W, Pati P, Vikesland PJ. Room temperature seed mediated growth of gold nanoparticles: mechanistic investigations and life cycle assesment. *Environ Sci Nano*. 2015;2(5):440-453. doi:10.1039/C5EN00026B
446. Liu X, Atwater M, Wang J, Huo Q. Extinction coefficient of gold nanoparticles with different sizes and different capping ligands. *Colloids Surfaces B Biointerfaces*. 2007;58(1):3-7. doi:10.1016/J.COLSURFB.2006.08.005
447. Dolinnyi AI. Extinction coefficients of gold nanoparticles and their dimers. Dependence of optical factor on particle size. *Colloid J*. 2017;79(5):611-620. doi:10.1134/S1061933X17050052/METRICS
448. Sanfilippo V, Caruso VCL, Cucci LM, Inturri R, Vaccaro S, Satriano C.

- Hyaluronan-Metal Gold Nanoparticle Hybrids for Targeted Tumor Cell Therapy. *Int J Mol Sci* 2020, Vol 21, Page 3085. 2020;21(9):3085. doi:10.3390/IJMS21093085
449. Link S, El-Sayed MA. Spectral Properties and Relaxation Dynamics of Surface Plasmon Electronic Oscillations in Gold and Silver Nanodots and Nanorods. *J Phys Chem B*. 1999;103(40):8410-8426. doi:10.1021/JP9917648/ASSET/IMAGES/LARGE/JP9917648F00014.JPEG
450. Gryns DB, De Nijs B, Salmon AR, et al. Citrate Coordination and Bridging of Gold Nanoparticles: The Role of Gold Adatoms in AuNP Aging. *ACS Nano*. 2020;14(7):8689-8696. doi:10.1021/ACSNANO.0C03050/ASSET/IMAGES/LARGE/NN0C03050\_0004.JPEG
451. Shahbazi N, Zare-Dorabei R. A Facile Colorimetric and Spectrophotometric Method for Sensitive Determination of Metformin in Human Serum Based on Citrate-Capped Gold Nanoparticles: Central Composite Design Optimization. *ACS Omega*. 2019;4(17):17519-17526. doi:10.1021/ACSOMEGA.9B02389/ASSET/IMAGES/LARGE/AO9B02389\_0002.JPEG
452. Wulandari P, Li X, Tamada K, Hara M. CONFORMATIONAL STUDY OF CITRATES ADSORBED ON GOLD NANOPARTICLES USING FOURIER TRANSFORM INFRARED SPECTROSCOPY. <https://doi.org/10.1142/S0218863508004032>. 2012;17(2):185-192. doi:10.1142/S0218863508004032
453. Zhang Y, Gu C, Schwartzberg AM, Chen S, Zhang JZ. Light-induced further agglomeration of metal particles. <https://doi.org/10.1117/12646308>. 2006;6131:111-120. doi:10.1117/12.646308
454. Plaisen S, Cheewasedtham W, Rujiralai T. Robust colorimetric detection based on the anti-aggregation of gold nanoparticles for bromide in rice samples. *RSC Adv*. 2018;8(38):21566-21576. doi:10.1039/C8RA03497D
455. Pellegrino T, Sperling RA, Alivisatos AP, Parak WJ. Gel Electrophoresis of Gold-DNA Nanoconjugates. *J Biomed Biotechnol*. 2007;2007:26796.

doi:10.1155/2007/26796

456. Fritzsche W, Taton TA. Metal nanoparticles as labels for heterogeneous, chip-based DNA detection. *Nanotechnology*. 2003;14(12). doi:10.1088/0957-4484/14/12/R01
457. Uludağ Y, Hammond R, Cooper MA. A signal amplification assay for HSV type 1 viral DNA detection using nanoparticles and direct acoustic profiling. *J Nanobiotechnology*. 2010;8(1):1-12. doi:10.1186/1477-3155-8-3/FIGURES/6
458. Mirsaidov U, Comer J, Dimitrov V, Aksimentiev A, Timp G. Slowing the Translocation of Double-Stranded DNA Using a Nanopore Smaller than the Double Helix. *Nanotechnology*. 2010;21(39):395501. doi:10.1088/0957-4484/21/39/395501
459. Smith CL, Milea JS, Nguyen GH. Immobilization of nucleic acids using biotin-strept(avidin) systems. *Top Curr Chem*. 2005;261:63-90. doi:10.1007/128\_017/COVER
460. Šnejdárková M, Svobodová L, Polohová V, Hianik T. The study of surface properties of an IgE-sensitive aptasensor using an acoustic method. *Anal Bioanal Chem*. 2008;390(4):1087-1091. doi:10.1007/S00216-007-1749-2/FIGURES/4
461. Hill HD, Millstone JE, Banholzer MJ, Mirkin CA. The role radius of curvature plays in thiolated oligonucleotide loading on gold nanoparticles. *ACS Nano*. 2009;3(2):418-424. doi:10.1021/NN800726E/ASSET/IMAGES/LARGE/NN-2008-00726E\_0009.JPEG
462. Schwartz JJ, Quake SR. High density single molecule surface patterning with colloidal epitaxy. *Appl Phys Lett*. 2007;91(8). doi:10.1063/1.2772762/326566
463. Cumba LR, Camisasca A, Giordani S, Forster RJ. Electrochemical Properties of Screen-Printed Carbon Nano-Onion Electrodes. *Molecules*. 2020;25(17):3884. doi:10.3390/molecules25173884
464. Kreft S, Wei D, Junge H, Beller M. Recent advances on TiO<sub>2</sub>-based photocatalytic CO<sub>2</sub> reduction. *EnergyChem*. 2020;2(6):100044. doi:10.1016/J.ENCHEM.2020.100044
465. Rehman ZU, Bilal M, Hou J, et al. Photocatalytic CO<sub>2</sub> Reduction Using TiO<sub>2</sub>-



- Based Photocatalysts and TiO<sub>2</sub> Z-Scheme Heterojunction Composites: A Review. *Mol* 2022, Vol 27, Page 2069. 2022;27(7):2069. doi:10.3390/MOLECULES27072069
466. Khataee AR, Kasiri MB. Photocatalytic degradation of organic dyes in the presence of nanostructured titanium dioxide: Influence of the chemical structure of dyes. *J Mol Catal A Chem.* 2010;328(1-2):8-26. doi:10.1016/J.MOLCATA.2010.05.023
467. Yang XN, Cui FY. Stability of nano-sized titanium dioxide in an aqueous environment: effects of pH, dissolved organic matter and divalent cations. *Water Sci Technol.* 2013;68(2):276-282. doi:10.2166/WST.2013.165
468. Jiao J, Wei Y, Zhao Z, et al. Photocatalysts of 3D ordered macroporous TiO<sub>2</sub>-supported CeO<sub>2</sub> nanolayers: Design, preparation, and their catalytic performances for the reduction of CO<sub>2</sub> with H<sub>2</sub>O under simulated solar irradiation. *Ind Eng Chem Res.* 2014;53(44):17345-17354. doi:10.1021/IE503333B/SUPPL\_FILE/IE503333B\_SI\_001.PDF
469. Yu L, Xie Y, Zhou J, Li Y, Yu Y, Ren Z. Robust and selective electrochemical reduction of CO<sub>2</sub>: the case of integrated 3D TiO<sub>2</sub>@MoS<sub>2</sub> architectures and Ti-S bonding effects. *J Mater Chem A.* 2018;6(11):4706-4713. doi:10.1039/C7TA11376E
470. Song Q, Shen B, Yu J, Cao S. A 3D Hierarchical Ti<sub>3</sub>C<sub>2</sub>T<sub>x</sub>/TiO<sub>2</sub> Heterojunction for Enhanced Photocatalytic CO<sub>2</sub> Reduction. *ChemNanoMat.* 2021;7(8):910-915. doi:10.1002/CNMA.202100155
471. Jiao J, Wei Y, Zhao Z, et al. Synthesis of 3D ordered macroporous TiO<sub>2</sub>-supported Au nanoparticle photocatalysts and their photocatalytic performances for the reduction of CO<sub>2</sub> to methane. *Catal Today.* 2015;258:319-326. doi:10.1016/J.CATTOD.2015.01.030
472. Browne MP, Urbanova V, Plutnar J, Novotný F, Pumera M. Inherent impurities in 3D-printed electrodes are responsible for catalysis towards water splitting. *J Mater Chem A.* 2020;8(3):1120-1126. doi:10.1039/C9TA11949C
473. Elkoro A, Soler L, Llorca J, Casanova I. 3D printed microstructured Au/TiO<sub>2</sub>

- catalyst for hydrogen photoproduction. *Appl Mater Today*. 2019;16:265-272. doi:10.1016/J.APMT.2019.06.007
474. Zhao C, Wang C, Gorkin R, Beirne S, Shu K, Wallace GG. Three dimensional (3D) printed electrodes for interdigitated supercapacitors. *Electrochem commun*. 2014;41:20-23. doi:10.1016/J.ELECOM.2014.01.013
475. Aguirre-Cortés JM, Moral-Rodríguez AI, Bailón-García E, Davó-Quiñonero A, Pérez-Cadenas AF, Carrasco-Marín F. 3D printing in photocatalysis: Methods and capabilities for the improved performance. *Appl Mater Today*. 2023;32:101831. doi:10.1016/J.APMT.2023.101831
476. Furugori S, Kobayashi A, Watanabe A, Yoshida M, Kato M. Impact of Photosensitizing Multilayered Structure on Ruthenium(II)-Dye-Sensitized TiO<sub>2</sub>-Nanoparticle Photocatalysts. *ACS Omega*. 2017;2(7):3901-3912. doi:10.1021/ACSOMEGA.7B00566/SUPPL\_FILE/AO7B00566\_SI\_002.CIF
477. Mongal BN, Tiwari A, Malapaka C, Pal U. Ruthenium(III)-bis(phenolato)bipyridine/TiO<sub>2</sub> hybrids: unprecedented photocatalytic hydrogen evolution. *Dalt Trans*. 2019;48(27):10070-10077. doi:10.1039/C9DT01506J
478. Ismael M. Highly effective ruthenium-doped TiO<sub>2</sub> nanoparticles photocatalyst for visible-light-driven photocatalytic hydrogen production. *New J Chem*. 2019;43(24):9596-9605. doi:10.1039/C9NJ02226K
479. Peng T, Dai K, Yi H, Ke D, Cai P, Zan L. Photosensitization of different ruthenium(II) complex dyes on TiO<sub>2</sub> for photocatalytic H<sub>2</sub> evolution under visible-light. *Chem Phys Lett*. 2008;460(1-3):216-219. doi:10.1016/J.CPLETT.2008.06.001
480. Athanas Anish B, Thangaraj S, Kalaiyar S. Co-sensitization of ruthenium(II) dye-sensitized solar cells by coumarin based dyes. *Chem Phys Lett*. 2018;699:32-39. doi:10.1016/J.CPLETT.2018.03.033
481. Leem G, Morseth ZA, Wee K-R, et al. Ruthenium Sensitizers Polymer-Based Ruthenium(II) Polypyridyl Chromophores on TiO<sub>2</sub> for Solar Energy Conversion. doi:10.1002/asia.201501384
482. Ali MM, Pervez W, Ghann W, Uddin J. Photophysical Studies of Ruthenium-

Based Complexes and the Performance of Nanostructured TiO<sub>2</sub> Based Dye Sensitized Solar Cells. *J Nanomed Nanotechnol.* 2019;10(6). doi:10.35248/2157-7439.19.10.538

483. Rajaramanan T, Natarajan M, Ravirajan P, Senthilnathanan M, Velauthapillai D. Ruthenium (Ru) Doped Titanium Dioxide (P25) Electrode for Dye Sensitized Solar Cells. *Energies* 2020, Vol 13, Page 1532. 2020;13(7):1532. doi:10.3390/EN13071532